March 2021

Defect Engineering in Strained Low-Dimensional ABO3 Perovskite Nanoparticles for Next-Generation Energy Storage

Tochukwu Ofoegbuna

DEFECT ENGINEERING IN STRAINED LOW-DIMENSIONAL ABO_3 PEROVSKITE NANOPARTICLES FOR NEXT-GENERATION ENERGY STORAGE

A Dissertation

Submitted to the Graduate Faculty of the
Louisiana State University and
Agricultural and Mechanical College
in partial fulfillment of the
requirements for the degree of
Doctor of Philosophy

in

The Gordon A. and Mary Cain Department of Chemical Engineering

by
Tochukwu Ofoegbuna
B.S., University of Houston, 2015
May 2021

Acknowledgements

I am extremely grateful to my Ph.D. advisor, Dr. James Dorman for allowing me to join his research group. I remember when we first met, he told me that, “although I do not have direct funding in this project, I am interested in this area and I would like for you to join us if you are also interested in this area.” This started a 5-year journey that has been filled with many long hours in the lab analyzing data and reading/writing papers. As a *researcher*, he has constantly motivated me to always aim to push my research to new directions, which will contribute to the body of knowledge available to the scientific community. This included learning experimental as well as computational techniques to improve the quality of my research. As a *teacher*, he made sure that I understood the importance of being able to effectively present and communicate my results. This has become an invaluable skill that I will constantly aim to improve upon. As a *mentor*, he was always available to meet with me to discuss any issues that I might be experiencing. Overall, the guidance I have received from him is the reason I am able to complete this dissertation and to become a more versatile researcher.

Furthermore, I would like to thank the other members of my dissertation committee (Dr. John Flake, Dr. Ying Wang, and Dr. Ayman Okeil) for their support, guidance, and valuable feedback. In particular, Dr. John Flake and his students (Benjamin Peterson and Evan Andrews), whose assistance and advice made this project what it is today. I would also like to thank Dr. Orhan Kizilkaya from Center for Advanced Microstructures & Devices, LSU for his assistance in performing the synchrotron experiments and Dr. Craig Plaisance from LSU Chemical Engineering Department, for his useful discussion regarding theoretical calculations. I would like to thank other collaborators of my research including: Dr. Stuart A. J. Thomson, Edinburgh Instruments Ltd. and Dr. Rongying Jin, LSU Physics Department, for their valuable support. I

would like to acknowledge the fellowship support from the Louisiana College of Engineering (CHE-1709902) and the financial support from the Board of Regents (LEQSF(2016-19)-RD-A-03). I would like to thank both my former (Dr. Smriti Sahu, Dr. Pragathi Darapaneni, and Behnam Safavinia) and current (Natalia Moura, Khashayar Ramezani Bajgiran, Yuming Wang, Cameron Roman, Bernard Whajah, and Jonathan Lucas) lab mates. I would also like to thank the undergraduate and high school students that have contributed to this work. I greatly appreciate the time and effort they put into this work.

Finally, I would like to thank my friends and family, my biggest source of support, especially over these past 5 years. This includes my mother (Josephine), father (Michael), brother (Chibuike), and sister (Ifoma), without whom this would not be possible. My close friends (Lily Shi, Khashayar Ramezani Bajgiran, Natalia Moura, Daniel Willis, and Vivian Chang) have helped to bring joy to this Ph.D. experience and I am utterly grateful to them.

Table of Contents

List of Tables

List of Figures

Abstract

The realization of renewable energy is dependent on the advancement of multi-functional materials for energy storage devices. As an example, the substantial progress observed in Li-ion batteries is a result of the discovery and subsequent industrial commercialization of cathode materials such as $LiFePO_4$ (LFP). Although these materials possess relatively high specific capacity (~170 mAh/g), their low room-temperature electronic conductivity has been identified as a limitation for future high-performance batteries. Metastable $SrBO_3$, (SBO, B = Nb, Ta, Mo, etc.) perovskite nanoparticles (NPs) with metallic properties offer an alternative route to improve the room-temperature electronic conductivity of LFP cathodes. Therefore, this work aims to demonstrate how the optoelectronic properties of metastable SBO perovskite NPs can be leveraged for applications in advanced energy storage. The layered film architecture is taken advantage of in order to synergistically couple the metallic conduction of the SBO perovskite internal layer with the high Li-ion conductivity of the olivine top layer to obtain improved electrochemical performance.

Despite the recent attention, the synthesis of SBO NPs using traditional wet-chemical methods result in B-site cations stabilized in highly oxidized states (i.e. Nb^{5+}, Ta^{5+}, Mo^{6+}, etc.), rather than the desired 4+ valency. These over-oxidized states, present as surface/bulk defect states, suppress the expected optoelectronic responses. For this reason, the engineering of these defect states to recover the optoelectronic properties of metastable SBO perovskites is the main objective of this work. To address this challenge, the facile oxygen-controlled CP/MSS method was developed. The low-pressure environment reduces the partial pressure of oxygen during the crystallization process which allows for the simultaneous intercalation of Sr ions and suppression of defect states. Finally, a reducing post-treatment allows for further inhibition of these defect

states, which triggers a change in the powder color (white, insulating to colored, metallic). These findings highlight the potential application of these materials as conductive scaffolds that otherwise would not be possible with traditional solution-based methods. As a proof of concept, a $LiFePO_4$ top layer is deposited onto these conductive SBO perovskites to demonstrate their potential application in Li-ion batteries. Incorporation of the conductive scaffold significantly improves the charge transport properties of LFP, highlighting the promising electrochemical potential of these engineered nanomaterials. Ultimately, this ability to modify the charge transport response using these conductive scaffold materials will contribute to the design/development of next-generation energy storage and conversion technology.

Chapter 1 . Introduction

1.1. Research Objective

The purpose of this research is to engineer defect states within metastable perovskite oxide (ABO_3, B = Nb, Ta, Mo, etc.) nanoparticles (NPs) to control the resulting optoelectronic properties for potential applications in advanced energy storage. The objective of the research includes:

- Developing a novel wet-chemical synthetic approach, which will enable the crystallization of ABO_3 perovskite nanostructures with multi-valent B-sites by controlling defect incorporation.
- Modifying the structure and composition of ABO_3 perovskite nanostructures and probe the resultant changes using various structural, optical, and electronic characterization combined with first-principles calculations.
- Demonstrating the tuning of charge transport properties using the metallic conductivity of the metastable ABO_3 perovskite. This ability to tune the charge transport properties of metal oxides will have implications for advanced energy storage devices such as Li-ion batteries.

These engineered materials will contribute to addressing the ~20-38% increase in energy demand highlighted by the U.S. Department of Energy (DOE) by impacting energy storage and conversion (Crabtree, Rublof et al. 2017, Mai, Jadun et al. 2018), serving as a conductive scaffold for light absorbers/converters, as seen in chalcogenide-based solar cells.

1.2. Motivation

It is estimated that the world's population will increase by 36% by the year 2040, translating to a 30% increase in the global energy demand (Leach and Dry 2018). At this point,

the energy storage market is predicted to grow from 0.5 to 950 GW (Figure 1.1(a)) becoming a $620 billion industry with China and the United States dominating the market (Henze 2018). The United States market, presented in blue, is expected to experience a ~300% increase during this period. In addition to energy storage devices, energy conversion technologies are also positioned to experience considerable growth during this period. The projected increase in global solar generation (Figure 1.1(b)) reflects the growing presence of photovoltaic technologies in the global market (EIA 2020). This increasing trend is also associated with the favorable governmental policies in the region with the United States being among the top five countries expected to experience considerable growth in its solar generation market. The remaining four locations (Middle East, India, China, and European countries) are in the Organization for Economic Cooperation and Development (OECD Europe). The observed growth in these two major global markets (i.e., energy storage and conversion) is attributed to the shifting attention to harnessing and integrating renewable energy sources.

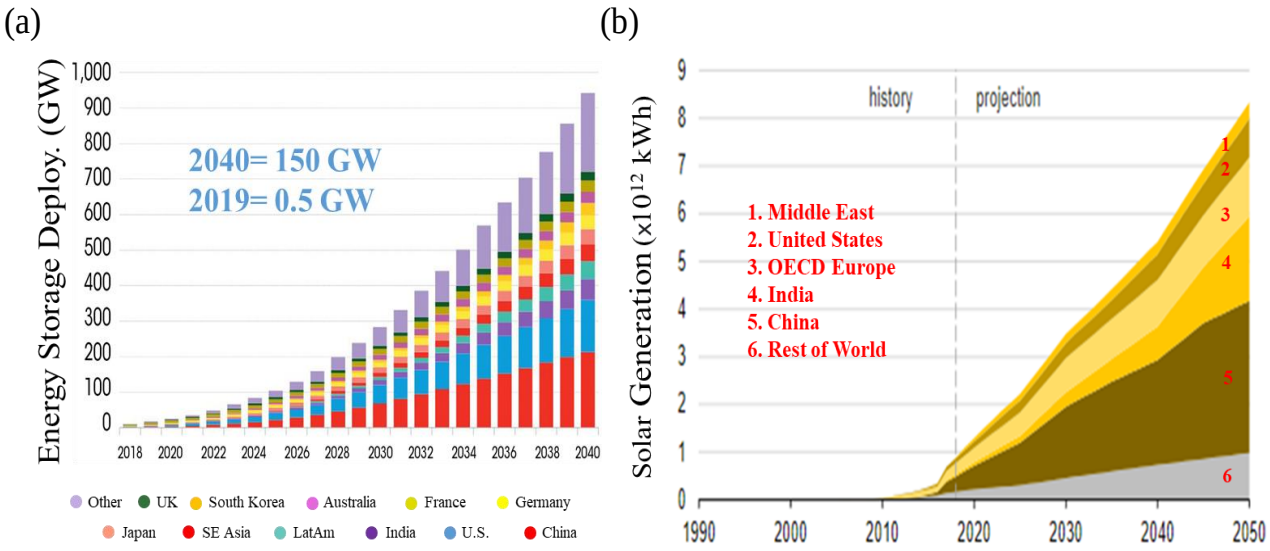

Figure 1.1 (a) Annual global energy storage deployment projections highlighting that by the year 2040 China (red) and United States (blue) will dominate the $620 billion industry (b) Annual global solar generation projections highlighting increasing solar energy growth due to the deployment of energy conversion technology (Henze 2018, EIA 2020).

Renewable energy is of interest as an alternative source of power to remedy the growing energy demand because it is derived from processes (i.e. solar, wind, geothermal, etc.) that can be readily replenished and offers lower emissions/pollutions. For instance, the greenhouse generation (GHG) of solar energy (16 - 73 g CO_2 equivalent kWh^{-1}) is orders of magnitude lower than coal and natural gas (413 - 1,144 g CO_2 equivalent kWh^{-1}) (Figure 1.2) (Edenhofer, Pichs-Madruga et al. 2011, Hernandez, Armstrong et al. 2019). The decreasing trend in the cost of deploying solar-based technology (from ~0.30 USD/kWh, 2010 to ~0.07 USD/kWh, 2021) has significantly enhanced the utility of solar energy (Agency IRENA 2020). Additionally, wind energy offers an energy source that is equally as clean as solar energy, with GHG emissions of 2 - 86 g CO_2 equivalent kWh^{-1} (Edenhofer, Pichs-Madruga et al. 2011, Wang and Wang 2015). Government policies such as the American Recovery and Reinvestment Act (United States, ~21 billion USD), Chinese Renewable Energy Law (China, ~612 billion USD), Korean Green New Deal (South Korea, ~7 billion USD) laid the foundation for making the deployment of wind-based technology economically viable (China 2011, Mundaca and Richter 2015, Lee and Woo 2020). Furthermore, in the United States, a cost savings of ~1.5 billion USD is predicted from using renewable energy systems to reduce GHG emissions (Igusky, Gasper et al. 2014). Despite the apparent environmental and financial impacts of renewable energy sources, it is important to note that renewable energy is "variable, uncertain, and location-specific", which demands for a flexible and high density energy storage method (Cebulla, Haas et al. 2018).

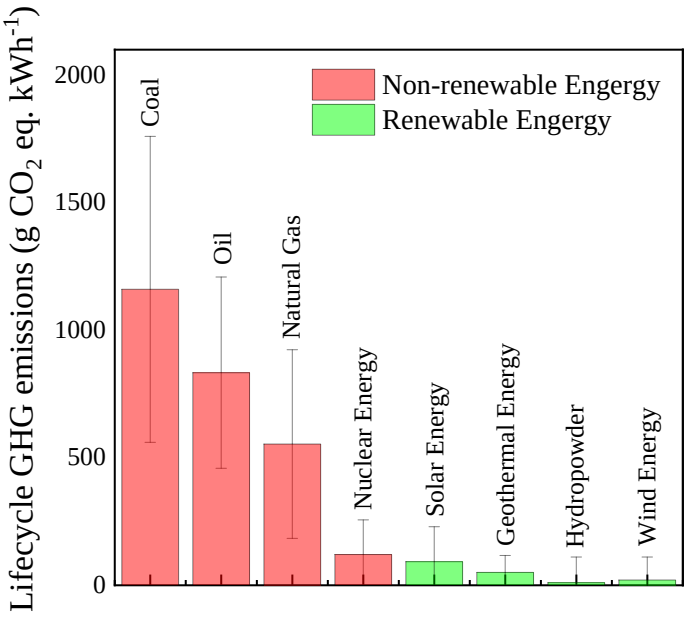

Figure 1.2 Greenhouse generation (GHG) for various energy sources. Renewable energy sources (green) in general offer lower GHG compared to non-renewable sources (red). Adapted from (Edenhofer, Pichs-Madruga et al. 2011).

In order to address the challenges of utilizing renewable sources to respond to the energy demand, the DOE highlights the need to develop multi-functional materials to accelerate advancements in current energy storage technologies (Crabtree, Rublof et al. 2017). As an example, multi-functional materials can be used to maximize the amount of electrochemically active material present in batteries, enabling improved understanding and control over electron/ion transport within complex electrode architectures (Crabtree, Rublof et al. 2017). Simultaneously, the Department of Defense (DOD) has expressed interest in the development of new multi-functional materials for their applications in medicine, catalysis science, environment, and national security (Nothwang 2012). For instance, the stored electrochemical energy in batteries are currently being applied to power portable medical devices, night vision goggles, communication devices, weapon optics, etc. (Strout 2020). The stored chemical energy in fuel cells can be utilized to reliably and sustainably convert hydrogen into electricity for unmanned

aerial vehicles (Gross, Poche Jr et al. 2011). Fuel cells can also be employed as primary and backup power units for wastewater treatment plants, communications and emergency networks, and data centers (Curtin, Gangi et al. 2012). The stored electrical energy in capacitors can be used to provide pulsed power for electromagnetic launch of projectiles, high-energy lasers, railguns, and other advanced weapons (Council 2003). Overall, advancements in multi-functional materials for energy storage applications is a challenge that directly impacts various fields.

1.3. Limitations in Ceramic-based Devices

Metals, polymers, and ceramics embody the basic building blocks of all materials (Table 1.1). Metals are characterized by their high electrical/thermal conductivity, the ability to be deformed without breaking, and high mechanical strength (Rösler, Harders et al. 2007). They are also often vulnerable to corrosion from their environment, which induces physical and chemical changes. These materials have been incorporated into batteries and fuel cells due to their high specific capacity (i.e., Li, 3860 mAh g^{-1}; Al, 2981 mAh g^{-1}; etc.), however, their chemical instability makes them unfavorable for widespread commercial applications (Li and Lu 2017, Biemolt, Jungbacker et al. 2020, Wang, Kerr et al. 2020). Polymers are macromolecules formed from the chemical bonding of smaller molecules (monomer) (McKeen 2017). Their strength, stiffness, and melting temperatures are generally much lower than that of metals and ceramics. They are popular for capacitors, batteries, and fuel cells due to their light weight and flexibility, which is necessary for portable devices. However, the internal temperatures of these devices can at times exceed the thermal stability of the material, contributing to device degradation (Bryan, Santino et al. 2016, McKeen 2017). Finally, all non-metallic and non-organic materials are referred to as ceramics, which includes compounds such as oxides, nitrides, and carbides (Rösler,

Harders et al. 2007). Due to this diverse selection of compounds, ceramics can be electrically/thermally insulating and conductive. This class of materials have specifically been utilized in capacitors, batteries, and fuel cells due to their wide application temperature range and resistance to harsh chemical environments (corrosion) (Hojo 2019). Unfortunately, ceramics tend to have lower specific capacity (~150-460 mAh g^{-1} (theoretical specific capacity of Li_2MnO_3)) in comparison to metals (Li, Yao et al. 2019). Despite their low specific capacity, it is expected that future energy storage devices will be increasingly reliant on these materials because of their overwhelming advantages.

Table 1.1 Classification of materials and application in energy storage devices (Rösler, Harders et al. 2007).

Material Types	Examples	Energy Storage Configuration	Advantages	Disadvantages
Metals	Li, Al, Zn, V, etc.	Batteries, Fuel Cells	High specific capacity	Chemical stability
Polymers	Polyvinylidene Difluoride (PVDF), Polyimide, etc.	Capacitors, Batteries, Fuel Cells	Flexible, Light weight	Thermal stability
Ceramics	$BaTiO_3$, $LiCoO_2$, etc.	Capacitors, Batteries, Fuel Cells	Wide application temperature range, Chemical stability	Low specific capacity

Ceramics are comprised of three major categories: (i) functional ceramics; (ii) structural ceramics and (iii) bioceramics. Functional ceramics refer to select ceramics designed for

applications requiring electric, magnetic or optical properties (Rödel, Kounga et al. 2009). Examples of functional ceramics include dielectrics, piezoelectrics, pyroelectrics, ferroelectrics, etc. Structural ceramics refer to ceramics that are designed to withstand mechanical or thermal loading (Pask 1989). Thus, these materials are developed by engineering the mechanical properties (brittle behavior, fracture toughness, etc.) rather than the electric, magnetic or optical properties. Bioceramics are specially designed ceramics for medical applications such as repairing or replacing damaged bone tissues (Frayssinet, Rouquet et al. 2011). These ceramics are developed to be mainly biocompatible and degradable, allowing for their removal after the bone is reconstructed. According to the 2010-2025 roadmap for advance ceramic materials (Figure 1.3) (Rödel, Kounga et al. 2009), significant growth/demand is especially predicted for functional ceramics as these have applications in energy storage, electronic, and environmental remediation. Based on Figure 1.3, ceramics as components for chemical/electrical energy storage (outlined in red) are of increasing relevance to contribute to the energy storage concerns introduced in Section 1.2.

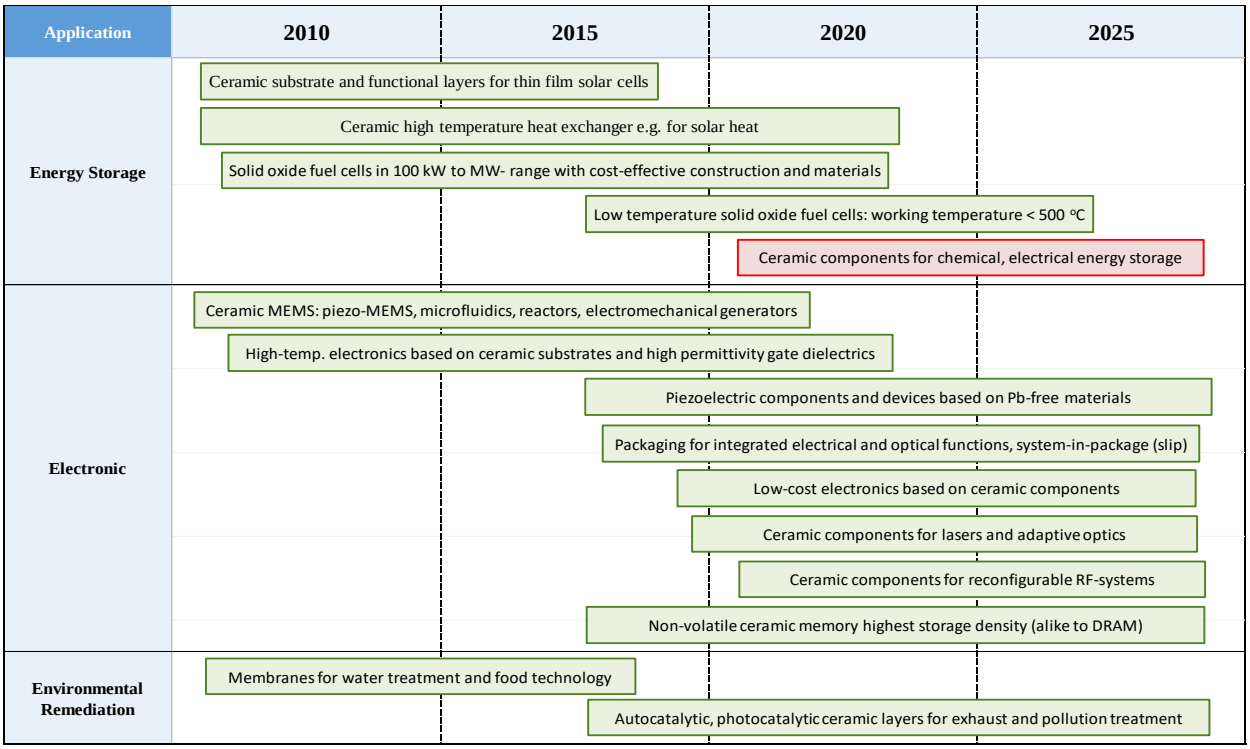

Figure 1.3 Roadmap for ceramic materials in the energy, electronic, and environmental applications. The roadmap shows that ceramic materials for chemical/electrical energy storage (in red) has tremendous growth opportunities for future technological development. Adapted from (Rödel, Kounga et al. 2009).

The key figures of merit for chemical/electrical energy storage devices are their energy and power densities, as depicted by the Ragone plot (Figure 1.4) (Ragone 1968). The main chemical/electrical energy storage devices include capacitors, supercapacitors, batteries, and fuel cells. Firstly, capacitors electrostatically store/release energy through the accumulation of charges on the surface of the active materials. Typically, the active material, a solid dielectric film, is placed between two metal electrodes and acts as a charge transport medium. This charge storage/delivery mechanism is fast (~μs to ms) because it is driven by surface transport, allowing for a high flux of energy for a short period of time (power density) (Han, Meng et al. 2015, Palneedi, Peddigari et al. 2018). Supercapacitors (electrochemical capacitors) address the

observed time issue of capacitors by utilizing a different charge storing mechanism. For these devices, energy is stored at the electrolyte-active material interface through the reversible adsorption of ions, which charges/discharges the electrical double-layer capacitance (Simon and Gogotsi 2010). As with capacitors, this surface storage method allows for very fast energy delivery as well as the added benefit of a longer time. Unlike (super)capacitors, batteries and fuel cells store/release charge in the bulk of the active material through the forming and breaking of chemical bonds (i.e., electrochemical reduction-oxidation reactions) (Simon and Gogotsi 2010). This process is slower (Palneedi, Peddigari et al. 2018), since it depends on surface and bulk transport, allowing for a small amount of energy over a long period of time (energy density). To address the challenges posed by the growing energy demand, there has been a push for designing devices with high energy and power densities (Figure 1.4). Along this line, multi-functional materials will be pivotal for designing next-generation energy storage devices, which possess the combination of battery (high energy density) and capacitor (high power density) characteristics in one electrochemical system. This objective is possible because multi-functional materials with the desired physical, electronic, and chemical properties allow for the surface/bulk charge transport response of the active material to be modified, leading to enhanced electrochemical performances (Goodenough, Abruna et al. 2007, Crabtree, Rublof et al. 2017). Therefore, the design of new multi-functional ceramic materials is paramount to the realization of next-generation energy storage technology.

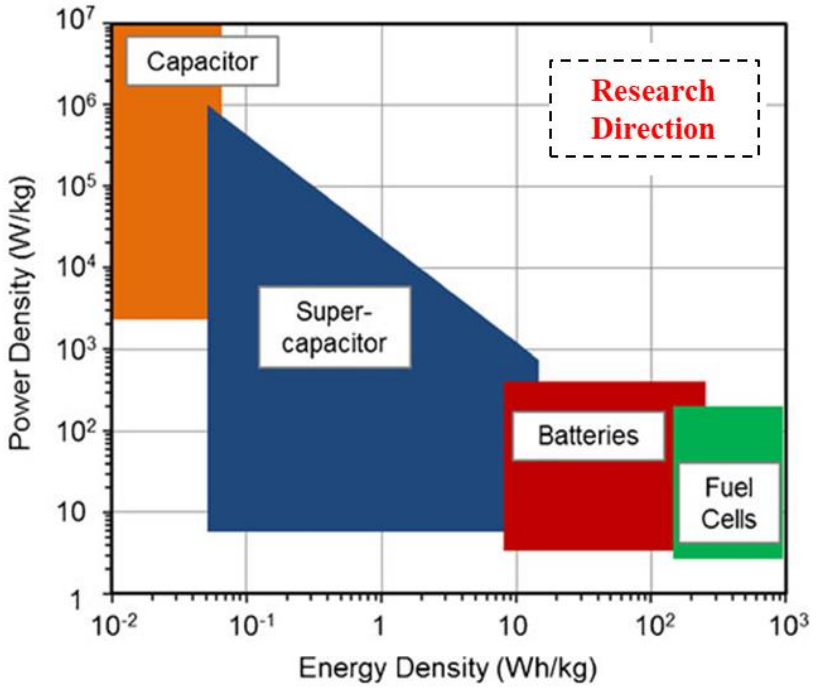

Figure 1.4 Research direction for energy storage devices. Adapted from (Meng, Gall et al. 2013).

Among chemical/electrical energy storage devices, Li-ion batteries have experienced prolonged success for more than 20 years due to their superior specific energy (~265 Wh/kg) and energy density (~690 Wh/L), especially when compared to other commercial rechargeable batteries (Reddy, Subba Rao et al. 2013, Abraham 2015). The success of this technology is firstly due to its robust and straightforward battery chemistry. During the charge cycle of a Li-ion battery, Li-ions flow from the cathode (positive electrode) to anode (negative electrode) via the electrolyte, which in turn drives electrons to flow in the same direction through the electrical leads to stabilize the charge at the anode, thus completing the electrochemical reaction (Park, Zhang et al. 2010). This process is subsequently reversed during the discharge cycle (Figure 1.5). Considering the above description, the general electrochemical reaction for charging/discharging a ceramic oxide cathode and graphitic anode is summarized as followed:

$$Li{-}MO_x \leftrightarrow MO_x + Li^+ + e^- \qquad E^o > 3.0\,V\ (vs\ Li/Li^+) \qquad (Cathode)$$

$$Li^+ + 6C + e^- \leftrightarrow LiC_6 \qquad E^o = 0.2\,V\ (vs\ Li/Li^+) \qquad (Anode)$$

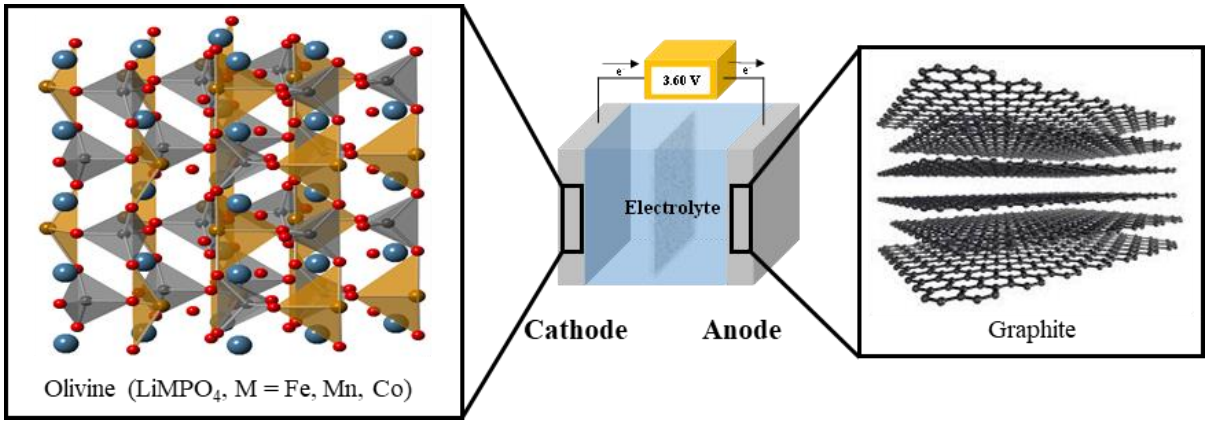

Figure 1.5 Energy storage based on Li-ion batteries. The figure depicts the charge cycle for this device. Adapted from (Park, Zhang et al. 2010, Wong, Ambrosi et al. 2012).

Secondly, the substantial progress observed in Li-ion batteries is a result of the discovery and subsequent industrial commercialization of ceramic oxide cathodes such as Spinel $LiMn_2O_4$ (LMO), Layered $LiCoO_2$ (LCO), and Olivine $LiFePO_4$ (LFP) (Park, Zhang et al. 2010). Table 1.2 summarizes key aspects of each material based on their electronic properties, electrochemical performance, and thermodynamics. In comparison to LFP (~10^9 Ω-cm), LCO (~10^4 Ω-cm) and LMO (~10^6 Ω-cm) possess higher electronic conductivity (Park, Zhang et al. 2010). Despite this difference, generally higher practical discharge capacities have been observed for LFP (~70-150 mAh g^{-1}). Interestingly, by improving the electronic conductivity of $LiCoO_2$ via Ni and Mn co-doping ($LiNi_xMn_yCo_zO_2$, NMC), the practical discharge capacity was increased from ~140 to ~150-210 mAh g^{-1} (Amin and Chiang 2016). This highlights the impact that electronic conductivity has on the performance of the cathode material. In addition to discharge capacity,

the structural stability of the cathode material is particularly important for large-scale applications. At elevated temperatures (>200 ℃), O_2 can be released from an unstable lattice during the cycling process (Sharifi-Asl, Lu et al. 2019). The released O_2 is very hazardous as it can fuel various possible combustion reactions with the organic solvents present in the electrolyte (onset of thermal reaction temperature ~220-245 ℃), which may trigger highly dangerous thermal runaway events (i.e. fires or explosions) (Martha, Haik et al. 2011). LMO, LCO, NCM become structurally unstable starting at ~190-260 ℃ due to structural transformations (Belharouak, Lu et al. 2006). The produced O_2 from these structures, in the presence of the electrolyte, forms strongly exothermic reactions (enthalpy of reaction: -439 J g^{-1}, LMO; -553 J g^{-1}, NMC; -940 J g^{-1}, LCO) (Julien, Mauger et al. 2014, Kriston, Adanouj et al. 2019). On the other hand, LFP possesses high structural stability due to the strong covalent P-O bonds in the tetrahedral PO_4^{3-} polyanionic backbone (bond energy ~350 kJ/mol) (Huggins 1953), stabilizing oxygen atoms in the crystal lattice at temperatures up to 600 ℃ (Martha, Haik et al. 2011, Wang, Yang et al. 2013). The high bond energy in LFP is attributed to the smaller P-O bond length (~1.56 Å) compared to the Mn/Co-O bond length in LMO/LCO (Mn-O bond length: ~1.94 Å and Co-O bond length: ~1.96 Å) (Laubach, Laubach et al. 2009, Delmas, Maccario et al. 2011, Yu, Guo et al. 2019). This stable structure inhibits the release of O_2 during high states of charging, thus creating less exothermic reactions with the electrolyte (enthalpy of reaction: -245 J g^{-1}) and making LFP a significantly safer cathode material (Wang, Yang et al. 2013, Julien, Mauger et al. 2014). For these reasons, LFP is considered a promising candidate material for next-generation energy storage devices compared to the other commercially available cathode materials.

Table 1.2 Comercially avaliable ceramic cathode materials for Li-ion batteries (Park, Zhang et al. 2010, Julien, Mauger et al. 2014, Amin and Chiang 2016).

Cathode Materials	Electronic Resistivity (Ω-cm)	Discharge Capacity (mAh g^{-1})	Enthalpy of Reaction (J g^{-1})
$LiCoO_2$ (LCO)	~10^4	~140	-940
$LiNi_xMn_yCo_zO_2$ (NMC)	~10^2	~150-210	-553
$LiMn_2O_4$ (LMO)	~10^6	~120	-439
$LiFePO_4$ (LFP)	~10^9	~70-150	-250

Although olivine LFP possess relatively high specific capacity and structural stability, its low room-temperature electronic conductivity (~10^9 Ω-cm) has been identified as a limitation for future high-performance energy storage devices (Wang and Hong 2007, Paolella, Turner et al. 2016). This is due to the fact that the ability for cathode materials to intercalate Li-ions, tied to their electrical and ionic conductivities, significantly impacts the formation and breaking of chemical bonds, which is necessary for battery operation (Park, Zhang et al. 2010). As presented in Table 1.2 Comercially avaliable ceramic cathode materials for Li-ion batteries (Park, Zhang et al. 2010, Julien, Mauger et al. 2014, Amin and Chiang 2016)., this intrinsic barrier (i.e. low electronic conductivity) has been circumvented through alio/isovalent doping, surface modification, and conductive scaffolding. In alio/isovalent doping, alkaline earth/transition metals are incorporated into the Li-ion sites (M1 sites) to decrease the formation of Fe-antisite defects (Fe-ions located in M1 sites), which block Li-ion diffusion pathway. As a result,

dramatic increases to the electronic conductivity of LFP are observed (~10^4 Ω-cm) (Wang and Hong 2007, Paolella, Turner et al. 2016). In the case of surface modification, a layer of carbon or metal oxide is deposited onto the surface of the active particles, which decreases the ion/electron diffusion path during the charging/discharging process and results in electronic conductivities ranging from ~10^4 to 10^3 Ω-cm (Bazzi, Dhindsa et al. 2012, Ni, Liu et al. 2013). Similar to surface modification, conductive support materials are taken advantage of to reduce the charge (ion/electron) transfer distance (Pang, Wang et al. 2018, Stokes, Boonen et al. 2019). Table 1.3 Methods utilized to improve the electrical resistivity of LFP (Ni, Liu et al. 2013, Amin and Chiang 2016, Paolella, Turner et al. 2016, Wu, Ji et al. 2016). Table 1.3 shows that the reduced charge transport as a result of the conductive scaffold (NMC) significantly improves the electrochemical performance. Although the electronic conductivity of the LFP-NMC assembly is not provided, it is expected that the resultant electronic conductivity will range from ~10^9 (pristine LFP) to ~10^2 Ω-cm (pristine NMC) (Amin and Chiang 2016, Wu, Ji et al. 2016). Among these methods, surface modification has been the most widely studied approach due to its ability to increase the surface activity of the particles and prevent deleterious interaction between the electrolyte and cathode material (Li, Wu et al. 2017). However, the high-rate capability and cycling stability problems posed by current surface modifiers (i.e. olivine and carbon materials) are not practical for long-term use. In this regard, conductive supporting materials offer a promising alternative approach for the design of high-performance batteries. Therefore, multi-functional ceramic oxides can be leveraged to modify the electronic properties of LFP, resulting in improved electrochemical performance.

Table 1.3 Methods utilized to improve the electrical resistivity of LFP (Ni, Liu et al. 2013, Amin and Chiang 2016, Paolella, Turner et al. 2016, Wu, Ji et al. 2016).

Cathode Materials	Electronic Resistivity (Ω-cm)	Discharge Capacity (mAh g^{-1})
$LiFePO_4$ (LFP)	~10^9	~70-150
Alio/isovalent Doping	~10^4	~80-150
Surface Modification	~10^4 to 10^3	~100-150
Conductive Scaffolding*	~10^9 to 10^2	~160-220

*The actual electronic conductivity is unknown but it is expected to range from pure LFP to the conductive support material.

1.4. Stabilizing the ABO_3 Crystal Structure

Ceramic oxides can be broadly divided into four categories: (i) A_xO_y oxides, (ii) $A_2B_2O_7$ pyrochlore, (iii) perovskite-like layered structure, and (iv) ABO_3 perovskites (Table 1.4). Additionally, the electrically conducting ceramic oxides in each group will be highlighted as these can be used for designing the conductive support. A_xO_y oxides are composed of any metal ion and oxygen, making up the largest category among ceramics. Most of the materials in this group are non-conductive, but PbO_2, RuO_2, and $(Y_2O_3)_x(ZrO_2)_{1-x}$ (YSZ) are three exceptions to this behavior. They possess electronic conductivities ranging from ~10^{-3} to 10^{-4} Ω-cm (Braun, Euler et al. 1980, Reddy and Mergel 2006, Pihlatie, Kaiser et al. 2011). The last three categories, referred to as complex oxides, are a popular class of ceramic materials to probe for multi-functionality owing to the exceptional flexibility of the A-site and B-site cations (A, B = select metal ions). Similar to AO oxides, the $A_2B_2O_7$ class, consisting of metal ions and oxygen arranged in the pyrochlore/fluorite configuration (Fuentes, Montemayor et al. 2018), is largely

non-conductive. However, $A_2Ru_2O_7$ and $A_2Ir_2O_7$-type structures have reported electronic conductivities of ~10^{-2} Ω-cm (Ryll, Brunner et al. 2010, Shang, Cao et al. 2019). The layered perovskite-like structure class includes Ruddlesden-Popper, double perovskite, Dion-Jacobson, brownmillerites, etc., which are distinct from the pyrochlore/fluorite structure in that they contain an inserted layer of A_xO_y oxide. In these materials, electronic conductivities of ~10^{-3} Ω-cm have been reported (Maeno, Hashimoto et al. 1994, Amow, Davidson et al. 2006). Finally, the ABO_3 class, arranged in the perovskite structure (Ji, Bi et al. 2020), possess electronic conductivities comparable to A_xO_y oxides (~10^{-4} Ω-cm) without the use of toxic or costly metals and with more structural possibilities (Appendix B). Therefore, the prominent electronic properties observed in the family of ABO_3 perovskites will be beneficial in the elucidation of potential conductive scaffold materials.

Table 1.4 Room temperature electrical conductivity for different conductive ceramic oxides (Braun, Euler et al. 1980, Reddy and Mergel 2006, Pihlatie, Kaiser et al. 2011).

Ceramics	**Electronic Resistivity (Ω-cm)**
A_xO_y oxides	$>10^{-4}$
$A_2B_2O_7$ Pyrochlore	$>10^{-2}$
Perovskite-like Layered Structures	$>10^{-3}$
ABO_3 Perovskites	$>10^{-4}$

The prototypical ABO_3 perovskite oxide structure is composed of a large-sized 12-coordinated cation in the A-site (AO_{12}) and smaller-sized 6-coordinated cation in the B-site (BO_6) (Figure 1.6(a)). In the three-dimensional ABO_3 framework, the A-site cation is located at the body center position and is surrounded by corner sharing BO_6 octahedra (Figure 1.6(b)). The B-site cations occupy each of the eight corners and O anions occupy the edge centers (Figure 1.6(b)). The stability of the A/B-site cation in the perovskite lattice is determined based on some function of their ionic radii. Notably, the Goldschmidt tolerance factor (t) has been extensively utilized to predict the stability and distortion of the perovskite crystal structure (Goldschmidt 1926) and calculated using the following expression:

$$t = \frac{r_A + r_O}{\sqrt{2}(r_B + r_O)} \tag{1.1}$$

where r_A, r_B, and r_O represents the ionic radii of the A-site, B-site, and O atoms, respectively. Although, the tolerance factor has been instrumental in the prediction of ABO_3-type solids, its quantitative accuracy is ~70% (Liu, Cheng et al. 2020). Therefore, to improve upon the prediction of perovskite and non-perovskite structures, the new tolerance factor (τ) was recently developed (Bartel, Sutton et al. 2019). This tolerance factor has the following form:

$$\tau = \frac{r_O}{r_B} - n_A\left(n_A - \frac{r_A/r_B}{ln(r_A/r_B)}\right) \tag{1.2}$$

where, in addition to the respective ionic radii, the oxidation state of the A-site ion (n_A) is incorporated. Figure 1.6(c-d) shows a comparison of the two tolerance factor methods. The tolerance factor for a perovskite-type compound is predicted to range from t = 0.8 to 1.1 and τ = 1.0 to 4.0 (Bartel, Sutton et al. 2019). In comparison to the Goldschmidt method, the use of the new tolerance factor allows for an accuracy of ~92% for the classification of perovskite and non-perovskite structures (Liu, Cheng et al. 2020).

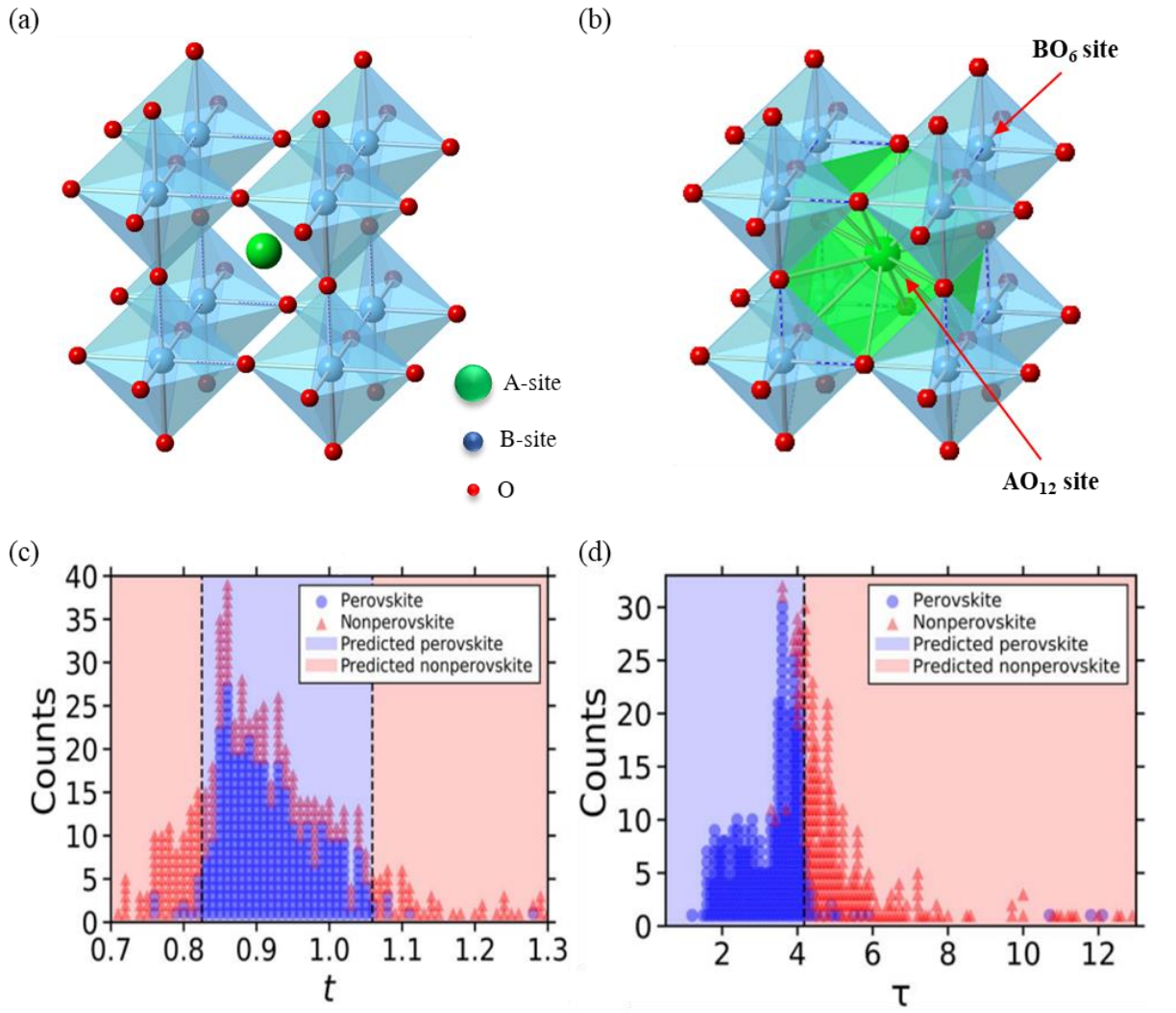

Figure 1.6 (a) General representation of the perovskite crystal structure. (b) Perovskite AO_{12} and BO_6 coordination sites. The screening of the ABO_3 crystal structure can be performed using the (c) Goldschmidt and (d) new tolerance factor tolerance factors (Bartel, Sutton et al. 2019).

The low quantitative accuracy of the Goldschmidt method has not prevented the construction of a generalized correlation between the tolerance factor and the ABO_3 crystal structure (Schinzer 2012). Based on experimental observations, this relationship has enabled the prediction of not only perovskite/non-perovskite structures but also crystallographic phases Figure 1.7 (Vieten, Bulfin et al. 2019). In general, an ideal cubic structure (i.e., $SrTiO_3$) has a

tolerance factor ranging from 0.9 - 1.0 (Raengthon, McCue et al. 2016). As the positive deviations become larger (tolerance factor >1.0), the crystal distorts via an elongating the B-O bong length, inducing displacive distortions in the BO_6. Perovskites exhibiting this distortion typically adopt lower symmetry states such as tetragonal/hexagonal (i.e., $BaTiO_3$) (Cheng, Alonso et al. 2009, Raengthon, McCue et al. 2016). Similarly, negative deviations (tolerance factor ~0.71-0.91) distort the ideal perovskite structure by compressing the B-O bond while elongating the A-O bond. The structure relieves the internal strain by rotating/tilting the BO_6 octahedra, usually creating an orthorhombic/rhombohedral lattice (i.e., $CaTiO_3$) (Raengthon, McCue et al. 2016, Sun, Alonso et al. 2020). When the tolerance factor is outside of 0.71-1.1, face-sharing octahedra polytypes (non-perovskite) are formed (i.e., ambient-pressure $BaIrO_3$) (Cheng, Alonso et al. 2009, Sun, Alonso et al. 2020). As mentioned above, the weakness with the Goldschmidt tolerance factor is that it only considers ionic radii, ignoring other factors, such as bond strengths, electronegativity differences, and the effect of different spin states, which influence the crystal structure and contribute to its low quantitative accuracy (Vieten, Bulfin et al. 2019). However, despite this simplification, it allows for the examination of many stable ABO_3 perovskites by showing that the desired crystal structure can be formed by controlling the effective radius of the A/B-O bond.

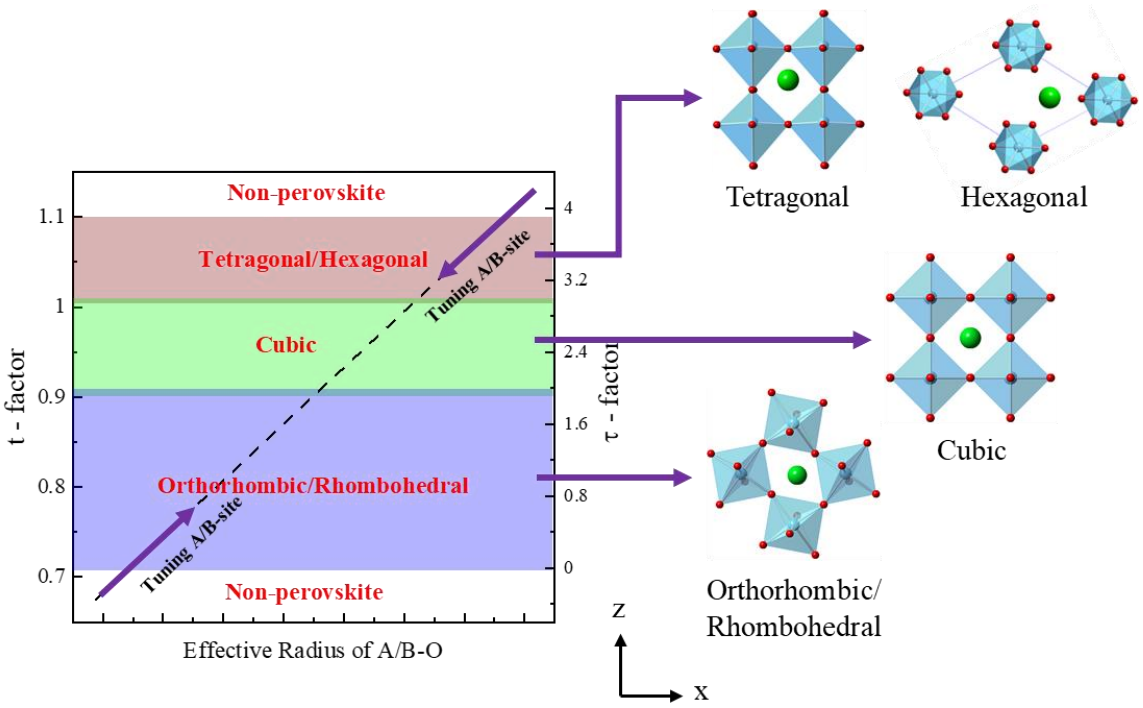

Figure 1.7 Generalized crystal structure prediction for ABO_3 perovskites based on the Goldschmidt tolerance factor: The black dashed line is a guide for the eyes. Adapted from (Schinzer 2012).

1.5. Electronic Structure of ABO_3 Perovskites

As demonstrated above, the crystal symmetry, which is a function of the effective radius of the A/B-O bond, can be utilized to drive lattice distorting mechanisms. The presence of these long-ranged distortions impact not only the crystal structure but also the ground state electronic structure of ABO_3 perovskites (Varignon, Bibes et al. 2019). For example, symmetry breaking modes such as octahedra breaking/rotation, Jahn-Teller-type distortions, etc., can transform an expected metallic ABO_3 compound to be insulating (Varignon, Bibes et al. 2019). Thus, the changes observed in the crystallographic structure of ABO_3 perovskites are strongly correlated to the resultant electronic structure and property (i.e., insulator, semiconductor, and metal).

To compare these electronic states, the band structure for a metallic, semiconducting, and insulating ABO_3 perovskite are illustrated in Figure 1.8. Metallic ABO_3 perovskites possess Fermi levels (E_F, highest energy level occupied by electrons at 0 K) that lie within the bands. In these systems, electrical current flows in the presence of an applied potential because there are unoccupied states for the mobile carriers (electrons) to readily move into at no energetic expense (Oberhofer, Reuter et al. 2017). Semiconducting materials exhibit a gap between the occupied valence band and the unoccupied conduction band, forming the band gap (E_g). These materials exhibit a E_F which lies in the E_g and possess less mobile carriers. In these systems, the E_g acts as a transport barrier for the conduction of electrons. Therefore, a potential large enough to overcome the bandgap has to be applied in order to excite electrons into the conduction band (thermalization). Holes, charge carrier of opposite polarity of electrons, are left behind in the valence band. This process creates mobile carriers in both the conduction band (electrons) and the valence band (holes), which allow electrical current to flow under a continuously applied potential (Kasap, Koughia et al. 2017). In the absence of a potential, the excited electrons relax from the conduction band into the valence band and the formed electron-hole pairs are eliminated (recombination). Finally, bandgaps > 4 eV result in insulating states, which possess somewhat similar electronic structures as the semiconducting state. However, greater thermalization energies are required to generate mobile carriers due to the larger bandgap energy.

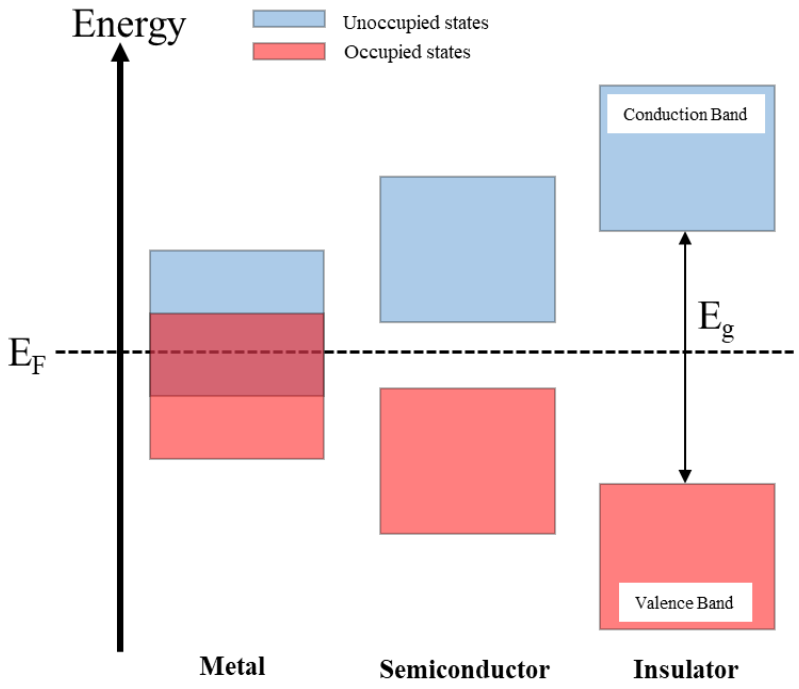

Figure 1.8 Electronic band diagram for a metallic, semiconducting, and insulating ABO_3 perovskite. The black dashed line denotes the Fermi-level. Adapted from (Berney Needleman 2014).

Based on this electronic classification scheme, specific examples from the library of ABO_3 perovskites are presented. In these examples, semiconducting and insulating structures will be provided together. Common conductive perovskite oxides include stoichiometric alkaline earth niobates ($ANbO_3$), vanadates (AVO_3), and molybdates ($AMoO_3$). These families possess electrical resistivities (ρ) ranging from ~10^{-2} to 10^{-5} Ω-cm and three main crystallographic ground states (cubic, space group: *Pm-3m*; hexagonal, space group: *P6-3m*; orthorhombic, space group: *Pnma*) (Macquart, Kennedy et al. 2010, Wan, Zhao et al. 2017). Common semiconducting/insulating perovskites include stoichiometric alkali/alkaline earth titanates ($ATiO_3$), stannates ($ASnO_3$), and cobaltites ($ACoO_3$). Additional semiconducting/insulating classes are formed when alkali earth metals are used as the A-site elements of ABO_3 (B = Nb, V,

and Mo). These families possess ρ >10^{-2} Ω-cm and various crystallographic ground states. Exceptions to these behaviors can be seen in the family of alkaline earth illeminite ($AFeO_3$) where both metallic ($SrFeO_3$) and semiconducting/insulating ($CaFeO_3$) crystals are present (Kawanaka, Kawawa et al. 2018). The crystal and electronic structures, introduced above, are combined in Figure 1.9 to illustrate that ~12 types of conductive perovskites are formed using the $SrBO_3$ stoichiometry. Based on this, it is reasonable to start with this perovskite family to identify potential candidate materials to be used as conductive supports. Nonetheless, the subsequent section will discuss the procedure implemented to determine the ideal A/B-site cation, which will be explored for further study. Overall, the crystal and electronic structures of ABO_3 perovskites are determined by the chosen A/B-site cation, thus necessitating a thorough selection process.

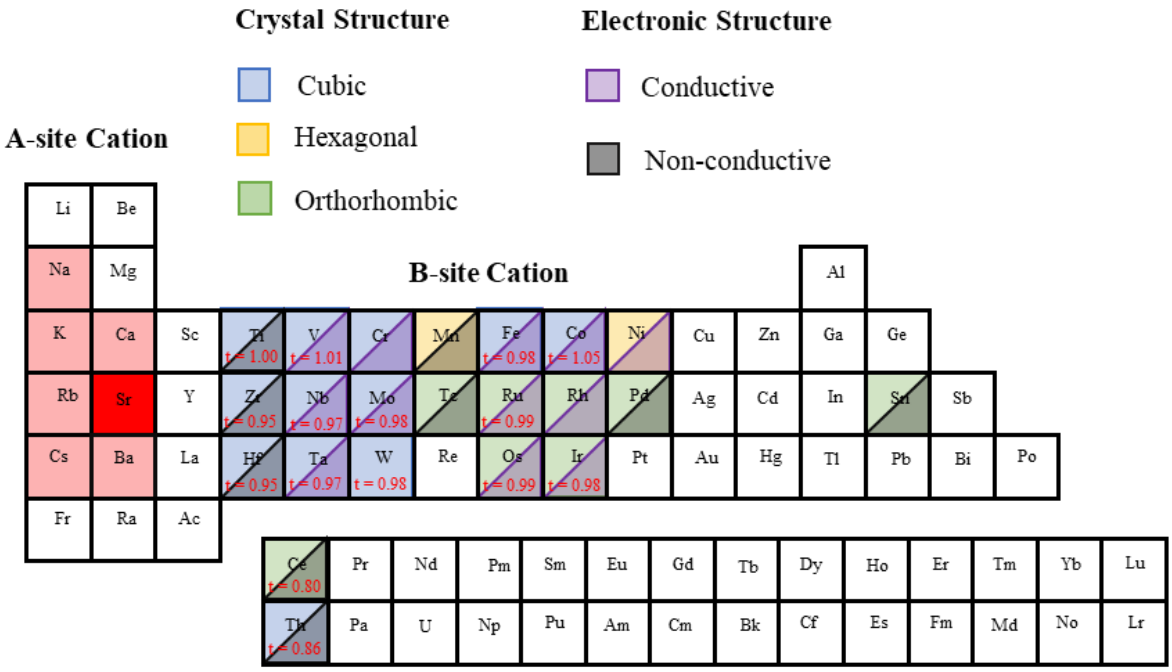

Figure 1.9 Summarization of crystal and electronic structure of ABO_3 perovskites. To illustrate this variation in crystal and electronic structure, A = Sr (in dark red) is used an example. The crystal (cubic, hexagonal, or orthorhombic) and electronic (conductive or insulator) structure for the formed perovskite is indicated by the color on the B-site cation.

1.6. A/B-site Selection and Defect Engineering

In ABO_3 perovskites, most of the A-site cations feature elements from Groups I (alkali earth metals; Na, K, etc.), II (alkaline earth metals; Sr, Ba, etc.), or RE (rare earth, La, Gd, etc.) elements. Typically, Groups I and II are preferred because their formal oxidation state is independent of temperature and oxygen partial pressure, therefore, the A-O interaction is highly stable (Vieten, Bulfin et al. 2019). RE ions, on the other hand, are not as selective as the Group I and II ions due to their multi-valency, which allows them to also target the B-site of the ABO_3 lattice (Jia 1991, Zeng, Xu et al. 2020). Although this unexpected B-site substitution has resulted in new functional properties (electrical, magnetic, optical, strain, etc.) (Zeng, Xu et al. 2020), it

also contributes to reducing the overall stability of the perovskite crystal by forming other unstable RE-B-O phases (Vijaya Kumar, Kuribayashi et al. 2009). To further highlight the stability of the A-O bond in the perovskite framework (Figure 1.9), the oxygen vacancy formation energy for various elements within the Groups I and II categories are plotted in Figure 1.10. These results along with the thermodynamic stability parameters (perovskite formation energies, phase stability, structural distortions, oxidation state, and ionic size) were calculated using high-throughput density functional theory to thoroughly compute more than 5,000 different compositions (Emery and Wolverton 2017). To specifically focus on the A-O bond and minimize effects from the B-O bond, multiple perovskite families were included in the plot. Additionally, only the families in which all the elements would form stable perovskite lattices were chosen, i.e. $ATiO_3$, $ASnO_3$, $AMoO_3$, etc. From the figure, one of the most stable A-site environments is generally formed using a Sr-O bond (in orange, bond energy ~4.0-5.5 eV/O atom), further motivating the use of this particular ABO_3 (A=Sr, SBO) stoichiometry.

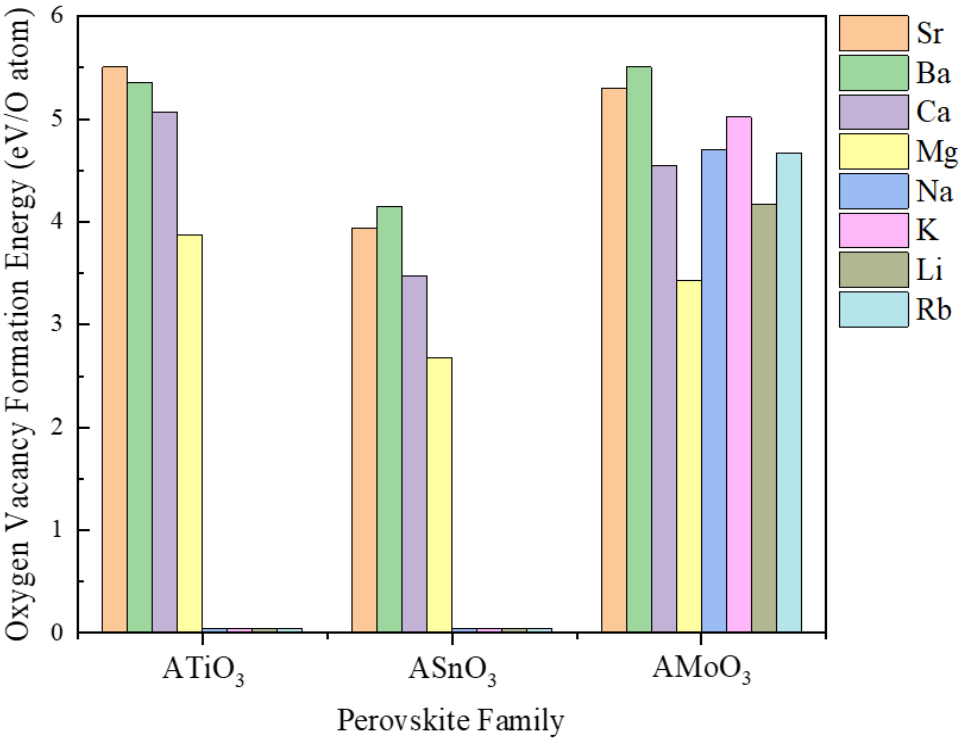

Figure 1.10 Stability of the A-O interactions in the ABO_3 perovskite structure. Adapted from (Emery and Wolverton 2017).

For the B-site species, transition metals (ranging from Groups IV - IX) are utilized as they can form stable complexes in combination with alkali/alkaline earth metals due to their multi-valency. To assist in the selection of potential B-site ions, the ρ of various thin-film/bulk SBO perovskites highlighted in Figure 1.9 are plotted in Figure 1.11 (see Appendix B for references). LFP and NMC are included as references. For instance, when the B-site cation is in Group IV (d^0 electronic configuration), the empty *d* orbitals result in a band gap around the E_F and measured electrical resistivities of ~10^2 Ω-cm. Examples of perovskites within this group include SBO (B = Ti, Zr, Hf) and their electronic properties originate from the formation of mobile carriers via thermalization of electrons in the valence band (insulator/semiconductor character) (Kasap, Koughia et al. 2017). When B-site cations from Groups V - IX (d^n, n > 0 electron configurations) are utilized, significant reduction (from ~10^2 Ω-cm to ~10^{-4} Ω-cm) to

the electrical resistivity is observed, resulting in possible metallic behavior. In this group, there are available free carriers from the *d* states of the B-site cation, which lie on the bands crossing the E_F. The electronic properties of these SBO (B = Co, Fe, Ru, etc.) perovskites originate from partially occupied orbitals (t_{2g}, n < 5 or e_g, n > 5) in the conduction band (metallic character) (Tsuda, Nasu et al. 2013). The SBO (B = Nb, Ta, Mo, and V, highlighted in red) perovskites possess electrical resistivities lower than NMC, which suggest favorable electronic properties as a scaffold material. Therefore, it is hypothesized that the use of B-site cations such as Nb, Ta, Mo, and V with tetravalent oxidation states, referred to as "metastable" as this is not the thermodynamically preferred oxidation state for these elements, will assist in improving the electronic properties of LFP.

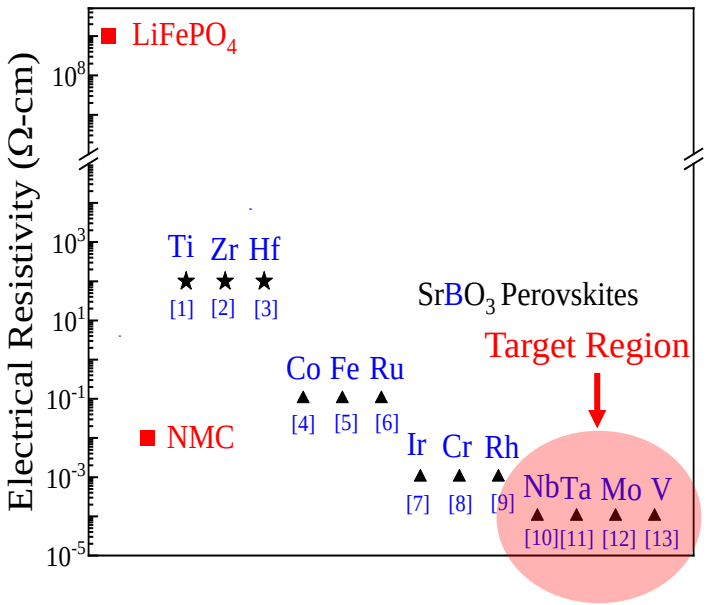

Figure 1.11 Electrical resistivity for SBO perovskites, LFP, and NMC.

Defect engineering (substitutional/interstitial doping, oxygen vacancy, and cation vacancy) offers an effective and versatile pathway for tuning the A/B-O interaction in the

perovskite lattice (Li, Shi et al. 2020). This tunability allows for control of the crystal (Section 1.4) and electronic (Section 1.5) structure of SBO perovskites. As an example, the incorporation of Sr atoms into the A-site of semiconducting/insulating $NaNbO_3$ perovskites (i.e., $Sr_xNa_{1-x}NbO_3$) induces an orthorhombic to cubic structural transitions and metallic like properties (Wan, Zhao et al. 2017, Wan, Yan et al. 2019). This combinatorial approach also allows for the control of structural and electronic features which otherwise would not be possible using a stoichiometric single A/B-site atomic arrangement. In the case of $Sr_xLa_{1-x}MnO_3$, both electronic conductivity from the $LaMnO_3$ lattice and ionic conductivity from the $SrMnO_3$ lattice are observed (Bidrawn, Kim et al. 2010). Similar mixed ionic/electronic conducting responses have been noted for other Sr-doped perovskites ($Sr_xLa_{1-x}CoO_3$ and $Sr_xSm_{1-x}CoO_3$), making them potential candidates for solid oxide fuel cells. The additional benefit of defect engineering is that it is compatible with both bottom-up (wet-chemical methods) and top-down (thin-film deposition methods) crystallization techniques. The combination of bottom-up and top-down approaches allows for the development of a robust design scheme, which is crucial for achieving a comprehensive understanding of the interplay between structure and property in ABO_3 perovskites (Li, Shi et al. 2020). As specific examples, these electronic properties, tailored using defect chemistry, have resulted in novel phenomena such as ferromagnetism, ferroelectricity, two-dimensional electron/hole gas, superconductivity, etc. More importantly, these responses are technologically significant for non-volatile memory (Chen, Zhang et al. 2017), thermoelectrics (Chen, Chen et al. 2017), and photovoltaics (Bera, Wu et al. 2014). Therefore, it is clear that this unique ability to utilize defects to engineer the electronic properties of SBO perovskites will contribute to the design/development of multi-functional materials for future energy storage and conversion devices.

1.7. Layered Film Architecture

In order to facilitate charge transport (Section 1.3) across the electrode/electrolyte interface, the top layer of LFP needs to be optimized to take advantage of the interplay between the electronic and ionic conductivity (Pouillet's and Ohm's laws). Accordingly, the conduction of carriers (electrons/ions) through a medium (electrode/electrolyte) is a function of the travel distance (Yao, Huo et al. 2011, Li, Wang et al. 2019). For thick top layers, the large charge transport distance prevents mobile carriers from the SBO layer to contribute to the electrochemical reaction due to resistive effects, resulting in the intrinsic properties of the shell layer dominating (LFP). Conversely, for very thin layers, resistive effects are no longer an issue, but the possibility of Li-ion intercalation into the internal layer is expected to compromise the electronic properties of the SBO material (i.e. transformation from d^n to d^0 electronic configuration). To prevent this, the electronic and ionic properties need to be synergistically coupled to boost the electrochemical performance. Specifically, a graded architecture consisting of an electrically conductive internal layer with an ionically conductive top layer is proposed as it will allow for the near-field coupling of these two effects in a single system. Furthermore, the presence of the shell layer will prevent lithiation of the internal conductive NP, which will result in a loss of electrical conductivity (Sun, Kotiuga et al. 2018). Since the metallic state of these metastable crystals is due to the available free carriers from the *d* states of the B-site cation, Li-ion incorporation into the SBO layer ($Li_xSr_{1-x}BO_3$) reduces the number free carriers, thus inducing a semiconducting/insulating state (Sun, Kotiuga et al. 2018). Therefore, in order to take advantage of both the electronic and ionic transport properties, the top layer thickness has to be controlled (Wu, Ji et al. 2016, Yao, Xia et al. 2018). Ultimately, this proposed SBO - LFP

layered film architecture (Figure 1.12) will facilitate the charge transport (Li-ion and electron insertion/extraction) via the top layer, allowing for improved electrochemical performance.

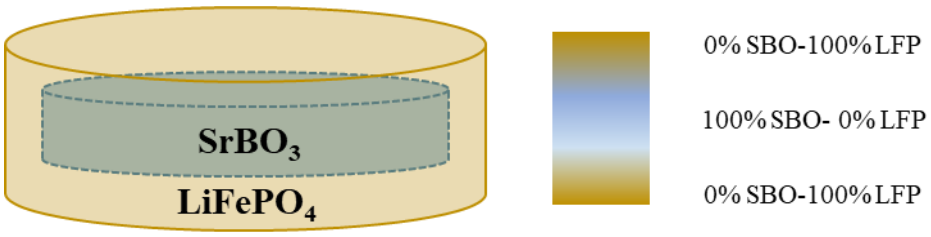

Figure 1.12 Layered film architecture using an electronic conductor ($SrBO_3$, SBO) as the internal material and Li-ion conductor ($LiFePO_4$, LFP) as the top layer.

1.8. Proposed Work and Outline of the Dissertation

This chapter outlined the crystal and electronic structure of defect-controlled $SrBO_3$ (SBO, B = Nb, Ta, Mo, etc.) perovskites with potential applications for advanced energy storage. As an example, the substantial progress observed in Li-ion batteries is a result of the discovery and subsequent industrial commercialization of cathode materials such as the Olivine-type structures ($LiMPO_4$, M = Fe, Mn, Co, etc.). Although these materials possess relatively high specific capacity (~170 mAh/g), their low room-temperature electronic conductivity has been identified as a limitation for future high-performance batteries. Therefore, this work attempts to overcome this major drawback by using metastable SBO perovskite oxide NPs with metallic properties to improve the room-temperature electronic conductivity of olivine $LiFePO_4$ (LFP). For this reason, it has been hypothesized that the layered film architecture will allow for the synergistic coupling of the electronic and ionic effects, enabling improved charge transport properties. Additionally, this design scheme utilizing metastable SBO perovskites results in multi-functional materials with tunable electronic properties, which can be used as conductive

scaffold for light absorbers/converters. This proposed architecture will facilitate the near-field coupling of ionic and electronic properties, thereby allowing for improved Li-ion and electron insertion/extraction. Previous studies have shown that the crystallization of these metastable structures with their expected electronic properties using solution-based chemistry remains a synthetic challenge (Xie, Hu et al. 2012, Guo, Hua et al. 2013, Rojas, Potticary et al. 2020). This synthetic challenge stems from the excess oxygen present using traditional wet-chemical methods (Mao, Banerjee et al. 2003, Mao and Wong 2005, Calderone, Testino et al. 2006, Souza, Santos et al. 2012).

Therefore, the first aspect of this work is to understand the crystallization of these metastable structures under wet-chemical conditions. The SBO NPs (~20 nm) were fabricated using a two-step co-precipitation/pressure-controlled molten salt technique. This novel synthetic route allows for these materials to be synthesized and characterized as NPs. The low-pressure atmosphere limits the available oxygen during the crystallization process, allowing for systematic control of defects (i.e. oxygen vacancies and dopant incorporation) and thereby stabilizing the B-site oxidation state. Next, the ability to systematically control the A/B-site chemical structure is studied using local/bulk characterization techniques. This is accomplished by incorporating dopants into the SBO lattice and monitoring the induced symmetry/structural changes using a structurally dependent photoluminescent probe (Eu^{3+}). Afterwards, a wet-chemical treatment that mirrors vacuum deposition processes was utilized to remove excess oxygen within the crystal lattice, modifying the resultant electronic properties of the SBO NPs. Furthermore, these experimental results are supported by first-principles calculations to fundamentally understand the effect of the treatment on the electronic structure and transport properties. Lastly, to synergistically couple the electronic and ionic conductivities, an olivine

LFP top layer was deposited around these conductive SBO NPs. Among the various B-site cations, Nb, Ta, and Mo were chosen due to their metallic behavior when stabilized in the $SrBO_3$ stoichiometry (Wan, Zhao et al. 2017, Ha and Lee 2020). These comprehensive results on SBO NPs represent the first of its kind, in which not only can these materials be synthesized but also the A/B-site chemical structure can be controlled. This control enables properties similar to what is reported for metallic thin-film/bulk crystals to be observed in the low-dimensional state. Additionally, this study demonstrates how the structure-property relationship can be utilized to obtain enhanced electrochemical performance via the use of these SBO NPs as internal materials. Ultimately, this ability to manipulate the electronic properties of LFP using metastable ABO_3 perovskite oxides will significantly impact the renewable energy industry by contributing to the design of multi-functional materials with improved electrochemical performances.

Chapter 2 describes the synthesis and characterization methods, including the scattering/spectroscopic and analytical techniques, employed in this study. Furthermore, the details regarding the first-principle phonon modes and electronic structure and transport simulations on the metastable SBO perovskites are discussed. Chapter 3 describes the crystallization of these metastable structures by stabilizing the B-site chemical structure (i.e. oxidation state). In Chapter 4, the developed synthetic method is further studied by highlighting control of the A-site chemical structure (i.e. coordination environment). In this work, the effect of Ca incorporation on the local/bulk A-site structure was monitored by performing *in-situ/ex-situ* photoluminescence spectroscopy coupled with standard characterization techniques (XRD and XAS). Next, although these metastable crystals can be synthesized, they do not possess the expected electronic properties and the engineering of the resultant electronic properties using a systematic H_2/Ar treatment is studied (Chapter 5). This analysis is combined with DFT and

BoltzTraP2 simulations to further understand the modified electronic properties. Finally, the coupling of the electronic properties of the synthesized nanomaterials with the ionic properties of LFP are presented in Chapter 6 along with future work. Overall, this work highlights the engineering of defect states in metastable ABO_3 perovskite NPs to control the optoelectronic properties for applications in advanced energy storage. A schematic diagram showing the research flow for the design of these engineered materials is shown below (Figure 1.13).

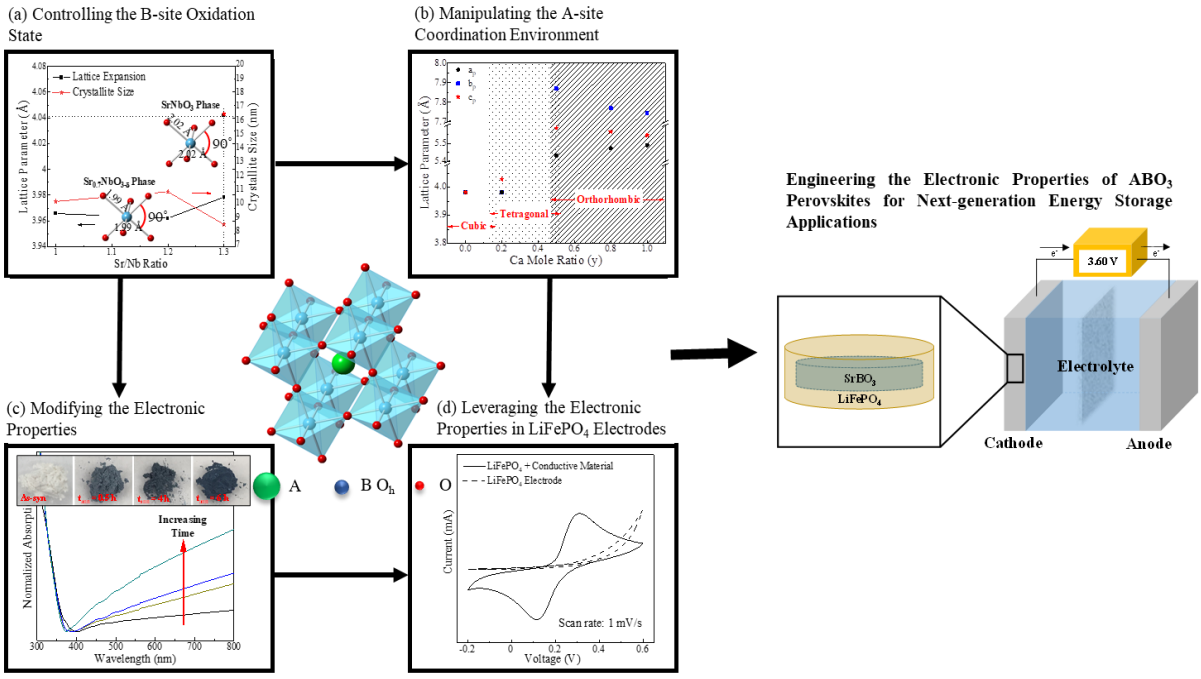

Figure 1.13 Schematic showing the research flow for the design/development of the engineered ABO_3 nanomaterials for advanced energy storage.

Chapter 2 . Experimental Methods[1]

This chapter explains the synthetic procedures and characterization techniques adopted for preparing the metastable ABO_3 perovskite NPs. As a first step, a novel synthetic method was developed to engineer the defect states, allowing for control of the A/B-site chemical structure (oxidation state and coordination environment). Next, material characterization, including structural (XRD, Raman, FTIR, and (HR)TEM/EDX), electronic (XAS and XPS), and optical (UV-Vis and PL spectroscopy), were performed to probe the crystal and electronic structure. This section also includes the electrochemical studies (electrical resistance measurements and impedance spectroscopy) that were performed to understand the transport properties of the NP and layered film assembly. The modeling approaches incorporated in this work to elucidate the geometric structure, electronic structure (density of states and band structures), and transport properties for these conductive perovskites are described in Appendix I.

2.1. Synthesis Methods

The synthesis of the layered architecture is divided into two-steps: 1) internal layer synthesis using the oxygen-controlled CP/MSS and 2) olivine top layer deposition using sol-gel chemistry. While traditional wet-chemical methods (Mao, Banerjee et al. 2003, Mao and Wong 2005, Zhou, Mao et al. 2007) have proved successful for preparing ABO_3 perovskites, the synthesis of perovskites with multiple B-site oxidation states and possessing metallic-like conduction remains a synthetic challenge (Kiselev 2007, Xie, Hu et al. 2012, Guo, Hua et al. 2013, Rojas, Song et al. 2017). For these reasons, a two-step co-precipitation/oxygen-controlled

[1] The synthetic methods and the description of characterization methods was "Reprinted (adapted) with permission from (T. Ofoegbuna, P. Darapaneni, S. Sahu, C. Plaisance, and J. A. Dorman, Stabilizing the B-site oxidation state in ABO3 perovskite nanoparticles. Nanoscale, 2019, 11(30), 14303-14311 and T. Ofoegbuna, K. R. Bajgiran, O. Kizilkaya, S. A. J. Thomson, A. T. Melvin, and J. A. Dorman, Photoluminescence Detection of Symmetry Transformations in Low-dimensional Ferroelectric ABO3 Perovskites. The Journal of Materials Chemistry C, 2020, 8(31), 10767-10773). Copyright (2019 and 2020) Royal Society of Chemistry."

molten salt technique followed by a H_2/Ar post-treatment was utilized in the synthesis of the nanocrystals. Additionally, the olivine $LiFePO_4$ top layer is deposited around the internal SBO layer (Wang, Wang et al. 2006, Dorman, Choi et al. 2012).

2.1.1. Two-step Co-precipitation/Oxygen-controlled Molten Salt Synthesis of Metastable ABO_3 Perovskite NPs

Co-precipitation method refers to the simultaneous precipitation of two or more cations in a homogeneous solution, enabling a more uniform particle composition to form (Rane, Kanny et al. 2018). Molten salt synthesis (MSS) utilizes the dissolution of precursors within a single ($NaNO_3$, T ~300 °C; NaCl, T ~800 °C; etc.) or eutectic (Na/KNO_3, T ~230 °C; Na/KCl, T ~650 °C; etc.) composition of salt solvents. For example, the phase diagram, displayed in Figure 2.1 shows that the eutectic composition for a Na/KNO_3 salt mixture is an equimolar ratio. Traditionally, the reaction mixture is heated under atmospheric conditions (P_{O2} ~160 Torr) and has resulted in improved control of the particle size and crystallinity (Mao and Wong 2005). For these reasons, the two-step co-precipitation/oxygen-controlled molten salt method incorporates aspects of these two techniques. In this synthetic method, a single-source amorphous complex precursor is prepared in the co-precipitation step and the subsequent MSS step promotes the crystallization of the amorphous precipitate by providing a low melting point salt solvent to facilitate the diffusion of reacting species (Alaparthi, Tian et al. 2013). Reduced oxygen partial pressures are known to limit oxidation of reactive compounds during the deposition/crystallization process allowing for systematic control of defects (i.e. Sr-vacancies, oxygen vacancies, and dopants) (Campion, Brown-Shaklee et al. 2013). For the synthesis of metastable ABO_3 perovskites (Ofoegbuna, Darapaneni et al. 2019, Ofoegbuna, Bajgiran et al. 2020), A-site (Sr, Ca, Eu) and B-site (Nb, Ta, Mo) nitrate or chloride precursors are dissolved into 200 mL of deionized water under vigorous magnetic stirring. The A-site to B-site molar

ratio is varied to control the extent of the reaction and the resultant stoichiometry. Ammonium hydroxide (NH_4OH), acting as the chelating agent (Zhang, Liu et al. 2018), was added dropwise into the solution until a pH of 9.5 was maintained. After stirring for 2 h, the white precipitate was filtered and washed several times with deionized water before drying overnight at 100 °C. The as-prepared powder was ground with a eutectic molar ratio of $NaNO_3$ and KNO_3 to form a homogeneous powder. The mixture was then transferred to a porcelain boat and heated in a tube furnace at 600 °C under oxygen-deficient atmospheres (vacuum or H_2/Ar) for 2 h to control the oxidation of the B-site cation. After cooling, the resultant powder is washed several times with deionized water and dried overnight at 100 °C to obtain SBO nanocrystals.

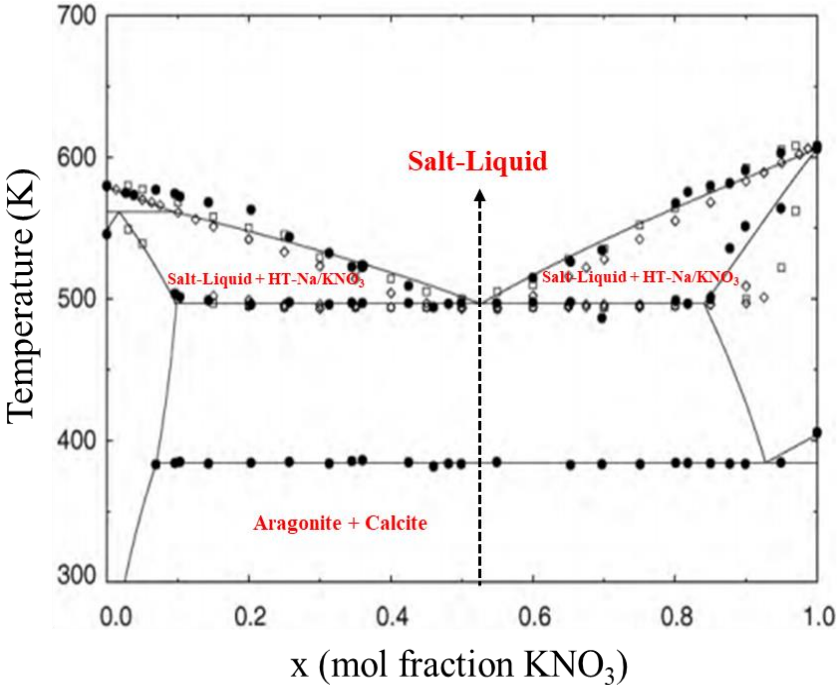

Figure 2.1 Phase diagram for a Na/KNO_3 salt mixture. Adapted from (Beneš, Konings et al. 2010).

2.1.2. Post-Treatment under Reducing (H_2/Ar) Atmospheres

Although the above synthesis stabilizes the B-site oxidation state, the resultant NPs still possesses a slight amount of B-site cations in multivalent stoichiometries (i.e. Nb^{5+}, Ta^{5+}, Mo^{6+}, etc.) (Ofoegbuna, Darapaneni et al. 2019). These multivalent states, present as surface/bulk defects, suppress the expected optoelectronic properties of the SBO NPs. It has been reported that metallic transitions can be induced upon thermal treatment of $SrTiO_3$ (STO) in reducing atmospheres (Szot, Speier et al. 2002, Tan, Zhao et al. 2014). Taking advantage of this thermal treatment method, the NPs were systematically treated in H_2/Ar atmosphere to modify their structure and composition. An insulator (white) to metal (colored) transition is induced from the suppression of these surface/ bulk defect states. Therefore, to induce metallic-like properties in these of metastable SBO perovskites, the as-synthesized NPs were annealed in a tube furnace at 800 °C under a H_2/Ar (5%/95%) atmosphere with an outlet gas flow rate of 0.3 L/min and varying time (0 - 6 h).

2.1.3. $LiFePO_4$ Top Layer Deposition

The low electronic conductivity (~10^6 to 10^9 Ω-cm), but reasonable Li-ion conductivity (~10^5 Ω-cm) of olivine $LiFePO_4$ makes it a potential candidate to test the highly conductive SBO scaffolding (Wang and Hong 2007). First, the as-synthesized SBO powder samples were uniaxially pressed into circular pellets (~150 mg, ø ~ 12.7 mm × 0.5 mm) at 3 ton and transferred to a quartz tube furnace to be annealed at 800 ℃ for 8 h in N_2 atmosphere. The prepared pellets were finally treated in H_2/Ar atmosphere at 800 ℃ for 6 h to modify their electronic properties. Next, the olivine top layer is deposited onto the sintered SBO pellets using an airbrush spray coating method (Lemaire, Sel et al. 2019). To do this, $LiFePO_4$ particles and PVDF were mixed with 400 μL of 1-methyl-2-pyrrolidinone (NMP) or Dimethylsulfoxide (DMSO). The slurry was

sprayed on top of the SBO pellets using a ZENY AB-130E-0.3 Dual-Action Multi-Purpose Airbrush kit and dried overnight in air at 80 °C. The $LiFePO_4$ particles used to prepare the slurry were synthesized using previously reported methods (Park, Xiao et al. 2012, Ma, Fan et al. 2015). Briefly, a $LiOH\text{-}H_2O$, H_3PO_4, ethylene glycol and a $FeSO_4\text{-}7H_2O$/ethylene glycol solutions were made and stirred for ~30 min. Next, the Fe-containing solution was rapidly added into the Li-containing solution and stirred for ~15 min. The final mixture was transferred into an autoclave and placed into a preheated oven (180 ℃) for 18 h. The obtained dark green precipitate was washed several times with deionized water and dried overnight at 100 °C. This layered film design will synergistically couple the metallic-like conduction of the SBO internal layer with the high Li-ion conductivity of the $LiFePO_4$ top layer to obtain enhanced electrochemical performance.

2.1.4. Solvothermal Synthesis of Structural References

$BaTiO_3$:Eu (BTO), $PbTiO_3$:Eu (PTO), $SrTiO_3$:Eu (STO), Ca-doped STO:Eu (CSTO), and $NaYF_4$:Eu (2 mol%) are used as structural references because their low temperature phase changes are well reported in literature. Table 2.1 shows the phase change temperatures for the structural references. Among them, $NaYF_4$ is the only reference not to undergo a structural transformation at low temperatures. The particles were prepared using previously reported solvothermal chemistries (Im, Jun et al. 2011, Lee, Moon et al. 2012, Chen, Bao et al. 2019, Ma, Li et al. 2019, Vaithiyanathan, Bajgiran et al. 2019). Solvothermal synthesis utilizes the heating of an aqueous (referred to as hydrothermal synthesis) or non-aqueous (i.e., ethanol, ethylene glycol, etc.) solvent in a sealed vessel and under autogenous pressure to facilitate the interaction of precursors. The liquid-phase chemical reaction follows three steps: formation of the supersaturated solution, nucleation, and crystal growth (Jin, Han et al. 2018). Similar to MSS, the

benefit of this method is the formation of particles with controlled size/shape and crystallinity (Li, Wu et al. 2016). For example, the phase diagram, displayed in Figure 2.2, shows that when water is used as the solvent, the synthesis range lies between its boiling point (1 atm, 100 ℃) and its critical point (220 atm, 374 ℃).

Table 2.1 Transition temperatures for structural references.

Chemical Composition	Transition Temperature (˚C)	Ref.
BTO	-80 and 0	Phys. Rev., 1960, 117 , 465
PTO	-100	Phys. Rev. B: Condens. Matter Mater. Phys., 1983, 28 , 3866
STO	-233 and -190	Phys. Rev., 1961, 124 , 1354; Phys. Rev. B: Condens. Matter Mater. Phys., 2008, 77 , 174101
CSTO	-233 to -150	Phys. Rev. B: Condens. Matter Mater. Phys., 2008, 77 , 174101
$NaYF_4$	-	Scientific reports, 2016, 6, 1, 1-11.

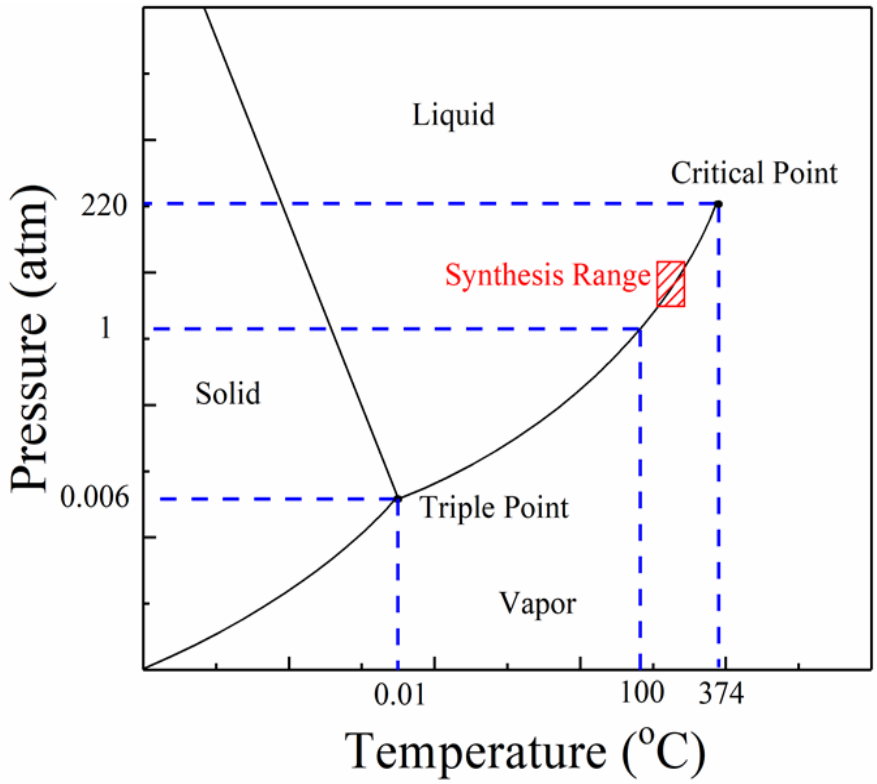

Figure 2.2 Phase diagram for water.

2.2. Characterization Methods

2.2.1. Electron Microscopy

The SBO NP size, structure, and elemental composition was determined by (HR)TEM and EDX measurements. TEM was performed using a JEOL JEM-1400 operating at an accelerating voltage of 120 kV and HRTEM was performed using a JEOL JEM-2011 operating at an accelerating voltage of 200 kV. The powder sample was dispersed in toluene at a ~2 mg/mL concentration and sonicated for 30 min. The prepared solution was then drop-caste on a lacey carbon type-A, 300 mesh copper grid and air dried prior to imaging. EDX was performed

using a FEI Quanta 3D FIB microscope equipped with an EDAX Apollo XL EDX detector operating at an accelerating voltage of 20 kV and a current of 4 nA. The working distance was maintained at ~10 mm. The samples were dried overnight at 80 ℃ on carbon tape and then sputtered with Pt for 5 min to limit charging.

2.2.2. X-ray Diffraction (XRD) and Rietveld Refinement

XRD was performed to understand the crystal growth and dopant incorporation in the SBO NPs. XRD data was obtained by using PANalytical X-ray diffractometer with a step size of 0.04° and dwell time of 60 s, using Cu $K_{\alpha 1}$ (λ=1.54 Å) as radiation source. The diffraction pattern of the NPs was collected by placing the finely crushed powder onto a zero-background sample holder and scanning from 5-70°. The approximate crystallite sizes were determined by averaging the sizes calculated by Scherrer equation (k = 0.94) for all the main peaks in the diffraction pattern (Patterson 1939). Furthermore, Rietveld refinement was performed on the resultant diffraction pattern using the GSAS II software (Larsson and Von Dreele 1994) for phase quantification. Full structural refinement was achieved via the refinement of the following: structural parameters (histogram scale factor, atomic coordinates, and isotropic atomic displacement parameter), cell parameters, peak shape parameters (Cagliotti parameters, sample displacement, phase fraction, size, and microstrain), and background parameters (10-coefficient log interpolate polynomial) (Rietveld 1969, Neiner, Okamoto et al. 2009). The Rietveld refinement details and procedure that was employed in this work for the structural refinement of single and multi-phase crystals are in given detail in the Appendices E and F.

2.2.3. Fourier Transform Infrared (FTIR) Spectroscopy

FTIR spectroscopy was performed to verify the presence of surface hydroxyl groups on the NPs. The FITR data was collected on a Bruker Tensor 27 FT-IR spectrometer equipped with

a DTGS detector, KBr beamsplitter, and MIRacle single reflection diamond/ZnSe attenuated total reflectance cell. The spectra were collected by averaging 128 scans in the range of 4000 to 400 cm^{-1} and with a resolution of 4 cm^{-1}.

2.2.4. Thermal Gravimetric Analysis (TGA) and Differential Scanning Calorimetry (DSC)

TGA-DSC studies were performed using a TA SDT Q600 DSC−TGA under a H_2/Ar (5%/95%) atmosphere with an inlet gas flow rate of ~29 mL/min to monitor the crystallization process of the NPs. Specifically, the effect of the H_2/Ar treatment was studied using as-synthesized SNO NPs. The temperature was increased from 25 to 800 °C at a rate of 10 °C/min and subsequently held at 800 °C for 6 h. The final oxygen deficiency (δ) was calculated using the initial oxygen non-stoichiometry (δ_o), the molar mass of the sample (M_o), the starting and final weight of the sample (m_o and m) and applying Eqn. 2.1 (Chen, Paulson et al. 2015).

$$\delta = \delta_o + \frac{M_o}{15.999}\left(1 - \frac{m}{m_o}\right) \quad (2.1)$$

2.2.5. Inductively Coupled Plasma Optical Emission Spectroscopy (ICP-OES)

ICP-OES analyses were performed using a Perkins Elmer Optima 8000 inductively coupled plasma optical emission spectrometer equipped with an auto sampler to measure the elemental concentrations. The samples for ICP-OES were prepared by digesting 9 mg of the SBO NPs in a HNO_3 and HCl solution which is heated to ~90 ^oC. Next, the digested sample is diluted to ~10 ppm using 2% HNO_3 solution. Similarly, an elemental standard (stock concentration: 1000 ppm) was diluted to 1, 10, and 20 ppm to build the calibration curve. The calibration curve is used to convert the measured intensities (cps) into concentration units (mg/L or ppm). To perform the measurements, the instrument is rinsed with a 2-5% HNO_3 solution for 5 min using an alternating pump (flow rate: 1 mL/min, 30 s) and flush (flow rate: 5 mL/min, 30 s) sequence. Next, the Ar (inlet pressure of ~120 psi and flow rate ~16-20 L/min) and N_2 (inlet

pressure of ~20 psi and flow rate ~1-5 L/min) gases are fully opened and the plasma is turned on. A properly ignited plasma should show gas flowing into the plasma (15 L/min), auxillary (0.2 L/min), and nebulizer (0.7 L/min) sections. Furthermore, the RF power should read 1500 Watts. Once these parameters are confirmed, the calibration curve for each element is developed using emission lines that offer low detection limit (DL, ~ppm), i.e. Sr I ($5s^2\ ^1S_0$-$5p\ ^1P_1^o$, 460.73 nm; DL~0.068 ppm) and Nb II ($4d^4\ ^5D_0$-$5p\ ^5F_2$, 269.71 nm; DL~0.069 ppm) (Ryabtsev, Churilov et al. 2000, Sansonetti and Nave 2010). The example calibration curve for Nb, displayed in Figure 2.3, shows statistically good linear fit as seen from the correlation coefficient (Corr Coeff) being close to 1.0. Following completion of the calibration curve, the same excitation wavelengths are used to analyze the sample.

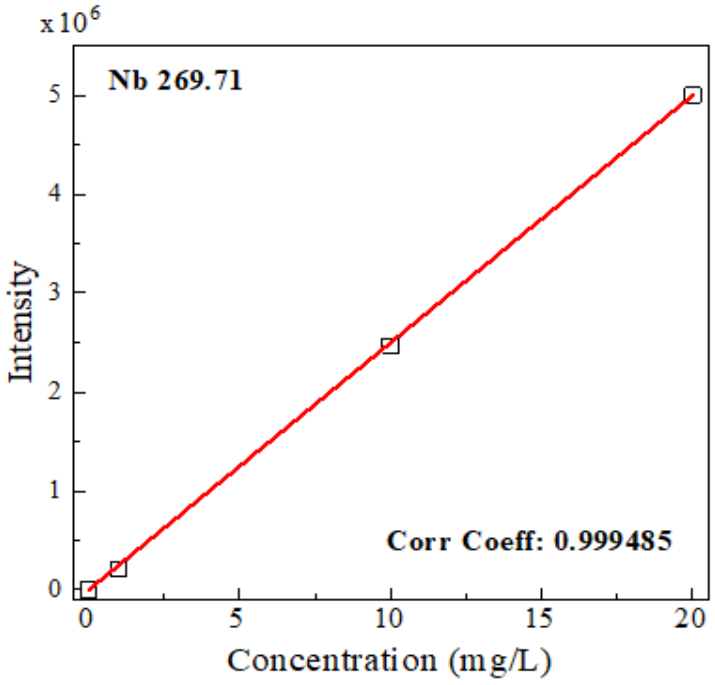

Figure 2.3 Calibration curve for Nb from a 1000 ppm Nb standard solution.

2.2.6. Iodometric Titration Studies

Iodometric titration was performed to investigate the oxygen vacancy concentration (δ) in the synthesized samples (Wang, Chen et al. 2019). Briefly, 9 mg of SNO NPs were dissolved in 3 mL of 2 M KI solution and degassed with flowing N_2 for 5 min in an Erlenmeyer flask. Next, 25 mL of 1 M HNO_3 was added to the mixture under vigorous stirring. 0.1 M $Na_2S_2O_3$, standardized against H_2O_2, was titrated into the solution under inert conditions until to the solution color changed from purple to blue. The endpoint of the titration is detected using a starch indicator. The titration was repeated three times and a blank titration (no sample) was performed to subtract atmospheric oxygen contribution.

For the $Na_2S_2O_3$ standardization reaction, prepare 30 mL of 0.04 M H_2O_2 (1.2 mmol) which yields 2.4 mmol of $Na_2S_2O_3$ (Eqns. 2.2 and 2.3). From the titration, 31 mL of $Na_2S_2O_3$ is utilized. Therefore, the actual concentration of $Na_2S_2O_3$ is 0.08 M.

$$H_2O_2 + 2KI + H_2SO_4 \rightarrow I_2 + K_2SO_4 + 2H_2O \quad (2.2)$$

$$I_2 + 2Na_2S_2O_3 \rightarrow Na_2S_4O_6 + 2NaI \quad (2.3)$$

For the oxygen vacancy calculation, literature report (Wang, Chen et al. 2019) was adapted to match the chemical formula determined by ICP-OES and Rietveld analysis: $Sr_{0.7}{}^{2+}Nb_{(1-\alpha-\beta)}{}^{4+}Nb_{\alpha}{}^{5+}Nb_{\beta}{}^{3+}O_{3-\delta}$.

Applying charge neutrality conditions to correlate δ to α and β:

$$\delta = 0.3 - \frac{1}{2}\alpha + \frac{1}{2}\beta \quad (2.4)$$

Dissolving sample in HCl/HNO_3 solution and reacting with KI drives the following half-reactions:

$$Nb^{5+} + 2I^{-} \rightarrow Nb^{3+} + I_2 \quad (2.5)$$

$$2Nb^{4+} + 2I^{-} \rightarrow 2Nb^{3+} + I_2 \quad (2.6)$$

Reaction for Iodine titration with a standard $Na_2S_2O_3$ solution:

$$2S_2O_3^{2-} + I_2 \rightarrow 2I^{-} + S_4O_6^{2-} \quad (2.7)$$

Concentration of formed I_2: from the titration, where *C* is the concentration (mmol/mL) and *V* is the volume (mL) of the $Na_2S_2O_3$ solution:

$$[I_2] = [Nb^{5+}] + 0.5[Nb^{4+}] \quad (2.8)$$

$$[I_2] = \frac{1}{2}CV \quad (2.9)$$

The molar mass of the oxygen-deficient $Sr_{0.7}NbO_{3-\delta}$, lattice (*M*) can be expressed in terms of the molar mass for the $Sr_{0.7}NbO_3$ lattice (M_o), oxygen (m_1), and δ:

$$M = M_o - m_1\delta \quad (2.10)$$

Rewriting Eqn. 2.8 in terms of α and β (using the chemical formula) and combining with Eqn. 2.9:

$$\frac{1}{2}CV = \alpha\left(\frac{m}{M}\right) + 0.5(1-\alpha-\beta)\left(\frac{m}{M}\right) \quad (2.11)$$

Substituting Eqns. 2.4 and 2.10 into 2.11:

$$\frac{1}{2}CV = (0.8-\delta)\left(\frac{m}{M_o - m_1\delta}\right) \quad (2.12)$$

Finally, solving for δ from Eqn. 2.12:

$$\delta = \left(\frac{M_oCV - 1.6m}{m_1CV - 2m}\right) \quad (2.13)$$

The δ was calculated using the molar mass of $Sr_{0.7}NbO_3$ (M_o, 228.53 mg/mmol), oxygen (m_1, 16 mg/mmol), mass of sample (m, 9 mg), concentration of $Na_2S_2O_3$ (C, 0.08 M), volume of the $Na_2S_2O_3$ solution (V, mL) and applying Eqn. 2.13. The calculated δ from the triplicate measurement are displayed in Table 2.2.

Table 2.2 Titration Results for SNO NPs.

Experiment	Volume $Na_2S_2O_3$ (V, mL)	Mole $Na_2S_2O_3$ (CV, mmol)	δ
Blank	0.100	0.008	-
Trial #1	0.500	0.040	0.30
Trial #2	0.400	0.032	0.41
Trial #3	0.400	0.032	0.41
Average	0.433±0.058	0.035±0.005	0.37±0.06

2.2.7. Raman Spectroscopy

The chemical bonding of the nanocrystals was studied using Raman spectroscopy to identify the distinct vibrational fingerprints of ABO_3 perovskites. Raman scattering measurements were collected on a Renishaw inVia Reflex Raman Spectrometer with a 0.05 mW diode laser at an excitation wavelength of 532 nm, exposure time of 0.5 s, and spectral resolution of 1 cm^{-1}. The diameter of the focused laser spot on the sample at 50x magnification was approximately 5 μm. Three scans were averaged to obtain the reported spectra. To resolve the active mode, the background was subtracted from the resulting spectra and the peak was

deconvoluted with Lorentzian peak functions using the OriginPro software (OriginLab Corporation, Northampton, MA, USA). Previous Raman studies (Tenne, Farrar et al. 2010, Abreu, Soares et al. 2016) on STO have demonstrated that lattice distortions drive a breakdown in its cubic symmetry. From these distortions, distinct transverse (TO) and longitudinal (LO) optical phonon modes appear and their vibrational frequencies are listed in Table 2.3. It is expected that due to the isostructural nature of SNO with STO, similar vibrational modes should be observed. Thus, STO is a good structural reference to assist in the identification of the active modes in SNO.

Table 2.3 Expected Vibrational Modes and Frequencies for STO.

Phonon Branch	**Symmetry**	**Published work on $SrTiO_3$ (cm^{-1})**
TO_1	F_{1u}	118
LO_1	F_{1u}	175
TO_2	F_{1u}	185
LO_2	F_{1u}	475
TO_4	F_{1u}	550
LO_4	F_{1u}	795

2.2.8. UV-Vis Absorption Spectroscopy

UV-Vis absorption spectroscopy was performed to relate electronic changes to optical modifications. The absorption spectra of the NPs were recorded using a Perkin-Elmer Lambda

900 UV/Vis/NIR spectrometer equipped with an integrating sphere and a center mounted sample holder. A 30 W deuterium and 100 W halogen lamp were used for UV and visible-IR light irradiation, respectively. The absorption scans were collected from 800 to 250 nm using a scan rate of 1 nm/s with a lamp change at 319 nm and no monochromator change. The powder samples were dried onto a glass substrate to perform UV-Vis measurements. The absorption spectra are processed by shifting the absorption minimum (λ = 417 nm) to 0 and normalizing the spectra against the maximum absorption. For the SBO NPs, two distinct absorption regions are observed in Figure 2.4. These absorptions coincide with the optical transition from the valence band to the conduction band (UV region, 300-400 nm) and the transition from the partially filled *d*-band near the Fermi-level to the conduction band (Vis-NIR region, 400-800 nm) (Xu, Randorn et al. 2012).

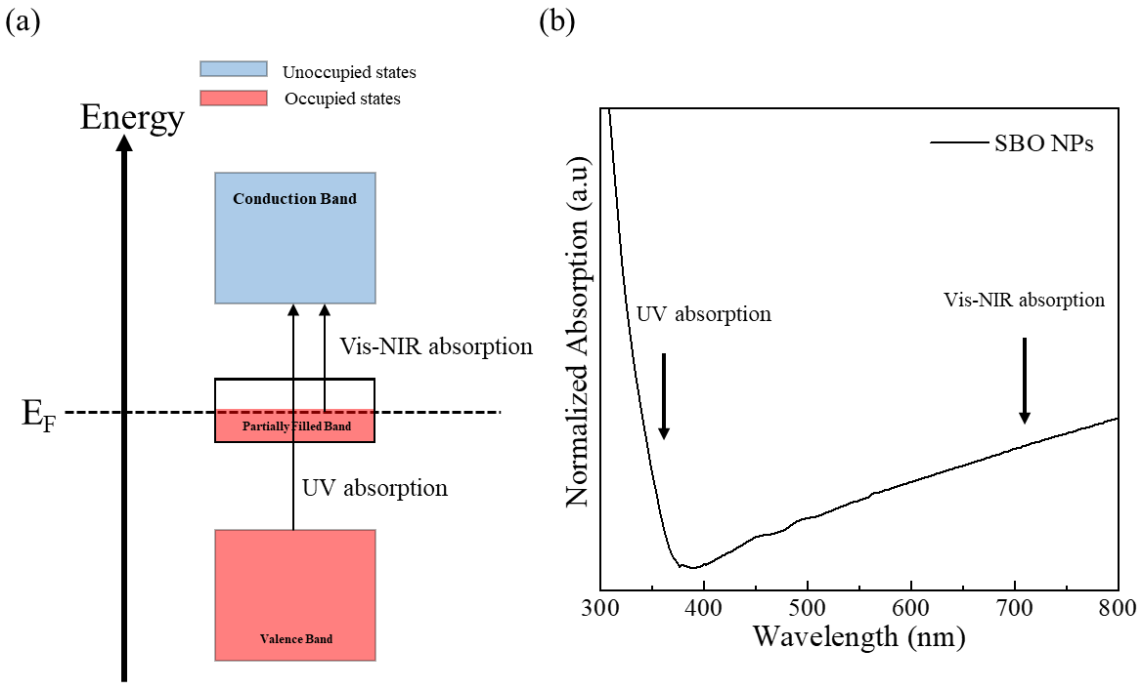

Figure 2.4 (a) Electronic structure and (b) absorption spectra for metastable SBO perovskites. Adapted from (Xu, Randorn et al. 2012).

2.2.9. Photoluminescence (PL) Spectroscopy

Rare-earth (RE) photoluminescence has been identified as an excellent probe to detect local structural changes due to the symmetry-dependent intra 4*f* transitions of the RE ions. In particular, trivalent europium (Eu^{3+}), owing to its characteristic magnetic (MT, $^5D_0$-$^7F_1$) and electric (ET, $^5D_0$-$^7F_2$) transitions (Tanner 2013, Bi, Bi et al. 2018, Wang, Darapaneni et al. 2020), has been employed in studying local symmetry changes in metal oxides (R Bajgiran, Darapaneni et al. 2019, Bajgiran, Dorman et al. 2020). Specifically, the emission intensity ratio of the ET to MT, defined as the asymmetry ratio (R-value), has a direct correlation to the Eu^{3+} occupied site symmetry (Bi, Bi et al. 2018). Figure 2.5 shows the Eu^{3+} photoluminescence in symmetric and non-symmetric crystal environments. The peaks positioned at ~580 and ~615 nm are indicative of the MT and ET, respectively. The R-value increases (from 0.83 to 1.59) as the A-site environment in a STO host crystal changes from high to low symmetry, highlighting the use of PL spectroscopy to probe local transformations.

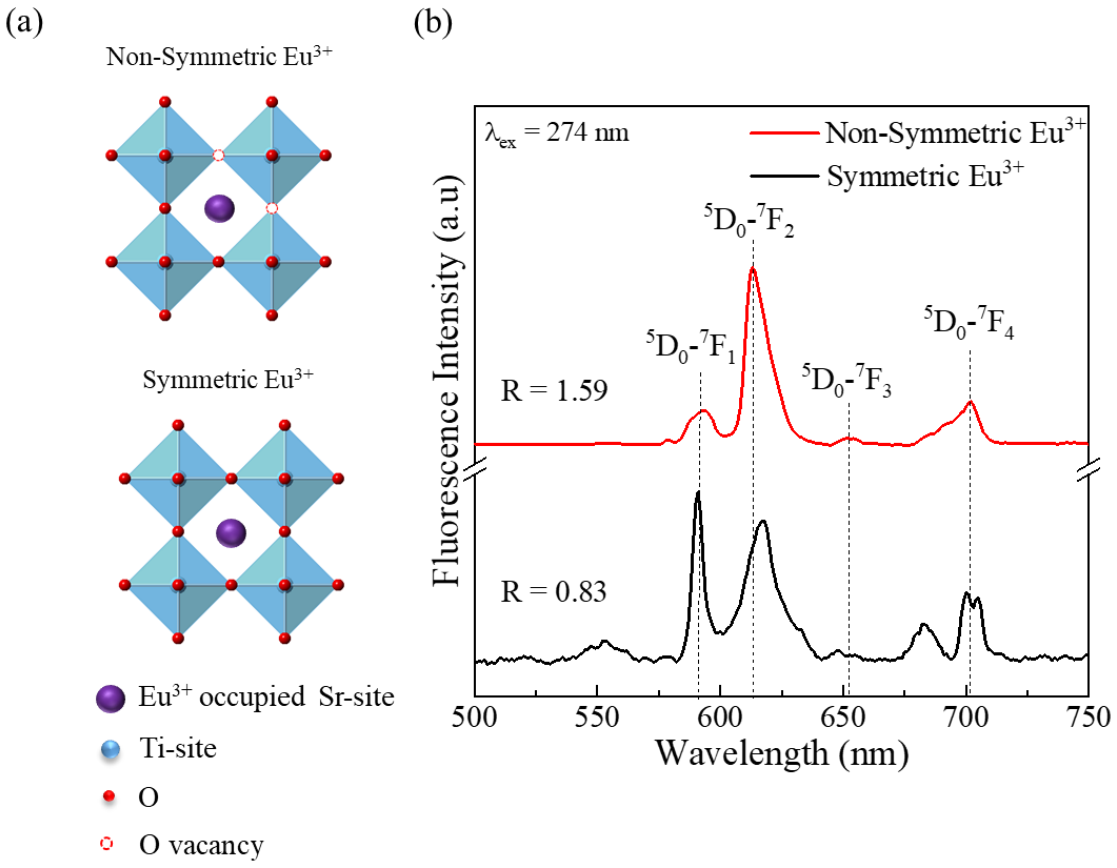

Figure 2.5 (a) Symmetric and non-symmetric A-site environment in STO host crystal and (b) corresponding photoluminescence response.

To demonstrate the ability of the facile wet-chemical approach to control the A/B-site environment of ABO_3 perovskites, *in-situ*/*ex-situ* PL spectroscopy was performed. *In-situ* refers to transformations (i.e. ferroelectric, structural, etc.) that are actively being monitored under the application of an external stimuli (i.e. temperature) and *ex-situ* refers to transformations investigated using dopants such as Ca. The *ex-situ* PL spectra were measured using an Edinburgh Instruments FLS1000 PL spectrometer equipped with a PMT detector and a 450 W ozone-free xenon arc lamp as the light source. Excitation and emission scans were collected with a 4 nm bandpass at a scan rate of 0.4 nm/s in the range of 240-400 nm (excitation) and 550-650 nm

(emission) with 1 nm step size. The powder samples were dispersed onto a quartz sample holder for PL measurements. The lifetime measurements were performed with a microsecond flash lamp (frequency: 25 Hz) over the range of 10 ms. For the *in-situ* temperature-dependent PL measurements, a LINKAM THMS600 temperature-controlled stage was added to the spectrometer setup. Liquid nitrogen was used as the cooling agent. Measurements were performed from -180 to 100 ^{o}C in 20 ^{o}C steps. The reported spectra are an average of three scans.

2.2.10. X-ray Spectroscopy Characterization

X-rays spectroscopy has been extensively applied in studying the chemical and electronic structure of a variety of low-dimensional systems such as nanocrystals (Zanchet, Hall et al. 2000). The toolbox of X-ray spectroscopic methods can be divided into two main categories (Venezia 2003): (1) methods designed to probe the creation of core holes and (2) methods designed to probe the decay of core holes. When X-ray photoelectrons interact with electrons in the core-level, the electrons are excited into higher energy states (core hole creation), which creates a detectable photoexcited electron, and the also possible relaxation (core hole decay) creates a detectable fluorescent photon (Baer and Engelhard 2010). In the first case, X-ray Photoelectron Spectroscopy (XPS) and X-ray Absorption Spectroscopy (XAS) are prime examples of using core hole creation to extract chemical/electronic information.

2.2.11. X-ray Absorption Spectroscopy (XAS)

XAS uses a synchrotron X-ray radiation source to study the geometric and electronic structure around the absorbing atom by creating core hole states (i.e. excitation from filled ground state to unoccupied excited state). In the unoccupied excited state, the ejected electrons remain bound to the atom, allowing for the valance levels to be studied. XAS utilizes two kinds

of X-ray sources, hard X-rays (>5 keV, atmospheric condition) and soft X-rays (<1 keV, vacuum condition). Concentrating on XAS using a soft X-ray source (soft XAS) (Figure 2.6), the low energy transitions of Sr (L-edges), Ca (L-edges), and O (K-edge) are probed (Thompson, Attwood et al. 2001). The energy at which these edges (absorption transitions) occur are highly element specific, further intensifying the use of soft XAS. During the collection of soft XAS data, the X-ray Absorption Near Edge Spectroscopy (XANES) region captures the low energy of the XAS spectrum where information pertaining to the oxidation state and orbital transition can be extracted. Figure 2.6 shows that features changes in this region has also been used as indicators of local structural transformations (Asokan, Jan et al. 2004, Kuepper, Falub et al. 2005). In this example, a $Ba_xLa_{1-x}MnO_3$ perovskite undergoes a cubic (x = 0) to hexagonal (x = 0.55) phase transition, which is seen in the O K-edge XANES spectra as a loss in peak splitting for the hybridized Mn 3*d* peak (~530 eV).

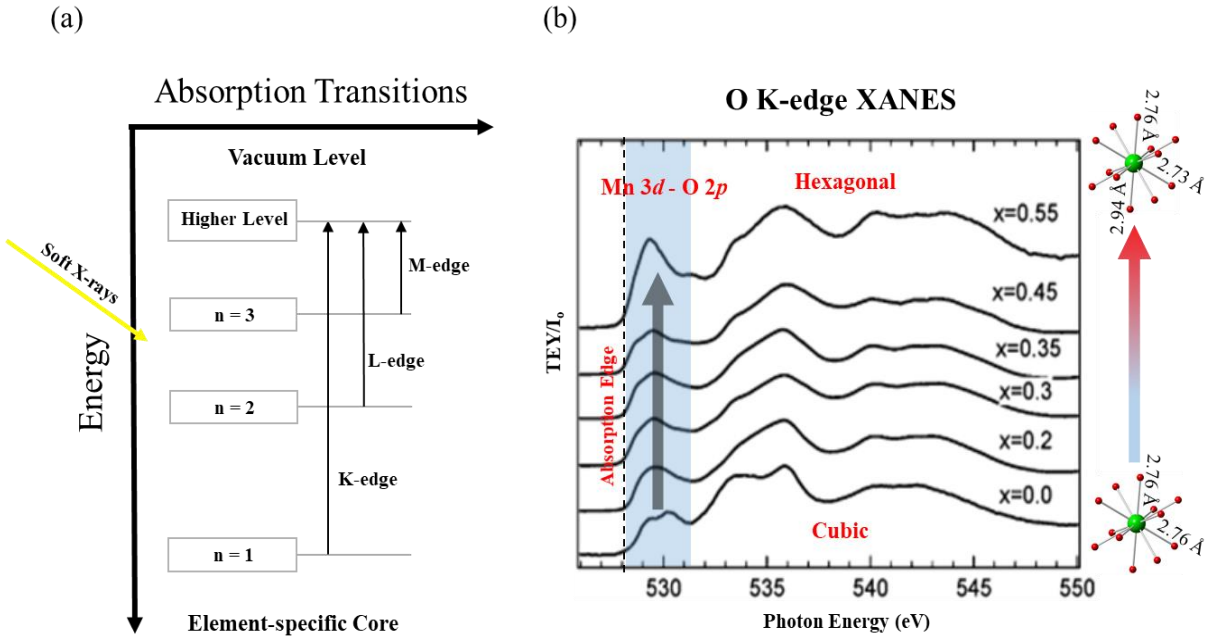

Figure 2.6 XAS energy transitions using a soft X-ray source and (b) O K-edge XANES spectra. Adapted from (Kuepper, Falub et al. 2005).

There are three detection modes (i.e. transmission, fluorescence, and total electron yield (TEY)) for data collection. The absorption cross-section (μ) is a function of the applied detection mode because the measured current (I) from the X-rays differs. For example, in the transmission mode, the μ is calculated based on the intensity ratio of the X-ray that incident (I_o) and passes through (I_t) the sample. This is expressed using the following equation: $\mu = \ln (I_o/I_t)$. Next, the fluorescence mode uses a ration of the incident to fluorescence of X-rays from the sample (I_F). This method is particularly useful in cases when weak transmission signals are expected, i.e. dilute samples. This detection method expresses μ using the following equation: $\mu = \ln (I_F/I_o)$. Lastly, the TEY mode considers the absorption and corresponding electron emission in the form of both photoelectrons and Auger electrons (I_E). Unlike the previously mentioned modes, this method is specific to soft XAS which limits the probing depth to ~2 nm. The μ is expressed as the following equation: $\mu = \ln (I_E/I_o)$.

In this study, soft XAS was performed to probe local electronic structural changes to corroborate observed bulk structural transformation from dopant incorporation. XAS measurements were conducted at the varied-line-spaced plane grating monochromator (VLSPGM, 0.2-1.2 keV) beamline of the Center for Advanced Microstructures and Devices (CAMD). In these measurements, changes in the local geometry and electronic structure of the crystal were studied by probing the XANES region of Ca ($L_{3,2}$-edge, ~453 eV) and O (K-edge, ~543 eV). The powder samples were attached to either Kapton or carbon tapes according to the beamline requirement and loaded into the sample chamber maintained at 2×10^{-9} Torr. The XANES data, collected using fluorescence and transmission detectors, was normalized and analyzed with the Athena software (Ravel and Newville 2005). Calcium oxide (CaO) powder was used as a reference for calibration purposes.

2.2.12. X-ray Photoelectron Spectroscopy (XPS)

XPS uses incident X-rays with known energies (*hv*) to determine the characteristic binding energy (*BE*) of an element by creating core hole states (i.e. excitation from filled ground state to vacuum level). In the vacuum level, photoelectrons are ejected after surface bombardment by monochromatic X-rays and the ejected electrons are subsequently collected at an analyzer/detector. The *BE* is calculated using the following conservation of energy relationship: $BE = hv + KE + \Phi$. In this equation, *KE* refers to the kinetic energy of the photoexcited electrons that interact with the analyzer/detector. Φ refers to the work function of the spectrometer (typically ranging from 2-5 eV). Once the *BE* is determined, chemical signatures such as oxidation state, binding environment, empirical formula, etc. can be extracted.

In this work, XPS was performed to verify that the synthesized nanocrystals are in oxidation states that stabilize the ABO_3 stoichiometry. XPS spectra were collected using a Scienta Omicron ESCA 2SR XPS system equipped with a monochromatic Al K_α (*hv*=1486.6 eV) X-ray source and a hemispherical analyzer with a 128-channel detector. The inherent gaussian width of the photon source was 0.2 eV. The pressure inside the chamber was maintained at 1.5×10^{-9} Torr. These measurements were also performed at the 5-m toroidal grating monochromator (TGM) beamline at CAMD. The beamline and endstation are described in detail elsewhere (Kizilkaya, Jiles et al. 2014). The beamline is equipped with an ultrahigh vacuum chamber endstation maintained at a base pressure of 10^{-10} Torr, a DAR-400 dual Mg/Al nonchromatic X-ray source, and an Omicron EA 125 hemispherical electron energy analyzer with a five-channel detector. The XPS spectra were collected in a constant pass energy mode with pass energy of 50 eV. The spectra were calibrated to adventitious C 1*s* peak at 284.6 eV. All peaks were fit (using CasaXPS software (Fairley 2009)) to symmetric Voigt functions (70% Gaussian and 30%

Lorentzian) and a Shirley background to determine peak positions and areas. The fitting parameters were generated with a Levenberg-Marquardt optimization algorithm. The peaks were compared with known standards.

2.2.13. Electrical Resistance Measurements

The electrical resistances were measured at room-temperature using a Model 6000 Quantum Design Physical Property Measurement System (QD PPMS) and a KEITHLEY 2601A multimeter. The as-synthesized powder samples were uniaxially pressed into circular pellets (~100 mg, ø ~ 6.5 mm × 0.9 mm) at 1 ton and transferred to a quartz tube furnace to be annealed at 800 ℃ for 8 h in N_2 atmosphere. Next, the pellets were treated in H_2/Ar atmosphere at 800 ℃ and with various times (0 - 6 h) to modify the electronic properties. The circular pellets were cut into rectangles and electrodes were soldered onto them. Silver paste was subsequently applied to minimize contact resistance between the electrode and the sample. Prior to performing the measurements, the pellets were air dried for ~2 days. To perform the QD PPMS measurement (4-point probe method) (Valdes 1954), the samples were wired to the sample puck and the measurement parameters were adjusted with the user bridge board. These parameters include channel set, current limit (*I*), power limit (*P*), voltage limit (*V*), calibration mode, and drive mode. The channel set depends on where the sample puck is connected in the instrument. The *I* ranges from ±0.01-5000 μA, the *P* ranges from 0.001-1000 μW, and the *V* ranges from 1-95 mV. To collect the resistance (*R*, Ω), the *I* was alternated within the limit of the instrument (i.e. ±0.01 to 5000 μA). Next, the *P*, *V*, calibration mode, and drive mode were set to 1000 μW, 95 mV, standard, and DC, respectively. This testing procedure is important because metals have voltage-independent (ohmic) and semiconductor/insulator have voltage dependent (non-ohmic behavior) behaviors. Therefore, for a metallic sample, the resistance will be constant no matter the *I* value

set, however, for a semiconductor/insulator, there is a minimum *I*. In the multimeter measurement (2-point probe method) (Wenner 1916), the *V* is swept from ±5 V and the corresponding *I* was recorded under the auto range setting. This testing procedure was cycled between the +V to -V to ensure reproducibility. The electrical resistivities (ρ, Ω-cm) were calculated by applying Ohm's and Pouillet's laws (Li, Wang et al. 2019).

2.2.14. Electrochemical Impedance (EIS) Spectroscopy

EIS measurements were performed to monitor changes in the charge transport for the conductive NPs and the layered film architecture. The EIS data was collected on a BioLogic SP-150 potentiostat/galvanostat with an oscillation voltage of 10 mV and a frequency range from 10^5 to 10^{-2} Hz. The measurements were carried out using a Li-ion coin cell (NP characterization) and a three-electrode cell setup (layered film architecture characterization) held at open-circuit voltage for 30 min and operating at room temperature. For the Li-ion coin cell, the active materials, carbon black, and poly(vinylidene fluoride) in a weight ratio of 70:20:10 in 400 µL of NMP were mixed to form a slurry. The mixed slurry was coated uniformly onto a thin copper/aluminum foil, dried overnight in air at 100 ℃. Coin cell batteries (CR2032/CR2016) were assembled using the SBO NPs as the working electrode, a polypropylene microporous film as the separator, and a lithium foil as the counter and reference electrode. A 1 M solution of $LiPF_6$ dissolved in ethylene carbonate and dimethyl carbonate (1:1 in volume ratio) was used as the electrolyte. The lithium half-cells were assembled in an Ar-filled glovebox with both water and oxygen contents below 40 ppm. For the three-electrode cell setup, the layered architecture as the working electrode, Pt wire as the counter electrode, and Ag/AgCl (BASi Inc., USA) as the reference electrode are placed in a 1 M $LiNO_3$ electrolyte. To prepare the working electrode, place a glass slide (1 × 25 × 75 mm) in acetone and sonicate it for ~30 min. After sonication, a

strip of Cu adhesive tape was applied onto the glass substrate, leaving extra room at one end for attaching the alligator clip. To prevent redox reactions from occurring between the Cu tape and the electrolyte, a protective layer of polyurethane tape was added until only ~3 mm of Cu tape was exposed. Next, Ag paste is applied onto the exposed region and the SBO pellet was placed on top. The assembly was dried overnight in an oven at 80 ℃. After drying, a slurry of LFP was sprayed/painted over the SBO pellet and, once again, dried overnight in an oven at 80 ℃. The final working electrode is displayed in Figure 2.7. The collected spectra were simulated and fitted with an equivalent circuit using the ZView software (Scribner Associates Inc.). The equivalent circuit model employed to characterize the non-aqueous systems is displayed in Eqn. 2.14 (Qian, Xu et al. 2012, Raccichini, Amores et al. 2019):

$$R_S(R_{SEI}CPE)(R_{CT}CPE_{CT})$$

(2.14)

where R_S, R_{SEI} resistance of electrolyte and solid-electrolyte interface (SEI); *CPE*, constant phase element of SEI; CPE_{CT}, R_{CT} constant phase element and charge transfer resistance of anode and cathode.

The aqueous systems were characterized using the model displayed in Eqn. 2.15 (He, Zhang et al. 2007):

$$R_S(R_{CT}CPE_{CT})$$

(2.15)

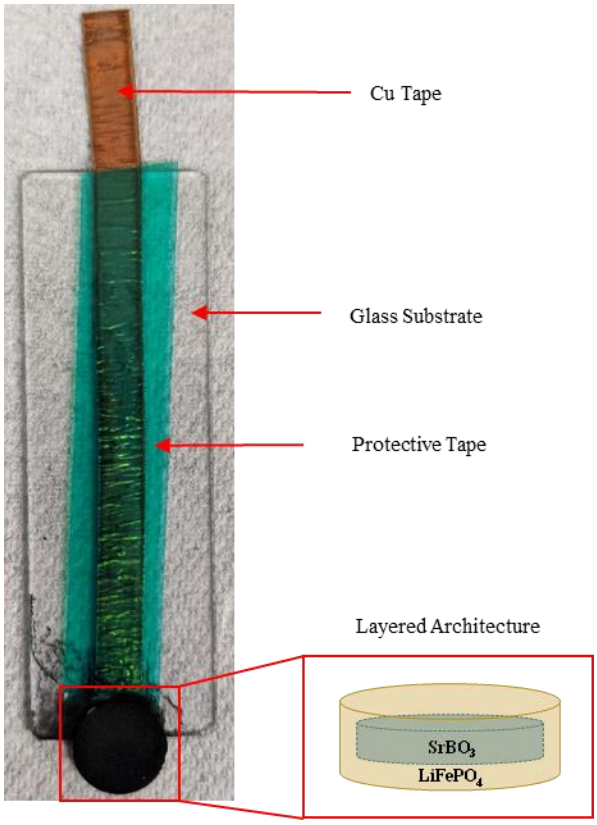

Figure 2.7 Working electrode setup to test the layered film architecture.

.

Chapter 3 . Stabilizing the B-site of SNO Nanoparticles via Wet-Chemical Synthesis[2]

3.1. Introduction

In order to prepare the metastable ABO_3 perovskites, a novel wet-chemical synthetic approach needs to be developed for these nanomaterials. Considering the case of SNO with ABO_3 stoichiometry, traditional solution-based methods prevent its crystallization by resulting in the thermodynamically stable pentavalent state of Nb. These over-oxidized Nb-sites form defect states, which contribute to suppressing the expected optoelectronic properties of SNO, thus necessitating the need for alternative methods. Previous studies on the thin-film analogue demonstrated that the preferential seeding of these defect states can be limited using oxygen-deficient atmospheres (Campion, Brown-Shaklee et al. 2013). For this purpose, the crystallization of SNO NPs (~20 nm) using a low-pressure wet-chemical synthesis route was studied. The elemental composition and crystal structure of the as-synthesized SNO crystals were studied using EDX and XRD. The Sr/Nb molar ratio was varied to shift product formation toward SNO and at a critical concentration (Sr/Nb=1.3), Sr-deficient ($Sr_{0.7}NbO_{3-\delta}$) and stoichiometric ($SrNbO_3$) phases were stabilized. Changes in the Nb-O bond length and phase quantification were determined from structural refinement. XPS, Raman spectroscopy, and DFT corroborate these results by confirming the formation of majority tetravalent Nb in octahedral coordination. These results suggest that the crystallization of SNO NPs under low oxygen partial pressures and with excess Sr can stabilize tetravalent Nb by suppressing the formation of Nb defect states. Finally, the optoelectronic properties were characterized (UV-Vis spectroscopic) demonstrating the control of structural properties of the material. While this ability to

[2] "Reprinted (adapted) with permission from (T. Ofoegbuna, P. Darapaneni, S. Sahu, C. Plaisance, and J. A. Dorman, Stabilizing the B-site oxidation state in ABO3 perovskite nanoparticles. Nanoscale, 2019, 11(30), 14303-14311. Copyright (2019) The Royal Society of Chemistry.".

synthetically stabilize the oxidation state of a transition metal in a perovskite matrix provides new insights into the understanding of coordination chemistry in metal oxides, it also enables innovative opportunities for these nanomaterials in advance optoelectronic applications such as plasmonic photocatalysis and perovskite solar cells. This work has been published as "Stabilizing the B-site Oxidation State in ABO_3 Perovskite Nanoparticles" in *Nanoscale*.

3.2. Structural Characterization on SNO NPs

Hydrothermal and MSS chemistries are well-established methods for crystallizing complex metal oxides with various photophysical properties (Mao and Wong 2005, Cho, Lee et al. 2010). Therefore, these methods were first tested to prepare the SNO NPs. Figure 3.1(a) shows that, rather than Sr-intercalation, Nb is oxidized to the pentavalent state, creating a Nb_2O_5 (orthorhombic, ICDD 27-1313) crystal structure after the hydrothermal reaction at 180 ℃. This was initially believed to be due to the type of mineralizer used in the synthesis (NH_4OH), so tetramethylammonium hydroxide (TMAOH) and NaOH were also used (Figure 3.1(b)). Literature reports have demonstrated that, in addition to the structure/reactivity of the precursor and temperature, the type of mineralizer plays an important role in determining the final composition (Mao, Banerjee et al. 2003, Zhang, Huang et al. 2018). The cation of the mineralizer can accelerate the crystallization rate by catalysing the intermediate metal (oxy)hydroxide structure (Zhang, Huang et al. 2018). As a result, it was expected that the closer ionic radius of Na^+ (~1.0 Å) will assist in the incorporation of Sr^{2+} (~1.2 Å) (Ouyang 2019), as seen with the crystallization of STO (Mao, Banerjee et al. 2003, Mallikarjunaiah, Damle et al. 2008). Instead, these results demonstrate that, under hydrothermal conditions, the oxidation of the Nb-site is fast and larger ionic radii cations (i.e., Sr^{2+}, ~1.2 Å; TMA^+, ~3.0 Å; NH_4^+, ~1.5 Å) cannot participate in the reaction (Mallikarjunaiah, Damle et al. 2008). However, smaller ionic radii cations (i.e.,

Na) have faster diffusions so they are able to be incorporated into the lattice during the oxidation, forming $NaNbO_3$ (orthorhombic, CODS 9014348).

To facilitate the intercalation of Sr-ions into the lattice, MSS was subsequently performed (Figure 3.1(c)). Although Sr-intercalation is no longer an issue, as seen by the crystallization of $Sr_2Nb_2O_7$ (ICSD 8-8703), $SrNb_6O_{16}$ (ICSD 13-0541), and $Sr_5Nb_4O_{15}$ (ICSD 28-1248), Nb is stabilized as highly oxidized states in these structures. These over-oxidized states form Nb defects and are favored using this approach. Owing to the similarity in ionic radius of Na with Sr, the possible exchange of these ions under a MSS environment was also studied (Figure 3.1(d)). This method uses a template structure coupled with a large concentration gradient to drive the cation of interest into the lattice. For example, this method has been previously demonstrated by the replacement of Na^+ with the larger-sized K^+ (~1.4 Å) (Xu, Zhen et al. 2007). The large Sr concentration, necessary for ion exchange, combined with the contamination from atmospheric oxygen contributed to the dominate crystallization of $SrCO_3$ (CODS 9000227) impurities over the formation of SNO (Mao, Banerjee et al. 2003). Overall, these results show that Nb defect states, formed due to the multi-valent Nb, are readily stabilized using traditional wet-chemical methods.

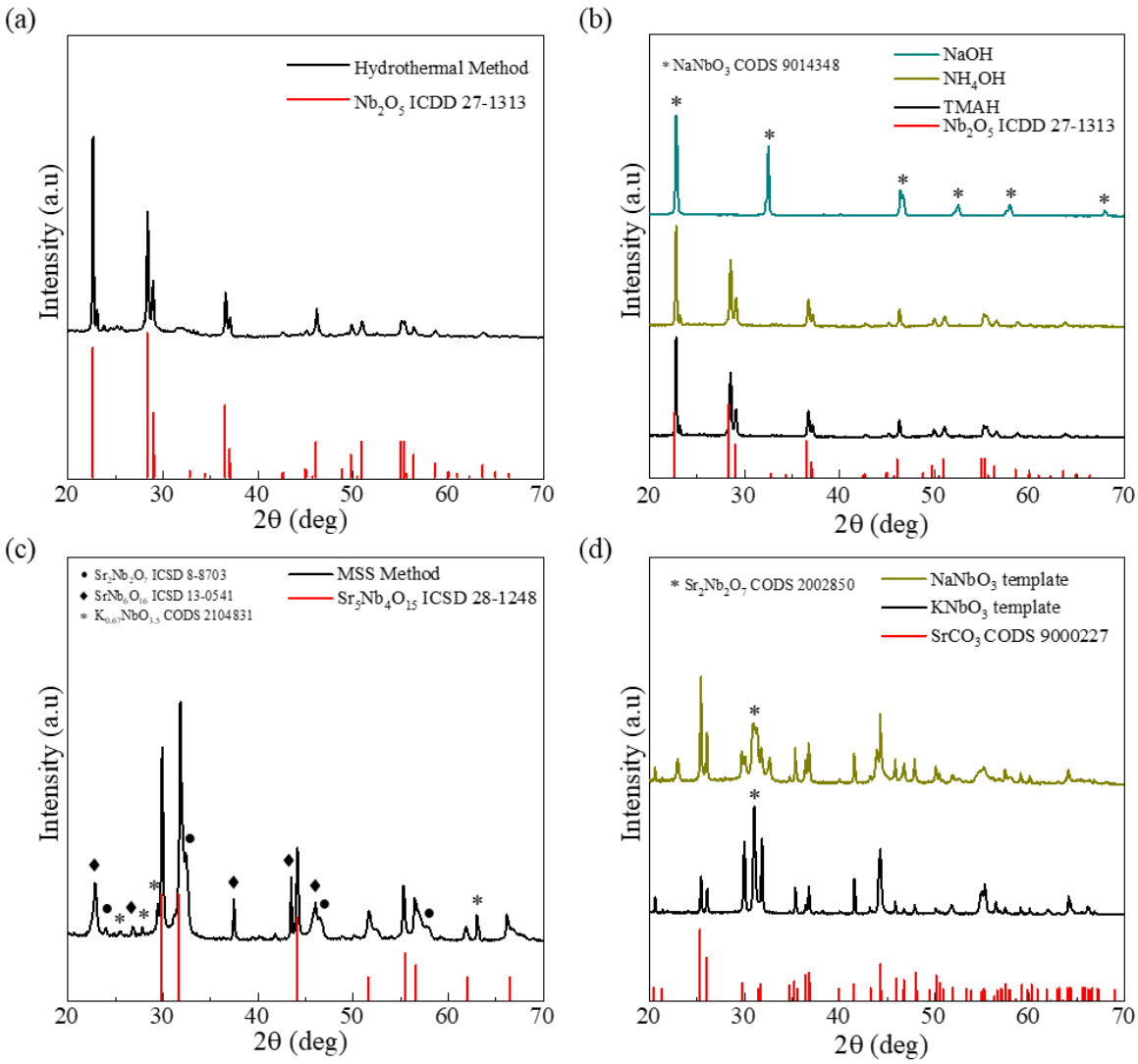

Figure 3.1 Synthesis of SNO NPs using traditional solution-based chemistries: (a-b) Hydrothermal and (b-c) MSS methods.

To address the problems observed from using traditional methods, the oxygen-controlled CP/MSS method was developed. In this synthetic method, a single-source amorphous complex precursor is prepared in the CP step and the subsequent MSS step promotes the crystallization of the amorphous precipitate by providing a low melting point salt solvent to facilitate the diffusion of reacting species (Alaparthi, Tian et al. 2013). Interestingly, a cubic $Sr_{0.7}NbO_3$ phase (space

group: *Pm-3m*, ICDD 19-2410) with lattice parameter a = 3.981 Å was formed which was not observed previously. Additionally, low intensity shoulder peaks are observed on the main diffraction peaks due to the crystallization of a secondary lattice. The (110) reflection is presented on the right to highlight these low intensity shoulder peaks which have been indexed to the $NaNbO_3$ (ICDD 19-1221) crystal structure. The remaining diffraction peaks, indicated by asterisks, are due to Nb defects, partially matching $SrNb_6O_{16}$ (ICDD 46-1287) and (K, Na)$SrNbO_x$-based complexes (Ridgley and Ward 1955, Surmin, Fertey et al. 2006, Liu, Gao et al. 2013, Lima, Sczancoski et al. 2016, Zhang, Pan et al. 2017). These observed Nb defect states are formed due to the thermodynamically stable pentavalent state which can be prevented by reducing the oxygen partial pressure during the reaction (Campion, Brown-Shaklee et al. 2013). Therefore, an analogous approach was implemented with a molten salt solvent under reduced oxygen atmospheres to shift the thermodynamic equilibrium to tetravalent Nb, as seen in Figure 3.2. While diffraction peaks associated with $NaNbO_3$ are not observed at lower oxygen partial pressures, diffractions for the Nb defect states remain. These results indicate that $NaNbO_3$ is formed directly from the oxidation of niobium in an oxygen-rich environment whereas the Nb defect states are formed by the oxidation of niobium during the CP step (Alaparthi, Tian et al. 2013).

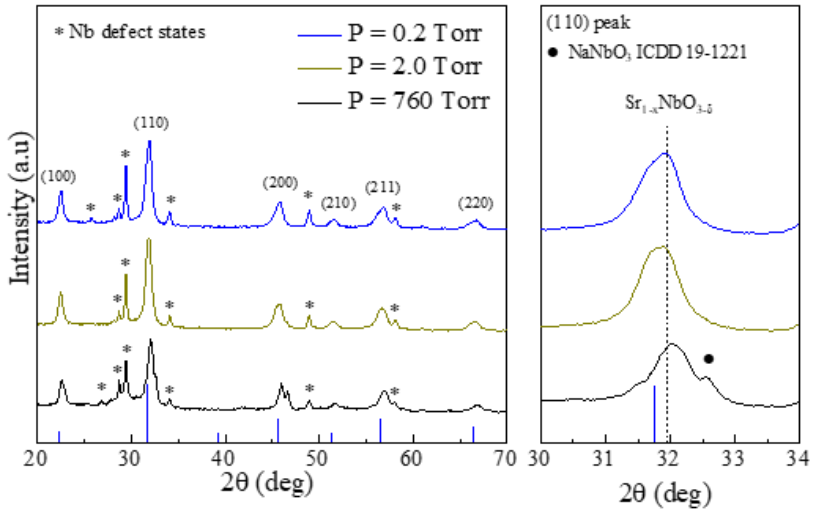

Figure 3.2 Pressure dependence of SNO (Sr/Nb=1.0) nanoparticles for 0.2, 2.0, and 760 Torr. The $NaNbO_3$ reflection is highlighted in the expanded view (circle). The asterisks indicate reflections from Nb defect states. The dashed lines are a guide to the eye for $Sr_{0.7}NbO_{3-\delta}$ (ICDD 19-2410, blue vertical marker) phase identification.

In order to prevent the oxidation within the CP step, non-stoichiometric A/B ratios have been employed to manipulate crystallization kinetics (Rabuffetti, Kim et al. 2008, Guo, Liu et al. 2012, Saint-Girons, Bachelet et al. 2016). To verify this effect during initial A-O-B bond formation, excess Sr was incorporated into the reaction mixture at reduced pressures (0.2 Torr) to inhibit the formation of unsaturated Nb^{4+} during precipitation. With increasing Sr content, a Sr-deficient to stoichiometric phase transition is observed (Figure 3.3) and indexed to cubic $SrNbO_3$ with space group *Pm-3m* (ICDD 6-3450, a = 4.040 Å).

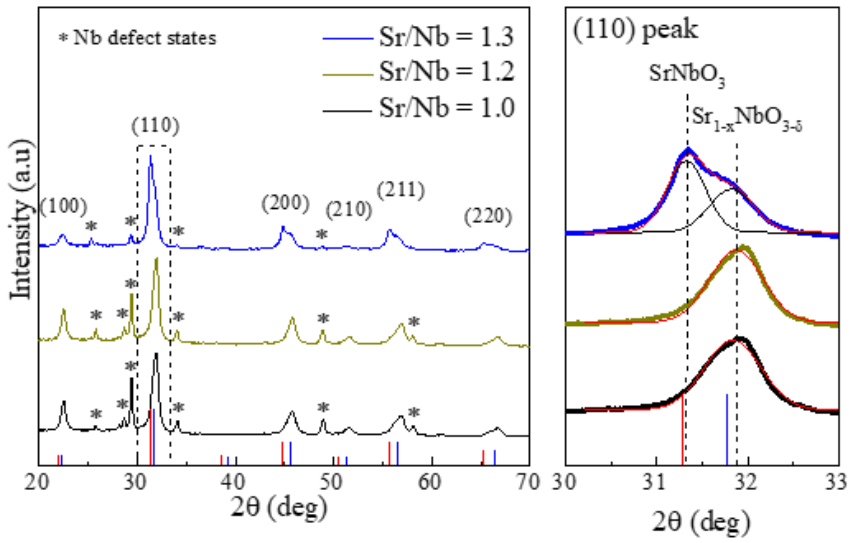

Figure 3.3 Concentration dependence of SNO (Sr/Nb =1.0, 1.2, and 1.3) nanoparticles synthesized under total pressure of 0.2 Torr. The dashed lines are a guide to the eye for $SrNbO_3$ (ICDD 6-3450, red vertical marker) and $Sr_{0.7}NbO_{3-\delta}$ (ICDD 19-2410, blue vertical marker) phase identification.

A magnified view of the (110) reflection peak highlights the shift in peak position upon Sr-enrichment. The lattice parameters and crystallite sizes were extracted for each composition (Table 3.2). The Sr-deficient phase was indexed to cubic $Sr_{0.7}NbO_3$ with the calculated lattice parameter matching the reported literature value (a = 3.981 Å) (Ridgley and Ward 1955). For the 1.3 molar ratio (Table 3.2), the stoichiometric phase is similar to those reported for thin films (4.042 Å) (Tomio, Miki et al. 1994), with a crystallite size of approximately 16 nm. Furthermore, quantitative composition analysis was performed on the 1.3 molar ratio sample using inductively coupled plasma optical emission spectrometry (ICP-OES). The as-determined Sr (49 mol%) and Nb (51 mol%) ratios agree with the theoretical $Sr_{0.7}NbO_{3-\delta}/SrNbO_3$ stoichiometry. These results demonstrate that the low-pressure MSS approach results in Sr-deficient ($Sr_{0.7}NbO_3$) and stoichiometric ($SrNbO_3$) phases.

Table 3.2 Comparison of the Lattice Parameters and Crystallite Size for SNO Nanoparticles Determined from Concentration Control Studies.

Sr/Nb Ratio	Lattice Parameter (Å)	Crystallite Size (nm)
1.0	3.966	10.26 ± 2.79
1.2	3.962	10.97 ± 2.43
1.3	3.970	8.61 ± 3.51

Table 3.2 Comparison of the Lattice Parameters and Crystallite Size for SNO (Sr/Nb = 1.3) Phases.

Sr/Nb = 1.3	Lattice Parameter (Å)	Crystallite Size (nm)
Sr-deficient phase	3.970	8.61 ± 3.51
Sr-rich phase	4.042	16.41 ± 6.76

Incorporating excess Sr into the synthesis limits the formation of Nb defect states as seen by the reduced defect peak intensity (Figure 3.3). Similar growth kinetics has been observed for the conversion of (wurtzite) InP to (zinc blende) $Ga_xIn_{1-x}P$ nanowires (Lehmann, Jacobsson et al. 2015, Dagytė, Heurlin et al. 2018). Ga is incorporated into the In occupied tetrahedral sites of the InP crystal in order to favor the formation of the zinc blende structure. In the presence of excess In, the diffusion of Ga into the crystal was inhibited, resulting in the formation of Ga-deficient nanowires with wurtzite structure. Based on the previously reported structure transition, the diffraction data indicates that the increased Sr/Nb molar ratio prevents the diffusion of Na^+/K^+

into the crystal. Next, the vacant Sr-sites begin to be occupied at higher Sr^{2+} concentrations, leading to the formation of stoichiometric $SrNbO_3$. The incorporation of these Sr^{2+} ions into vacant Sr-sites persists until 1.5 molar ratios. When the Sr^{2+} concentration is increased above the 1.5 molar ratio, the Sr-deficient lattice and Nb defect states are reformed (Figure 3.4). Therefore, it is important to maintain a critical Sr concentration to stabilize a majority Nb^{4+} by limiting the formation of Nb defects.

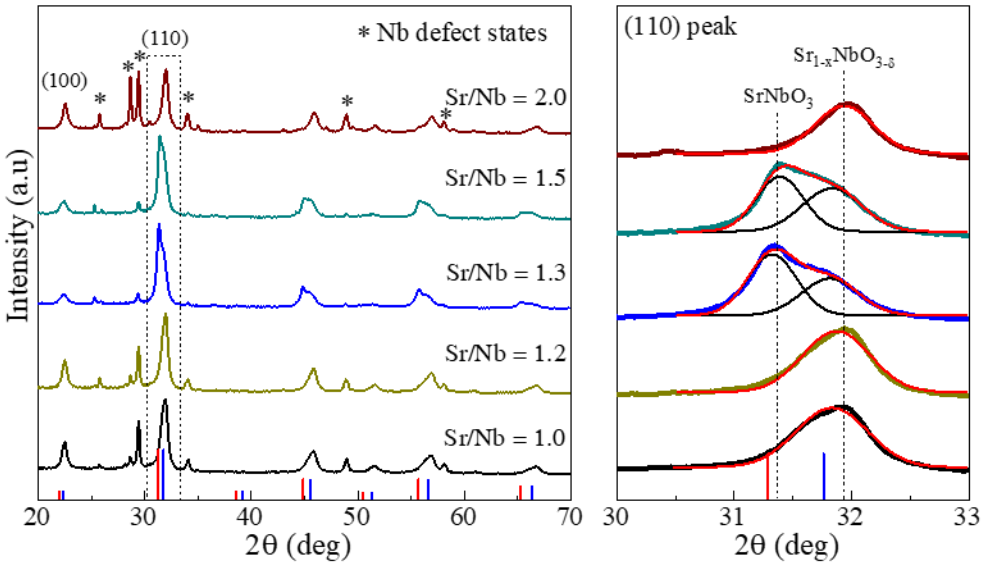

Figure 3.4 Concentration dependence of SNO (Sr/Nb =1.0, 1.2, 1.3, 1.5, and 2.0) nanoparticles synthesized under total pressure of 0.2 Torr. The diffraction highlights Sr intercalation at Sr/Nb molar ratios above 1.3.

Rietveld refinement was performed to quantify the ratio of stoichiometric and Sr-deficient phases present in the SNO (Sr/Nb = 1.3) NPs. The final diffraction pattern was refined using the cubic space group *Pm-3m* (no. 221) $SrNbO_3$ (Tomio, Miki et al. 1994) and $Sr_{0.7}NbO_3$ (Ridgley and Ward 1955) as structural models for the stoichiometric and Sr-deficient phases, respectively. This was determined by first refining the diffraction pattern using Nb defects such

as $SrNb_6O_{16}$ and (K, Na)$SrNbO_x$-based complexes, resulting in (χ^2 > 5). Next, Rietveld refinement was systematically performed using $Sr_{0.68}NbO_3$, $Sr_{0.69}NbO_3$, $Sr_{0.70}NbO_3$, $Sr_{0.71}NbO_3$, and $Sr_{0.72}NbO_3$ to determine the stoichiometry of the Sr-deficient phase. The refined lattice parameter was subsequently compared with the calculated values (Table 3.2). The similar procedure was performed on the stoichiometric phase. Since the aim of the structural refinement was to quantify the SNO phases, the reflections due to the Nb defect states were excluded from the final structural refinement. However, it was possible to obtain good structural agreement (R_p = 3.65%, R_{wp} = 4.47%, and χ^2 = 2.64) even when the reflections associated with the Nb defect states were included. A summary of the crystallographic data and final refinement details are listed in . The fits were deemed to be good based on these parameters coupled with visual confirmation from Figure 3.5(a-b). Both structural parameters show good agreement with previous studies (Ridgley and Ward 1955, Tomio, Miki et al. 1994). From the refined crystal structure, the amount of $SrNbO_3$ and $Sr_{0.7}NbO_3$ is estimated to be 53 and 47 wt% respectively. The schematic drawing in Figure 3.5(c) highlights the effect of the phase transition on the Nb octahedral coordination environment (NbO_6). The multi-valent Nb site creates two distinct binding environments, possessing average Nb-O bond lengths of 1.99 Å and 2.02 Å. It is also important to highlight that in the refinement, the occupancy of the anion sites for the Sr-deficient phase were kept unchanged to represent the $Sr_{0.7}NbO_3$ stoichiometry.

Table 3.3 Crystallographic Data, Refined Atomic Coordinates, and Structural Parameters at Room Temperature for SNO (Sr/Nb = 1.3) Phases based on X-ray Diffraction Data.

Parameters	**$SrNbO_3$**	**$Sr_{0.7}NbO_3$**
wavelength (Å)	1.541	
temperature (K)	300	
2θ range (˚)	20-70	
space group	Pm-3m (No. 221)[a]	Pm-3m (No. 221)[b]
Z	1.0	
goodness-of-fit	1.73	
Lattice Parameters		
a, b, c (Å)	4.042(7)	3.982(7)
α, β, γ (˚)	90	90
V ($Å^3$)	66.075	63.176
Atomic Coordinates		
Sr (x,y,z)	0, 0, 0	1/2, 1/2, 1/2
Nb (x,y,z)	1/2, 1/2, 1/2	0, 0, 0
O (x,y,z)	0, 1/2, 1/2	1/2, 0 , 0
Structural Parameters		
Sr-O (Å)	2.858(7)	2.816(2)
Nb-O (Å)	2.021(4)	1.991(4)
O-Nb-O (deg)	180	180
O-Nb-O (deg)	90	90
Nb-O-Nb (deg)	180	180

[a-b] space group ref.: ICSD 6-3450, ICSD 19-2410. The occupancy was fixed to 1 at all atom sites for the $SrNbO_3$ structure and to 0.7 at the Sr site and 1 at Nb and O sites for the $Sr_{0.7}NbO_3$ structure. For the $SrNbO_3$, the isotropic displacement parameter U_{iso} is 0.036(2), 0.002(9), and 0.045(1) $Å^2$ for Sr, Nb, and O sites, respectively. For the $Sr_{0.7}NbO_3$, the isotropic displacement parameter U_{iso} is 0.016(4), 0.005(5), and 0.001(8) $Å^2$ for Sr, Nb, and O sites, respectively.

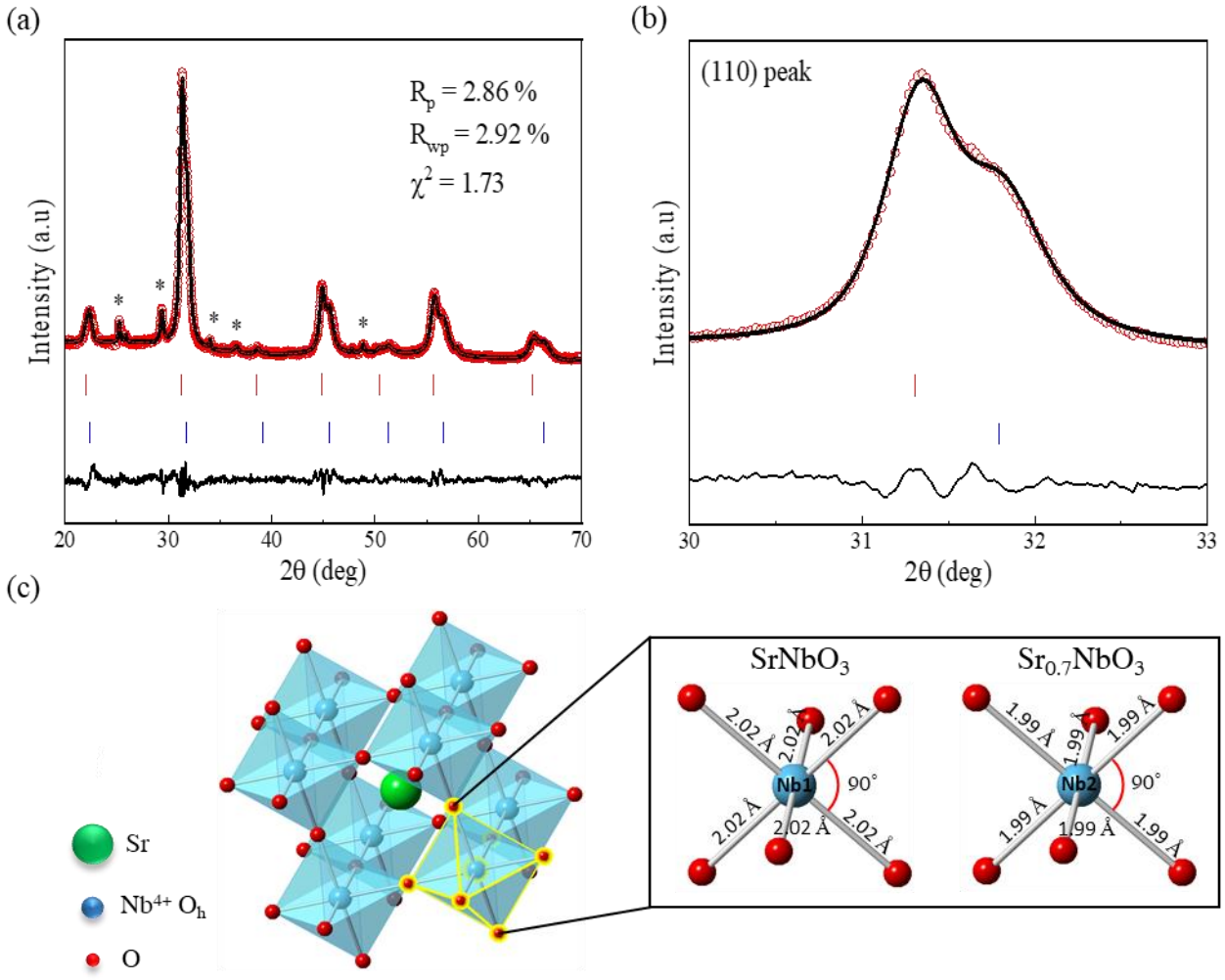

Figure 3.5 (a) XRD pattern and Rietveld refinement for SNO (Sr/Nb=1.3) nanoparticle recorded at room temperature with λ = 1.541 Å. The upper symbols illustrate the observed data (circles) and the calculated pattern (solid line). The vertical markers show calculated positions of Bragg reflections. The red and blue vertical marks indicate the Bragg peak positions of $SrNbO_3$ (wt = 52.96%) and $Sr_{0.7}NbO_3$ (wt = 47.04%) respectively. The lower curve represents the difference between observed and calculated intensities. Impurity peaks are indicated in asterisks and were excluded from the refinement. (b) enlarged XRD pattern showing fit for (110) peak. (c) Illustration of refined crystal structure and Nb coordination environments.

3.3. Probing the Oxidation State of SNO NPs

To corroborate the SNO crystal structures identified by diffraction studies, the oxidation states of Sr, Nb, and O in the SNO (Sr/Nb=1.3) NPs were determined using XPS (Figure 3.6). The detailed scan of the Sr 3*d* region, presented in Figure 3.6(b), shows two sharp peaks around 132.8 eV (Sr $3d_{5/2}$) and 134.6 eV (Sr $3d_{3/2}$) corresponding to Sr^{2+} (Haasch, Breckenfeld et al. 2014). The Nb ($3d_{5/2}$ and $3d_{3/2}$) peaks, Figure 3.6(c), of the as-synthesized SNO NPs are located at lower binding energies compared to the Nb_2O_5 (Nb^{5+}) reference powder. Based on the Nb_2O_5 reference, the Nb^{5+} oxidation states are positioned at 206.5 eV (Nb $3d_{5/2}$) and 209.3 eV (Nb $3d_{3/2}$). However, in the SNO sample, lower energy states (206.2 eV and 209.0 eV) are observed, which agree with reported Nb^{4+} structures (Isawa, Itti et al. 1994, Shibagaki and Fukushima 1999, Aufray, Menuel et al. 2009, Posadas, O'Hara et al. 2014, Seo, Hisatomi et al. 2018). Furthermore, the difference between the binding energy of SNO and the Nb_2O_5 reference is ~0.3 eV, which is within the resolution of the instrument, suggesting that the majority species is Nb^{4+}. The O 1*s* spectra (Figure 3.6(d)) after deconvolution identifies four peaks located at 529.2 (SNO lattice) (Isawa, Itti et al. 1994, Haasch, Breckenfeld et al. 2014), 530.0 ($Sr_{0.7}NbO_{3-\delta}$ lattice) (Saint-Girons, Bachelet et al. 2016), 531.5 (nearby oxygen vacancies) (Tan, Zhao et al. 2014), and 532.6 eV (surface OH) (Dupin, Gonbeau et al. 2000). As such, an oxygen vacancy of δ~0.35 can be extracted from both XPS and refinement data and is in agreement with literature (Ridgley and Ward 1955). This value of δ was further verified analytically by performing three parallel iodometric titration experiments (Karppinen, Matvejeff et al. 2002, Conder, Pomjakushina et al. 2005) (detailed calculations are described in the experimental section). Based on these titrations, the value of δ was calculated as ~0.37±0.06, which is within 3% of the previously determined value (~0.35). These results point to the fact that vacancy formation is necessary to maintain the

Nb oxidation state of the $Sr_{0.7}NbO_{3-\delta}$ lattice (Efstathiou, Xu et al. 2013, Darapaneni, Kizilkaya et al. 2018, Roh, Lee et al. 2018).

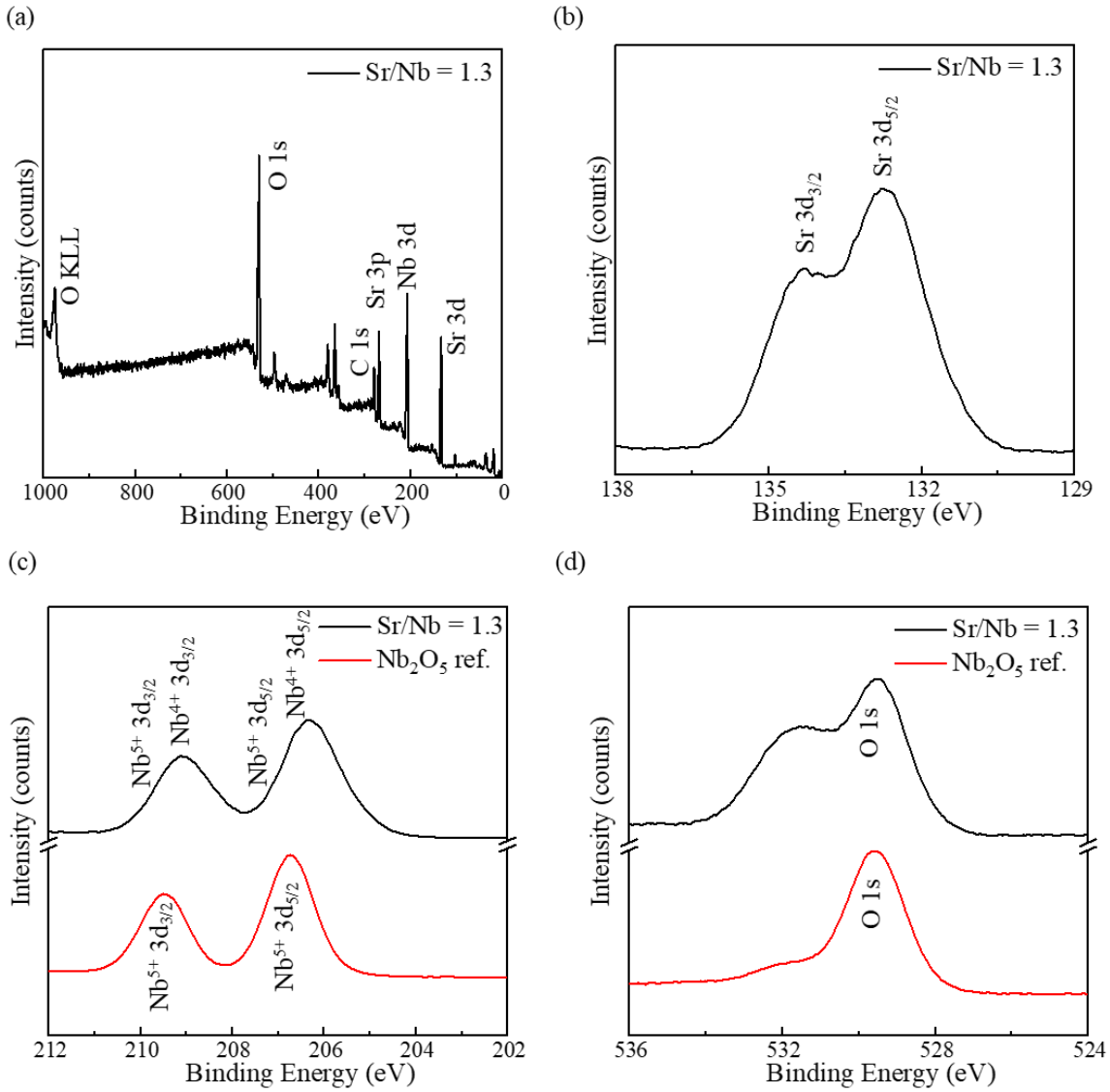

Figure 3.6 X-ray photoelectron spectra for SNO (Sr/Nb=1.3) NPs synthesized under total pressure of 0.2 Torr: (a) survey scan (b) Sr 3*d*, (c) Nb 3*d*, and (d) O 1*s* spectra. Nb_2O_5 (red) is plotted as an oxidation state reference.

3.4. Elucidating the Lattice Vibrational Modes

To verify octahedral (O_h) site symmetry around the majority tetravalent Nb-site, Raman spectra were collected for the SNO samples (Figure 3.7(a)). Despite crystals with cubic symmetry (*Pm-3m)* not expected be Raman active, symmetrically forbidden modes have been observed in analogous structures (STO) due to octahedron distortions (Ouillon, Pinan-Lucarre et al. 2002, Rabuffetti, Kim et al. 2008, Tenne, Farrar et al. 2010, Abreu, Soares et al. 2016, Jyothi, Kumari et al. 2017). Five characteristic peaks, positioned at ~130, 250, 430, 560, and 830 cm^{-1}, have been deconvoluted and assigned to different transverse (TO) and longitudinal (LO) optic modes (Figure 3.7(b)) (Rabuffetti, Kim et al. 2008, Tenne, Farrar et al. 2010, Abreu, Soares et al. 2016). Table 3.4 compares the experimental modes of SNO with the reported values for STO to highlight the good agreement due to their isostructural nature.

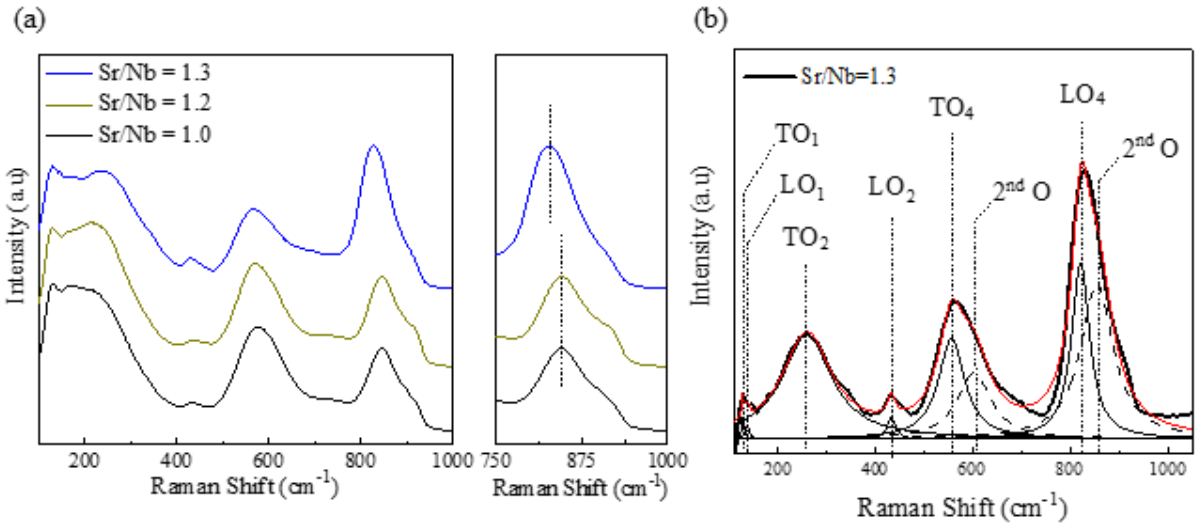

Figure 3.7 (a) Normalized Raman spectra for SNO (Sr/Nb=1.0, 1.2, and 1.3) NPs with an expanded view to highlight red shift in F_{1u} peak position and intensity enhancement (b) Deconvoluted Raman spectrum.

Table 3.4 Comparison of Experimental SNO (Sr/Nb=1.3) Raman Spectrum with Reported STO Frequencies.

Phonon Branch	Symmetry	Experimental SNO Frequency (cm^{-1})	Reported STO Frequency (cm^{-1})
TO_1	F_{1u}	128	118
LO_1	F_{1u}	145	175
LO_2	F_{1u}	434	475
TO_4	F_{1u}	562	550
LO_4	F_{1u}	826	795

Furthermore, no shift in peak position is seen with an increase in molar ratio from 1.0 to 1.2 suggesting that not enough of the Sr-vacant sites are being filled by the excess Sr^{2+} ions to noticeable change the overall Sr-deficiency of the crystal (Guo, Liu et al. 2012). At the higher Sr/Nb ratio, the higher frequency peak red-shifts and this is attributed to the formation of stoichiometric $SrNbO_3$ (Hirata, Ishioka et al. 1996). Furthermore, the enhancement of the ~830 cm^{-1} peak intensity relative to the peak positioned at ~560 cm^{-1} is due to surface structure effects (Jehng and Wachs 1991, Ouillon, Pinan-Lucarre et al. 2002, Tenne, Farrar et al. 2010). These results in conjunction with the previously presented XPS analysis demonstrate that the majority Nb^{4+} is locked into O_h coordination.

3.5. Simulating the Phonon Frequencies using DFT

Partial phonon density of states (DOS) calculations were performed to provide a geometrical description of the vibrational modes responsible for the experimentally observed

peaks in the Raman spectrum of SNO (Sr/Nb=1.3). The identified vibrational modes are visualized in Figure 3.8. According to these calculations (Figure 3.9), the phonon mode positioned at 162 cm^{-1} corresponds to Nb motion against O vibrations in the presence of an O vacancy and the calculated peak at 326 cm^{-1} involves the vibrations of O ions against Sr cation in the presence of a Sr vacancy. The final peak positioned at 626 cm^{-1} is attributed to O vibration against Nb ions in the presence of an O vacancy. Furthermore, in order to mirror the nanoparticle surface observed from XPS and FTIR spectroscopy, surface calculations were performed using a defect-free cubic $SrNbO_3$ cell with terminal niobium atoms bonded to hydroxyl groups (Nb^{4+}-OH) resulting in a Raman active mode at 981 cm^{-1}. The deviation from experiment is ascribed to a simplified representation of the NbO_x-OH on the nanoparticle surface modeled by DFT as described in literature (Jehng and Wachs 1991, Music, Schmidt et al. 2017, Darapaneni, Moura et al. 2019). This calculation shows that the highest wavenumber band originates from the stretching of the Nb-O bond in hydroxyl activated NbO_6 octahedra. Overall, these first-principles calculations demonstrate that the observed Raman activity for these nanocrystals is due to a combination of surface effects and point defects. As such, these DFT and Raman results highlight the presence of vibrational modes consistent with a perovskite structure for these Nb^{4+} stabilized SNO NPs.

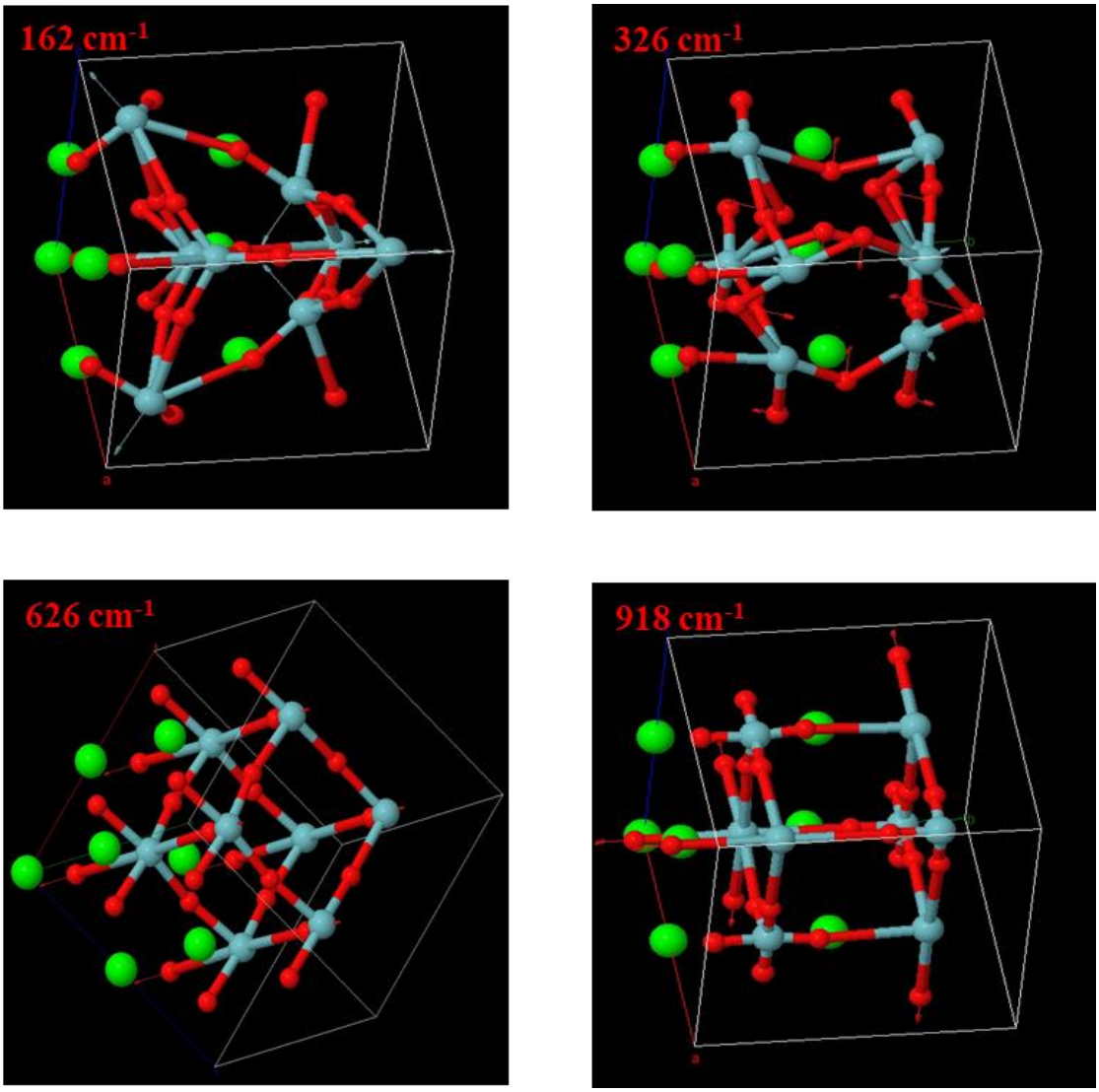

Figure 3.8 Visualizations of the simulated phonon vibrations for SNO. The direction of the atomic motion are indicated with arrows and the vibrational frequency corresponding to these movements are presented in red on the left had corner.

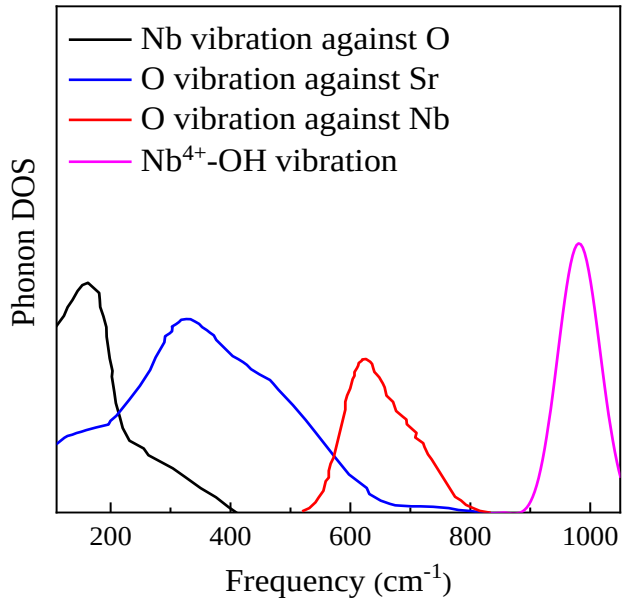

Figure 3.9 Simulated partial phonon density of states for SNO (Sr/Nb=1.3).

3.6. Restoring the Optoelectronic Responses via H_2/Ar Post-treatment

To probe the optical response of the SNO nanocrystals, UV-Vis absorption measurements were performed on the synthesized powders. The absorption spectra (Figure 3.10(a)) shows no visible absorption upon Sr-enrichment despite the formation of $Sr_{1-x}NbO_{3-\delta}$ as seen visually. However, literature reports a shift from red/bronze for stoichiometric SNO which shifts to blue/black with decreasing Sr concentrations (x= 0.3) (Ridgley and Ward 1955, Wan, Zhao et al. 2017). Therefore, the white color of these SNO NPs is attributed to the presence of Nb defects within the crystal, which contribute to the observed insulating response (Efstathiou, Xu et al. 2013, Wan, Zhao et al. 2017, Oka, Hirose et al. 2018). In order to suppress the presence of these Nb defect states, the as-synthesized SNO (Sr/Nb=1.3) NPs were annealed under H_2/Ar atmosphere at 800 °C. The resulting powders have a dark grey appearance and an enhanced optical absorption in the visible region (Figure 3.10(a)). Moreover, the resultant diffraction

pattern for the annealed sample shows the SNO crystal with significantly reduced Nb defect states (Figure 3.10(b)). For comparison, the SNO (Sr/Nb=1.0) NPs were annealed in reducing atmospheres and similar reductions to the defect states were observed, however, there is no significant change to the nanoparticle absorbance (Figure 3.10(c-d)). Therefore, it is important to minimize the formation of these Nb defect states during the molten salt step to obtain enhanced absorption. Although further investigation is needed to understand the effect of H_2/Ar annealing on the electronic structure, the present results demonstrate the presence of colored SNO nanocrystals.

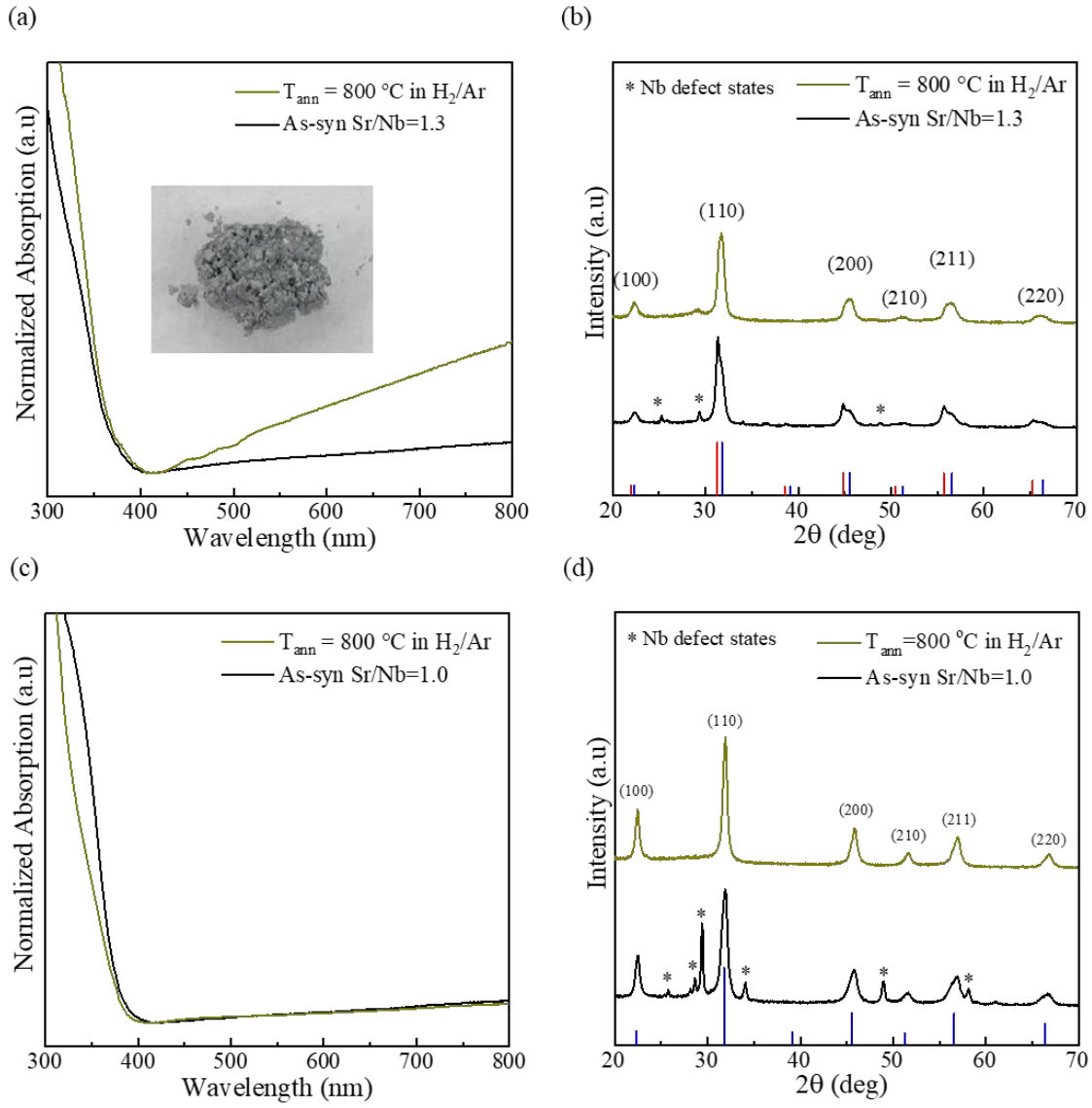

Figure 3.10 Optical absorption spectra and diffraction pattern for as-synthesized and H_2/Ar annealed SNO (a-b) Sr/Nb=1.3 and (c-d) Sr/Nb = 1.0 NPs. In Sr/Nb = 1.0, the diffraction patterns highlight the absence of Nb defect states, but no significant change in the absorption is observed after the annealing process. However, for Sr/Nb = 1.3, the absorption is improved by suppressed the Nb defect states and the inset of the absorption spectra shows the colored appearance of the particles after H_2/Ar treatment.

3.7. Summary

Overall, this chapter discusses how SNO NPs were crystallized using a novel wet-chemical technique, i.e. oxygen-controlled CP/MSS method. Traditional wet-chemical methods have been utilized to successfully crystallize perovskite oxides NPs such as STO. For this reason, this synthetic approach was also leveraged in the synthesis of the SNO NPs. These initial tests specifically demonstrate that Sr-incorporation and Nb defect state formation are major issues for preparing SNO NPs using solution-based chemistry. The facile oxygen-controlled CP/MSS method was designed to address these two major problems. In this synthetic method, an amorphous Sr-Nb-O framework is formed during the CP step and subsequently crystallized during the MSS step. More importantly, the low-pressure environment reduces the presence of oxygen during the crystallization process which allows for the simultaneous intercalation of Sr ions and suppression of defect states. Specifically, loss of Sr ions is reduced by inhibiting the formation of secondary structures (i.e., $SrCO_3$, etc.), prevalent in oxygen-rich atmospheres. This in turn allows for more Sr ions to contribute to the crystallization of SNO. Furthermore, the ability to directly vary the Sr concentration during the crystallization allows for the Nb defect states to also be suppressed, especially when the Sr/Nb molar ratio is ~1.3. Finally, a reducing post-treatment allows for further inhibition of the Nb defect states, which triggers a change in the powder color (white to colored). Structural, optical, and electronic results consistently affirm that the suppression of these defect states is responsible for forming SNO NPs with the expected optoelectronic responses. Ultimately, the demonstrated wet-chemical approach provides a fundamental framework for the synthesis of low-dimensional perovskites, which have the potential to advance the fields of photocatalysis and photovoltaics.

Chapter 4 . Controlling the Local A-site Environment of SNO Perovskites[3]

4.1. Introduction

The effect of these defect states on the A-site chemical structure was also investigated since the A-site environment also determines the stability of the perovskite oxide lattice (Bartel, Sutton et al. 2019). To study this, SNO was utilized as a representative structure and the Sr-sites were replaced with Ca ions. The impact of this A-site substitution on the formation of defect states was subsequently probed. From the systematic incorporation of Ca into the SNO host lattice, symmetry/structure transformations were induced, which are strongly correlated to novel responses such as ferroelectricity. As seen with STO, Ca doped into the SNO lattice is expected to induce local dipoles by the off-centered Ca ions, resulting in a macroscopic ferroelectric (FE) response (Ramirez, Lummen et al. 2019). For this reason, $Ca_xSr_{1-x}NbO_3:Eu^{3+}$ (2 mol%, CSNO) NPs were synthesized using the developed technique as traditional wet-chemical approaches suffer from the limitations highlighted in Chapters 2 and 3. Model CSTO:Eu, BTO:Eu, and PTO:Eu (2 mol%) NPs were also synthesized to assist in the identification of the FE responses. Since these crystals do not possess multi-valent B-site cations, traditional wet-chemical methods were employed in their preparation. Previous studies in these materials have demonstrated that FE transformations are a function of composition (Rischau, Lin et al. 2017) and temperature (Acosta, Novak et al. 2017). Therefore, *in-situ/ex-situ* PL coupled with XRD and XAS studies were performed to monitor the composition- and temperature-induced phase transformations. For the PL measurements, the resulting structural/FE changes in the A-site environment were studied using Eu as a photoluminescent probe. Ultimately, coupling the reported (Asmara, Wan et al.

[3] "Reprinted (adapted) with permission from (T. Ofoegbuna, K. R. Bajgirian, O. Kizilkaya, S. A. J. Thomson, A. T. Melvin, and J. A. Dorman, Photoluminescence Detection of Symmetry Transformations in Low-Dimensional Ferroelectric ABO3 Perovskites, Journal of Materials Chemistry C, 8, 10767-10773). Copyright (2020) The Royal Society of Chemistry.".

2017) low-loss response of SNO with FE behavior will make it a promising candidate material for multiple energy and data storage applications (Beechem, Goldflam et al. 2018, Zhang, Li et al. 2018). This work has been published as "Photoluminescence Detection of Symmetry Transformations in Low-Dimensional Ferroelectric ABO_3 Perovskites" in *Journal of Materials Chemistry C*.

4.2. Monitoring Changes in the Bulk Structure in SBO (B = Nb) NPs

To study the effect of defect states on the A-site, Ca was incorporated into the SNO lattice using the oxygen-controlled CP/MSS approach (Figure 4.1(a)). As with the SNO synthesis, the oxygen partial pressure was reduced by performing the synthesis under low-pressure (P=0.2 Torr). This method proved effective for the synthesis of SNO by significantly suppressing the formation of defect states. Incorporation of Ca into the Sr-site of SNO resulted in the formation of a structure matching $CaNbO_3$ (CNO) (space group: *Pnma*, ICSD 47-1668). Unlike in SNO, there is a large concentration of defect states in CNO. Although these defect states are formed, the fact that the perovskite lattice is also formed, suggests that the A-site is stable using this synthetic method. As seen in the MSS of SNO (Chapter 2), an unstable A-site would result in the formation of only Nb defect states, i.e. degrade the ABO_3 crystal structure (Bartel, Sutton et al. 2019). Nevertheless, to suppress the presence of these defect states, a H_2/Ar atmosphere was utilized (Figure 4.1(b)). The crystal structures of the SNO and CNO NPs affirm the crystallization of cubic (C, $SrNbO_3$) and orthorhombic (O, $CaNbO_3$) phases, which is subsequently verified using Rietveld refinement (Figure 4.1(c-d) and Table 4.1). These results demonstrate that, while it is possible suppress the defect formation, the A-site environment remains relatively stable using the oxygen-controlled CP/MSS method.

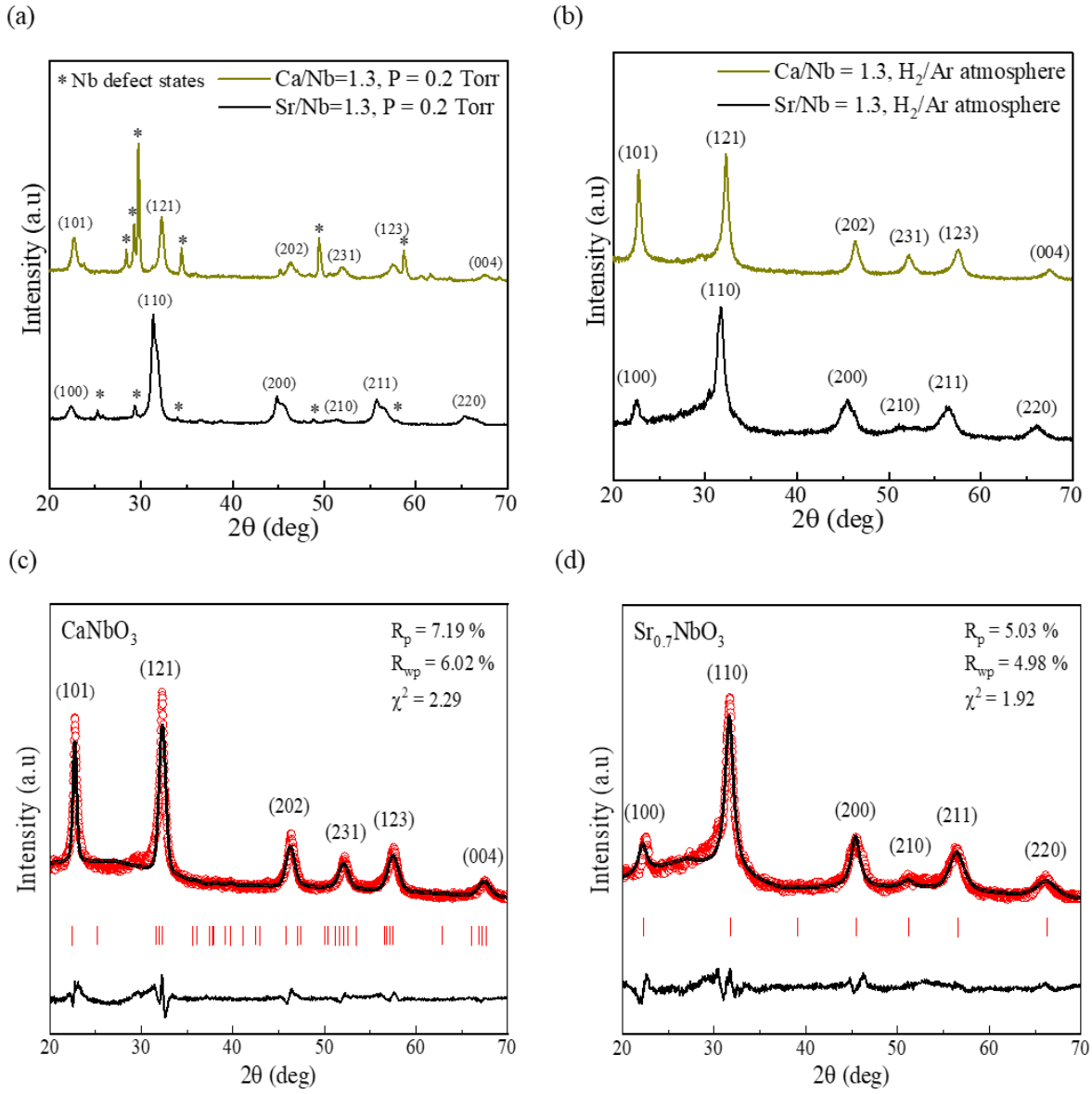

Figure 4.1 Diffraction pattern for CNO:Eu and SNO:Eu (2 mol%) NPs synthesized in (a) low-pressure and (b) H2/Ar atmospheres. (c-d) corresponding Rietveld refinement for the samples prepared using H_2/Ar atmosphere. Reported spectra were collected at room temperature with λ = 1.541 Å. The upper symbols illustrate the observed data (circles) and the calculated pattern (solid line). The vertical markers show calculated positions of Bragg reflections and the lower curve represents the difference between observed and calculated intensities.

Table 4.1 Crystallographic Data and Refined Lattice Parameters for SNO and CNO NPs based on X-ray Diffraction Data.

Parameters	**$Sr_{0.7}NbO_3$**	**$CaNbO_3$**
wavelength (Å)	1.541	
temperature (K)	300	
2θ range (˚)	20-70	
space group	Pm-3m (No. 221)[a]	Pnma (No. 62)[b]
	Lattice Parameters	
a (Å)	3.988(0)	5.591(6)
b (Å)	3.988(0)	7.873(2)
c (Å)	3.988(0)	5.526(7)
α, β, γ (˚)	90	90
V ($Å^3$)	63.411	243.306
	Atomic Coordinates	
Sr/Ca (x,y,z)	0.5, 0.5, 0.5	0.02602, 0.25, 0.02512
Nb (x,y,z)	0, 0, 0	0, 0, 0.5
O1 (x,y,z)	0.5, 0, 0	0.03976, 0.25, 0.54792
O2 (x,y,z)	-	0.19040, -0.022, 0.73890

[a-b] space group ref.: ICSD 19-2410, ICSD 47-1668. The occupancy was fixed to 0.7 at the Sr site and 1 at Nb and O sites for the $Sr_{1-x}NbO_3$ structure and to 1 at all atom sites for the $Ca_{1-x}NbO_3$ structure. For the $Sr_{1-x}NbO_3$, the isotropic displacement parameter U_{iso} is 0.021(0), 0.017(9), and 0.044(5) $Å^2$ for Sr, Nb, and O sites, respectively. For the $Ca_{1-x}NbO_3$, the isotropic displacement parameter U_{iso} is 0.060(7), 0.003(9), 0.025(2), and 0.043(0) $Å^2$ for Ca, Nb, O1, and O2 sites, respectively.

To study the resulting structural/FE transformation in depth, Ca was systematically doped into the SNO lattice, i.e. CSNO (Figure 4.2 and Table 4.2). Four intermediate doping concentrations (x = 0.1, 0.2, 0.5, and 0.8) are also shown along with a magnified view in the 2θ range of 20 to 35˚. The compounds with low Ca concentration (x = 0.1 and 0.2) exhibit what appears to be a shift toward the tetragonal (T) phase based on a comparison with STO (ICDD 70-6460). However, the fitting of these structures was not able to be performed since no structural models are available. The change from C to T phase with Ca composition can be seen from the

presence of $(100)_C$, $(110)_C$, and $(101)_T$ peaks. At x = 0.5, the crystal is a mixture of phases, based on the constant peak splitting as well as the shift in the diffraction peak to higher angles. A pure O phase is formed when x > 0.8, as evident from the appearance of $(101)_O$ and $(121)_O$ reflections.

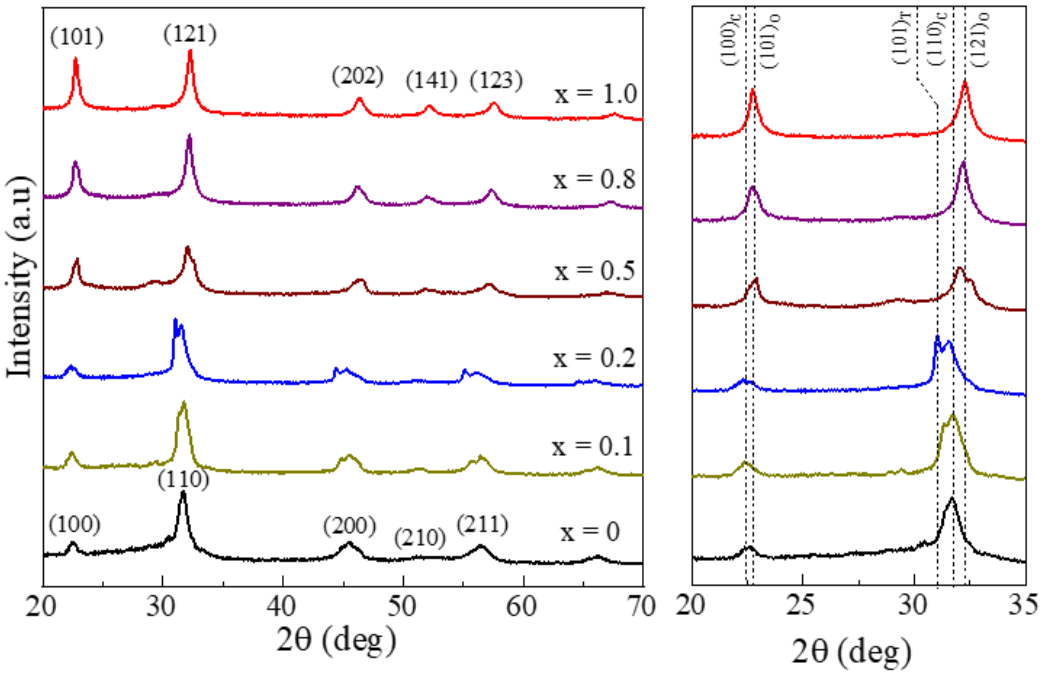

Figure 4.2 Diffraction pattern for CSNO:Eu (2 mol%) nanoparticles. The magnified view of the diffraction pattern, on the right, highlights the formation of T and O reflections with increased Ca incorporation. Miller indices are based on $Sr_{0.7}NbO_3$ (ICDD 19-2410) and $CaNbO_3$ (ICDD 47-1668) references.

Table 4.2 Lattice Parameter and Crystal Structure for CSNO:Eu (2 mol%) NPs.

x	a (Å)	b (Å)	c (Å)	V (Å^3)	Crystal Structure
0	3.98	3.98	3.98	63.13	C
0.1	3.98	3.98	4.04	64.03	C and T
0.2	3.98	3.98	4.03	63.85	C and T
0.5	5.67	7.97	5.33	241.06	Mixture
0.8	5.75	7.91	5.29	240.81	O
1.0	5.75	7.88	5.28	239.49	O

4.3. Relating the Bulk and Local Structure in SBO (B = Nb) NPs using XAS

XAS analysis was performed to confirm these symmetry/structural transformations. This technique is sensitive to changes in the local (<10 Å) geometric and electronic structure around the X-ray absorbing atom (Dorman, Choi et al. 2012, Darapaneni, Kizilkaya et al. 2018). Figure 4.3(a-b) show the normalized Ca $L_{3,2}$-edge and O K-edge XANES spectra of the CSNO NPs along with a CaO reference spectrum. The Ca L-edge spectra are divided into the L_3-edge (electron transition from $2p_{3/2}$ to 3*d*, ~349 eV) and the L_2-edge (electron transition from $2p_{1/2}$ to 3*d*, ~353 eV), appearing due to large 2*p* core hole spin-orbit coupling (Rez and Blackwell 2011). The major features observed in the Ca $L_{3,2}$-edge XANES spectra, denoted as **a_1, a_2, b_1**, and **b_2**, are predominantly attributed to the spin-orbit coupling of Ca 2*p* core states and the splitting of the 3*d* orbitals due to the crystal-field by surrounding O ions (De Groot, Fuggle et al. 1990, Asokan, Jan et al. 2004). For all investigated CSNO samples, the Ca $L_{3,2}$-edge XANES spectra (data for x = 0 is not shown since there is no Ca atom) shows significant reduction to the **a_1** and

b_1 peak intensities. This peak reduction confirms that Ca doped into the CSNO lattice is incorporated into the A-site (CaO_{12}) rather than the B-site (CaO_6), as a spectrum similar to the CaO reference would be expected for octahedrally coordinated Ca (Borg, King et al. 1992). The O K-edge XANES spectra were collected to verify that the presence of Ca in the A-site is responsible for the structural changes observed in the CSNO NPs. The three spectral features observed in the O K-edge spectra are ascribed to the hybridization of Nb 4*d*-O 2*p* (~528.5-531.5 eV), the hybridization of Sr 5*s*/Ca 4*s*-O 2*p* (~532.4 eV), and the additional visible small peaks (~533.3-540.0 eV) are attributed to Nb 5*sp*/Ca 4*sp*-O 2*p* orbital hybridization (Rini, Zhu et al. 2009, Jethva, Katba et al. 2019). From the XANES spectra, Ca doping to the onset of phase transition (x = 0.1 and 0.5), results in a loss of definition in the hybridized Nb 4*d* (e_g orbital) and Sr 5*s*/Ca 4*s* peaks. Similar spectral changes have been observed for $Ba_xLa_{1-x}MnO_3$ which undergoes a C (x = 0) to H (hexagonal, x = 1) phase transition (Kuepper, Falub et al. 2005). This suggests that there is no long-range ordering as these phase transitions occur and therefore, a disordered cubic structure accurately describe these systems (De Groot, Grioni et al. 1989, Darapaneni, Kizilkaya et al. 2018).

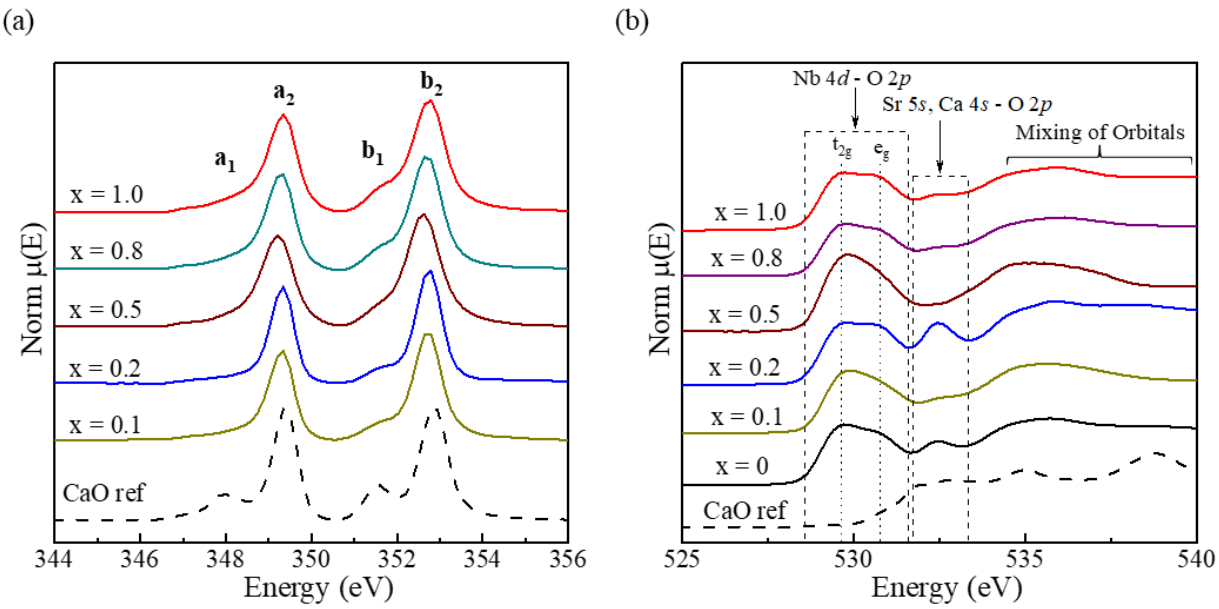

Figure 4.3 (a) Ca L-edge and (b) O K-edge XANES spectra of $Ca_xSr_{1-x}NbO_3$:Eu (2 mol%) NPs.

4.4. Probing the Local A-site Changes in SBO (B = Nb) NPs via *Ex-situ* PL

Next, Model CSTO:Eu, BTO:Eu, and PTO:Eu (2 mol%) NPs were synthesized as references for the composition and temperature-induced phase transitions (Im, Jun et al. 2011, Lee, Moon et al. 2012, Chen, Bao et al. 2019, Ma, Li et al. 2019). XRD of the CSTO affirms the crystallization of C (*Pm-3m*), T (*I4/mcm*), and O (*Pnma*) phases at the same Ca concentrations as in CSNO and agrees with literature values for these expected phases (Figure 4.4(a)) (Qin, Becerro et al. 2000). The assigned phases are further validated using Raman spectroscopy (Figure 4.4(b)), which highlights the formation of new vibrational modes with increased Ca incorporation. These modes are labeled according to literature (Qin, Wu et al. 2002, Rabuffetti, Kim et al. 2008, Goethals, Bedidi et al. 2019). The XRD patterns confirm the formation of BTO (*P4mm*, ICDD 5-0626) and PTO (*P4mm*, ICDD 6-0452) in T phase (Figure 4.4(c-d)).

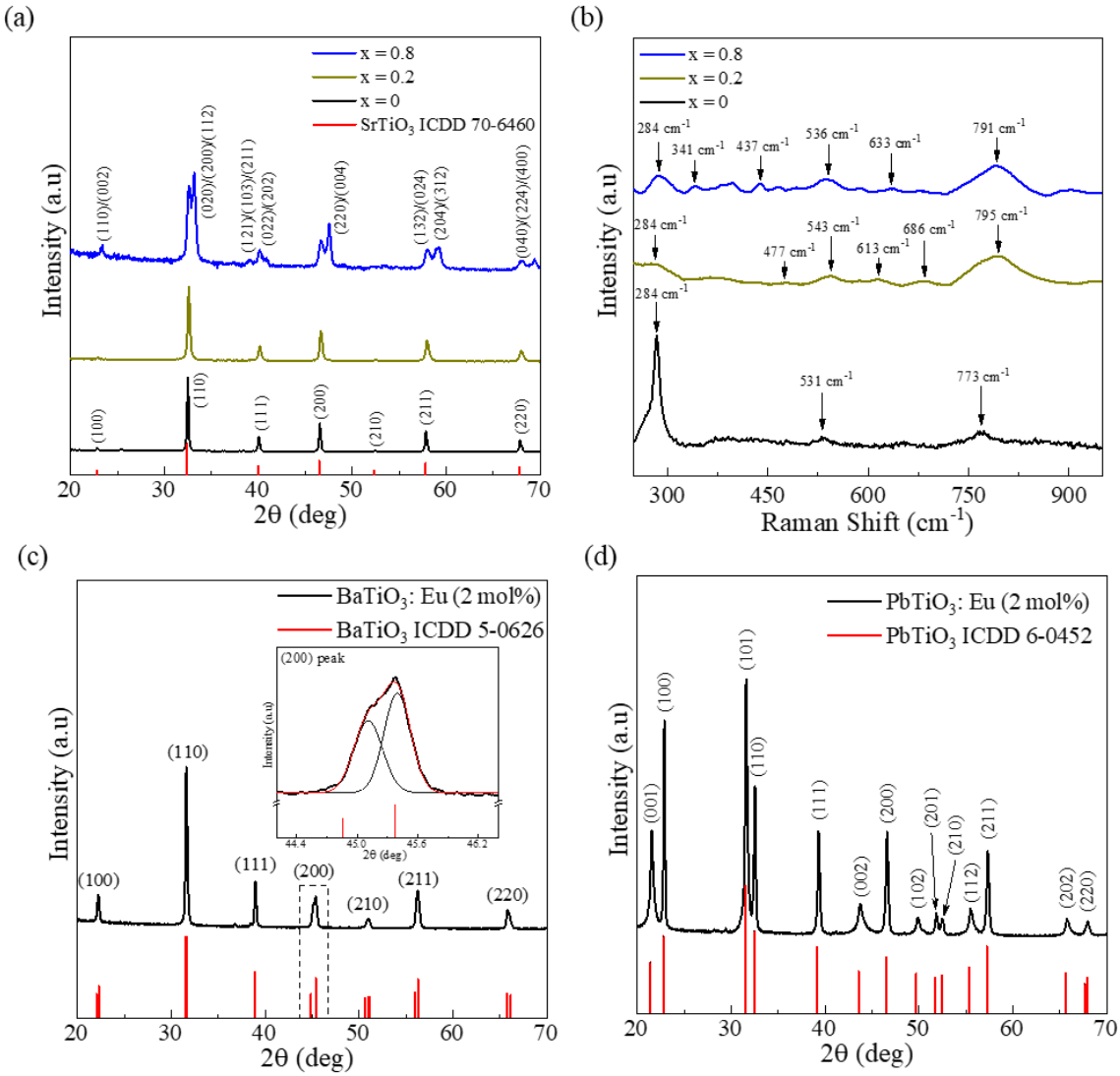

Figure 4.4 (a) Diffraction pattern and (b) Raman spectra for the CSTO:Eu (2 mol%) NPs, highlighting the composition-induced phase change. Diffraction pattern for Eu-doped (a) BTO and (b) PTO NPs

The symmetry changes in the A-site environment induced from the reconstruction of the CSTO and CSNO lattice as a result of Ca doping was probed using *ex-situ* PL spectroscopy. The collected emission spectra and extracted asymmetry ratio (emission intensity ratio of $^5D_0$-$^7F_1$ and $^5D_0$-$^7F_2$, R-value) (Tanner 2013, Bi, Bi et al. 2018) for the NPs, are shown in Figure 4.5(a-c). The horizontal dashed lines in Figure 4.5(d) indicate the measured R-values for STO, BTO, and PTO

NPs. As shown in the figure, for the CSTO NPs, an increase in the R-value (reduction in symmetry) is observed and is consistent with the XRD trend, i.e., C to T and T to O (from 2.7 ± 0.1 to 4.7 ± 0.1). This increasing trend signifies that the crystallographic symmetry (long-range structure) mirrors the spectroscopic symmetry (local structure) (Tanner 2013). Although similar responses have been reported in literature for CSTO (Jiang, Fang et al. 2009, Wu, Nien et al. 2012), these results demonstrate that, in addition to starting and final phases, intermediate phases can also be identified using PL.

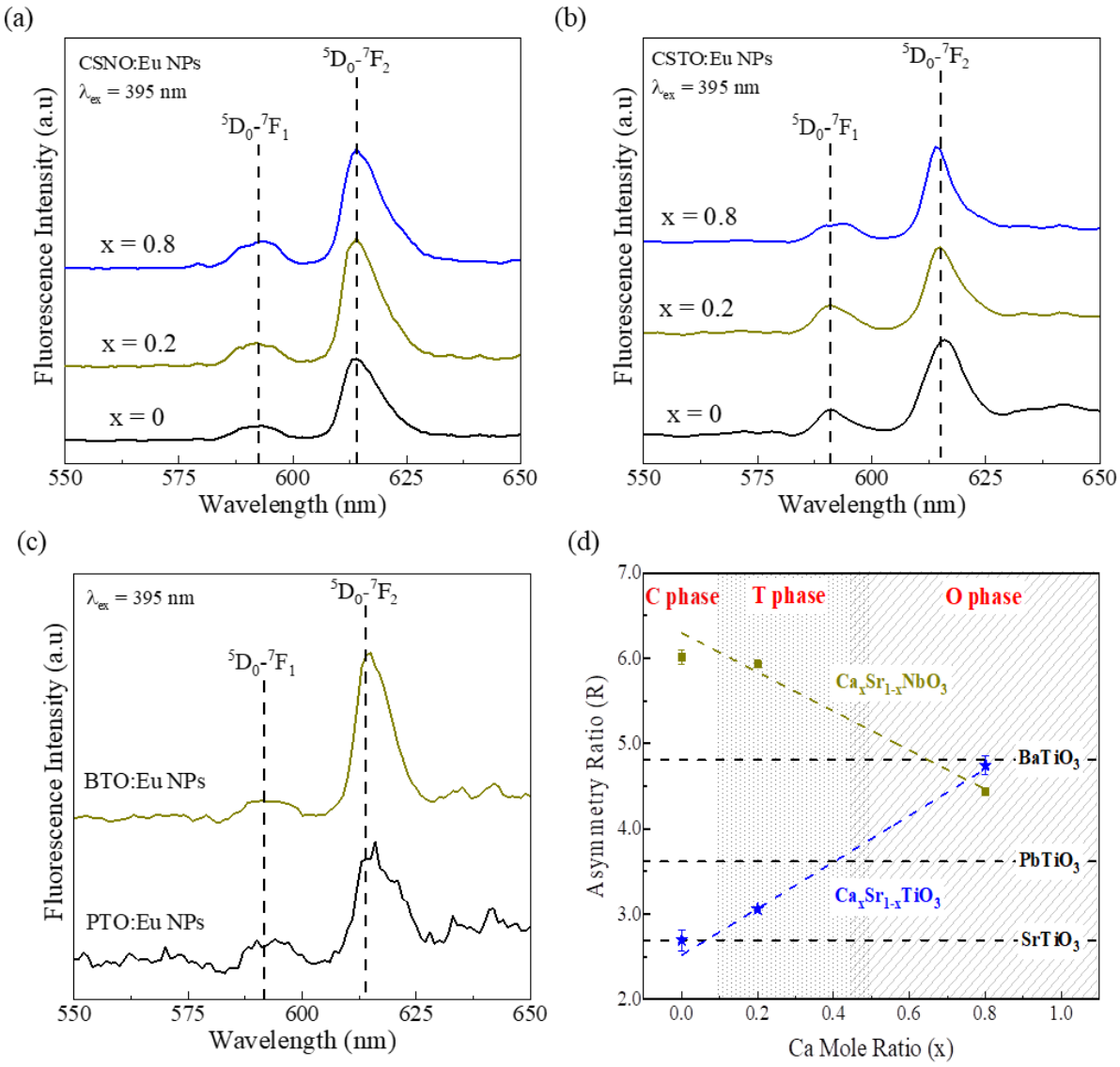

Figure 4.5 PL emission spectra for the (a) CSNO, (b) CSTO, (c) BTO and PTO NPs. (d) corresponding Asymmetry ratio (R) for the synthesized NPs. The dashed lines are a guide for the eye. C, T, and O phase identifications are based on XRD and XAS results.

Interestingly, the observed R-value for CSNO (6.0 ± 0.1) does not change when x < 0.2, suggesting that no initial structural changes have occurred possibly due to the presence of two phases. These observations also coincide with the XRD results. At higher doping concentrations, the R-value decreases (4.4 ± 0.1) suggesting a higher symmetry site surrounding the Eu^{3+} ion,

counter to what is seen for CSTO. The difference in the PL response with Ca doping is attributed to the CSTO being synthesized using a hydrothermal route (Chapter 2). Since traditional methods such as hydrothermal method are performed under oxygen-rich environments, the amount of oxygen defects are expected to be considerable less. As a result, less oxygen defects are expected in the synthesized particles. However, this approach is not suitable for preparing the SNO NPs, due to the preferential stabilization of the pentavalent oxidation state as described in Chapter 3. This motivated the development of the low-pressure synthetic method. It is believed that the presence of defects (oxygen vacancy) surrounding the A-site is responsible for this high R-value which subsequently decreases with increasing Ca concentration. PL lifetime experiments were performed on the CSNO samples to probe the composition-induced symmetry change (Figure 4.6 and Table 4.3). As with the other characterization methods, the lifetime measurements of x = 0 and 0.2 did not show significant changes (i.e. within fitting error). At higher Ca concentrations (x = 0.8), a pronounced increase (> 200 μs) is observed in the lifetime. Since lifetime is a function of the local symmetry, the increase is attributed to the formation of the low-symmetry O phase (Stanulis, Katelnikovas et al. 2019).

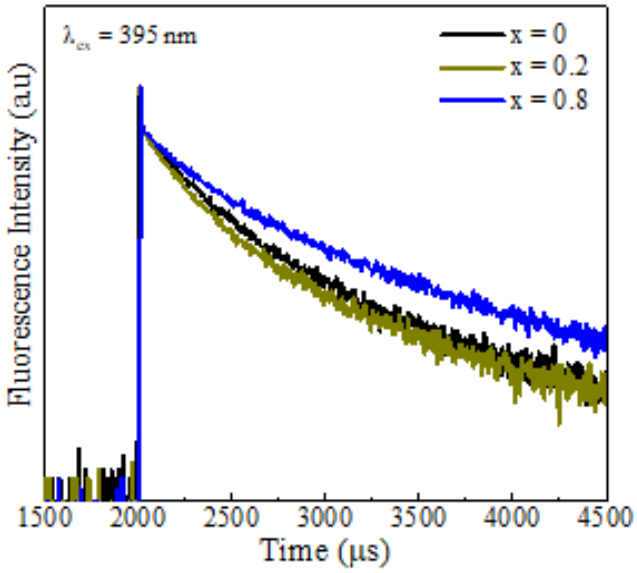

Figure 4.6 Room-temperature lifetime measurements for CSNO:Eu (2 mol%) NPs.

.

Table 4.3 Lifetime for CSNO:Eu (2 mol%) NPs Fit to a Double-Exponential Decay Curve

x	τ_1 (μs)	τ_2 (μs)
0	179.03	571.99
0.2	174.46	629.20
0.8	211.04	798.55

4.5. Correlating the Local A-site Changes to Transition Temperatures via *In-situ* PL

To understa*In-situ* PL measurements were performed to probe the effect of temperature changes on the symmetry of the crystal. To verify that any observed changes to the R-value are due to FE/structural changes, a crystal which does not possess low-temperature phase changes was initially tested. For example, $NaYF_4$ transitions from the H to the C phase at T > 670 K, which makes it ideal for this test (Janjua, Gao et al. 2018). Therefore, $NaYF_4$:Eu (space group: *P-6*, JCPDS 17-6069) NPs in the H phase was used as the control (Figure 4.7(a-b)) (Yang, Chen et al. 2016, Vaithiyanathan, Bajgiran et al. 2019). The reference $NaYF_4$ sample showed little changes in the R-value with temperature (1.69 ± 0.01), indicating that without structural changes the R-value does not considerable change.

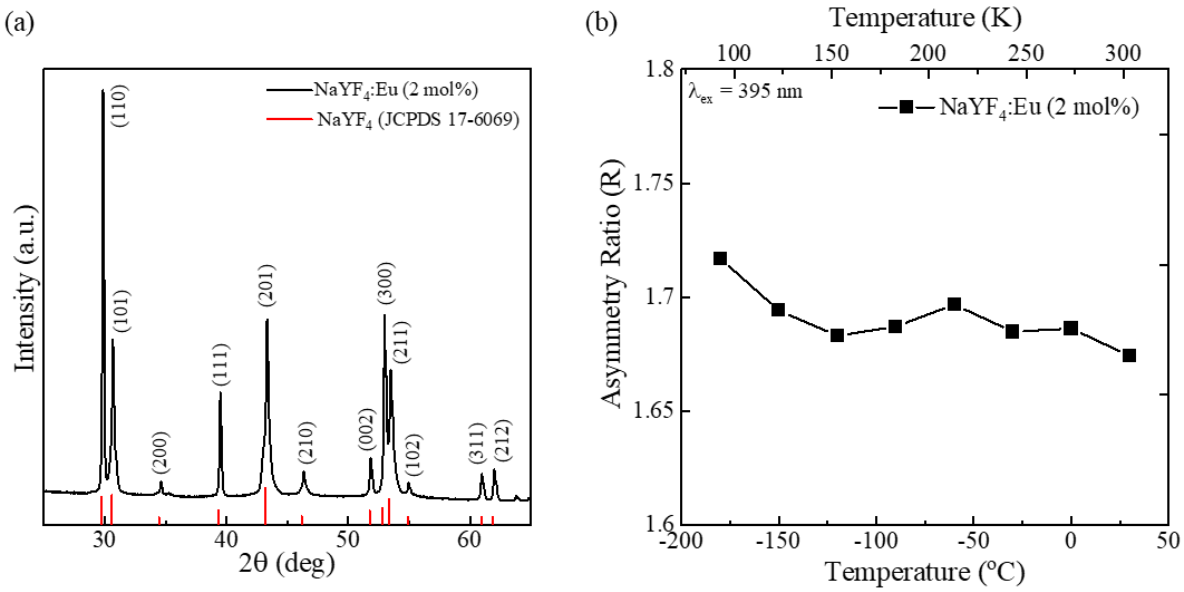

Figure 4.7 (a) Crystal structure and (b) corresponding asymmetry ratio for $NaYF_4$: Eu (2 mol%) NPs in H phase. The plot highlights the absence of structural transformations in $NaYF_4$ at low-temperatures.

As there is a large body of work pertaining to the FE/structural transition temperatures of BTO, PTO, and CSTO (Sawaguchi and Charters 1960, Mitsui and Westphal 1961, Kobayashi, Uesu et al. 1983, Geneste and Kiat 2008), these crystals are well-suited to test the *in-situ* method before being applied to the material of interest (CSNO). Figure 4.8(a-c) shows the expected A/B-site atomic motions, which drive the resulting structual/symmetry transformations in the FE references. The temperature-dependent PL measurement on BTO (Figure 4.9(a)) shows a pronounced drop in the R-value starting at 25 °C and leveling off around -100 °C and this coincides well with reported T to rhombohedral (R) and R to O structural transition temperatures (Sawaguchi and Charters 1960). In the case of PTO, the low-temperature T to O phase change (-100 °C, Table 4.1) only slightly distorts the crystal (a/b~1.0002) (Kobayashi, Uesu et al. 1983). At this temperature, there is a distinct decrease in signal standard deviation from ±0.1 to ±0.03 which is attributed to long-range ordering in the NP crystal structure (Figure 4.9(b)). Similar temperature-dependent analysis of CSTO (Figure 4.9(c)) shows that the R-value begins to increase when the temperature drops below -50 °C for x = 0 and at around -20 °C for x = 0.2 due to the start of the C to T phase transformation. According to reported XRD/dielectric experiments (Table 4.4) (Mitsui and Westphal 1961, Geneste and Kiat 2008), the C to T transition temperature is expected to fall outside the PL capabilities and, thus could not be determined. Nonetheless, these results highlight that the local symmetry of CSTO (x = 0.2) still retains some C character at room temperature even though the longer-range structure, probed via XRD and Raman, appears T. This presence of C nature contributes to ferroelectricity suppression in this T phase as seen in literature (Mitsui and Westphal 1961). Further increasing the concentration to x = 0.8 results in similar behavior to PTO, i.e., negligible response with

temperature followed by a noticeable decrease in the standard deviation (between -100 to -80 °C), suggesting an overall increase in crystal uniformity throughout the NP.

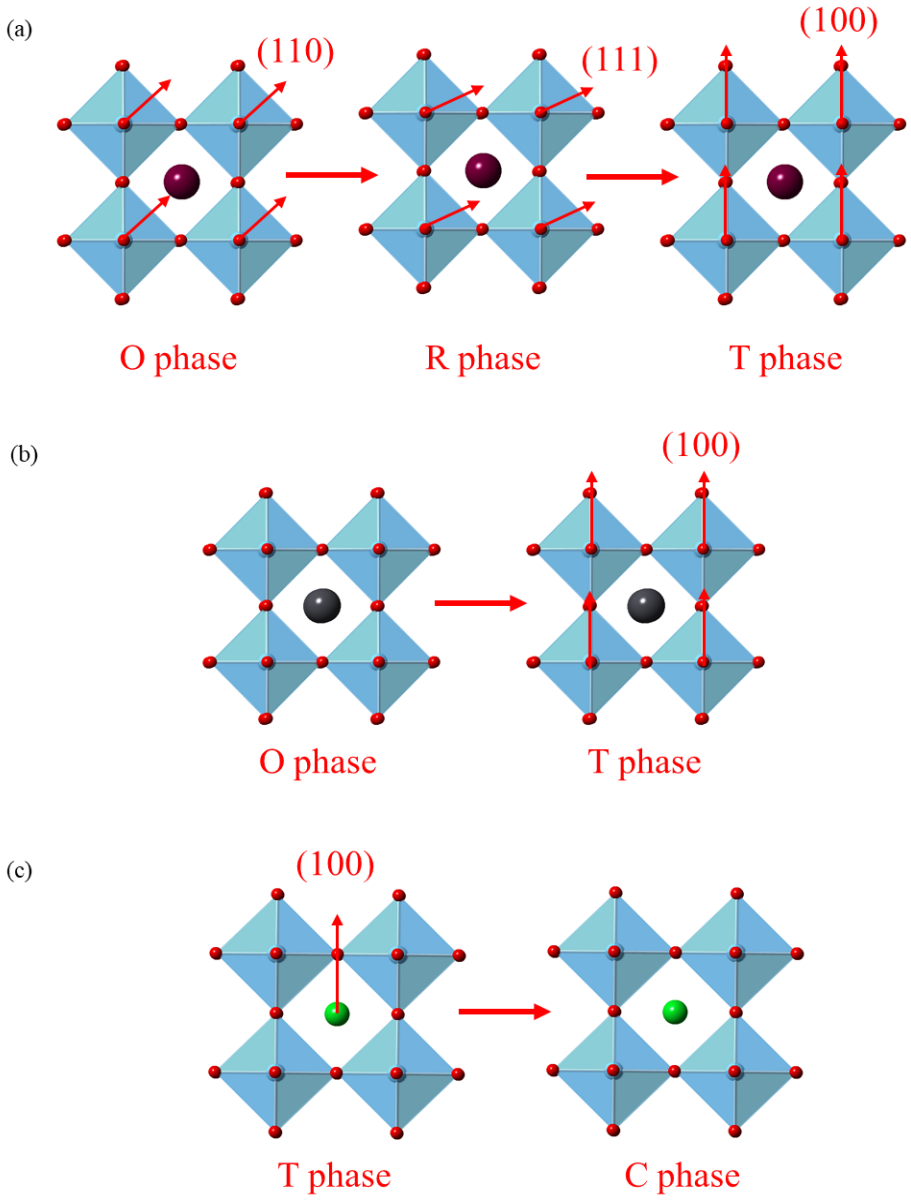

Figure 4.8 Crystal representation of the phase transformations for (a) BTO, (b) PTO, and (c) STO as a function of temperature.

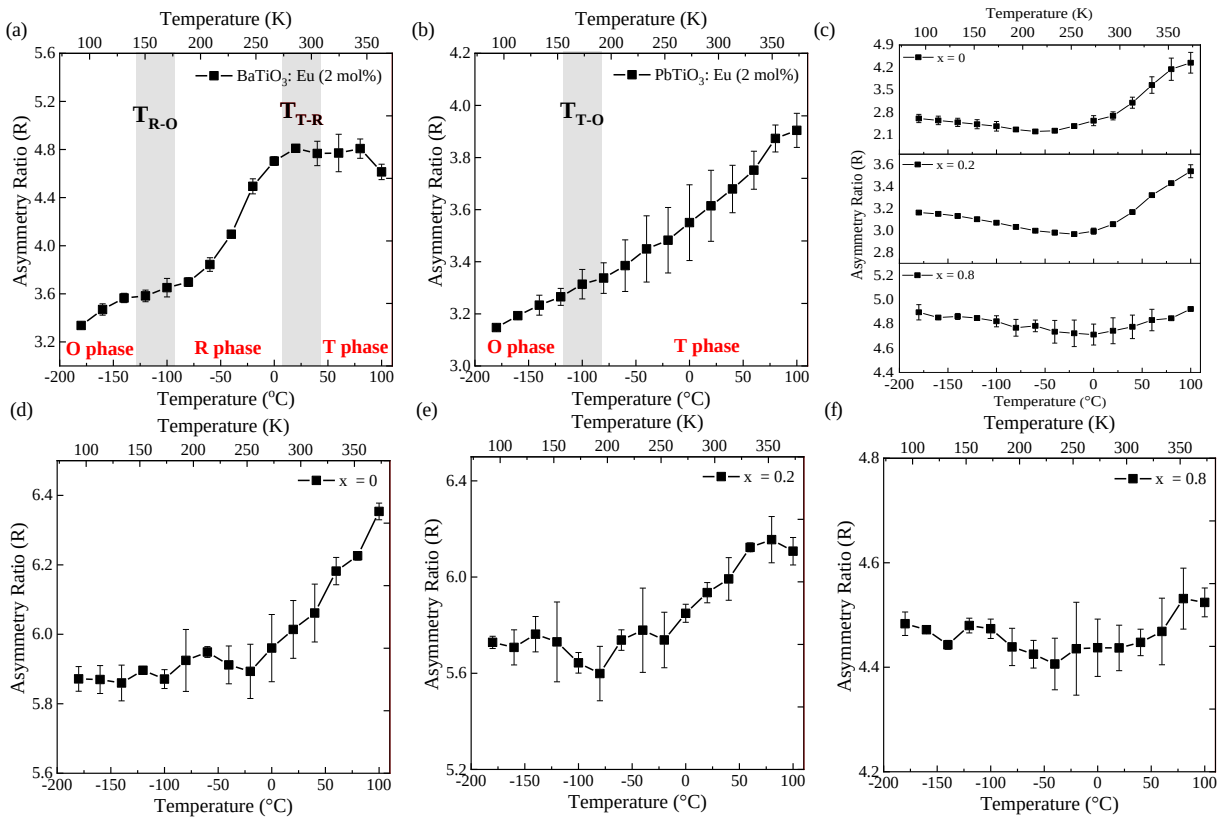

Figure 4.9 *In-situ* temperature-dependent PL for (a) BTO:Eu, (b) PTO:Eu, (c) CSTO:Eu and (d-f) CSNO:Eu (2 mol%) nanoparticles. The PL emission spectra were collected with an excitation of 395 nm. The C, T, O, and R phases are indicated in the BTO and PTO plots.

Table 4.4 Transition temperatures for select FE perovskite oxides.

Chemical Composition	Transition Temperature (Bulk, °C)[a]	Transition Temperature (Local, °C)[b]
BTO	-80 and 0	-120 and 30
PTO	-100	-100
STO	-233[c] and -190[c]	-50
CSTO	-233[c] to -150	0

[a]Bulk comes from literature.
[b]Local comes from our work using *in-situ* PL measurements.
[c]Temperatures below *in-situ* PL measurement range.

Next, the CSNO samples were subjected to the same temperature-dependent measurements (Figure 4.9(d-f)). There is a similar trend in the PL spectra for the CSNO as in the CSTO samples at all doping concentrations. However, for the concentration x = 0.2, there is an initial high R-value drop-off, which can also be seen in the BTO sample at ~50 °C, highlighting a possible similarity in their short-range structures. From this, it can be concluded that there is a difference in the long-range ordering, and respective phase transformations, in the CSNO crystals as a function of Ca doping. Additionally, despite the presence of oxygen vacancies from the low-pressure synthesis, this comparison with CSTO, BTO, and PTO NPs suggests that these materials (CSNO) have the potential to exhibit FE phase transitions upon Ca doping. Overall, the *in-situ/ex-situ* PL measurements provide valuable information about the impact of synthesis

conditions on the local and long-range structure which can be leveraged to quickly screen for FE-type phase transitions in next generation materials.

4.6. Summary

In summary, the effect of the defect states on the A-site chemical structure was studied. This work demonstrates that the formation of defect states is sensitive to the A-site element, as seen with the incorporation of Ca into the SNO lattice. Although, under the low-pressure condition, the CNO nanocrystal resulted in the formation of more defects states, the perovskite lattice was also formed. This indicates that this oxygen-controlled CP/MSS method is able to form A-sites that are very stable. As a result of the incorporation of Ca into the A-site, a symmetry/structural transformation is induced. These lattice changes have been associated with novel phenomena such as ferroelectricity and are a function of composition/temperature. Therefore, to further study these possible structural/FE changes, the Ca concentration (x) was systematically varied. This drives two successive transformations in CSNO, converting the high-symmetry cubic lattice into a low-symmetry tetragonal (x~0.2) and, later, orthorhombic (x~0.8) phase. Interestingly, comparison of these structural changes with CSTO, shows that the A-site symmetry of CSNO is more disordered due to the oxygen defects formed using oxygen-deficient crystallization method. Furthermore, as the samples are cooled, the CSNO (x=0.2) sample behaves similar to FE BTO, indicating a strong resemblance in their local structure. Ultimately, this ability to design stable ABO_3 perovskites and manipulate their short- and long-range structure, will be beneficial in the elucidation of novel phenomena with applications to energy storage.

Chapter 5 . Manipulating the Structure and Composition of Metastable SBO (B = Nb, Ta, and Mo) Perovskites

5.1. Introduction

Although these metastable crystals were synthesized in Chapter 4, they do not possess the expected optoelectronic properties. It is believed that the presence of defect states limit charge transport by modifying the available free carriers (Neagu and Irvine 2011, Wan, Zhao et al. 2017). As previously observed, these defect states can be suppressed by taking advantage of a post-treatment reduction (i.e., H_2/Ar). However, in order to leverage these NPs as conductive scaffolds, the spatial distribution (i.e., surface or bulk) of these defect states needs to be studied as this directly impact the resultant optoelectronic properties (Lee, Oh et al. 2018, Darapaneni, Moura et al. 2019). On the surface, these defects act as charge carrier traps whereas bulk defects act as transport barriers (Tan, Zhao et al. 2014), motivating the need to prevent their formation. For this purpose, the structure and composition of SBO (B = Nb, Mo, Ta) NPs was modified using a H_2/Ar treatment and the resultant structural, optical, and electronic changes were probed using a combination of scattering, spectroscopic, and computational techniques. To understand the effect the H_2/Ar treatment has on the surface and deep defect states of the SBO NPs, the samples were systematically treated at various times (0-6 h). XRD, (HR)TEM, TGA-DSC, XPS, and UV-Vis results show that increasing the annealing time results in a systematic change in the structure/composition and powder color (white, insulator to colored, metal). The electrochemical measurements revealed that a metallic-like state is stabilized in these oxygen-reduced NPs due to the suppression of deep (t > 0.5 h) rather than surface (t < 0.5 h) defects. Furthermore, DFT and Boltzmann Transport calculations demonstrate that the n-type (SNO and SMO) and p-type (STaO) conduction of these NPs is responsible for their transport properties. These comprehensive results suggest that post-processing the as-synthesized SBO NPs in oxygen-

reduced atmosphere can be used to restore their expected optoelectronic properties by suppressing surface/bulk defect states. This control enables properties similar to what is reported for metallic thin-film/bulk crystals to be observed in the low-dimensional state. This work is prepared to be submitted for review.

5.2. Modifying the Structure and Composition

The as-synthesized SBO NPs were annealed in a H_2/Ar atmosphere at 800 ^{o}C for t = 6 h to induce metallic responses. As shown Figure 5.1(a), the prepared samples possess reflections that match with reported crystallographic references (B = Nb, ICDD 19-2410; B = Ta, ICDD 20-0384; B = Mo, ICDD 78-5977), which is subsequently verified using a combination of Rietveld refinement (Figure 5.1(b-d)) and ICP-OES analyses. Based on the statistical and visual agreements (Table 5.1 and Table 5.2), the stoichiometries for the NPs were determined to be cubic *Pm-3m* $Sr_{0.7}NbO_3$ (a = 3.955(4) Å), $Na_{0.9}Sr_{0.1}(Na_{0.4}Ta_{0.6})O_3$ (a = 3.946(4) Å), and $SrMoO_3$ (a = 3.976(0) Å). TEM and EDX (Figure 5.2) results show that the synthesized NPs have particle sizes of ~20 nm with the expected elements present. The observed Na and K fluorescence in the B = Nb sample is attributed to residual salts from the molten salt bath instead of the incorporation of both cations into the crystal.

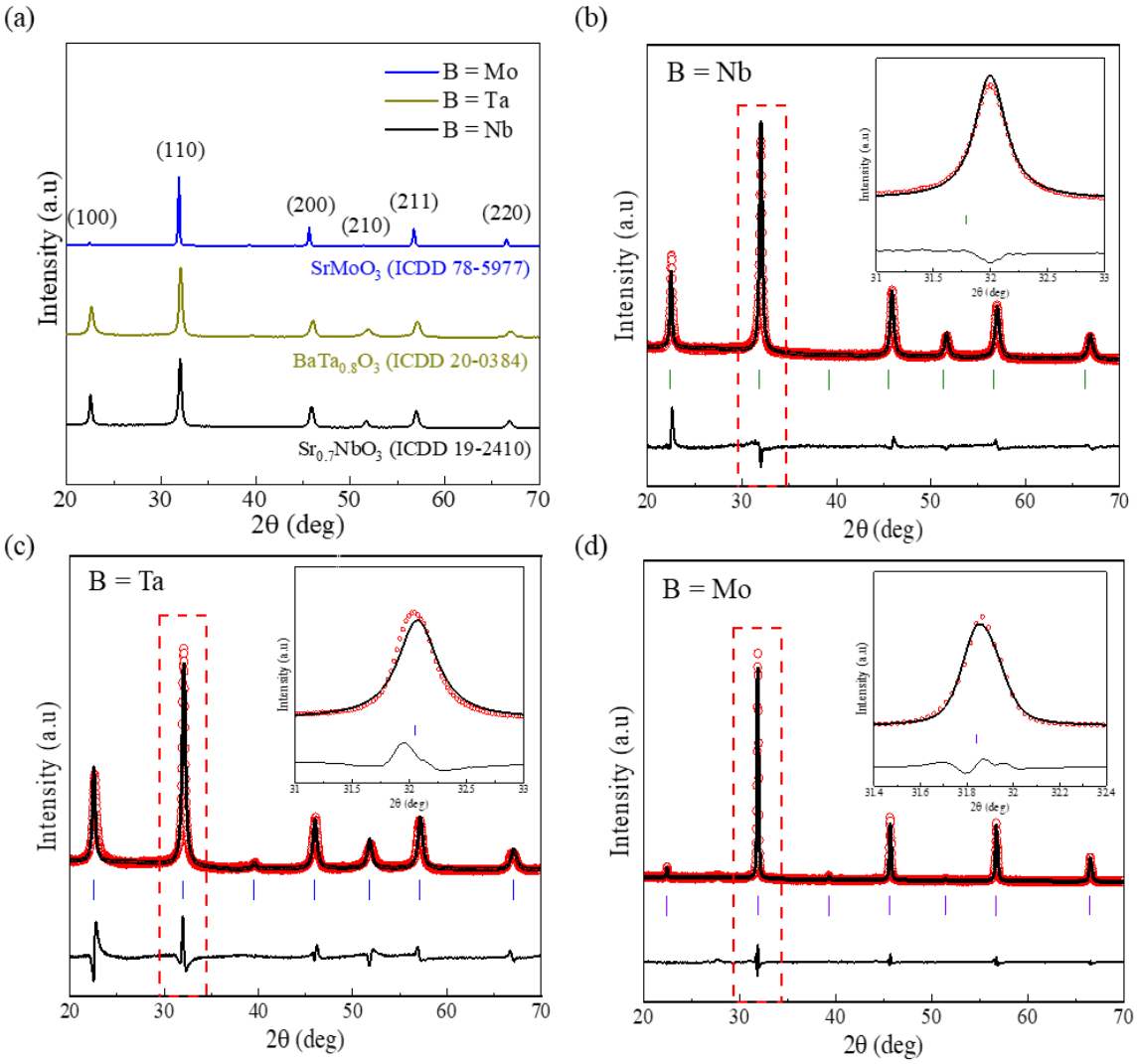

Figure 5.1 (a) XRD pattern and (b-d) Rietveld refinement for SBO (B = Nb, Ta, and Mo) NPs. The upper symbols illustrate the observed data (circles) and the calculated pattern (solid line). The Bragg reflections ($Sr_{0.7}NbO_3$ - green, $Na_{0.9}Sr_{0.1}(Na_{0.4}Ta_{0.6})O_3$ - blue, and $SrMoO_3$ - purple) and difference curve are shown in the plot. Inset shows enlarged view of the (110) peak (red box).

Table 5.1 Crystallographic Data, Refined Atomic Coordinates, and Structural Parameters at Room Temperature for SNO and SMO NPs annealed under H_2/Ar atmosphere based on X-ray Diffraction Data.

Parameters	**B = Nb**	**B = Mo**
wavelength (Å)	1.541	
temperature (K)	300	
2θ range (˚)	20-70	
space group	Pm-3m (No. 221)	
Z	1.0	
R_p, R_{wp} (%)	6.71, 6.10	5.85, 5.81
χ^2	2.27	1.96
	Lattice Parameters	
a, b, c (Å)	3.955(4)	3.976(0)
α, β, γ (˚)	90	90
V (Å^3)	61.881	62.850
	Atomic Coordinates	
Sr (x,y,z)	1/2, 1/2, 1/2	1/2, 1/2, 1/2
B (x,y,z)	0, 0, 0	0, 0, 0
O (x,y,z)	1/2, 0 , 0	1/2, 0 , 0
	Structural Parameters	
Sr-O (Å)	2.796(9)	2.811(4)
B-O (Å)	1.977(7)	1.987(9)
O-B-O (deg)	180	180
O-B-O (deg)	90	90
B-O-B (deg)	180	180

The occupancy was fixed to 0.7 at the Sr site and 1 at Nb and O sites for the B = Nb structure and 1 at all atom sites for the B = Mo structure. For the B = Nb, the isotropic displacement parameter U_{iso} is 0.071(7), 0.003(3), and 0.029(8) for Sr, Nb, and O sites, respectively. For the B = Mo, the isotropic displacement parameter U_{iso} is 0.016(7), 0.014(8), and 0.025(3) for Sr, Mo, and O sites, respectively.

Table 5.2 Crystallographic Data, Refined Atomic Coordinates, and Structural Parameters at Room Temperature for STaO NPs annealed under H_2/Ar atmosphere based on X-ray Diffraction Data.

Parameters	**B = Ta**
wavelength (Å)	1.541
temperature (K)	300
2θ range (˚)	20-70
space group	Pm-3m (No. 221)
Z	1.0
R_p, R_{wp} (%)	11.53, 10.12
χ^2	8.57
Lattice Parameters	
a, b, c (Å)	3.946(4)
α, β, γ (˚)	90
V (Å^3)	61.463
Atomic Coordinates	
Sr/Na1 (x,y,z)	1/2, 1/2, 1/2
Ta/Na2 (x,y,z)	0, 0, 0
O (x,y,z)	1/2, 0, 0
Structural Parameters	
Sr/Na1-O (Å)	2.791(0)
Ta/Na2-O (Å)	1.973(0)
O-Sr/Na1-O (deg)	90
O-Ta/Na2-O (deg)	90
Sr/Na1-O-Sr/Na1 (deg)	180
Ta/Na2-O-Ta/Na2 (deg)	180

The occupancy was refined for the Sr, Na, Ta, and O sites of the B = Ta structure. The isotropic displacement parameter U_{iso} is 0.094(8), 0.011(8), 0.026(8), 0.012(0), 0.011(4), and 0.024(0) for Sr, Ta, Na1, Na2, and O sites, respectively.

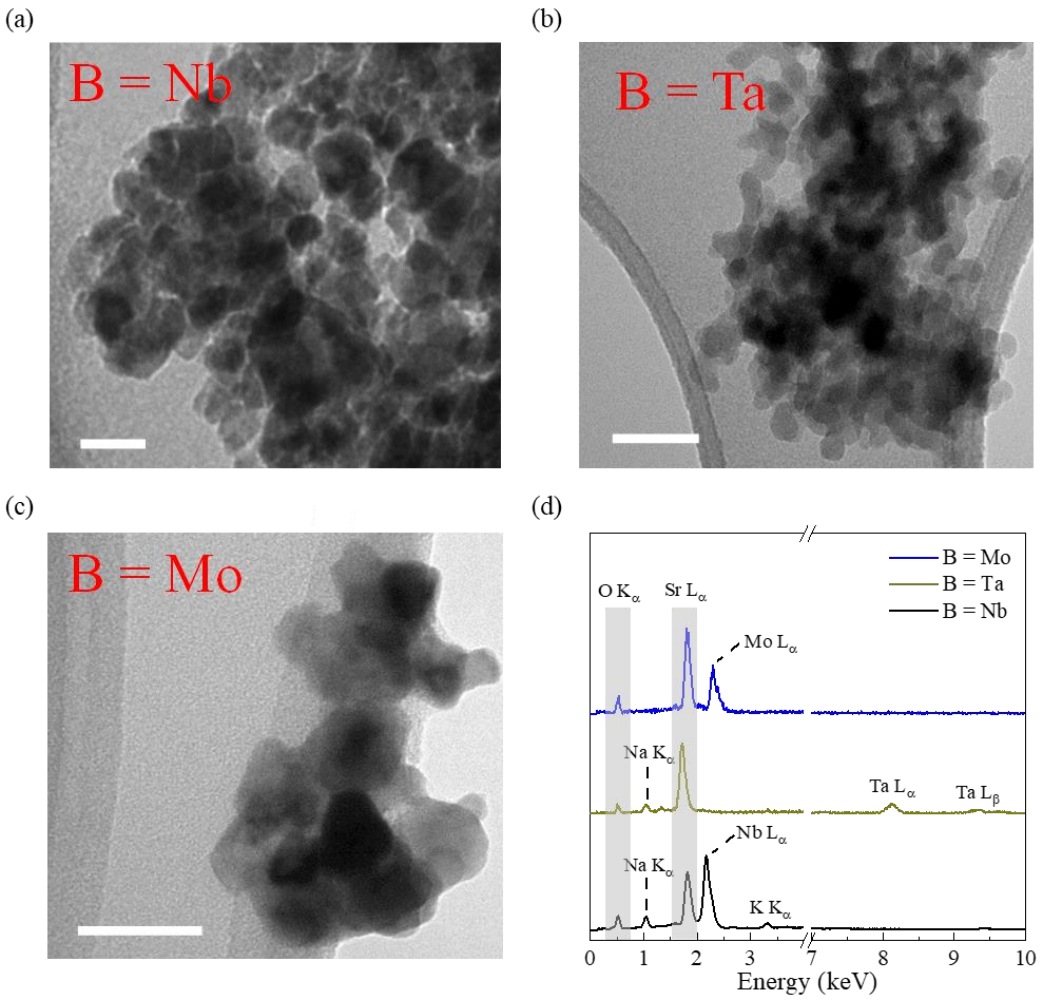

Figure 5.2 TEM images of SBO NPs synthesized by co-precipitation/molten salt method followed by H_2/Ar treatment (a) B = Nb, (b) B = Ta, (c) B = Mo NPs, and (d) corresponding EDX spectra. The scale bar in the TEM image is 50 nm.

To systematically study the effect of the H_2/Ar treatment time on the structural (surface and deep defect states) and optoelectronic (insulating and metallic-like states) properties of the SBO NPs, the SNO sample was reduced at two intermediate times, t = 0.5 and 4 h. The crystal structures (Figure 5.3(a)), refined using $SrNbO_3$ and $Sr_{0.7}NbO_3$ as structural models (Figure 5.3(b) and Table 5.3), show a shift to the single-phase $Sr_{0.7}NbO_3$ after a 0.5 h reduction. The formation of the $Sr_{0.7}NbO_3$ crystal phase after 0.5 h suggests that the Nb defect states, likely

present at the surface, can be readily reduced. Quantification of the reduction process (Figure 5.3(c)) shows a persistent weight loss (~1.2%) between 250 and 800 °C, which is attributed to the partial removal of oxygen from the SNO lattice as a result of reduction to the multi-valent B-site cation (Hou, Yao et al. 2019). The broad exothermic peak positioned at ~470 °C is ascribed to the subsequent bonding of mobile Sr and O atoms with the surface Nb defects (Hanzig, Hanzig et al. 2015, Cowin, Lan et al. 2016, Jin, Batuk et al. 2019), thus forming a Sr-Nb-O framework. No phase changes are observed as a result of this loss in lattice oxygen ions, which is seen during ion exsolution (Chen, Paulson et al. 2015, Sengodan, Choi et al. 2015, Sun, Zhang et al. 2016, Wu and Lin 2017, Hou, Yao et al. 2019). The loss in lattice oxygen ions persists at 800 °C for ~5 h, as demonstrated by the additional weight loss of ~1.2%, corresponding to an overall oxygen deficiency of δ'~0.34 (Chen, Paulson et al. 2015). The observed δ' also agrees with iodometric titration analysis of the SNO NPs treated under similar conditions. While no obvious weight loss was detected with further increase to the reduction time (> 5 h), suggesting completion of the reduction process (Hou, Yao et al. 2019, Zhu, Troiani et al. 2019), the observed increased heat flow during this time is most likely due to continued formation of the Sr-Nb-O network from deep Nb defects. This trend is consistent with the SMO and STaO perovskites, highlighting that it is not a function of the B-site ion.

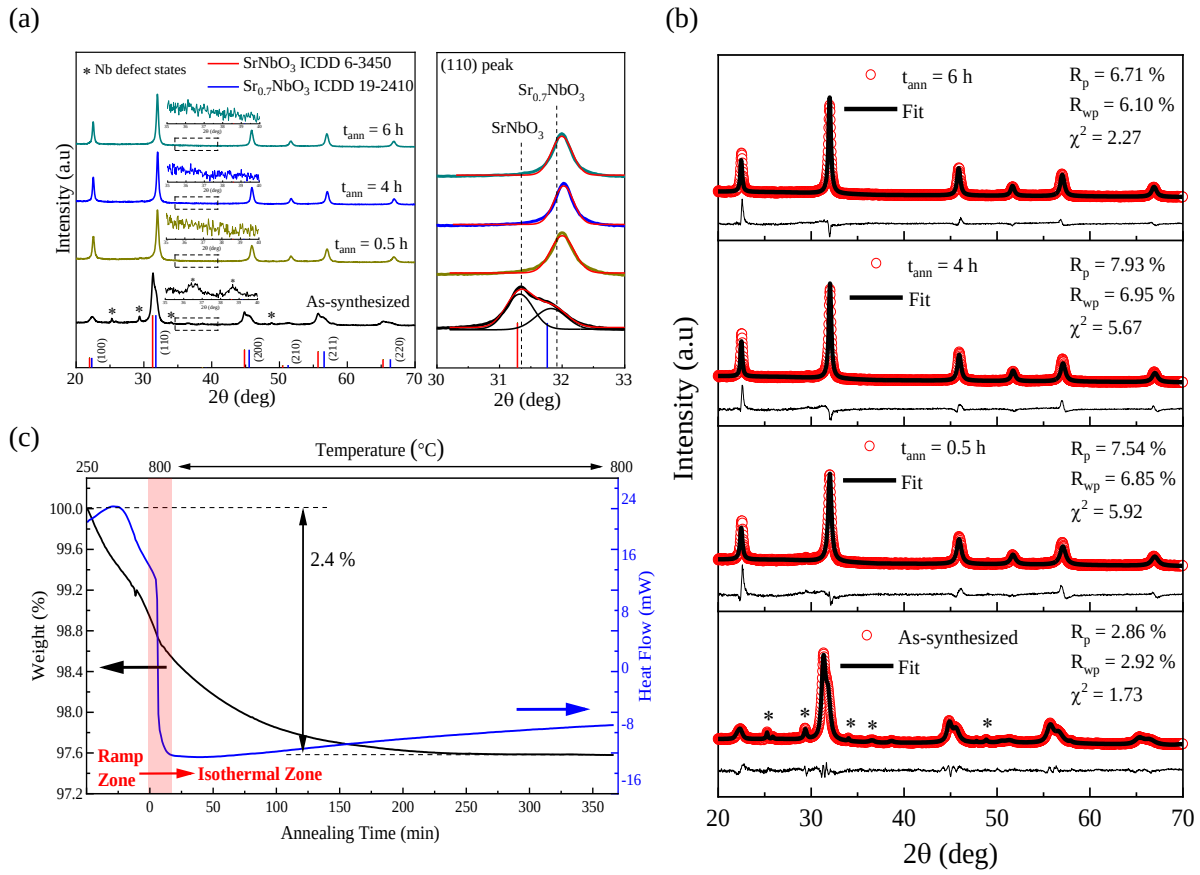

Figure 5.3 (a) XRD patterns and (b) Rietveld refinement for as-synthesized and H_2/Ar treated (T = 800 °C, t_{ann} = 0.5, 4, and 6 h) SNO NPs. (c) TGA-DSC curve monitoring the H_2/Ar treatment process. The dashed lines are a guide to the eye for $Sr_{0.7}NbO_3$ to $SrNbO_3$ phase transition. In the refinement, the upper symbols illustrate the observed data (circles) and the calculated pattern (solid line). The lower curve represents the difference between observed and calculated intensities. Nb defect states, present in the as-synthesized samples and removed in the treated samples, are denoted with asterisks.

Table 5.3 Crystallographic Data, Refined Atomic Coordinates, and Structural Parameters at Room Temperature SNO NPs annealed under H_2/Ar atmosphere based on X-ray Diffraction Data.

Parameters	**t_{ann} = 0.5 h**	**t_{ann} = 4 h**	**t_{ann} = 6 h**
wavelength (Å)		1.541	
temperature (K)		300	
2θ range (˚)		20-70	
space group		Pm-3m (No. 221)	
Z		1.0	
R_p, R_{wp} (%)	7.54, 6.85	7.93, 6.95	6.71, 6.10
χ^2	5.92	5.67	2.27
	Lattice Parameters		
a, b, c (Å)	3.950(4)	3.950(1)	3.955(4)
α, β, γ (˚)	90	90	90
V (Å^3)	62.850	61.441	61.881
	Atomic Coordinates		
Sr (x,y,z)	1/2, 1/2, 1/2	1/2, 1/2, 1/2	1/2, 1/2, 1/2
B (x,y,z)	0, 0, 0	0, 0, 0	0, 0, 0
O (x,y,z)	1/2, 0 , 0	1/2, 0 , 0	1/2, 0 , 0
	Structural Parameters		
Sr-O (Å)	2.793(4)	2.793(1)	2.796(9)
B-O (Å)	1.975(2)	1.975(0)	1.977(7)
O-B-O (deg)	180	180	180
O-B-O (deg)	90	90	90
B-O-B (deg)	180	180	180

The occupancy was fixed to 0.7 at the Sr site and 1 at Nb and O sites for the t_{ann} = 0.5, 4, and 6 h structure. For the t_{ann} = 0.5 h, the isotropic displacement parameter Uiso is 0.075(4), 0.000(5), and 0.016(8) for Sr, Nb, and O sites, respectively. For the t_{ann} = 4 h, the isotropic displacement parameter Uiso is 0.082(6), 0.002(5), and 0.015(3) for Sr, Nb, and O sites, respectively. For the t_{ann} = 6 h, the isotropic displacement parameter Uiso is 0.071(7), 0.003(3), and 0.029(8) for Sr, Nb, and O sites, respectively.

5.3. Optical Absorption Changes of the SBO NPs

In addition to reducing the multi-valent Nb-sites, a systematic change in the powder color (i.e. white to blue) and optical absorption occurred (Figure 5.4(a)). These reduced SNO NPs have similar spectrum in the UV region (300−400 nm) but exhibit significant enhancement in their

optical absorption in the visible to near-infrared region (400−800 nm) as a function of the annealing time. The first noticeable color change (from white to light blue, $t < 0.5$ h) is ascribed to the removal of surface defects that are periodically arranged within the lattice (Figure 5.3(a)). These defect sites are eliminated during the reduction treatment, transforming the initially white powder (insulating) to a light blue (conductive). With reduction times > 0.5 h, the powder become darker, which is attributed to the subsequent partial removal of deep defects and reordering of the bulk crystal. The STaO (white to grey) and SMO (white to black) samples exhibited similar responses to SNO (Figure 5.4(b-c)). The observed color changes did not fade even after exposing the powders to air for more than 6 months, suggesting that the crystals are highly stable under ambient conditions (Qiu, Li et al. 2014). However, after annealing the metastable crystals in air, they revert back to their thermodynamically stable (white powder) state, similar to previous reports, which is likely due to oxidation of the B-site cations (Wan, Zhao et al. 2017, Wells, Zou et al. 2018, Stoner, Murgatroyd et al. 2019). From the above analysis, the observed optical changes are clear indicators of a gradual structural transformation induced from the suppression of defect states (surface, $t < 0.5$ h and deep, $t > 0.5$ h).

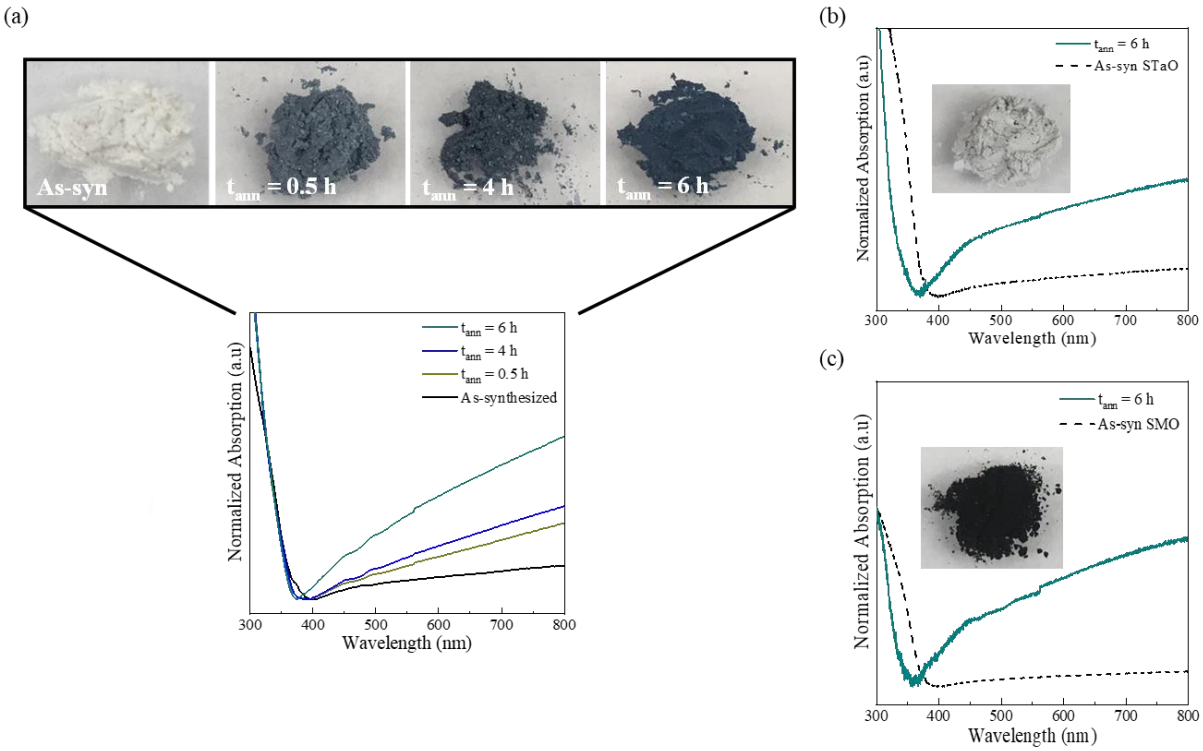

Figure 5.4 Optical absorption spectra for as-synthesized and H_2/Ar treated (a) SNO (T = 800 ^oC, t_{ann} = 0.5, 4, and 6 h), (b) STaO (T = 800 ^oC, 6 h), and (c) SMO (T = 800 ^oC, 6 h) NPs. The corresponding powder color are shown in the absorption plot.

5.4. Oxygen Binding Environment

Previous studies have demonstrated that oxygen vacancies (V_O) can be generated in metal oxides under oxygen-reduced conditions resulting in changes to the electronic structure and powder appearance (Shin, Joo et al. 2012, Qiu, Lai et al. 2014, Qiu, Li et al. 2014, Tan, Zhao et al. 2014, Sengodan, Choi et al. 2015, Bayeh, Kabtamu et al. 2019, Safavinia, Wang et al. 2020). Therefore, to verify that the visual changes are not due to the formation of V_O, the binding environment of O in the SNO NPs was probed (Figure 5.5(a)). The deconvoluted O 1*s* XPS spectra of the as-synthesized NPs identifies four peaks assigned to $SrNbO_3$ lattice oxygen (529.2 eV), $Sr_{0.7}NbO_{3-\delta}$, lattice oxygen (530.0 eV), oxygen defects (531.5 eV), and surface hydroxyls

(532.6 eV) (Liu, Chen et al. 2017, Safavinia, Wang et al. 2020). The surface hydroxyl peak is removed during the reduction treatment with the remaining peaks unchanged. The removal of the hydroxyl peak after 0.5 h corresponds with the initial change in the visual appearance suggesting the surface defects significantly impact the NPs electronic properties. The change in the area ratio of the main SNO lattice oxygens ($Sr_{0.7}NbO_{3-\delta}$, and $SrNbO_3$) for the as-synthesized compared with the treated samples are consistent with the crystal structure evolution (Figure 5.5(b) and Table 5.4). The V_O peak area sharply decreases upon reduction (0.5 h, -36%) with relatively little change throughout the remaining reduction process (Figure 5.5(c)). The fact that the V_O peak area does not increase during the reduction processes indicates that the formation of oxygen defects does not contribute to the optical response. Additionally, the HRTEM images on the reduced SNO NPs show *d*-spacings of 2.90 and 3.90 Å corresponding to the (110) and (100) lattice planes of $Sr_{0.7}NbO_{3-\delta}$, (Figure 5.5(d)). The homogeneous crystal composition observed in the images further confirms the absence of exsolution-induced phase changes as a result of the extended treatment (Sengodan, Choi et al. 2015, Sun, Zhang et al. 2016, Wu and Lin 2017, Hou, Yao et al. 2019). These results reveal that, although V_O-type defects are present, the optical changes from the reduction process are a result of suppressing surface/deep defect states.

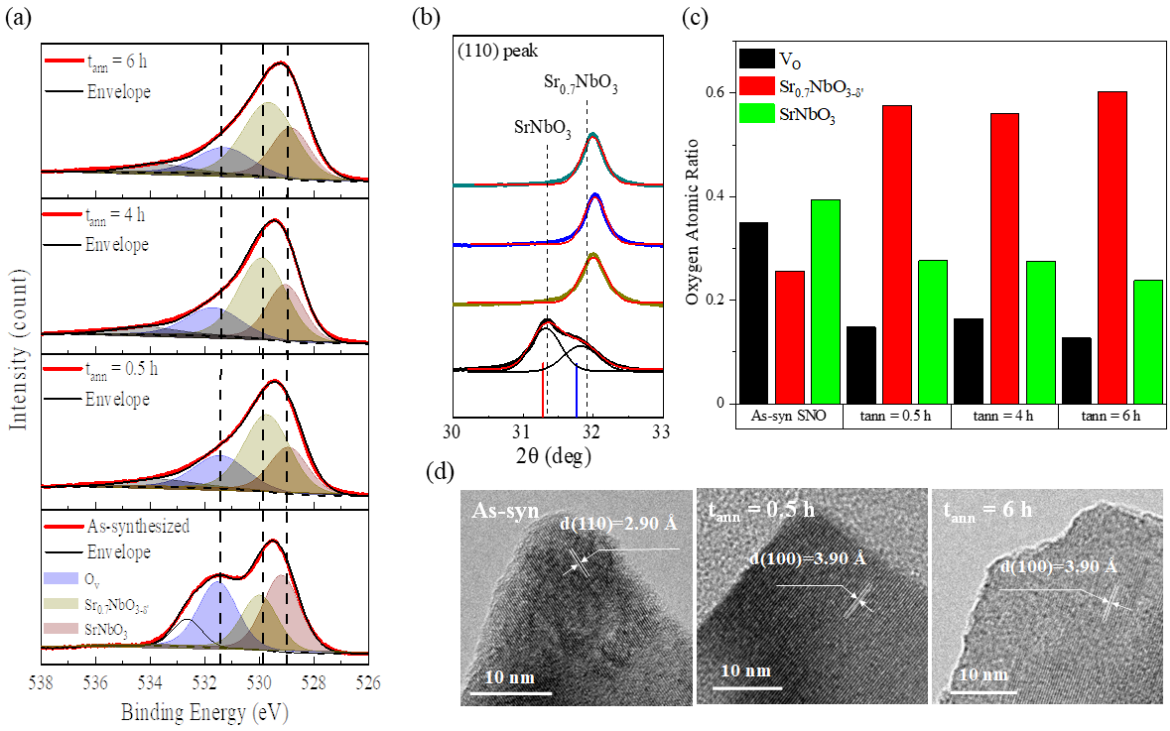

Figure 5.5 (a, c) XPS, (b) XRD and (d) HRTEM images for as-synthesized and H_2/Ar treated SNO NPs. The (110) peak is included to highlight the structural transformation also observed in the XPS spectra. The dashed lined in the XPS spectra are a guide for the eyes. The HRTEM images with short (0.5 h) and long (6 h) H_2/Ar annealing times highlight the absence of exsolved metallic particles and only shows a homogeneous $Sr_{0.7}NbO_{3-\delta}/SrNbO_3$ crystal

Table 5.4 Area under the Peak of O 1*s* in the SNO NPs.

Powder Sample	$SrNbO_3$ Area	$Sr_{0.7}NbO_{3-\delta'}$ Area	V_O Area
As-syn SNO	38%	27%	35%
t_{ann} = 0.5 h	25%	51%	24%
t_{ann} = 4 h	28%	52%	20%
t_{ann} = 6 h	26%	50%	18%

5.5. Effect of H_2/Ar Treatment on the Crystallization of SBO NPs

The proposed reduction mechanism for these SNO NPs is summarized in Figure 5.6. Upon heating the as-synthesized NPs in an oxygen-reduced environment, Sr and O atoms diffuse across the grain boundaries, presumably from the stoichiometric to the Sr-deficient phase. Next, the diffused atoms bind with surface Nb defects at ~470 ℃, forming a stable Sr-Nb-O network (Figure 5.6(a)). The fact that this process is relatively fast (t < 0.5 h) suggests that the loss of chemisorbed hydroxyl groups occurring at this temperature makes the bond formation step kinetically favorable. This bond formation induces structural transformations that drive the appearance of metallic character (color change) (Lee, Choi et al. 2017). With increased treatment time, the network expands by binding the diffused atoms with defects located deeper within the crystal. This process is kinetically slow based on the longer times needed (t > 0.5 h). In the final step, the bi-phasic structure is reorganized into a single-phase Sr-deficient lattice ($Sr_{0.7}NbO_{3-\delta'}$, δ'~0.34; Figure 5.6(b)) with no other observed crystal changes (Chen, Paulson et al. 2015, Sengodan, Choi et al. 2015, Wu and Lin 2017). The δ' agrees with the previously reported

oxygen deficiency (δ ~0.35) (Chapter 3), further demonstrating that the Sr-deficient lattice is the final crystal structure. Additionally, the suppression of these surface/deep defects creates significant changes to the optical absorption of the NPs. Thus, the structural and optical results provide strong evidence that these SBO NPs potentially undergo an insulator-to-metal transitions (IMT) (white, insulating to colored, metallic-like) when thermally treated in an oxygen-reduced environment.

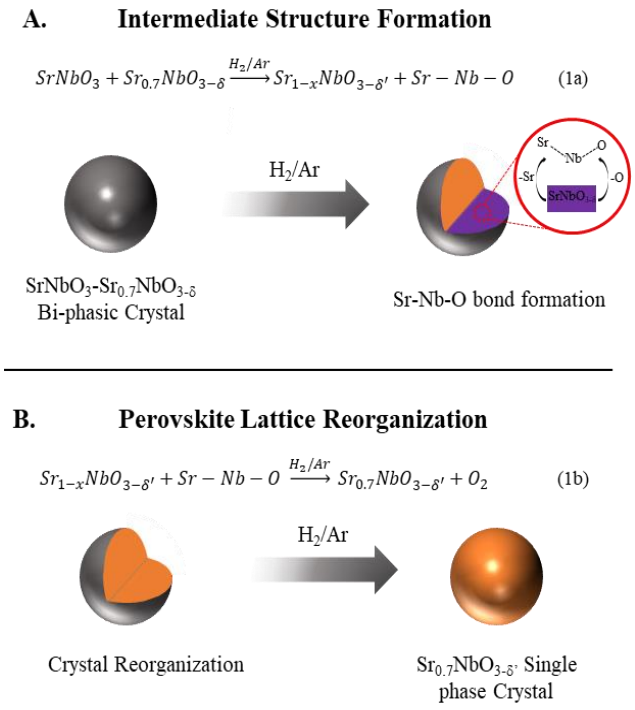

Figure 5.6 Schematic representation for the proposed mechanism for the treatment of SNO NPs in H_2/Ar atmosphere.

5.6. Effect of Suppressing Surface/Bulk Defects on the Electronic Properties

EIS spectroscopy was performed to further characterize the electrical activity during the IMT for these NPs. This technique has been used to monitor changes in the electronic conductivity of reduced $W_{18}O_{49}$ (Bayeh, Kabtamu et al. 2019), TiO_2 (Qiu, Li et al. 2014), and

$SrTiO_3$ (Call, Brogan et al. 2018). The corresponding Nyquist plots for the reduced SNO NPs are shown in Figure 5.7(a). The electrical resistances extracted from the optimized fit ($\chi^2 < 10^{-3}$) are summarized in Table 5.5. The EIS measurements focused on the high frequency region (>200 mHz) where the electrolyte, SEI, and anode/cathode electrode (Eom, Lee et al. 2017) are dominant and excluded the low frequency Li-ion diffusion (Qiu, Li et al. 2014). The slight increase in capacitance observed after the 0.5 h treatment is attributed to the reduction of surface defects, which hinders bulk charge transport (Yao, Pham et al. 2015, Kim, Nandi et al. 2019). This capacitive behavior subsequently decreases proportionally with annealing time due to the suppression of bulk defects, facilitating the depletion of accumulated surface charges (Lück and Latz 2019). After the 6 h treatment, a homogeneous structure is obtained, which can effectively transport charges and reduces the total capacitance. As expected, the enhanced electronic conductivity of the NPs also contributes to systematically reducing the electrode cell resistance. Specifically, the R_{CT} of the as-synthesized SNO electrode (4.31 kΩ) is reduced to 254 Ω after 6 h, demonstrating that the suppression of the deep defects substantially reduces charge transfer resistances. Conversely, an increase (from 252 Ω to 1.97 kΩ) in the R_{SEI} is observed as a result of the IMT, which is associated with enhanced electrical transport that leads to considerable electrolyte decomposition and SEI growth (Franco, Rucci et al. 2019). As seen from changes in the capacitance and resistance (R_{CT}, R_{SEI}), when t < 0.5 h, the electrical activity of the NPs is driven by surface transport. Unfortunately, surface defects act as trap states that localize free carriers (Tan, Zhao et al. 2014), thus reducing carrier mobility and impeding bulk transport. However, when t > 0.5 h, bulk transport dominates and a dramatic change in the electronic properties, i.e. an insulating to metallic-like state is observed. The suppression of deep defects improves charge transport by increasing the number of free carriers and carrier mobility. Similar

to SNO, qualitative and quantitative variations were observed for the reduced STaO and SMO NPs as a result of their modified electronic properties (Figure 5.7(b-c) and Table 5.6). These results suggest that the IMT is largely influenced from the inhibition of bulk rather than surface defect formation.

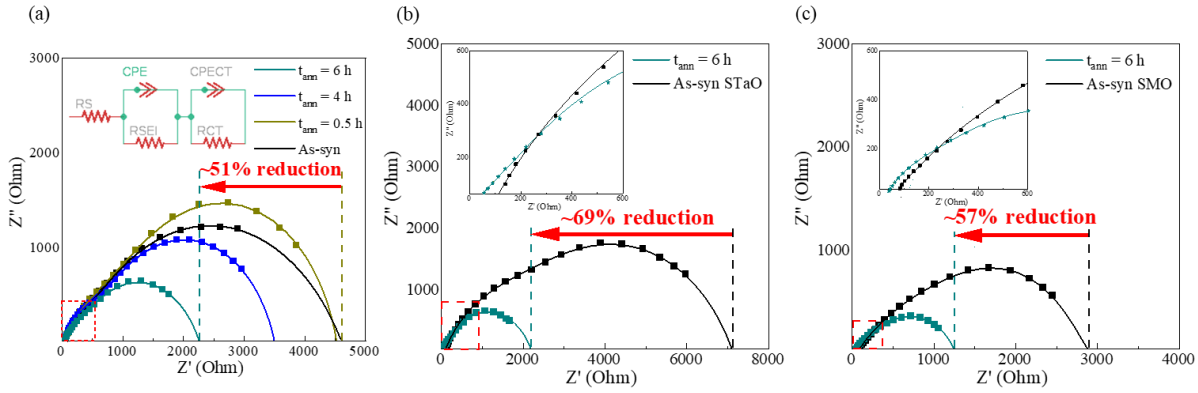

Figure 5.7 EIS for as-synthesized and H_2/Ar treated (a) SNO, (b) STaO, and (c) SMO. For the SNO curve, the inset of the SNO shows the circuit design and, for the STaO and SMO curves, the inset presents an enlarged view of the high frequency region of the EIS spectra (red dashed box).

Table 5.5 Extracted EIS fit parameters for SNO NPs.

Material	**R_S (Ω)**	**R_{SEI} (Ω)**	**R_{CT} (Ω)**	**$R_{electrode}$ (Ω)**
As-Syn	41.8	252.1	4314.0	4607.9
t_{ann} = 0.5 h	33.6	1146.0	3346.0	4525.6
t_{ann} = 4 h	48.3	2853.0	600.1	3501.4
t_{ann} = 6 h	38.9	1969.0	254.2	2262.1

Table 5.6 Extracted EIS fit parameters for STaO and SMONPs.

Material	R_S (Ω)	R_{SEI} (Ω)	R_{CT} (Ω)	$R_{electrode}$ (Ω)
As-Syn STaO	75.9	1957.0	5094	7126.9
t_{ann} = 6 h	12.9	2133.0	68.1	2213.9
As-Syn SNO	46.9	722.8	2145.0	2914.7
t_{ann} = 6 h	27.0	1066.0	173.8	1266.8

The induced metallic-like nature of these SBO NPs was further investigated by measuring the current-voltage (I-V) response. The electrical resistivities (ρ), plotted from -5.0 to 5.0 V, were calculated by applying Ohm's and Pouillet's laws (Li, Wang et al. 2019). The current value for the as-synthesized SNO NPs was beyond the detection resolution of the instrument due to their intensely insulating nature, but demonstrated a systematic decrease in resistivity (1.1×10^{3} Ω-cm for 6 h) with treatment time (Figure 5.8(a)) (Yang, Ko et al. 2010, Wang, Dash et al. 2016). Although a similar quantitative ρ reduction was observed for SMO (from 2.6×10^{-4} for 4 h to 1.7×10^{-4} Ω-cm for 6 h; Figure 5.8(b)), a non-ohmic response was observed for the STaO after 6 h (Figure 5.8(c)). It is important to note that the measured ρ for SMO is considerably lower than the ρ for SNO and STaO. The measured ρ for SMO is in good agreement with the thin-film counterpart (Macquart, Kennedy et al. 2010), signifying the complete removal of deep defect states in the sample. However, in the case of SNO and STaO, the ρ is higher than literature values (Oka, Hirose et al. 2014, Wan, Zhao et al. 2017) due to the presence of deep defects. From these results, it is evident that the defect stability in these metastable crystals follows the

order of Mo < Nb < Ta. This trend is closely correlated with the descending sequence of electronegativity observed for the B-site ions (Mo ~2.2; Nb ~1.6; Ta ~1.5) (Li and Xue 2006). As the electronegativity of the B-O bond increases, it presumably becomes more challenging to stabilize defects during the H_2/Ar treatment, thus facilitating the crystal formation (Neagu and Irvine 2011, Salg, Zeinar et al. 2020). It is reasonable to conclude from these electrical transport results that the suppression of deep defect states is responsible for the metallic-like behavior of the treated SBO NPs.

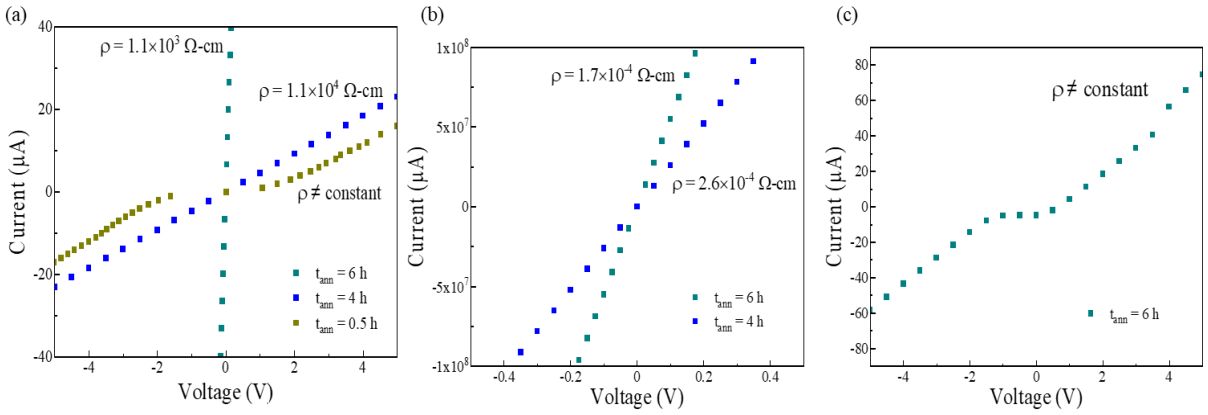

Figure 5.8 I-V curve for as-synthesized and H_2/Ar treated (a) SNO, (b) SMO, and (c) STaO. The voltage was collected from -5 to 5 V. An enlarged view for SMO, -0.4 to 0.4 V, is presented to highlight the reduction in electrical resistivity.

5.7. Theoretical Calculations

To further substantiate the claim that the deep defect states modify the electronic properties of these SBO NPs, the ρ were calculated. In these calculations, DFT, with no Hubbard U correction (Anisimov, Zaanen et al. 1991), was utilized to describe the electronic interactions of the SBO perovskites (Oka, Hirose et al. 2018, Bigi, Orgiani et al. 2020). This was tested by

performing initial calculations on stoichiometric SBO (Figure 5.9(a-c)). Comparison of these results (calculated optical transition: SNO, E_g ~2.3 eV; STaO, E_g ~3.0 eV; SMO, E_g ~1.1 eV) with computational reports (Ali, Khan et al. 2015, Kaneko, Mishima et al. 2019, Mehmood, Ali et al. 2019, Stoner, Murgatroyd et al. 2019, Park, Roth et al. 2020) show good agreement. Although E_g, which arises from the O 2*p*-B 4*d* or *5d* t_{2g} interband transition, is experimentally observed to be >3-4 eV (Park, Roth et al. 2020), DFT is known to underestimate this transition energy. Furthermore, the ρ values were calculated by utilizing the Boltzmann Transport theory as implemented in the BoltzTraP2 code (Figure 5.9(d-f)). As displayed in Table 5.7, the calculated ρ at the Fermi level is consistent with reported values (Oka, Hirose et al. 2018, Ha and Lee 2020, Park, Roth et al. 2020).

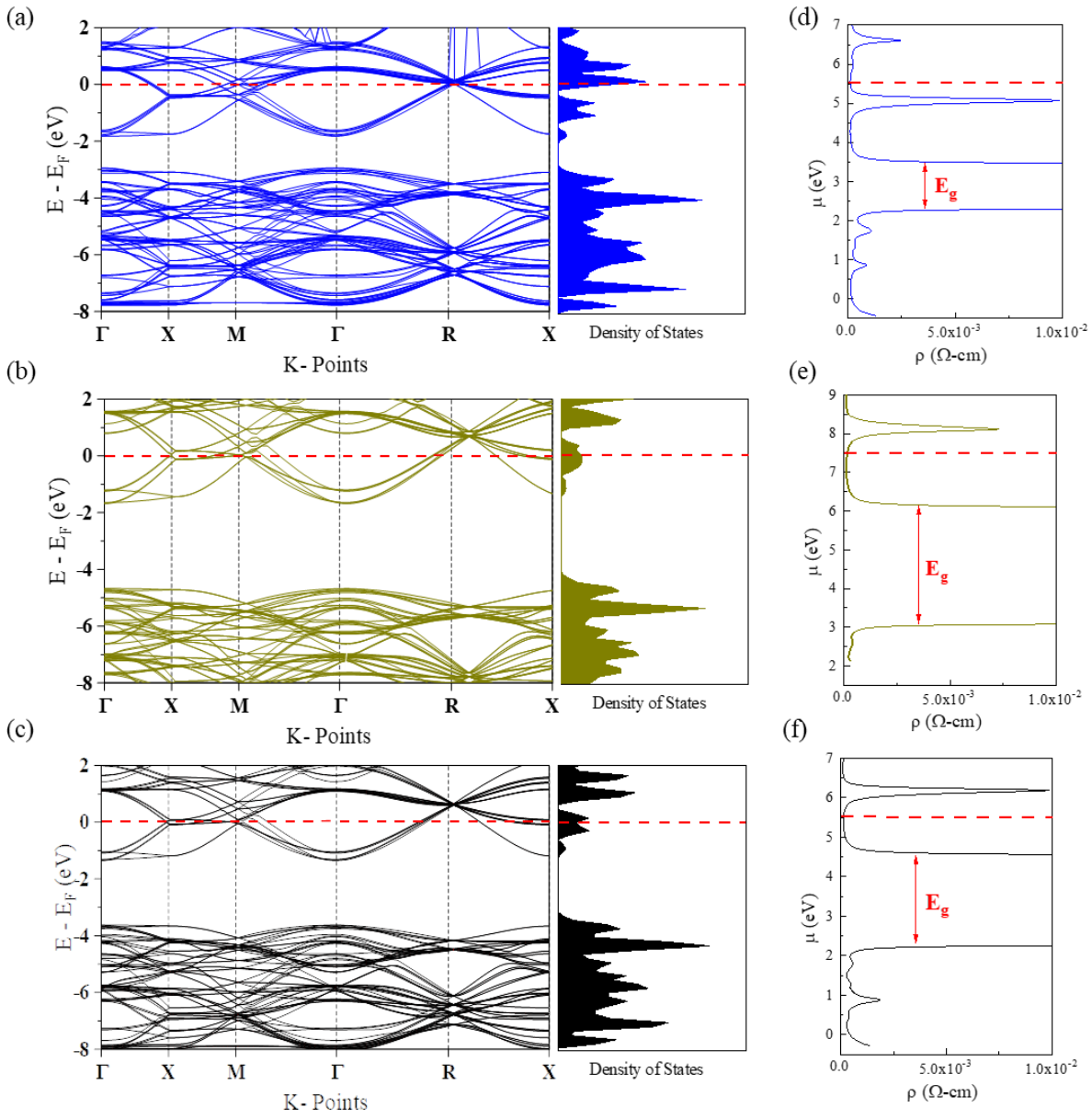

Figure 5.9 Band structure, total density of state, and electrical resistivity (ρ) calculations for the defect-free (a, d) SMO, (b, e) STaO, and (c, f) SNO. The ρ calculations were performed at 300 K. The Fermi level is indicated with a dashed red line in all plots.

Table 5.7 Calculated and measured electrical resistivity (ρ) for SBO NPs.

Crystal Structures	Calculated ρ for Defect-free SBO (Ω-cm)	Calculated ρ for Defective SBO (Ω-cm)	Measured ρ for Defective SBO (Ω-cm)	Reported ρ (Ω-cm)
B = Mo	1.7×10^{-4}	1.7×10^{-4}	1.7×10^{-4}	$(\sim0.2\text{-}2.0)\times10^{-4}$
B = Ta	1.5×10^{-4}	2.1×10^{-2}	-	$(\sim12)\times10^{-4}$
B = Nb	1.7×10^{-4}	2.1×10^{-4}	1.1×10^{3}	$(\sim1.0\text{-}69.0)\times10^{-4}$

Next, to mirror the measured SBO stoichiometries, the following models were utilized: (i) for SMO, no Sr (V_{Sr}) and O (V_O) vacancies were incorporated into the corresponding defect-free model, (ii) for SNO, 2 V_{Sr} and 2 V_O vacancies were introduced into the corresponding defect-free model, and (iii) for STaO, 10 Na atoms (7 A-site, 3 B-site) and 5 V_O were introduced into the corresponding defect-free model. The calculated band structures and density of states (DOS) for the defective SBO NPs show that the Fermi level sits in the respective bands (Figure 5.10(a-c), dashed red line), revealing that the observed electronic conductivity of these metastable crystals is a result of n-type (SNO and SMO) and p-type (STaO) behavior. Additionally, in comparison to reduced STO and TiO_2 (Szot, Speier et al. 2002, Cushing, Meng et al. 2017), the Fermi level for these defective SBO perovskites lies deep within either the conduction (SNO/SMO) or the valence (STaO) band. For SNO and SMO, the n-type conductivity arises from the partially occupied t_{2g} bands of the metal *d* orbitals (Macquart, Kennedy et al. 2010, Ha and Lee 2020). In the case of STaO, it is believed that the partial

substitution of Na into the Sr/Ta-sites of STaO significantly dopes hole carriers into the top of the valence band, resulting in the p-type conductivity (Triggiani, Muñoz-García et al. 2016). From the above calculations, the electronic structure of the metastable SBO perovskites is determined to be conducive to n- or p-type transport, depending on the nature of the B-site ion, making them robust conductors.

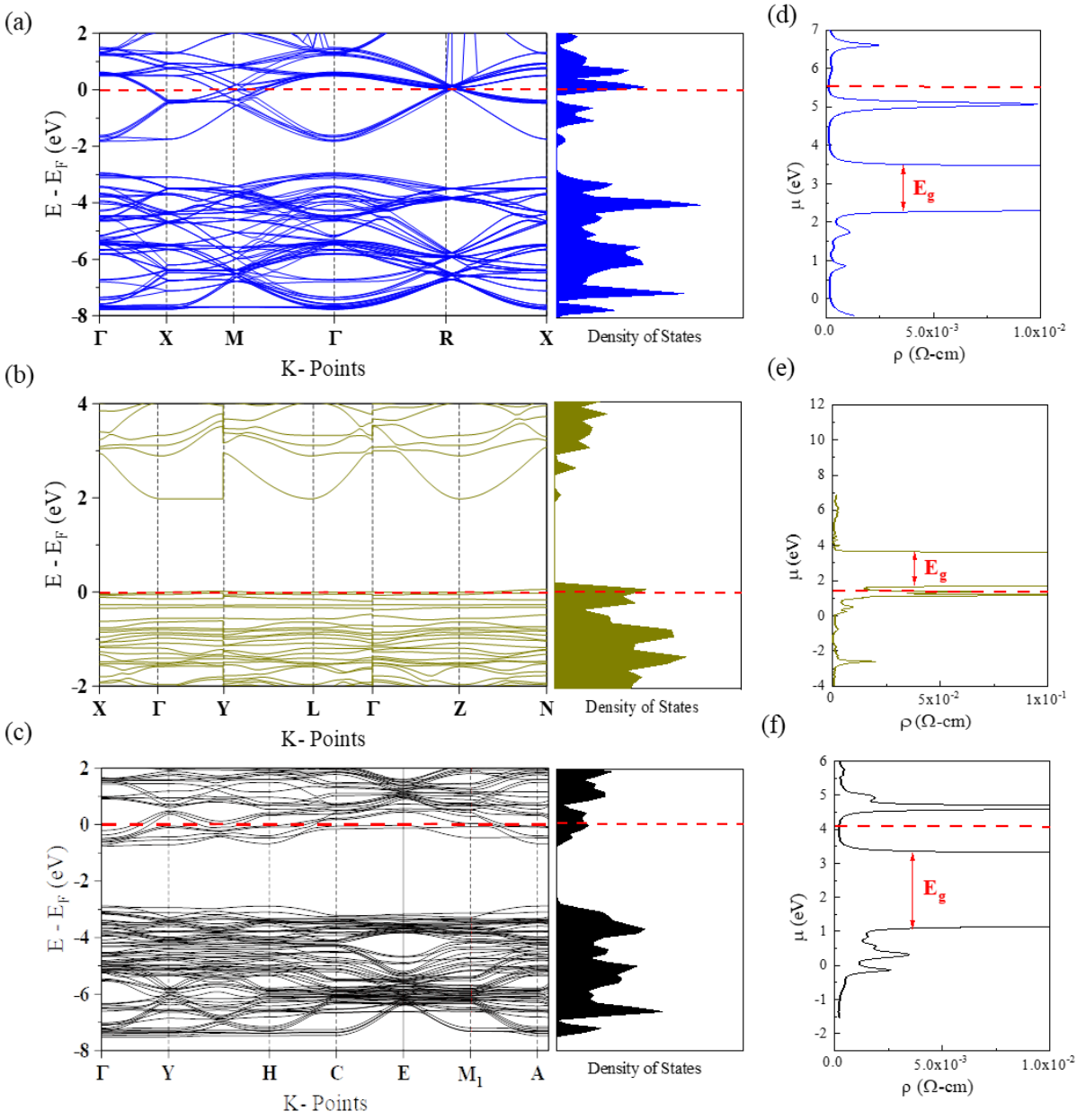

Figure 5.10 Band structure, total density of states, and electrical resistivity (ρ) calculations for the defective (a, d) SMO, (b, e) STaO, and (c, f) SNO. The ρ calculations were performed at 300 K. The Fermi level is indicated with a dashed red line in all plots

Similarly, the ρ for the defective SBO perovskites were calculated and presented in Figure 5.10(d-f) and Table 5.7. According to these transport calculations, the ρ of STaO is higher than that of SNO and SMO, which is consistent with the response observed experimentally. The

calculated ρ for the SMO agrees with the measured values, further highlighting the absence of deep defect states in the sample after the reduction treatment. However, in the case of SNO and STaO, the deep defect states are more difficult to fully suppress (Figure 5.8(a) and (d)), resulting in the observed difference between the experimental and calculated ρ values. This behavior is consistent with other SNO calculations that reported inhibited electronic transport due to the presence of bulk defect states (Wan, Zhao et al. 2017). These results demonstrate that the variation in the measured electrical resistivity of the SBO NPs can be explained by changes in the deep defect states. Thus, the computational findings coincide well with the experimental observations noted above. Overall, these results effectively demonstrate the ability to synthesize metastable ABO_3 perovskites and systematically modify their electronic properties, which has potential applications in future electrochemical devices.

5.8. Summary

In summary, this chapter discusses suppressing the defect states of the metastable NPs to recover their expected optoelectronic properties. Specifically, this comprehensive study demonstrates that the defect states are spatially distributed in the NPs, i.e., surface and bulk. Therefore, to understand the effect these surface/bulk defects have on the resultant optoelectronic properties, the SBO NPs were systematically treated under a reducing atmosphere. The surface defect states are partially stabilized by hydroxyl groups and can be quickly removed (treatment time, $t < 0.5$ h). This rapid treatment results in a noticeable change in the powder color (white to light blue), which is tied to the formation of stable Sr-Nb-O bonds that occur at this time. With $t > 0.5$ h, this bond formation extends deeper into the crystal, suppressing bulk defects and resulting in the powder becoming darker. At this point, the final lattice structure and composition is $Sr_{0.7}NbO_{3-\delta'}$, $\delta' \sim 0.34$. Based on the optical absorption and electrical activity of the NPs, the

suppression of the deep rather than surface defect states is responsible for inducing the IMT. DFT calculations reveal that n-type (B = Nb and Mo) and p-type (B = Ta) conduction is responsible for the observed metallic-like behavior. Finally, DFT and Boltzmann Transport calculations demonstrate that the expected electronic transport properties of the NPs are quenched due to highly oxidized B-site states present in the bulk of the crystal. Ultimately, these findings outline a novel approach for the design/development of conductive ABO_3 perovskites, which are technologically significant for next-generation electrochemical devices.

Chapter 6 . Summary and Future Work

Metastable SBO perovskites have attracted interest for their metallic responses making them promising materials for optoelectronic devices. Despite the recent attention, the wet-chemical synthesis of SBO NPs results in B-site cations that are stabilized in highly oxidized states (i.e. Nb^{5+}, Ta^{5+}, Mo^{6+}, etc.), instead of the desired 4+ valency. These over-oxidized states, present as surface/bulk defect states, suppress the expected optoelectronic responses. For this reason, the engineering of these defect states to recover the optoelectronic properties of metastable SBO perovskites was investigated using various scattering/spectroscopic characterization methods. SNO was first tested to develop a wet-chemical procedure for preparing these conductive nanocrystals. The developed oxygen-controlled CP/MSS method allows for the simultaneous intercalation of Sr ions and suppression of defect states, which is not observed using traditional wet-chemical methods. The oxygen-deficient atmosphere is vital for improving the Sr incorporation, as it prevents the noted loss of Sr due to the formation of secondary structures, especially at high Sr concentrations. This ability to directly increase the concentration of Sr ions taking part in the crystallization of SNO also allows for the suppression of Nb defect states. Additionally, by identifying and mitigating low concentrations of Nb defects using a reducing post-synthesis, the system could be driven from an apparent white (insulating) to colored (metallic) state. To further corroborate the formation of the SNO lattice, first-principles density functional theory (DFT) calculations were performed in collaboration with Dr. Craig Plaisance's group in the Department of Chemical Engineering, LSU. These experimental and computational findings point toward the potential application of these materials as conductive scaffolds that otherwise would not be possible with traditional solution-based methods.

Building on this work, the effect of these defect states on the A-site chemical structure was also investigated. As an analogue material to STO, SNO was utilized as a representative structure and the Sr-sites were replaced with Ca ions to form the CNO structure. Using the low-pressure approach, a larger concentration of defect states was formed in CNO compared to the SNO lattice. Nonetheless, the ABO_3 perovskite structure, stabilized in both crystals, demonstrates that the A-site environement remains relatively stable using the oxygen-controlled CP/MSS method. This is not seen using traditional wet-chemical methods, which form only the defect states. As a result of incorporating Ca into the A-site, a symmetry/structural transformation is induced, which is expected to produce ferroelectric (FE) polarization due to the off-centered Ca ions, as seen with STO (CSTO). The systematic A-site substitution of Ca into the SNO host lattice (CSNO) required a H_2/Ar atmosphere to fully prevent the formation of the defect states. This initiated two successive transformations, converting the high-symmetry cubic lattice into a low-symmetry T (x~0.2) and, later, O (x~0.8) phase. Comparison of these structural changes with CSTO, shows that the A-site symmetry of CSNO is more disordered due to the presence of oxygen defects formed from the oxygen-deficient crystallization method. Furthermore, upon cooling the T phase, the local environment appears conducive to FE behavior. This ability to induce symmetry/structural transformations by manipulating the local and extended structure of ABO_3 perovskites, will be beneficial for elucidating novel phenomena with applications to energy storage.

As a next step in utilizing these materials as conductive scaffolds, the spatial distribution of the defect states (i.e., surface or bulk) has a direct effect on the optoelectronic responses. Therefore, to inhibit the presence of the surface/bulk defect states, a wet-chemical post-treatment that mirrors vacuum deposition processes is needed. For this purpose, the synthesized NPs were

systematically treated under an oxygen-reduced (H_2/Ar) atmosphere to restore the expected metallic properties. The first noticeable color change (from white to light blue) is ascribed to the removal of surface Nb defects. At longer reduction times, a dark powder with broad visible absorption is formed, which is attributed to the subsequent partial removal of deep Nb defects and reordering of the bulk crystal. The structural reorganization, which starts at ~470 °C, is driven by the bonding of mobile Sr and O atoms with surface/bulk Nb defect states, thus forming a stable Sr-Nb-O framework. After the reorganization, the final lattice structure and composition is $Sr_{0.7}NbO_{3-\delta'}$, δ'~0.34 without any ex-solved phases. Similar optoelectronic behaviors (insulator, white to colored, metallic-like) are observed with the synthesis of other metastable SBO perovskites (B = Ta, Mo), highlighting that this structure/composition transformation is not a function of the B-site cation. In essence, these findings demonstrate that by engineering the surface/bulk defect states of the metastable crystals, the resulting optoelectronic properties can be tuned.

Although the previous studies affirm the restoration of the expected optoelectronic responses for these NPs via the suppression of surface/bulk defect states, the electronic properties for these crystals remains unclear. Therefore, to probe the modified electronic properties, EIS and electrical resistivity measurements were performed in collaboration with Dr. John Flake's group and Dr. Rongying Jin's group in the Departments of Chemical Engineering and Physics, LSU. Surface defects act as trap states that localize free carriers, thus reducing carrier mobility and impeding bulk transport. Although there is improved charge transport from suppressing these surface defect states, it is not enough to trigger bulk transport. However, when the deep defect states are removed, bulk transport dominates and a dramatic change in the electronic properties, i.e. an insulating to metallic-like state is observed. Therefore, the removal

of these bulk defects creates a homogeneous structure, which can effectively transport charges due to the increased number of free carriers and carrier mobility. The observed experimental results were corroborated using DFT and Boltzmann Transport calculations with the assistance of Dr. Craig Plaisance's group. The calculated band structures and DOS reveal that the observed electronic conductivity of these metastable crystals is a result of n-type (SNO and SMO) and p-type (STaO) behavior. For SMO, the calculated ρ coincides with the measured values due to the absence of deep defect states in the sample. However, in the case of SNO and STaO, the deep defect states are more difficult to fully suppress, resulting in the observed difference between the experimental and calculated ρ values. The combined experimental and computational results demonstrate that the formation of bulk defect states significantly influence the resulting electronic properties of the SBO NPs. Overall, this ability to engineer the defect states of metastable ABO_3 perovskites opens new avenues in various fields such as energy storage/conversion, which can take advantage of these electrically conductive materials.

While this work demonstrates the capability of metastable SBO perovskites as conductive scaffolds for electrochemical applications, it was not able to fully investigate the topic of study. Therefore, future work building on these results is described below. As a proof of concept, a $LiFePO_4$ top layer is deposited onto these conductive SBO perovskites to demonstrate their potential application in Li-ion batteries. This use of a conductive scaffold/skeleton to modify electrochemical performances has been previously demonstrated using B_4C (Chen, Li et al. 2012), and TiC/C (Yao, Huo et al. 2011, Yao, Xia et al. 2018). Among the prepared conductive nanomaterials, SMO was selected based on its superior electronic properties after removal of surface/bulk defect states (Chapter 5). The LFP (space group: *Pnma*, ICDD 40-1499) particles were synthesized using a reported solvothermal recipe (Figure 6.1(a)). Details regarding the

synthetic process are described in Chapter 2. The LFP particles were then prepared into a homogeneously mixed slurry and applied around the SMO scaffold.

To probe the changes in the charge transport of LFP as a result of incorporating the conductive SMO internal layer, EIS measurements were performed. The Nyquist plots are shown in Figure 6.1(b) and the extracted resistances are summarized in Table 6.1. As references, the pure LFP and the LFP slurry were included in the plots. The incorporation of the SMO scaffold significantly reduces the electrode cell resistance, which is in line with the expected behavior of these conductive materials. Specifically, the changes observed for R_S are attributed to slight changes in the electrode distance (Doppelhammer, Pellens et al. 2020). More importantly, the R_{CT} of the LFP electrode (680.0 kΩ) is reduced to 26.1 Ω due to the significantly improved charge transport. This improved charge transport is also observed in the reduced capacitance. For pure LFP, the low intrinsic electronic conductivity (~10^9 Ω-cm) results in the large capacitance and R_{CT}. Conductive additives such as carbon black (~10^{-2} to 10^{-1} Ω-cm) are added to the electrode slurry to address this issue, which is consistent with the observed reduced R_{CT} (Pantea, Darmstadt et al. 2003). Incorporation of the conductive scaffold material further reduces the R_{CT}, indicating that the electronic properties of SMO play an important role in modifying the charge transport responses of LFP (He, Zhang et al. 2007, Atta, Ali et al. 2013). Ultimately, these results demonstrate that the near field coupling of ionic and electronic conductivity via the layered film architecture results in improving the charge transport properties of LFP.

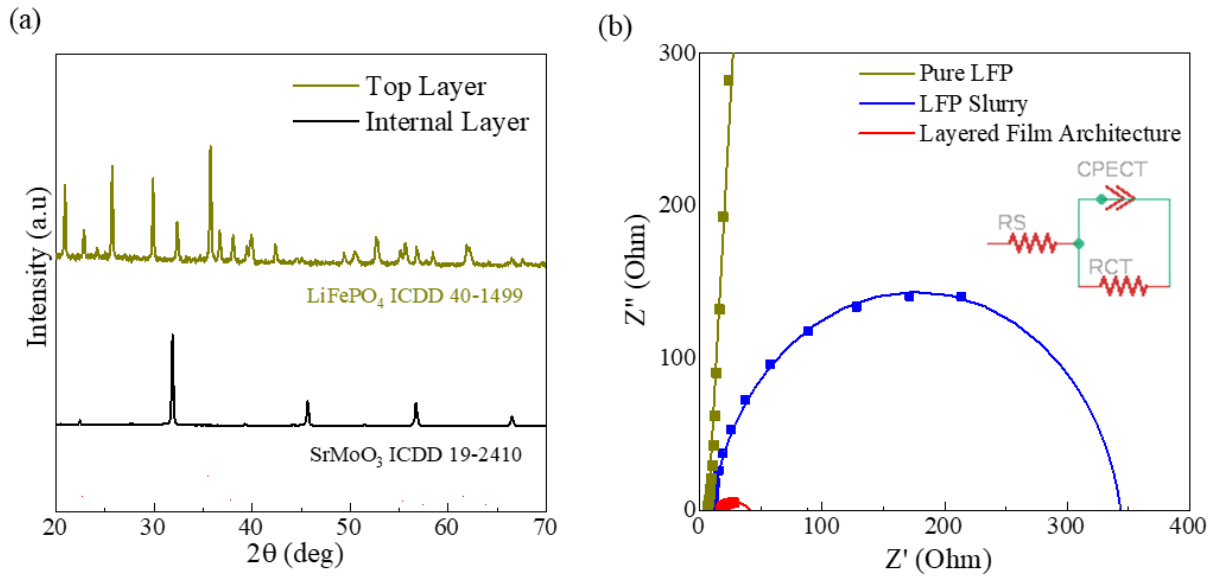

Figure 6.1 (a) Diffraction pattern for the components of the layered film architecture. (b) EIS spectra of the pure LFP, LFP slurry, and layered film architecture. All EIS measurements were performed using a 1 M $LiNO_3$ electrolyte.

Table 6.1 Extracted impedance spectroscopy fit parameters for LFP, Slurry LFP, and Layered Film Architecture.

Material	**R_S (Ω)**	**R_{CT} (Ω)**	**$R_{electrode}$ (Ω)**
Pure LFP	6.8	6.8×10^5	6.8×10^5
LFP Slurry	9.6	334.0	343.6
Layered Film Architecture	15.6	26.1	41.7

In addition to their applied use in energy storage, it was suggested that these materials can also be utilized in energy conversion technology. Chalcogenide perovskites provide an alternative route to address the structural instability and toxicity issues posed by inorganic-

organic halide perovskites (Swarnkar, Mir et al. 2019). A notable example includes $BaZrS_3$ (E_g~1.7-1.8 eV, structural stability: 500-600 °C), which has been demonstrated to possess a bandgap suitable for tandem solar cells (Comparotto, Davydova et al. 2020). Therefore, this combined experimental and computational approach will allow for the development of various potential (oxy)chalcogenide perovskites (i.e., $SrNbO_{3-x}S_x$, $SrMoO_{3-x}S_x$, etc.) by using the formed metastable oxides as structural templates (Gupta, Ghoshal et al. 2020). Additionally, this ability to synthetically induce structural transformations can be used to explore various phase-dependent optoelectronic properties (i.e., crystallographic disorder, band tuning, etc.) for both fundamental studies and device applications. As scaffold materials, these metastable perovskites can act as electron transporting layers due to their semiconducting/insulating nature (E_g > 4.0), which allows for electron injection into their conduction band, as seen in dye-sensitized solar cells (DSSC) (O'Regan and Grätzel 1991). Simultaneously, their degenerate conduction band gives them superior electron transport properties (carrier mobility: 2.47 $cm^2 V^{-1} s^{-1}$) especially when compared to mesoporous TiO_2 (carrier mobility: 0.1 $cm^2 V^{-1} s^{-1}$) (Tiwana, Parkinson et al. 2010, Wan, Zhao et al. 2017), a commonly employed scaffold material for DSSC.

Moreover, the developed SBO-LFP layered film architecture can be applied in memory storage. Conventional computing systems based on complementary metal-oxide-semiconductors (CMOS) designs suffer from high energy consumption and heat generation (Fuller, Gabaly et al. 2017, Yang, Shang et al. 2018), prompting the need for alternative approaches such as neuromorphic computing. In particular, neuromorphic computers comprising of non-volatile redox transistors (NVRTs) with functionalities that mirror Li-ion batteries utilize the reversible intercalation and deintercalation of Li, a relatively low energy process in metal oxides (~0.11 to 0.25 eV) (Nikam, Kwak et al. 2019), for resistance switching. These layered film materials are

especially important because the coupling of the remarkable low-loss response of SNO (Asmara, Wan et al. 2017, Wells, Zou et al. 2018) with the Li-ion conduction of LFP, will allow for reduced heat dissipation.

Finally, the goal of this thesis was to engineer defect states within metastable SBO perovskite oxide NPs to control the resulting optoelectronic properties for potential applications in advanced energy storage. Although the ability to modify the structure and composition of the SBO NPs in order to recover their expected optoelectronic properties is demonstrated in Chapter 5, the exact electrochemical performance of these scaffold materials for Li-ion batteries has not been determined. Instead, the EIS results show a distinct reduction in the electrode resistances due to the enhanced charge transport, highlighting the promising electrochemical potential of these nanomaterials. To test the feasibility of these materials, they can be incorporated into a Li-ion battery coin cell assembly as reported (Nie, Ong et al. 2020) and the performance can be subsequently evaluated.

Appendix A. Permission to Use Copyrighted Materials

A.1. Permission to Use Chapter 3 Text and Figures

Royal Society of Chemistry - License Terms and Conditions

This is a License Agreement between Tochukwu Ofoegbuna ("You") and Royal Society of Chemistry ("Publisher") provided by Copyright Clearance Center ("CCC"). The license consists of your order details, the terms and conditions provided by Royal Society of Chemistry, and the CCC terms and conditions.

All payments must be made in full to CCC.

Order Date	29-Jan-2021	Type of Use	Republish in a thesis/dissertation
Order license ID	1093929-1	Publisher	RSC Pub
ISSN	2040-3364	Portion	Chapter/article

LICENSED CONTENT

Publication Title	Nanoscale	Rightsholder	Royal Society of Chemistry
Article Title	Stabilizing the B-site oxidation state in ABO3 perovskite nanoparticles.	Publication Type	Journal
Author/Editor	Guo jia na mi ke xue zhong xin (China), Royal Society of Chemistry (Great Britain)	Start Page	14303
Date	01/01/2009	End Page	14311
Language	English	Issue	30
Country	United Kingdom of Great Britain and Northern Ireland	Volume	11

REQUEST DETAILS

Portion Type	Chapter/article	Rights Requested	Main product and any product related to main product
Page range(s)	14303-14311	Distribution	Worldwide
Total number of pages	9	Translation	Original language of publication
Format (select all that apply)	Print, Electronic	Copies for the disabled?	No
Who will republish the content?	Academic institution	Minor editing privileges?	Yes
Duration of Use	Life of current edition	Incidental promotional use?	Yes
Lifetime Unit Quantity	Up to 499	Currency	USD

NEW WORK DETAILS

Title	DEFECT ENGINEERING IN STRAINED LOW-DIMENSIONAL ABO3 PEROVSKITE NANOPARTICLES FOR NEXT-GENERATION ENERGY STORAGE	Institution name	Louisiana State University
		Expected presentation date	2021-03-02
Instructor name	Tochukwu Ofoegbuna		

ADDITIONAL DETAILS

Order reference number	N/A	The requesting person / organization to appear on the license	Tochukwu Ofoegbuna

REUSE CONTENT DETAILS

Title, description or numeric reference of the portion(s)	Stabilizing the B-site oxidation state in ABO3 perovskite nanoparticles.	Title of the article/chapter the portion is from	Stabilizing the B-site oxidation state in ABO3 perovskite nanoparticles.
Editor of portion(s)	Dorman, James A.; Plaisance, Craig; Sahu, Smriti; Darapaneni, Pragathi; Ofoegbuna, Tochukwu	Author of portion(s)	Dorman, James A.; Plaisance, Craig; Sahu, Smriti; Darapaneni, Pragathi; Ofoegbuna, Tochukwu
Volume of serial or monograph	11	Issue, if republishing an article from a serial	30
Page or page range of portion	14303-14311	Publication date of portion	2018-12-31

PUBLISHER SPECIAL TERMS AND CONDITIONS

Permission is granted as long as the article is fully acknowledged and a link is given back to the article on our Platform. Please go to rsc.li/permissions for details. Please note that if the material specified above or any part of it appears with credit or acknowledgement to a third party then you must also secure permission from that third party before reproducing that material.

CCC Republication Terms and Conditions

1. Description of Service; Defined Terms. This Republication License enables the User to obtain licenses for republication of one or more copyrighted works as described in detail on the relevant Order Confirmation (the "Work(s)"). Copyright Clearance Center, Inc. ("CCC") grants licenses through the Service on behalf of the rightsholder identified on the Order Confirmation (the "Rightsholder"). "Republication", as used herein, generally means the inclusion of a Work, in whole or in part, in a new work or works, also as described on the Order Confirmation. "User", as used herein, means the person or entity making such republication.

2. The terms set forth in the relevant Order Confirmation, and any terms set by the Rightsholder with respect to a particular Work, govern the terms of use of Works in connection with the Service. By using the Service, the person transacting for a republication license on behalf of the User represents and warrants that he/she/it (a) has been duly authorized by the User to accept, and hereby does accept, all such terms and conditions on behalf of User, and (b) shall inform User of all such terms and conditions. In the event such person is a "freelancer" or other third party independent of User and CCC, such party shall be deemed jointly a "User" for purposes of these terms and conditions. In any event, User shall be deemed to have accepted and agreed to all such terms and conditions if User republishes the Work in any fashion.

3. Scope of License; Limitations and Obligations.

   3.1. All Works and all rights therein, including copyright rights, remain the sole and exclusive property of the Rightsholder. The license created by the exchange of an Order Confirmation (and/or any invoice) and payment by User of the full amount set forth on that document includes only those rights expressly set forth in the Order Confirmation and in these terms and conditions, and conveys no other rights in the Work(s) to User. All rights not expressly granted are hereby reserved.

   3.2. General Payment Terms: You may pay by credit card or through an account with us payable at the end of the month. If you and we agree that you may establish a standing account with CCC, then the following terms apply: Remit Payment to: Copyright Clearance Center, 29118 Network Place, Chicago, IL 60673-1291. Payments Due: Invoices are payable upon their delivery to you (or upon our notice to you that they are available to you for downloading). After 30 days, outstanding amounts will be subject to a service charge of 1-1/2% per month or, if less, the maximum rate allowed by applicable law. Unless otherwise specifically set forth in the Order Confirmation or in a separate written agreement signed by CCC, invoices are due and payable on "net 30" terms. While User may exercise the rights licensed immediately upon issuance of the Order Confirmation, the license is automatically revoked and is null and void, as if it had never been issued, if complete payment for the license is not received on a timely basis either from User directly or through a payment agent, such as a credit card company.

   3.3. Unless otherwise provided in the Order Confirmation, any grant of rights to User (i) is "one-time" (including the editions and product family specified in the license), (ii) is non-exclusive and non-transferable and (iii) is subject to any and all limitations and restrictions (such as, but not limited to, limitations on duration of use or circulation) included in the Order Confirmation or invoice and/or in these terms and conditions. Upon completion of the licensed use, User shall either secure a new permission for further use of the Work(s) or immediately cease any new use of the Work(s) and shall render inaccessible (such as by deleting or by removing or severing links or other locators) any further copies of the Work (except for copies printed on paper in accordance with this license and still in User's stock at the end of such period).

   3.4. In the event that the material for which a republication license is sought includes third party materials (such as photographs, illustrations, graphs, inserts and similar materials) which are identified in such material as having been used by permission, User is responsible for identifying, and seeking separate licenses (under this Service or otherwise) for, any of such third party materials; without a separate license, such third party materials may not be used.

   3.5. Use of proper copyright notice for a Work is required as a condition of any license granted under the Service. Unless otherwise provided in the Order Confirmation, a proper copyright notice will read substantially as follows: "Republished with permission of [Rightsholder's name], from [Work's title, author, volume, edition number and year of copyright]; permission conveyed through Copyright Clearance Center, Inc. " Such notice must be provided in a reasonably legible font size and must be placed either immediately adjacent to the Work as used (for example, as part of a by-line or footnote but not as a separate electronic link) or in the place where substantially all other credits or notices for the new work containing the republished Work are located. Failure to include the required notice results in loss to the Rightsholder and CCC, and the User shall be liable to pay liquidated damages for each such failure equal to twice the use fee specified in the Order Confirmation, in addition to the use fee itself and any other fees and charges specified.

3.6. User may only make alterations to the Work if and as expressly set forth in the Order Confirmation. No Work may be used in any way that is defamatory, violates the rights of third parties (including such third parties' rights of copyright, privacy, publicity, or other tangible or intangible property), or is otherwise illegal, sexually explicit or obscene. In addition, User may not conjoin a Work with any other material that may result in damage to the reputation of the Rightsholder. User agrees to inform CCC if it becomes aware of any infringement of any rights in a Work and to cooperate with any reasonable request of CCC or the Rightsholder in connection therewith.

4. Indemnity. User hereby indemnifies and agrees to defend the Rightsholder and CCC, and their respective employees and directors, against all claims, liability, damages, costs and expenses, including legal fees and expenses, arising out of any use of a Work beyond the scope of the rights granted herein, or any use of a Work which has been altered in any unauthorized way by User, including claims of defamation or infringement of rights of copyright, publicity, privacy or other tangible or intangible property.

5. Limitation of Liability. UNDER NO CIRCUMSTANCES WILL CCC OR THE RIGHTSHOLDER BE LIABLE FOR ANY DIRECT, INDIRECT, CONSEQUENTIAL OR INCIDENTAL DAMAGES (INCLUDING WITHOUT LIMITATION DAMAGES FOR LOSS OF BUSINESS PROFITS OR INFORMATION, OR FOR BUSINESS INTERRUPTION) ARISING OUT OF THE USE OR INABILITY TO USE A WORK, EVEN IF ONE OF THEM HAS BEEN ADVISED OF THE POSSIBILITY OF SUCH DAMAGES. In any event, the total liability of the Rightsholder and CCC (including their respective employees and directors) shall not exceed the total amount actually paid by User for this license. User assumes full liability for the actions and omissions of its principals, employees, agents, affiliates, successors and assigns.

6. Limited Warranties. THE WORK(S) AND RIGHT(S) ARE PROVIDED "AS IS". CCC HAS THE RIGHT TO GRANT TO USER THE RIGHTS GRANTED IN THE ORDER CONFIRMATION DOCUMENT. CCC AND THE RIGHTSHOLDER DISCLAIM ALL OTHER WARRANTIES RELATING TO THE WORK(S) AND RIGHT(S), EITHER EXPRESS OR IMPLIED, INCLUDING WITHOUT LIMITATION IMPLIED WARRANTIES OF MERCHANTABILITY OR FITNESS FOR A PARTICULAR PURPOSE. ADDITIONAL RIGHTS MAY BE REQUIRED TO USE ILLUSTRATIONS, GRAPHS, PHOTOGRAPHS, ABSTRACTS, INSERTS OR OTHER PORTIONS OF THE WORK (AS OPPOSED TO THE ENTIRE WORK) IN A MANNER CONTEMPLATED BY USER; USER UNDERSTANDS AND AGREES THAT NEITHER CCC NOR THE RIGHTSHOLDER MAY HAVE SUCH ADDITIONAL RIGHTS TO GRANT.

7. Effect of Breach. Any failure by User to pay any amount when due, or any use by User of a Work beyond the scope of the license set forth in the Order Confirmation and/or these terms and conditions, shall be a material breach of the license created by the Order Confirmation and these terms and conditions. Any breach not cured within 30 days of written notice thereof shall result in immediate termination of such license without further notice. Any unauthorized (but licensable) use of a Work that is terminated immediately upon notice thereof may be liquidated by payment of the Rightsholder's ordinary license price therefor; any unauthorized (and unlicensable) use that is not terminated immediately for any reason (including, for example, because materials containing the Work cannot reasonably be recalled) will be subject to all remedies available at law or in equity, but in no event to a payment of less than three times the Rightsholder's ordinary license price for the most closely analogous licensable use plus Rightsholder's and/or CCC's costs and expenses incurred in collecting such payment.

8. Miscellaneous.

8.1. User acknowledges that CCC may, from time to time, make changes or additions to the Service or to these terms and conditions, and CCC reserves the right to send notice to the User by electronic mail or otherwise for the purposes of notifying User of such changes or additions; provided that any such changes or additions shall not apply to permissions already secured and paid for.

8.2. Use of User-related information collected through the Service is governed by CCC's privacy policy, available online here:https://marketplace.copyright.com/rs-ui-web/mp/privacy-policy

8.3. The licensing transaction described in the Order Confirmation is personal to User. Therefore, User may not assign or transfer to any other person (whether a natural person or an organization of any kind) the license created by the Order Confirmation and these terms and conditions or any rights granted hereunder; provided, however, that User may assign such license in its entirety on written notice to CCC in the event of a transfer of all or substantially all of User's rights in the new material which includes the Work(s) licensed under this Service.

8.4. No amendment or waiver of any terms is binding unless set forth in writing and signed by the parties. The Rightsholder and CCC hereby object to any terms contained in any writing prepared by the User or its principals, employees, agents or affiliates and purporting to govern or otherwise relate to the licensing transaction described in the Order Confirmation, which terms are in any way inconsistent with any terms set forth in the Order Confirmation and/or in these terms and conditions or CCC's standard operating procedures, whether such writing is prepared prior to, simultaneously with or subsequent to the Order Confirmation, and whether such writing appears on a copy of the Order Confirmation or in a separate instrument.

8.5. The licensing transaction described in the Order Confirmation document shall be governed by and construed under the law of the State of New York, USA, without regard to the principles thereof of conflicts of law. Any case, controversy, suit, action, or proceeding arising out of, in connection with, or related to such licensing transaction shall be brought, at CCC's sole discretion, in any federal or state court located in the County of New York, State of New York, USA, or in any federal or state court whose geographical jurisdiction covers the location of the Rightsholder set forth in the Order Confirmation. The parties expressly submit to the personal jurisdiction and venue of each such federal or state court.If you have any comments or questions about the Service or Copyright Clearance Center, please contact us at 978-750-8400 or send an e-mail to support@copyright.com.

A.2. Permission to Use Chapter 4 Text and Figures

Royal Society of Chemistry - License Terms and Conditions

This is a License Agreement between Tochukwu Ofoegbuna ("You") and Royal Society of Chemistry ("Publisher") provided by Copyright Clearance Center ("CCC"). The license consists of your order details, the terms and conditions provided by Royal Society of Chemistry, and the CCC terms and conditions.

All payments must be made in full to CCC.

Order Date	29-Jan-2021	Type of Use	Republish in a thesis/dissertation
Order license ID	1093926-1	Publisher	Royal Society of Chemistry
ISSN	2050-7526	Portion	Chapter/article

LICENSED CONTENT

Publication Title	Journal of materials chemistry. C, Materials for optical and electronic devices	Rightsholder	Royal Society of Chemistry
Article Title	Photoluminescence detection of symmetry transformations in low-dimensional ferroelectric ABO3 perovskites	Publication Type	Journal
		Start Page	10767
		End Page	10773
Author/Editor	Royal Society of Chemistry (Great Britain)	Issue	31
Date	01/01/2012	Volume	8
Language	English		
Country	United Kingdom of Great Britain and Northern Ireland		

REQUEST DETAILS

Portion Type	Chapter/article	Rights Requested	Main product and any product related to main product
Page range(s)	10767-10773	Distribution	Worldwide
Total number of pages	7	Translation	Original language of publication
Format (select all that apply)	Print, Electronic	Copies for the disabled?	No
Who will republish the content?	Academic institution	Minor editing privileges?	Yes
Duration of Use	Life of current edition	Incidental promotional use?	Yes
Lifetime Unit Quantity	Up to 499	Currency	USD

NEW WORK DETAILS

Title	DEFECT ENGINEERING IN STRAINED LOW-DIMENSIONAL ABO3 PEROVSKITE NANOPARTICLES FOR NEXT-GENERATION ENERGY STORAGE	Institution name	Louisiana State University
		Expected presentation date	2021-03-02
Instructor name	Tochukwu Ofoegbuna		

ADDITIONAL DETAILS

Order reference number	N/A	The requesting person / organization to appear on the license	Tochukwu Ofoegbuna

REUSE CONTENT DETAILS

Title, description or numeric reference of the portion(s)	Photoluminescence detection of symmetry transformations in low-dimensional ferroelectric ABO3 perovskites	Title of the article/chapter the portion is from	Photoluminescence detection of symmetry transformations in low-dimensional ferroelectric ABO3 perovskites
Editor of portion(s)	Dorman, James A.; Melvin, Adam T.; Thomson, Stuart A. J.; Kizilkaya, Orhan; Bajgiran, Khashayar R.; Ofoegbuna, Tochukwu	Author of portion(s)	Dorman, James A.; Melvin, Adam T.; Thomson, Stuart A. J.; Kizilkaya, Orhan; Bajgiran, Khashayar R.; Ofoegbuna, Tochukwu
Volume of serial or monograph	8	Issue, if republishing an article from a serial	31
Page or page range of portion	10767-10773	Publication date of portion	2019-12-31

PUBLISHER SPECIAL TERMS AND CONDITIONS

Permission is granted as long as the article is fully acknowledged and a link is given back to the article on our Platform. Please go to rsc.li/permissions for details. Please note that if the material specified above or any part of it appears with credit or acknowledgement to a third party then you must also secure permission from that third party before reproducing that material.

CCC Republication Terms and Conditions

1. Description of Service; Defined Terms. This Republication License enables the User to obtain licenses for republication of one or more copyrighted works as described in detail on the relevant Order Confirmation (the "Work(s)"). Copyright Clearance Center, Inc. ("CCC") grants licenses through the Service on behalf of the rightsholder identified on the Order Confirmation (the "Rightsholder"). "Republication", as used herein, generally means the inclusion of a Work, in whole or in part, in a new work or works, also as described on the Order Confirmation. "User", as used herein, means the person or entity making such republication.

2. The terms set forth in the relevant Order Confirmation, and any terms set by the Rightsholder with respect to a particular Work, govern the terms of use of Works in connection with the Service. By using the Service, the person transacting for a republication license on behalf of the User represents and warrants that he/she/it (a) has been duly authorized by the User to accept, and hereby does accept, all such terms and conditions on behalf of User, and (b) shall inform User of all such terms and conditions. In the event such person is a "freelancer" or other third party independent of User and CCC, such party shall be deemed jointly a "User" for purposes of these terms and conditions. In any event, User shall be deemed to have accepted and agreed to all such terms and conditions if User republishes the Work in any fashion.

3. Scope of License; Limitations and Obligations.

   3.1. All Works and all rights therein, including copyright rights, remain the sole and exclusive property of the Rightsholder. The license created by the exchange of an Order Confirmation (and/or any invoice) and payment by User of the full amount set forth on that document includes only those rights expressly set forth in the Order Confirmation and in these terms and conditions, and conveys no other rights in the Work(s) to User. All rights not expressly granted are hereby reserved.

   3.2. General Payment Terms: You may pay by credit card or through an account with us payable at the end of the month. If you and we agree that you may establish a standing account with CCC, then the following terms apply: Remit Payment to: Copyright Clearance Center, 29118 Network Place, Chicago, IL 60673-1291. Payments Due: Invoices are payable upon their delivery to you (or upon our notice to you that they are available to you for downloading). After 30 days, outstanding amounts will be subject to a service charge of 1-1/2% per month or, if less, the maximum rate allowed by applicable law. Unless otherwise specifically set forth in the Order Confirmation or in a separate written agreement signed by CCC, invoices are due and payable on "net 30" terms. While User may exercise the rights licensed immediately upon issuance of the Order Confirmation, the license is automatically revoked and is null and void, as if it had never been issued, if complete payment for the license is not received on a timely basis either from User directly or through a payment agent, such as a credit card company.

   3.3. Unless otherwise provided in the Order Confirmation, any grant of rights to User (i) is "one-time" (including the editions and product family specified in the license), (ii) is non-exclusive and non-transferable and (iii) is subject to any and all limitations and restrictions (such as, but not limited to, limitations on duration of use or circulation) included in the Order Confirmation or invoice and/or in these terms and conditions. Upon completion of the licensed use, User shall either secure a new permission for further use of the Work(s) or immediately cease any new use of the Work(s) and shall render inaccessible (such as by deleting or by removing or severing links or other locators) any further copies of the Work (except for copies printed on paper in accordance with this license and still in User's stock at the end of such period).

   3.4. In the event that the material for which a republication license is sought includes third party materials (such as photographs, illustrations, graphs, inserts and similar materials) which are identified in such material as having been used by permission, User is responsible for identifying, and seeking separate licenses (under this Service or otherwise) for, any of such third party materials; without a separate license, such third party materials may not be used.

   3.5. Use of proper copyright notice for a Work is required as a condition of any license granted under the Service. Unless otherwise provided in the Order Confirmation, a proper copyright notice will read substantially as follows: "Republished with permission of [Rightsholder's name], from [Work's title, author, volume, edition number and year of copyright]; permission conveyed through Copyright Clearance Center, Inc. " Such notice must be provided in a reasonably legible font size and must be placed either immediately adjacent to the Work as used (for example, as part of a by-line or footnote but not as a separate electronic link) or in the place where substantially all other credits or notices for the new work containing the republished Work are located. Failure to include the required notice results in loss to the Rightsholder and CCC, and the User shall be liable to pay liquidated damages for each such failure equal to twice the use fee specified in the Order Confirmation, in addition to the use fee itself and any other fees and charges specified.

3.6. User may only make alterations to the Work if and as expressly set forth in the Order Confirmation. No Work may be used in any way that is defamatory, violates the rights of third parties (including such third parties' rights of copyright, privacy, publicity, or other tangible or intangible property), or is otherwise illegal, sexually explicit or obscene. In addition, User may not conjoin a Work with any other material that may result in damage to the reputation of the Rightsholder. User agrees to inform CCC if it becomes aware of any infringement of any rights in a Work and to cooperate with any reasonable request of CCC or the Rightsholder in connection therewith.

4. Indemnity. User hereby indemnifies and agrees to defend the Rightsholder and CCC, and their respective employees and directors, against all claims, liability, damages, costs and expenses, including legal fees and expenses, arising out of any use of a Work beyond the scope of the rights granted herein, or any use of a Work which has been altered in any unauthorized way by User, including claims of defamation or infringement of rights of copyright, publicity, privacy or other tangible or intangible property.

5. Limitation of Liability. UNDER NO CIRCUMSTANCES WILL CCC OR THE RIGHTSHOLDER BE LIABLE FOR ANY DIRECT, INDIRECT, CONSEQUENTIAL OR INCIDENTAL DAMAGES (INCLUDING WITHOUT LIMITATION DAMAGES FOR LOSS OF BUSINESS PROFITS OR INFORMATION, OR FOR BUSINESS INTERRUPTION) ARISING OUT OF THE USE OR INABILITY TO USE A WORK, EVEN IF ONE OF THEM HAS BEEN ADVISED OF THE POSSIBILITY OF SUCH DAMAGES. In any event, the total liability of the Rightsholder and CCC (including their respective employees and directors) shall not exceed the total amount actually paid by User for this license. User assumes full liability for the actions and omissions of its principals, employees, agents, affiliates, successors and assigns.

6. Limited Warranties. THE WORK(S) AND RIGHT(S) ARE PROVIDED "AS IS". CCC HAS THE RIGHT TO GRANT TO USER THE RIGHTS GRANTED IN THE ORDER CONFIRMATION DOCUMENT. CCC AND THE RIGHTSHOLDER DISCLAIM ALL OTHER WARRANTIES RELATING TO THE WORK(S) AND RIGHT(S), EITHER EXPRESS OR IMPLIED, INCLUDING WITHOUT LIMITATION IMPLIED WARRANTIES OF MERCHANTABILITY OR FITNESS FOR A PARTICULAR PURPOSE. ADDITIONAL RIGHTS MAY BE REQUIRED TO USE ILLUSTRATIONS, GRAPHS, PHOTOGRAPHS, ABSTRACTS, INSERTS OR OTHER PORTIONS OF THE WORK (AS OPPOSED TO THE ENTIRE WORK) IN A MANNER CONTEMPLATED BY USER; USER UNDERSTANDS AND AGREES THAT NEITHER CCC NOR THE RIGHTSHOLDER MAY HAVE SUCH ADDITIONAL RIGHTS TO GRANT.

7. Effect of Breach. Any failure by User to pay any amount when due, or any use by User of a Work beyond the scope of the license set forth in the Order Confirmation and/or these terms and conditions, shall be a material breach of the license created by the Order Confirmation and these terms and conditions. Any breach not cured within 30 days of written notice thereof shall result in immediate termination of such license without further notice. Any unauthorized (but licensable) use of a Work that is terminated immediately upon notice thereof may be liquidated by payment of the Rightsholder's ordinary license price therefor; any unauthorized (and unlicensable) use that is not terminated immediately for any reason (including, for example, because materials containing the Work cannot reasonably be recalled) will be subject to all remedies available at law or in equity, but in no event to a payment of less than three times the Rightsholder's ordinary license price for the most closely analogous licensable use plus Rightsholder's and/or CCC's costs and expenses incurred in collecting such payment.

8. Miscellaneous.

8.1. User acknowledges that CCC may, from time to time, make changes or additions to the Service or to these terms and conditions, and CCC reserves the right to send notice to the User by electronic mail or otherwise for the purposes of notifying User of such changes or additions; provided that any such changes or additions shall not apply to permissions already secured and paid for.

8.2. Use of User-related information collected through the Service is governed by CCC's privacy policy, available online here:https://marketplace.copyright.com/rs-ui-web/mp/privacy-policy

8.3. The licensing transaction described in the Order Confirmation is personal to User. Therefore, User may not assign or transfer to any other person (whether a natural person or an organization of any kind) the license created by the Order Confirmation and these terms and conditions or any rights granted hereunder; provided, however, that User may assign such license in its entirety on written notice to CCC in the event of a transfer of all or substantially all of User's rights in the new material which includes the Work(s) licensed under this Service.

8.4. No amendment or waiver of any terms is binding unless set forth in writing and signed by the parties. The Rightsholder and CCC hereby object to any terms contained in any writing prepared by the User or its principals, employees, agents or affiliates and purporting to govern or otherwise relate to the licensing transaction described in the Order Confirmation, which terms are in any way inconsistent with any terms set forth in the Order Confirmation and/or in these terms and conditions or CCC's standard operating procedures, whether such writing is prepared prior to, simultaneously with or subsequent to the Order Confirmation, and whether such writing appears on a copy of the Order Confirmation or in a separate instrument.

8.5. The licensing transaction described in the Order Confirmation document shall be governed by and construed under the law of the State of New York, USA, without regard to the principles thereof of conflicts of law. Any case, controversy, suit, action, or proceeding arising out of, in connection with, or related to such licensing transaction shall be brought, at CCC's sole discretion, in any federal or state court located in the County of New York, State of New York, USA, or in any federal or state court whose geographical jurisdiction covers the location of the Rightsholder set forth in the Order Confirmation. The parties expressly submit to the personal jurisdiction and venue of each such federal or state court.If you have any comments or questions about the Service or Copyright Clearance Center, please contact us at 978-750-8400 or send an e-mail to support@copyright.com.

Appendix B. Thin-film/Bulk Electronic Resistivities

B = Nb

D. Y. Wan, Y. L. Zhao, Y. Cai, T. C. Asmara, Z. Huang, J. Q. Chen, J. Hong, S. M. Yin, C. T. Nelson, M. R. Motapothula, and B. X. Yan, *Nature Communications*, 2017, 8(1), 1-9

B = Mo

I. Nagai, N. Shirakawa, S. I. Ikeda, R. Iwasaki, H. Nishimura, and M. Kosaka, *Applied Physics Letters*, 2005, 87(2), 024105

H. H. Wang, D. F. Cui, Y. L. Zhou, Z. H. Chen, F. Chen, T. Zhao, H. B. Lu, G. Z. Yang, M. C. Xu, Y. C. Lan, and X.L. Chen, *Journal of Crystal Growth*, 2001, 226(2-3), 261-266

B = Ti

L. Zhang, Y. Wang, and R. Engel-Herbert, *Journal of Applied Physics*, 2016, 119(4), 045301

B = Ru

Y. J. Chang, J. I. Kim, and C. U. Jung, *Journal of Magnetics*, 2008, 13(2), 61-64

B = Fe

E. Enriquez, A. Chen, Z. Harrell, X. Lü, P. Dowden, N. Koskelo, M. Janoschek, C. Chen, and Q. Jia, *Applied Physics Letters*, 2016, 109(14), 141906

B = V

A. Boileau, A. Cheikh, A. Fouchet, A. David, R. Escobar-Galindo, C. Labbé, P. Marie, F. Gourbilleau, and U. Lüders, *Applied Physics Letters*, 2018, 112(2), 021905

B = Zr

J. A. Labrincha, J. R. Frade, and F. M. B. Marques, *Solid State Ionics*, 1993, 61(1-3), 71-75

B = Hf

V. Hien-Hoang, T. M. Nhung-Nguyen, and H. J. Kim, *Current Applied Physics*, 2020, 20(9), 1031-1035

B = Ir

A. Biswas, K. S. Kim, and Y. H. Jeong, *Journal of Applied Physics*, 2014, 116(21), 213704

B = Co

A. Aguadero, D. Pérez-Coll, J. A. Alonso, S. J. Skinner, and J. Kilner, *Chemistry of Materials*, 2012, 24(14), 2655-2663.

B = Rh

J. Nichols, S. F. Yuk, C. Sohn, H. Jeen, J. W. Freeland, V. R. Cooper, and H. N. Lee, *Physical Review B*, 2017, 95(24), 245121

B = Cr

K. H. L. Zhang, P. V. Sushko, R. Colby, Y. Du, M. E. Bowden, and S. A. Chambers, *Nature Communications*, 2014, 5(1), 1-7

Appendix C. Chemicals and MSDS

C.1. Chemicals Used

Strontium Nitrate ($Sr(NO_3)_2$, Alfa Aesar, 99.0%, ACS grade)

Calcium Nitrate ($Ca(NO_3)_2$-H_2O, Beantown Chemical, 99.9995% trace metals basis)

Europium Hexahydrate ($Eu(NO_3)_2$-$6H_2O$, Alfa Aesar, 99.99% REO)

Barium Nitrate ($BaNO_3$, Alfa Aesar, 99+%, ACS grade)

Lead (II) Nitrate ($Pb(NO_3)_2$, Acros Organics, 99.999% trace metals basis)

Lithium Nitrate ($LiNO_3$, Sigma Aldrich)

Lithium Hydroxide (LiOH, Sigma Aldrich, >98%)

Iron(II) Sulfate Heptahydrate ($FeSO_4$-$7H_2O$, Sigma Aldrich, >99%)

Niobium (V) Chloride ($NbCl_5$, Alfa Aesar, 99.0% metals basis)

Ammonium Molybdate ($(NH_4)_6Mo_7O_{24}.4H_2O$, Sigma Aldrich)

Tantalum Chloride ($TaCl_5$, Alfa Aesar, 99.99% metals basis)

Ammonium hydroxide (NH_4OH, 28-30%, ACS grade)

Titanium (IV) isopropoxide (TTIP, Acros Organics, 98%)

Sodium nitrate ($NaNO_3$, high purity grade, VWR Amresco, 99.0%)

Potassium nitrate (KNO_3, ACS grade, VWR Amresco)

Sodium Thiosulfate ($Na_2S_2O_3$, Spectrum Chemical Mfg. Corp., anhydrous ≥ 97%)

Potassium Iodide (KI, VWR BDH Chemicals, ACS)

Hydrogen Peroxide (H_2O_2, VWR BDH Chemicals, 3%)

Hydrochloric acid (HCl, VWR BDH Chemicals, 36-38.5%, ACS grade)

Sulfuric Acid (H_2SO_4, Sigma Aldrich, 95 - 98% , ACS grade)

Nitric Acid (HNO_3, MiliporeSigma, 65%)

Ethylene Glycol ($(CH_2OH)_2$, Koptec)

C.2. Safety Notes on Chemicals (NFPA Scale)

$Sr(NO_3)_2$: Health (acute effects) = 2, Flammability = 0, Reactivity = 0. See MSDS for details

$Ca(NO_3)_2$-H_2O: Health (acute effects) = 2, Flammability = 0, Reactivity = 1. See MSDS for details

$Eu(NO_3)_2$-$6H_2O$: Health (acute effects) = 2, Flammability = 3, Reactivity = 3. See MSDS for details

$BaNO_3$: Health (acute effects) = 2, Flammability = 1, Reactivity = 1. See MSDS for details

$Pb(NO_3)_2$: Health (acute effects) = 3, Flammability = 0, Reactivity = 3. See MSDS for details

$LiNO_3$: Health (acute effects) = 2, Flammability = 1, Reactivity = 1. See MSDS for details

LiOH: Health (acute effects) = 3, Flammability = 0, Reactivity = 0. See MSDS for details

$FeSO_4$-$7H_2O$: Health (acute effects) = 2, Flammability = 1, Reactivity = 1. See MSDS for details

$NbCl_5$: Health (acute effects) = 3, Flammability = 0, Reactivity = 1. See MSDS for details

$(NH_4)_6Mo_7O_{24}.4H_2O$: Health (acute effects) = 2, Flammability = 1, Reactivity = 0. See MSDS for details

$TaCl_5$: Health (acute effects) = 3, Flammability = 0, Reactivity = 0. See MSDS for details

NH_4OH: Health (acute effects) = 3, Flammability = 0, Reactivity = 0. See MSDS for details

TTIP: Health (acute effects) = 2, Flammability = 1, Reactivity = 1. See MSDS for details

$NaNO_3$: Health (acute effects) = 2, Flammability = 1, Reactivity = 3. See MSDS for details

KNO_3: Health (acute effects) = 1, Flammability = 0, Reactivity = 2. See MSDS for details

$Na_2S_2O_3$: Health (acute effects) = 1, Flammability = 0, Reactivity = 0. See MSDS for details

KI: Health (acute effects) = 1, Flammability = 0, Reactivity = 0. See MSDS for details

H_2O_2: Health (acute effects) = 2, Flammability = 0, Reactivity = 0. See MSDS for details

HCl: Health (acute effects) = 3, Flammability = 0, Reactivity = 1. See MSDS for details

H_2SO_4: Health (acute effects) = 3, Flammability = 0, Reactivity = 2. See MSDS for details

HNO_3: Health (acute effects) = 4, Flammability = 0, Reactivity = 0. See MSDS for details

$(CH_2OH)_2$: Health (acute effects) = 2, Flammability = 1, Reactivity = 1. See MSDS for details

Appendix D. Chemical Synthesis

D.1. Co-precipitation/Oxygen-controlled MSS of SBO Nanoparticles

1. For the synthesis of SNO (Sr/Nb = 1.3) NPs, 343.9 mg (1.625 mmol) of $Sr(NO_3)_2$ and 337.7 mg (1.25 mmol) of $NbCl_5$ were added to a 200 mL of deionized water in a beaker
2. Next, NH_4OH was added to the solution until the pH was 9.5
3. This mixture was stirred for 2 h and the precipitate was filtered
4. After 2 h, the precipitate is allowed to dry over night at 80 ℃ in an oven
5. The dried precipitate is mixed with 255.2 mg of $NaNO_3$ and 304.1 mg of KNO_3
6. The mixture is placed into a pistol and mortar and mixed until homogeneous
7. The mixture was placed into a 10 mL ceramic boat and sealed with a 7 mL ceramic boat
8. Next, the mixture was vacuumed until either the pressure was 0.2 Torr or, alternatively, the tube furnace is purged with a gas (H_2/Ar, N_2, etc.) for 15 min
9. The reactant mixture was then heated to 600 ºC for 2 h under the oxygen-deficient atmosphere
10. After cooled, the fittings were removed, and the ceramic boat was recovered
11. When the temperature of the ceramic boat reached room-temperature, deionized water was added to the product mixture
12. This reaction mixture was then transferred to centrifuge tubes and was centrifuged at 8000 rpm for 15-20 min
13. This process of washing the NPs was repeated several times and the final powder was dried overnight at 80 ℃
14. For the synthesis of other SBO (B = Ta/Mo) NPs, the Sr/B-site ratio was also fixed to 1.3 and the pH was adjusted accordingly to drive their precipitation.

D.2. H_2/Ar Post-Treatment of SBO Nanoparticles

1. The prepared powders (white) were placed into a ceramic boat (size: 7 mL) and placed into the 1-inch quartz tube
2. The correct-sized fitting seals were placed onto the quartz tube
3. Subsequently, the H_2/Ar gas was purged through the tube furnace for 15 min
4. The furnace was then heated to 800 ℃ at various times (0.5, 4, and 6 h)
5. Afterwards, the tube furnace was allowed to cool to room-temperature under the flowing H_2/Ar gas
6. After cooled, the fittings were removed, and the ceramic boat was recovered

D.3. Coating of the $LiFePO_4$ Top Layer onto the SBO Internal Layer

1. First, pellets of the SBO NPs were prepared by taking ~100 mg of the as-synthesized powders and loading them into a pellet die

2. A force of 3 tons was applied to the powders for 30 min
3. The pellets were transferred into ceramic boats and loaded into the 1-inch quartz tube
7. Using the same conditions as Section C.2, specifically, N_2 as the gas atmosphere, 800 ℃ as the temperature, and 8 h as the densification time
8. After the densification process, the electronic properties of the SBO pellets were recovered by following the treatment procedure outlined in Section D.2.
9. Finally, a slurry containing a mixture of $LiFePO_4$, PVDF, and activated carbon was spray coated over the SBO pellet
10. The new layer is dried overnight at 80 ℃

Appendix E. Rietveld Refinement Details

Rietveld refinement was performed on the resultant diffraction pattern using the GSAS II software (Larsson and Von Dreele 1994) for phase quantification and identification. In this approach, a non-linear least squares algorithm is utilized to minimize the residual function (WSS) (Lutterotti 2006).

$$WSS = \sum_i \frac{\left(I_i^{exp} - I_i^{calc}\right)^2}{I_i^{exp}} \quad \text{(C.1.1)}$$

where I_i^{exp} and I_i^{calc} are associated with the measured and calculated intensities of the diffraction pattern. The first term is extracted from X-ray diffraction (XRD) measurements and the second term is described based on the following expression:

$$I_i^{calc} = S_F \sum_{j=1}^{N\ phases} \frac{f_j}{V_j^2} \sum_{k=1}^{N\ peaks} L_k \left|F_{k,j}\right|^2 S_j\left(2\theta_i - 2\theta_{k,j}\right) P_{k,j} A_j + bkg_i \quad \text{(C.1.2)}$$

The calculated spectrum uses a polynomial function in terms of the bragg angle, 2θ:

$$bkg(2\theta_i) = \sum_{n=0}^{N_b} a_n (2\theta_i)^n \quad \text{(C.1.3)}$$

where N_b and a_n are the polynomial degree and coefficients.

A scale factor (S_j) is incorporated into the spectrum, described as the following:

$$S_j = S_F \frac{f_j}{V_j^2} \quad \text{(C.1.4)}$$

where S_F, f_j, and V_j are associated with the beam intensity, phase volume fraction, and phase cell volume, respectively.

The calculated spectrum also depends on the Lorentz-polarization factor (L_k) and Generalized structure factor ($|F_{k,j}|^2$):

$$\left|F_{k,j}\right|^2 = m_k \left| \sum_{n=1}^{N} f_n e^{-B_n \frac{(\sin\theta)^2}{\lambda^2}} \left(e^{2\pi i (hx_n + ky_n + lz_n)} \right) \right|^2 \quad \text{(C.1.5)}$$

where N is the number of atoms, x_n,y_n,z_n is the coordinates of the nth atom, f_n is the atomic scattering factor, m_k is the multiplicity of the k reflections (with h, k, l miller indices), and B_n is a temperature factor (Debye-Waller).

The absorption factor (A_j) for a Bragg-Brentano set-up is described as followed:

$$A_j = \frac{1}{2\mu} \quad \text{(C.1.6)}$$

where μ is the linear absorption coefficient of the sample.

The texture (or preferred orientations, $P_{k,j}$), described using the March-Dollase formula, is presented below:

$$P_{k,j} = \frac{1}{m_k} \sum_{n=1}^{m_k} \left(P_{MD}^2 (\cos\alpha_n)^2 + \frac{(\sin\alpha_n)^2}{P_{MD}} \right)^{-3/2} \quad \text{(C.1.7)}$$

where P_{MD} is the March-Dollase parameter, α_n is the angle between the preferred orientation vector and the crystallographic plane hkl (in the crystallographic cell coordinate system).

Next, the profile shape functions ($S_j(2\theta_i\text{-}2\theta_{k,j})$) can be described as Gaussian, Cauchy, Voigt and Pseudo-Voigt, etc. For example, for a Pseudo-Voigt type profile shape, S_j = PV and the equation can be depicted as followed:

$$PV(2\theta_i - 2\theta_k) = I_n \left[\eta_k \left(\frac{1}{1 + S_{i,k}^2} \right) + (1 - \eta_k) e^{-S_{i,k}^2 \ln(2)} \right] \quad \text{(C.1.8)}$$

$$S_{i,k} = \frac{2\theta_i - 2\theta_k}{\omega_k} \quad \text{(C.1.9)}$$

$$\omega^2 = W + V\tan\theta + U(\tan\theta)^2 \quad \text{(C.1.10)}$$

$$\eta = \sum_{n=0}^{N_g} c_n (2\theta)^n \quad \text{(C.1.11)}$$

The details regarding the expression for other profile shape functions are provided elsewhere (Young and Wiles 1982). Overall, these parameters are optimized via the refinement of structural parameters (histogram scale factor, atomic coordinates, and isotropic atomic displacement parameter), cell parameters, peak shape parameters (Cagliotti parameters, sample displacement, phase fraction, size, and microstrain), and background parameters (10-coefficient log interpolate polynomial) in the GSAS II software (Rietveld 1969, Neiner, Okamoto et al. 2009). Finally, the quality of the fits was determined using three statistical parameters (R_p, residual of least-squares refinement; R_{wp}, weighted residual; χ^2, goodness of fit).

$$R_p = \frac{\sum |y_{io} - y_{ic}|}{\sum y_{io}} \quad \text{(C.1.12)}$$

$$R_{wp} = \left[\frac{\sum w_i (y_{io} - y_{ic})^2}{\sum w_i y_{io}^2}\right]^{1/2} \quad \text{(C.1.13)}$$

$$\chi^2 = \left[\frac{R_{wp}}{R_{exp}}\right]^2 \quad \text{(C.1.14)}$$

where R_p quantifies the difference between the observe and the calculated data point, R_{wp} weights the residual so that higher intensity data points are more important than low intensity data points (fitting the diffraction peaks is more important than fitting the background), and χ^2 compares the calculated and experimental data.

Appendix F. Rietveld Refinement Procedure

Below is a detailed procedure for performing structural refinement of XRD Data extracted on a Panalytical X-ray Diffractometer using the GSAS II software. It is important to keep in mind adaptions to this procedure may be needed depending on the type of crystal structure as well as the number of phases present. First single phase and then multi-phase refinement will be demonstrated.

F.1. Single Phase Refinement

1. The executable file to download and install the GSAS II software on Windows can be found at this link: https://subversion.xray.aps.anl.gov/trac/pyGSAS/wiki/InstallWindows
2. Import the SAMPLE_NAME.RAW (diffraction data file) and the INST_XRY.PRM (instrument parameter file). The .RAW file can be generated during the step to convert the acquired XRD data using the HighScore software (refer to the guidelines on using the XRD). The .PRM file is available at https://subversion.xray.aps.anl.gov/pyGSAS/Tutorials/LabData/data/ and no further modification is needed to be made prior to downloading the file.
3. Import the phase data using the .CIF file or manually add the phase data. CIF files can be downloaded from online databases (i.e. CODS, Materials project, etc.) or from a quick google searching.
4. Select import on the upper row of the GUI, then select phase, and choose from CIF file
5. From there you will be prompted to select the CIF file for the phase and it will ask you to connect the phase to the measured data.
6. When the information is inputted correctly the screen should look like Figure F.1.1, where the measured diffraction is visible in one of the GUI and in the other a phase tab is visible. In the data table, the .RAW file is visible.

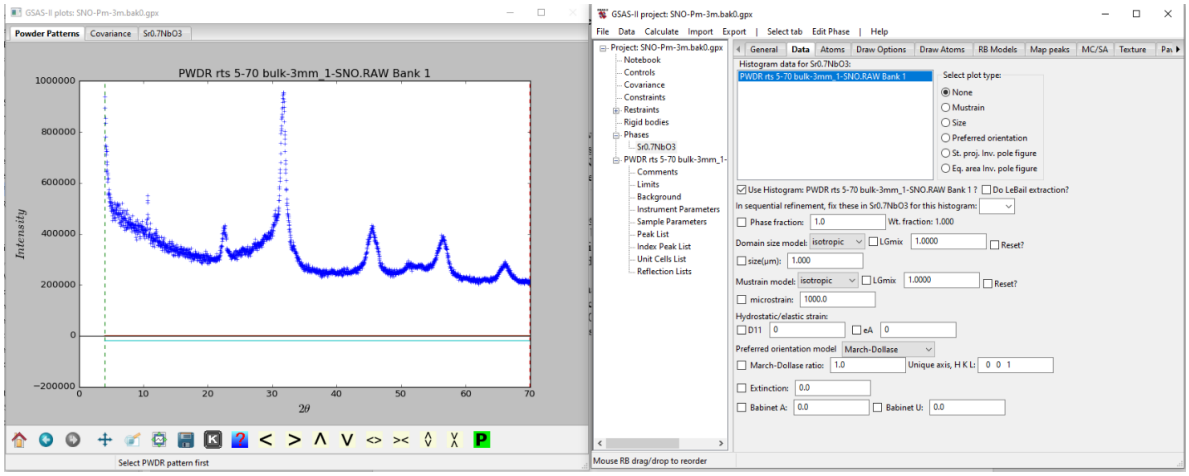

Figure F.1.1 First refinement using the crystallographic and background information.

7. To manually input the phase data, the expected space group, unit cell, and atomic positions must be specified, which can be found from experimental databases (i.e. ICDD, JCPDS, etc.).
8. Go to the data tab and select add new phase. The phase should be named accordingly.
9. After the phase is created, connect the powder data to the phase by performing the following procedure: select the data tab on the lower row, click on edit phase on the upper row, and click add powder histogram. This will create a screen similar to Figure F.1.2, where the powder data can be selected.

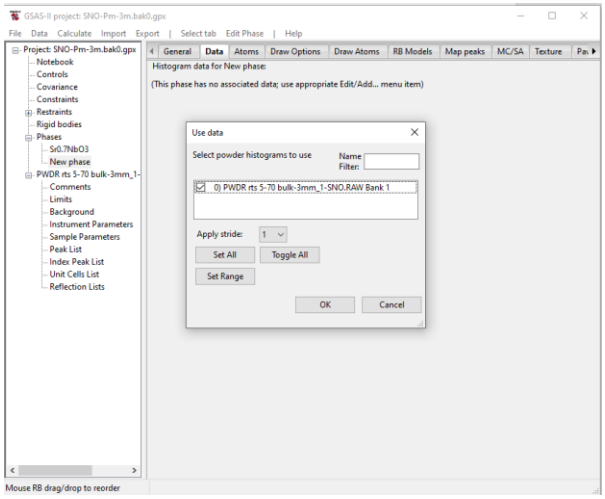

Figure F.1.2 Adding new phase and connecting it to the measured data.

10. Next, select the general tab and input the crystallographic information for the new phase (i.e. space group and lattice parameters).
11. After putting the information, select the atoms tab on the lower row, select edit atoms on the upper tab, and select append atom. This will allow you to create atoms.
12. Append the same number of number of atoms provided by the reference. For example, for Pm-3m $Sr_{0.7}NbO_3$, there are 3 atoms.
13. Once the atoms are created they are defaulted as H. To change them to other elements, double click on the H and a periodic table will appear.
14. Next, the coordinates (x, y, z), site fraction, and isotropic displacement parameter are changed in the same fashion to satisfy the reference file or ICP-OES data.
15. Figure F.1.3 shows a completed atoms tab for $Sr_{0.7}NbO_3$.

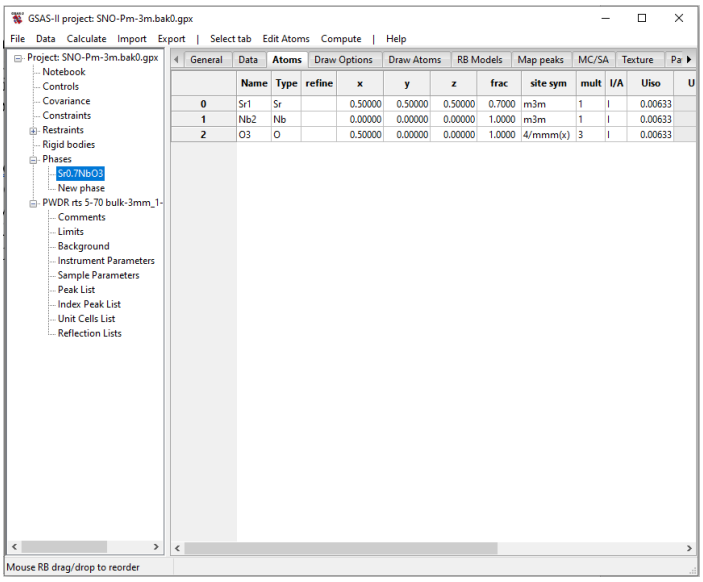

Figure F.1.3 Completed Atoms Tab for Adding a New Phase

16. Steps 5-13 are in the case where the phase needs to be manually inputted. If that is not the case, then proceed to step 15.
17. Click on Background located on the left and under the PWDR rts 5-70 bulk…. Section. Set it to a 10-coefficient log-interpolate. Press calculate on the upper row and then refine.
18. Figure F.1.4 shows the first refinement based on crystallographic information and background information.

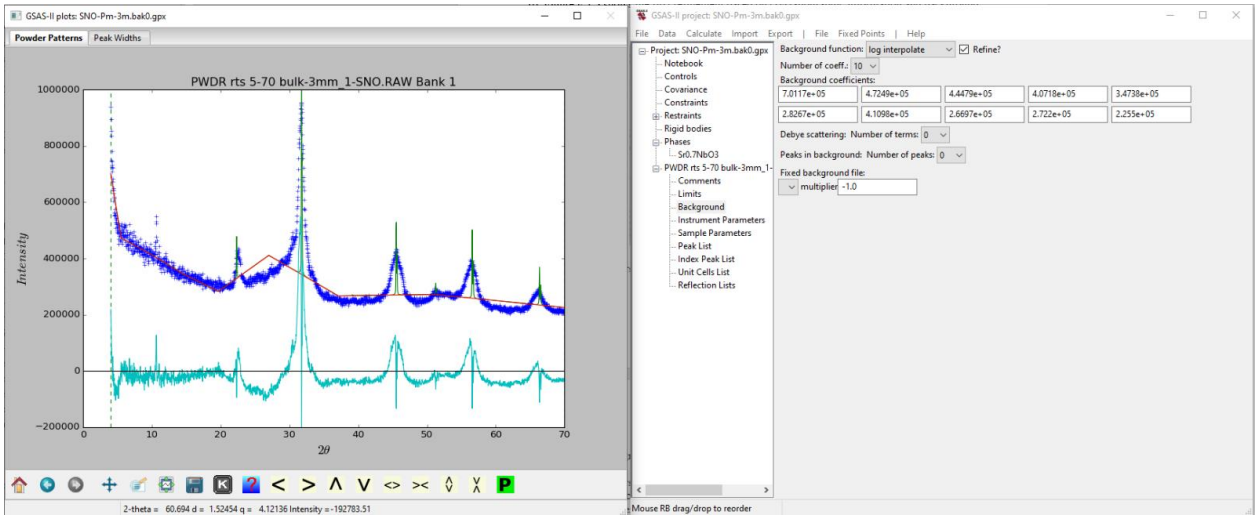

Figure F.1.4 First refinement is the background.

19. Go to the sample parameter tab on the left under the PWDR rts 5-70 bulk…. Section.
20. Adjust the histogram scale factor to increase or decrease the intensity of the calculated spectrum.
21. At this point, the calculated peaks should have larger intensity than the measured data, as seen in Figure F.1.4. If that is not the case, then increase the histogram scale factor, and press refine once more.
22. Next, click on the sample phase, and in the general tab, refine the unit cell. This is done by checking the box next to the unit cell, click calculate, and then refine. Keep the box checked for the remainder of the procedure.
23. For the background and histogram scale factor the refine box was already checked. However, in the following steps, checking the refine box, pressing calculate, and then refine will be referred to as “refining”.
24. Within the data tab, refine the size.
25. Refine phase fraction, however, not necessary for single phase.
26. Refine microstrain, which is also in the same tab.
27. At this point, the calculated and measured spectra should start to match each other, as seen in Figure F.1.5.

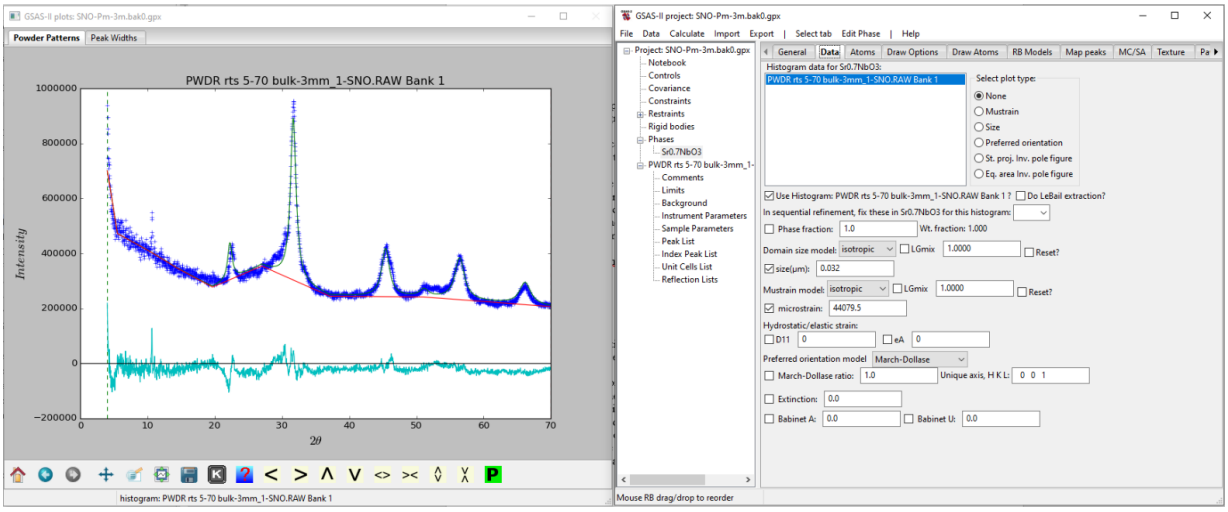

Figure F.1.4 Refinement of the background, histogram scale factor, lattice parameter, size, and microstrain.

28. In the sample parameter tab under the PWDR rts 5-70 bulk…. Section, refine the displacement parameter
29. In the instrument parameter tab under the PWDR rts 5-70 bulk…. Section, refine, the parameters U,V, and W. Each parameter should be refined individually.
30. At this point, a better fit should be observed. Minimized error (green plot).
31. Refine atomic coordinates (x, y, x) to correct for peak intensity. This is done by clicking on the “refine” tab next to “type” and selecting X-coordinate.

32. In addition to refining the atomic coordinates, refine isotropic displacement parameter/thermal parameter (Uiso). This is done by clicking on refine and selecting X-coordinate and U-thermal parameters.
33. Note: the site fraction (F) can be refined in the same way and must be done after refining the X-coordinate. It is not preferred to refine the site fraction. In certain instances, it is better to leave the F fixed to avoid uncontrolled fitting.
34. Figure F.1.5 shows the final refined diffraction.
35. Check that the Uiso is positive and that the lattice parameters are reasonable.

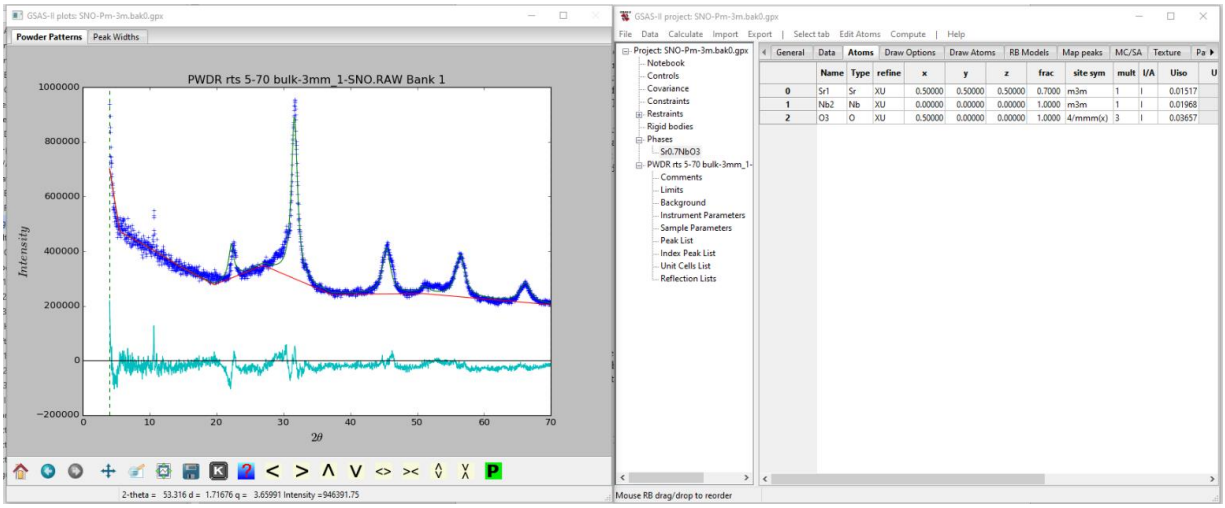

Figure F.1.5 Final refined diffraction pattern

36. Finally, check the quality of the fit by confirming that both statistical (R_p, R_{wp} and $\chi^2 < 10$) and visual results agree with the measured spectrum.
37. If the refinement passes the check, export CIF file by selecting the export tab in the upper row, choosing entire project as, and Full CIF
38. Export calculated curve and difference curve by selecting the export tab in the upper row, choosing powder data as, and CSV file
39. If the refinement does not pass the checks, open one of the backup files (filename.bak0.gpx) and restart the refinement procedure.
40. Additionally, throughout the refinement process create multiple copies of the file before pressing refine in case the refinement becomes unstable.

F.2. Multiple Phase Refinement

1. Repeat steps 1-6 for single phase refinement to import the other phases from .CIF files
2. Repeats steps 5-13 for single phase refinement to add the other phases manually.
3. Refine the background.

4. Since there are multiple phases, we will have to distinguish refine “individually” and “together”. Refine individually means to check the box for one phase parameter (lattice parameter, size, microstrain, etc.) for one of the phases and got to the calculate and press refine. Refine together means to chck the box for one phase parameter for one phase and select the same parameter for the other phases. Then got to the calculate tab and press refine.
5. With this distinction made, refine the lattice parameter for each phase individually.
6. Next, refine the size for each phase individually.
7. Refine the phase fraction for each phase together.
8. Refine the microstrain for each phase together
9. Repeat steps 28-30 for single phase refinement
10. Refine the atomic coordinates for each phase together.
11. Refine the Uiso for each phase together
12. Check that the Uiso is positive and that the lattice parameters are reasonable.
13. At this point the refinement should converge (refer to step 36 for single phase refinement for convergence conditions).
14. Repeat steps 37-40 for single phase refinement

Additional information can be found using the following sources:

1. Online tutorial videos with interactive examples (exercise files are also made available) by Argonne National Laboratory (https://subversion.xray.aps.anl.gov/pyGSAS/trunk/help/Tutorials.html)
2. Online powerpoint lectures by Scott A. Speakman (MIT), Frank Girgsdies (Fritz-Haber-Institut der Max-Planck-Gesellschaft), and Brian H. Toby (Argonne National Laboratory)
3. Rietveld Refinement Guidelines (J. Appl. Cryst., 1999, 32, 36-50)

Appendix G. Operating Procedures

G.1. Tube Furnace

G.1.1. Heating using the Tube Furnace

1. The vacuum chamber has an inlet pump which is not connected to the chamber but an extension through which the samples can be taken out or placed inside without disturbing the vacuum inside the chamber
2. Thoroughly inspect tube for cracks (i.e. star crack, etc.) before use. If a crack is spotted put the tube into a box and properly label the box for disposal.
3. Place sample into a crucible boat and slide sample/crucible set to the center of the tube.
4. Place alumina foam insulation blocks into the tube so only half of the block is visible
5. Turn the power switch ON (green button)
6. Adjust the temperature using the up/down arrows. The tube furnace uses a fixed ramp rate to reach the set point temperature.

G.1.2. Heating under Vacuum Atmosphere using the Tube Furnace

1. The vacuum chamber has an inlet pump which is not connected to the chamber but an extension through which the samples can be taken out or placed inside without disturbing the vacuum inside the chamber
2. Thoroughly inspect tube for cracks before use.
3. Follow steps 1-3 for placing sample into the tube furnace
4. Place vacuum attachments (O-ring and stainless-steel clamps) onto the tube and screw them securely in place
5. Check to make sure the valve for the oven is closed and the valve for the tube furnace is open.
6. Connect the pump to the power and let warm up for 1-2 min
7. Open the valve (directly on top of the vacuum pump) to start pulling air out of the tube furnace. Keep the valve open until the pressure reaches 1 torr.
8. Close the valve to tighten/check the vacuum connections
9. Open the valve a second time to pump down to the pressure of interest.
10. Once the pressure is reached begin the heating step by following steps 4-5
11. After the experiment is completed, open the valve on the tube to let air into the tube furnace. This will cause the pressure to increase.
12. Once the pressure reaches atmospheric conditions (760 torr), close the vacuum pump valve and unplug the pump.
13. Unscrew the vacuum attachments to remove the sample

G.1.3. Oven with Vacuum Connections

1. The vacuum chamber has an inlet pump which is not connected to the chamber but an extension through which the samples can be taken out or placed inside without disturbing the vacuum inside the chamber
2. Open vacuum oven and place sample, then close vacuum oven

3. Once the sample is placed, follow steps 4-6 from heating under vacuum using the tube furnace
4. Begin pulling vacuum in the oven by rotating the vacuum knob.
5. The vacuum pressure can be recorded based on the pressure reading the top left corner
6. Once pressure is reached turn on the heating element (by flipping the green switch)
7. Follow steps 10-11 after the experiment is completed in the heating under vacuum using the tube furnace section
8. Turn off the heating and remove the sample

Appendix H. Synchrotron Experiments

H.1. Soft X-ray Beamline

1. The Variable Line Spacing-Plane Grating Monochromator (VLS-PGM) beam line is used for the elements with lower edge energies around 200-1000 eV. As soft X-rays have low energy, the air absorbs UV-light in the X-rays. Therefore, the samples are placed in vacuum for these measurements. The K edges for lower atomic number elements and L and M edges for higher atomic number elements are measured. There are two types of gratings present in the monochromator. One for lower energy which ranges from 200-500 eV and the other one from 500-1000 eV. For the SBO samples, a higher monochromator grating is employed for all the measurements on this beam line.

H.1.1. Sample Preparation

1. For powders sample, the double-sided carbon tape is cut into four small squares and it is stuck on both the sides of the circular sample holder
2. Very little amount of sample is taken with a spatula and then it is spread uniformly on the tape with the help of a brush and excess sample is slowly pushed off the sample holder without contaminating the other sample

H.1.2. Equipment Design

1. The vacuum chamber has an inlet pump which is not connected to the chamber but an extension through which the samples can be taken out or placed inside without disturbing the vacuum inside the chamber
2. An entrance slit near the beam ring and an exit slit near the sample are present in the beam line which will determine the resolution of the measurement
3. The pump inlet to the vacuum chamber is closed and the green valve near the load lock chamber is slowly opened
4. The screws of the load lock chamber are unscrewed and the sample holder is carefully placed inside it with the help of tweezers
5. The load lock valve is then closed and the screws are finger tightened and the valve is opened while closing the blue valve
6. Now the pressure is monitored and the valve is opened once the vacuum inside is at high pressure
7. It takes around 90 minutes for the chamber to be pumped out of air and after that the beam is turned on, which takes about 10 min for warming up

H.1.3. Sample Measurement

1. All the shutters are closed till the beam is near the slit and it takes about 10 min to warm up
2. The shutters are slowly opened except for the Gate valve 5. The entrance slit is kept at 100 μm (144) and the exit slit is increased to 150 μm (300)
3. The lab view software is opened on the first computer and VLS mirror software is opened on the second one. In the first computer, Utilities is selected. Then hit on go white light and then one single click on white light. We can see the monochromator moving as the energy is changing to white energy

4. The sample inside the chamber is adjusted along the X,Y and Z axes by turning the respective knobs and it is ensured that the white light beam hits the center of the sample
5. Now the exit slit is turned again to 100 μm (121) and on the software Go back to main button is clicked
6. In the main utilities window, go to energy is clicked and the energy for our specific element of interest is entered manually. This value is usually greater than the edge energy value
7. When the monochromator stops rotating, the Gate valve is opened by pressing on the monitor screen and the input values for our scan are given.
8. Now the optimize I_o is selected and the Z position and pitch are made sure that they are non-zero five-digit numbers. The incremenet value is given as 100 and hit on go to see if the current in the Keithley meter is increasing or not. We can go in the opposite direction too by decreasing the values to maximize the current
9. The window on the first computer is closed by hitting on back to main and the go button is clicked next to the Grating value to begin the scan
10. After the scan is completed, it directs you to a path and we can create a new folder in the Dataparti (:C) drive with the date and name
11. Copy a log.txt file from any of the other folders and save it in your folder by clearing the text in it
12. The sample scan is now saved by its name and then log.txt file is selected
13. To begin another scan of the same sample but for another element, change the energy range and optimize the current for every new scan and also change the slit widths if necessary
14. For rotating the sample holder to measure samples on the other side, close the gate valve 5 and then rotate the black long knob in clock-wise direction and again adjust the position such that the white light beam will fall on the center of the sample
15. After finishing all the measurements, close the gate valve 5 and all the shutters are closed one by one from right to left. They are opened in the reverse order
16. The data collected can be processed in Athena simultaneously while performing the scans and the change in the absorption edges is observed

Appendix I. Computational Details

First-principles simulations were performed to provide a geometric and electronic description for the experimentally observed responses. These simulations were performed in collaboration with Dr. Craig Plaisance, Department of Chemical Engineering. The details regarding the calculations are presented below.

I.1. Phonon Density of States Calculations using VASP

Planewave density functional theory (DFT) calculations were performed using the Vienna Ab-Initio Simulation Package (VASP) (Kresse and Furthmüller 1996, Kresse and Furthmüller 1996) to analyze the characteristics observed in the Raman spectrum of the SNO NPs. The phonon density of states (DOS) calculations used the Perdew−Burke−Ernzerhof (PBE) functional (Perdew, Burke et al. 1996) to account for exchange and correlation and the projector augmented wave (PAW) method (Blöchl 1994) to describe wave functions in the atomic core regions. All calculations were performed with a plane-wave cutoff energy of 396 eV and a 4 × 4 × 4 Γ-centered *k*-point grid. A 2 × 2 × 2 supercell was used for all calculations with the experimentally determined unit cell lattice parameter of 4.042 Å (Wan, Zhao et al. 2017). Prior to computing force constants, the atomic positions in the supercell were optimized until the force on each atom was less than 0.05 eV/Å. Force constants were calculated using the finite difference method with a displacement of 0.01 Å. The Phonopy package (Togo, Oba et al. 2008) was used to calculate phonon densities of states based on the obtained force constants.

To provide a geometrical description of the vibrational modes responsible for the experimentally observed peaks in the Raman spectrum, a SNO crystal was constructed. A ball and stick rendering of this crystal is presented in Figure I.1.1. The presented model is an

expansion of the calculated crystal to highlight the difference in the surface and bulk structure. The hydroxyl groups, bonded to the surface of the crystal, create surface vibrations (>800 cm^{-1}). The Sr and O vacancies, present deep within the crystal, contribute to distorting the bulk vibrations (<800 cm^{-1}).

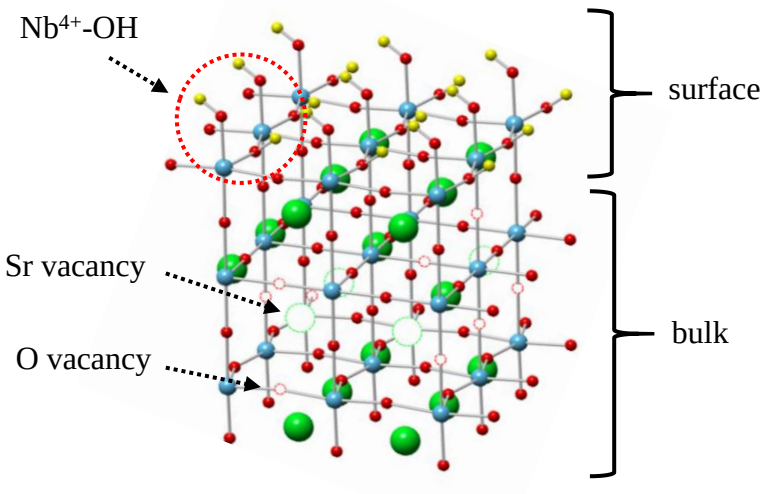

Figure I.1.1 SNO NPs model used for Phonon Calculations. The supercell contains Sr (green), Nb (blue), O (red), and H (yellow) atoms. The model is presented in ball and stick form to highlight the presence of Nb^{4+}-OH groups on the surface and point defects (Sr and O vacancies) in the bulk of the nanoparticle.

I.2. Electronic Density of States Calculations using VASP

The electronic structure of the SBO (B = Nb, Ta, and Mo) NPs were also calculated using DFT as implemented in the VASP code. Similar to Section 2.3.1., electronic DOS calculations apply the PBE functional to account for exchange and correlation and the PAW method to describe wave functions in the atomic core regions. The Na 3s2p, Sr 4s4p5s, Nb 4p5s4d, Mo 4p5s4d, Ta 6s5d, and O 2s2p orbitals were treated as valence states. The calculations were performed with a plane-wave cutoff energy of 396 eV and a 3 × 3 × 3 Γ-centered *k*-point grid. A 2 × 2 × 2 supercell, with experimentally determined unit cell lattice parameters (Macquart,

Kennedy et al. 2010, Oka, Hirose et al. 2014, Wan, Zhao et al. 2017), was utilized in these calculations. For the determination of the Kohn-Sham orbital populations, a Methfessel-Paxton (second-order) method was used with a smearing width of 0.2 eV. The atomic positions in the supercell were optimized until the force on each atom was less than 0.05 eV $Å^{-1}$.

In these calculations, standard DFT (i.e. no Hubbard *U* correction (Anisimov, Zaanen et al. 1991)) was utilized to describe the electronic interactions in these SBO structures (Oka, Hirose et al. 2018, Bigi, Orgiani et al. 2020). This was tested by performing initial calculations using 2 × 2 × 2 stoichiometric SBO supercells and were constructed using experimentally reported lattice parameters of a = 4.042 Å (B = Nb), a = 3.950 Å (B = Ta), and a = 3.976 Å (B = Mo). A representation of the supercell for the stoichiometric crystal is presented in Figure I.2.1. Next, Sr vacancies were introduced into the defect-free structure to mirror the measured stoichiometries and equal amounts of O vacancies were utilized to ensure that the supercell was neutrally charged. For example, eliminating two Sr atoms and two O atoms from the SNO supercell creates a structure with $Sr_{0.75}NbO_{2.75}$ (0% Nb^{5+}, d^1 electron configuration) stoichiometry.

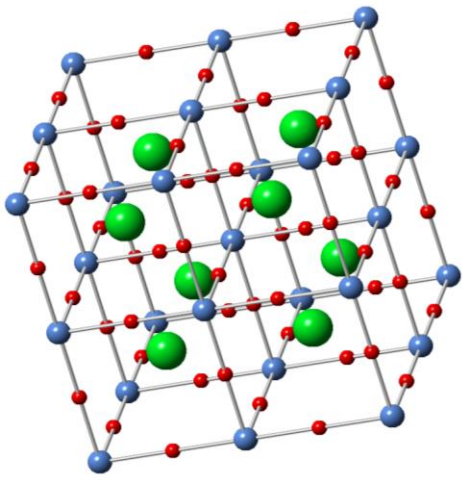

Figure I.2.1 SBO (B = Nb, Ta, and Mo) supercell used for Electronic Calculations. The defect-free supercell contains 40 atoms: 8 Sr (green), 8 Nb (clue), and 24 O (red). Point defects (Sr and O vacancies) are introduced into the model in order to mirror the measured structure.

I.3. Electronic Band Structure Calculations using VASP

The VASP code was similarly utilized to calculate the electronic band structure. In these calculations, the optimized geometries (lattice parameters and atomic positions) from the electronic DOS calculations were used as inputs to simulate the band structures. The high symmetry *k*-points in the Brillouin zone for the calculated band structure were generated using the automatic-flow for materials discovery (AFLOW) software (Curtarolo, Setyawan et al. 2012). The resultant band structures were visualized using p4vasp (http://www.p4vasp.at/#/), VASPKIT (Wang, Xu et al. 2019), and OriginPro softwares. Examples of the visualized bands structure for defect-free SNO using the p4vasp and Origin software packages are presented in Figure I.3.1.

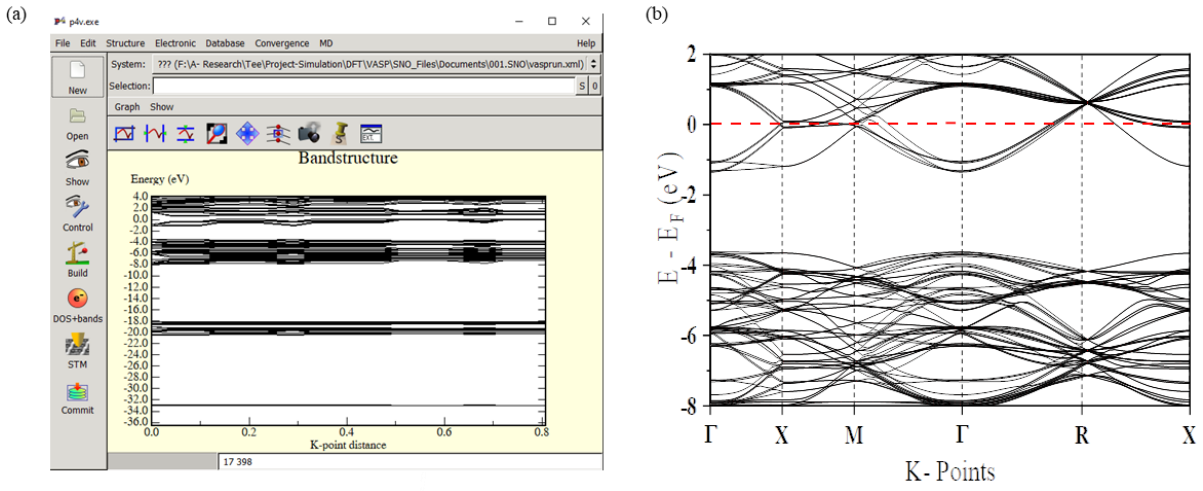

Figure I.3.1 Band structure visualization for defect-free SNO using (a) p4vasp and (b) OriginPro softwares.

I.4. Electronic Transport Calculations using BoltzTraP2

The electronic transport properties were subsequently calculated using the semi-classical Boltzmann Transport theory within the rigid band (RBA) and constant relaxation time (CRTA) approach as implemented in the BoltzTraP2 code (Madsen and Singh 2006, Madsen, Carrete et al. 2018). BoltzTraP2 operates in three spaces (real space, *k* space, and energy space) with the transfer from *k* space to energy space around the Fermi level (chemical potential) via the DOS, being of particularly importance. The RBA assumes that modifying the lattice environment (i.e. temperature, doping, etc.), does not significantly alter the band structure. The CRTA means that the calculated thermoelectric coefficients (i.e. conductivity (electrical and thermal), Seebeck coefficient, Hall coefficient, etc.) become independent of the scattering rate (τ). To run the BoltzTraP2 simulations, the band structure data from VASP should be generated using *k*-points along all lines in the Brillouin zone. Using a smoothed Fourier interpolation algorithm, the band structure is projected onto a mesh containing a denser sampling of *k*-points. Finally, the interpolated band structure was integrated to obtain the thermoelectric coefficients.

In this work, the electrical resistivities were calculated for the stoichiometric and defective SBO perovskites. The supercell model has periodic boundary conditions, allowing for systematic defect incorporation. This study also uses a $2 \times 2 \times 2$ supercell containing Sr and O vacancies to mirror the measured crystal structure. After performing VASP calculations, the band structure is projected onto a mesh containing 5 times the *k*-points. A τ of ~4 fs, which is suitable for these SBO perovskites (Zhang, Feng et al. 2017), was used for all calculations to convert the calculated conductivity per relaxation time (σ/τ) into electrical resistivity (ρ).

Bibliography

Abraham, K. (2015). "Prospects and limits of energy storage in batteries." *The Journal of Physical Chemistry Letters* **6**(5): 830-844.

Abreu, Y. G., et al. (2016). "Monitoring the Structural and vibrational properties in RE-doped SrTiO3 ceramic powders." *The Journal of Physical Chemistry C* **120**(30): 16960-16968.

Acosta, M., et al. (2017). "BaTiO3-based piezoelectrics: Fundamentals, current status, and perspectives." *Applied Physics Reviews* **4**(4): 041305.

Agency IRENA, I. R. E. (2020). *Renewable Power Generation Costs in 2019*, International Renewable Energy Agency (IRENA).

Alaparthi, S. B., et al. (2013). "Synthesis and photoluminescence properties of La2Zr2O7: Eu3+@ YBO3 core@ shell nanoparticles." *Nanotechnology* **25**(2): 025703.

Ali, Z., et al. (2015). "Theoretical studies of the paramagnetic perovskites MTaO3 (M= Ca, Sr and Ba)." *Materials Chemistry and Physics* **162**: 308-315.

Amin, R. and Y.-M. Chiang (2016). "Characterization of electronic and ionic transport in Li1-xNi0. 33Mn0. 33Co0. 33O2 (NMC333) and Li1-xNi0. 50Mn0. 20Co0. 30O2 (NMC523) as a function of Li content." *Journal of The Electrochemical Society* **163**(8): A1512.

Amow, G., et al. (2006). "A comparative study of the Ruddlesden-Popper series, Lan+ 1NinO3n+ 1 (n= 1, 2 and 3), for solid-oxide fuel-cell cathode applications." *Solid State Ionics* **177**(13-14): 1205-1210.

Anisimov, V. I., et al. (1991). "Band theory and Mott insulators: Hubbard U instead of Stoner I." *Physical Review B* **44**(3): 943.

Asmara, T. C., et al. (2017). "Tunable and low-loss correlated plasmons in Mott-like insulating oxides." *Nature Communications* **8**.

Asokan, K., et al. (2004). "The electronic structure of Ba1− xCaxTiO3 probed by X-ray absorption spectroscopy." *Journal of Solid State Chemistry* **177**(8): 2639-2643.

Atta, N. F., et al. (2013). "The electrochemistry and determination of some neurotransmitters at SrPdO3 modified graphite electrode." *Journal of The Electrochemical Society* **160**(7): G3144.

Aufray, M., et al. (2009). "New synthesis of nanosized niobium oxides and lithium niobate particles and their characterization by XPS analysis." *Journal of Nanoscience and Nanotechnology* **9**(8): 4780-4785.

Baer, D. R. and M. H. Engelhard (2010). "XPS analysis of nanostructured materials and biological surfaces." *Journal of electron spectroscopy and related phenomena* **178**: 415-432.

Bajgiran, K., et al. (2020). "Dipole-Modulated Downconversion Nanoparticles as Label-Free Biological Sensors." *ACS Sensors* **5**(1): 29.

Bartel, C. J., et al. (2019). "New tolerance factor to predict the stability of perovskite oxides and halides." *Science Advances* **5**(2): eaav0693.

Bayeh, A. W., et al. (2019). "Hydrogen-Treated Defect-Rich W18O49 Nanowire-Modified Graphite Felt as High-Performance Electrode for Vanadium Redox Flow Battery." *ACS Applied Energy Materials* **2**(4): 2541-2551.

Bazzi, K., et al. (2012). "Nanostructured high specific capacity C-LiFePO4 cathode material for lithium-ion batteries." *Journal of materials research* **27**(2): 424.

Beechem, T. E., et al. (2018). "Tunable Infrared Devices via Ferroelectric Domain Reconfiguration." *Advanced Optical Materials* **6**(24): 1800862.

Belharouak, I., et al. (2006). "Safety characteristics of Li (Ni0. 8Co0. 15Al0. 05) O2 and Li (Ni1/3Co1/3Mn1/3) O2." *Electrochemistry communications* **8**(2): 329-335.

Beneš, O., et al. (2010). "A DSC study of the NaNO3–KNO3 system using an innovative encapsulation technique." *Thermochimica acta* **509**(1-2): 62-66.

Bera, A., et al. (2014). "Perovskite oxide SrTiO3 as an efficient electron transporter for hybrid perovskite solar cells." *The Journal of Physical Chemistry C* **118**(49): 28494-28501.

Berney Needleman, D. (2014). Optical design guidelines for spectral splitting photovoltaic systems: A sensitivity analysis approach, Massachusetts Institute of Technology.

Bi, K., et al. (2018). "Ultrafine core-shell BaTiO3@ SiO2 structures for nanocomposite capacitors with high energy density." *Nano Energy* **51**: 513-523.

Bidrawn, F., et al. (2010). "Dopants to enhance SOFC cathodes based on Sr-doped LaFeO3 and LaMnO3." *Journal of Power Sources* **195**(3): 720-728.

Biemolt, J., et al. (2020). "Beyond Lithium-Based Batteries." *Materials* **13**(2): 425.

Bigi, C., et al. (2020). "Direct insight into the band structure of SrNbO 3." *Physical Review Materials* **4**(2): 025006.

Blöchl, P. E. (1994). "Projector augmented-wave method." *Physical Review B* **50**(24): 17953.

Borg, A., et al. (1992). "Ca 3d unoccupied states in Bi 2 Sr 2 CaCu 2 O 8 investigated by Ca L 2, 3 x-ray-absorption near-edge structure." *Physical Review B* **46**(13): 8487.

Braun, H., et al. (1980). "Electronic conductivity of lead dioxide powder: separation of core and surface resistance of the particles." *Journal of Applied Electrochemistry* **10**(4): 441-448.

Bryan, A. M., et al. (2016). "Conducting polymers for pseudocapacitive energy storage." *Chemistry of Materials* **28**(17): 5989-5998.

Calderone, V. R., et al. (2006). "Size and shape control of SrTiO3 particles grown by epitaxial self-assembly." *Chemistry of Materials* **18**(6): 1627-1633.

Call, R. W., et al. (2018). "Impedance spectroscopy study of SrTiO3 pulse laser deposited photoelectrodes." *Thin Solid Films* **655**: 27-33.

Campion, M. J., et al. (2013). "Crystallization Atmosphere and Substrate Effects on the Phase and Texture of Chemical Solution Deposited Strontium Niobate Thin Films." *Journal of the American Ceramic Society* **96**(3): 743-749.

Cebulla, F., et al. (2018). "How much electrical energy storage do we need? A synthesis for the US, Europe, and Germany." *Journal of Cleaner Production* **181**: 449-459.

Chen, G., et al. (2017). "Flexible nonvolatile resistive memory devices based on SrTiO3 nanosheets and polyvinylpyrrolidone composites." *Journal of Materials Chemistry C* **5**(37): 9799-9805.

Chen, J., et al. (2017). "Ultrahigh Thermoelectric Performance in SrNb0. 2Ti0. 8O3 Oxide Films at a Submicrometer-Scale Thickness." *ACS Energy Letters* **2**(4): 915-921.

Chen, M., et al. (2015). "Surface and bulk study of strontium-rich chromium ferrite oxide as a robust solid oxide fuel cell cathode." *Journal of Materials Chemistry A* **3**(45): 22614-22626.

Chen, T., et al. (2019). "Hydrothermal synthesis of perovskite CaTiO 3 tetragonal microrods with vertical V-type holes along the [010] direction." *Crystengcomm* **21**(32): 4763-4770.

Chen, X., et al. (2012). "Conductive rigid skeleton supported silicon as high-performance Li-ion battery anodes." *Nano letters* **12**(8): 4124-4130.

Cheng, J.-G., et al. (2009). "A new perovskite polytype in the high-pressure sequence of BaIrO3." *Journal of the American Chemical Society* **131**(21): 7461-7469.

China, K. (2011). "China's 12th Five-Year Plan: Energy." *Energy*.

Cho, I.-S., et al. (2010). "SrNb 2 O 6 nanotubes with enhanced photocatalytic activity." *Journal of Materials Chemistry* **20**(19): 3979-3983.

Comparotto, C., et al. (2020). "Chalcogenide Perovskite BaZrS3: Thin Film Growth by Sputtering and Rapid Thermal Processing." *ACS Applied Energy Materials* **3**(3): 2762-2770.

Conder, K., et al. (2005). "Oxygen content determination in perovskite-type cobaltates." *Materials research bulletin* **40**(2): 257-263.

Council, N. R. (2003). *Materials Research to Meet 21st-Century Defense Needs*, National Academies Press.

Cowin, P. I., et al. (2016). "Conductivity and redox stability of new double perovskite oxide Sr 1.6 K 0.4 Fe 1+ x Mo 1− x O 6− δ (x= 0.2, 0.4, 0.6)." *Journal of Materials Science* **51**(8): 4115-4124.

Crabtree, G., et al. (2017). Basic Research Needs for Electrical Energy Storage. Report of the Basic Energy Sciences Workshop on Electrical Energy Storage, March 27-29, 2017, DOESC (USDOE Office of Science (SC)).

Curtarolo, S., et al. (2012). "AFLOW: an automatic framework for high-throughput materials discovery." *Computational materials science* **58**: 218-226.

Curtin, S., et al. (2012). State of the States. Fuel Cells in America 2012, Fuel Cells 2000.

Cushing, S. K., et al. (2017). "Effects of defects on photocatalytic activity of hydrogen-treated titanium oxide nanobelts." *ACS Catalysis* **7**(3): 1742-1748.

Dagytė, V., et al. (2018). "Growth kinetics of Ga x In (1− x) P nanowires using triethylgallium as Ga precursor." *Nanotechnology* **29**(39): 394001.

Darapaneni, P., et al. (2018). "Weak Field Tuning of Transition-Metal Dopant Hybridization in Solid Hosts." *The Journal of Physical Chemistry C* **122**(39): 22699-22708.

Darapaneni, P., et al. (2018). "Weak Field Tuning of Transition Metal Dopant Hybridization in Solid Hosts." *The Journal of Physical Chemistry C*.

Darapaneni, P., et al. (2019). "Effect of Moisture on Dopant Segregation in Solid Hosts." *The Journal of Physical Chemistry C*.

De Groot, F., et al. (1990). "L 2, 3 x-ray-absorption edges of d 0 compounds: K+, Ca 2+, Sc 3+, and Ti 4+ in O h (octahedral) symmetry." *Physical Review B* **41**(2): 928.

De Groot, F., et al. (1989). "Oxygen 1s x-ray-absorption edges of transition-metal oxides." *Physical Review B* **40**(8): 5715.

Delmas, C., et al. (2011). Lithium deintercalation in LiFePO 4 nanoparticles via a domino-cascademodel. *Materials For Sustainable Energy: A Collection of Peer-Reviewed Research and Review Articles from Nature Publishing Group*, World Scientific**:** 180-186.

Doppelhammer, N., et al. (2020). "Moving Electrode Impedance Spectroscopy for Accurate Conductivity Measurements of Corrosive Ionic Media." *ACS Sensors* **5**(11): 3392-3397.

Dorman, J. A., et al. (2012). "Optimizing the crystal environment through extended x-ray absorption fine structure to increase the luminescent lifetimes of Er3+ doped Y2O3 nanoparticles." *Journal of applied physics* **111**(8): 083529.

Dorman, J. A., et al. (2012). "Elucidating the effects of a rare-earth oxide shell on the luminescence dynamics of Er3+: Y2O3 nanoparticles." *The Journal of Physical Chemistry C* **116**(18): 10333-10340.

Dupin, J.-C., et al. (2000). "Systematic XPS studies of metal oxides, hydroxides and peroxides." *Physical Chemistry Chemical Physics* **2**(6): 1319-1324.

Edenhofer, O., et al. (2011). "Renewable Energy Sources and Climate Change Mitigation: Summary for Policymakers."

Efstathiou, P., et al. (2013). "An investigation of crystal structure, surface area and surface chemistry of strontium niobate and their influence on photocatalytic performance." *Dalton Transactions* **42**(22): 7880-7887.

EIA, U. (2020). Energy information administration. International Energy Outlook. US Department of Energy.

Emery, A. A. and C. Wolverton (2017). "High-throughput dft calculations of formation energy, stability and oxygen vacancy formation energy of abo 3 perovskites." *Scientific data* **4**(1): 1-10.

Eom, K., et al. (2017). "A stable lithiated silicon–chalcogen battery via synergetic chemical coupling between silicon and selenium." *Nature Communications* **8**: 13888.

Fairley, N. (2009). *CasaXPS Manual 2.3. 15: CasaXPS Processing Software for XPS Spectra*, Casa Software Limited.

Franco, A. A., et al. (2019). "Boosting rechargeable batteries R&D by multiscale modeling: myth or reality?" *Chemical reviews* **119**(7): 4569-4627.

Frayssinet, P., et al. (2011). "Calcium Phosphates for Cell Transfection."

Fuentes, A. F., et al. (2018). "A critical review of existing criteria for the prediction of pyrochlore formation and stability." *Inorganic chemistry* **57**(19): 12093-12105.

Fuller, E. J., et al. (2017). "Li-ion synaptic transistor for low power analog computing." *Advanced Materials* **29**(4): 1604310.

Geneste, G. and J.-M. Kiat (2008). "Ground state of Ca-doped strontium titanate: Ferroelectricity versus polar nanoregions." *Physical Review B* **77**(17): 174101.

Goethals, J., et al. (2019). "Experimental study of trivalent rare-earth element incorporation in CaTiO 3 perovskite: evidence for a new substitution mechanism." *Physics and Chemistry of Minerals* **46**(10): 1003-1015.

Goldschmidt, V. M. (1926). "Die gesetze der krystallochemie." *Naturwissenschaften* **14**(21): 477-485.

Goodenough, J. B., et al. (2007). Basic Research Needs for Electrical Energy Storage. Report of the Basic Energy Sciences Workshop on Electrical Energy Storage, April 2-4, 2007, DOESC (USDOE Office of Science (SC)).

Gross, T. J., et al. (2011). Beyond Demonstration: the Role of Fuel Cells in DoD's energy strategy, LOGISTICS MANAGEMENT INST (LMI) MCLEAN VA.

Guo, D., et al. (2013). "Defect-Induced and UV-Irradiation-Enhanced Ferromagnetism in Cubic Barium Niobate." *The Journal of Physical Chemistry C* **117**(27): 14281-14288.

Guo, Y., et al. (2012). "Ferroelectricity and superparamagnetism in Sr/Ti nonstoichiometric SrTiO 3." *Physical Review B* **85**(10): 104108.

Gupta, T., et al. (2020). "An Environmentally Stable and Lead-Free Chalcogenide Perovskite." *Advanced Functional Materials* **30**(23): 2001387.

Ha, Y. and S. Lee (2020). "Oxygen-Vacancy-Endurable Conductors with Enhanced Transparency Using Correlated 4d2 SrMoO3 Thin Films." *Advanced Functional Materials*: 2001489.

Haasch, R. T., et al. (2014). "Single crystal perovskites analyzed using X-ray photoelectron spectroscopy: 1. SrTiO3 (001)." *Surface Science Spectra* **21**(1): 87-94.

Han, F., et al. (2015). "Dielectric capacitors with three-dimensional nanoscale interdigital electrodes for energy storage." *Science Advances* **1**(9): e1500605.

Hanzig, F., et al. (2015). "Crystallization dynamics and interface stability of strontium titanate thin films on silicon." *Journal of applied crystallography* **48**(2): 393-400.

He, P., et al. (2007). "Lithium-ion intercalation behavior of LiFePO4 in aqueous and nonaqueous electrolyte solutions." *Journal of The Electrochemical Society* **155**(2): A144.

Henze, V. (2018). Energy Storage is a $620 Billion Investment Opportunity to 2040. Bloomberg New Energy Finance. **2018**.

Hernandez, R. R., et al. (2019). "Techno–ecological synergies of solar energy for global sustainability." *Nature Sustainability* **2**(7): 560-568.

Hirata, T., et al. (1996). "Vibrational spectroscopy and X-ray diffraction of perovskite compounds Sr1− xMxTiO3 (M= Ca, Mg; 0≤ x≤ 1)." *Journal of Solid State Chemistry* **124**(2): 353-359.

Hojo, J. (2019). *Materials Chemistry of Ceramics*, Springer.

Hou, N., et al. (2019). "A-site ordered double perovskite with in situ exsolved core–shell nanoparticles as anode for solid oxide fuel cells." *ACS applied materials & interfaces* **11**(7): 6995-7005.

Huggins, M. L. (1953). "Bond energies and polarities1." *Journal of the American Chemical Society* **75**(17): 4123-4126.

Igusky, K., et al. (2014). "Seeing is Believing: Creating a New Climate Economy in the United States."

Im, B., et al. (2011). "Fabrication of nanoporous MTiO3 (M = Pb, Ba, Sr) perovskite array films with unprecedented high structural regularity." *Crystengcomm* **13**(24): 7212-7215.

Isawa, K., et al. (1994). "Photoelectron spectroscopic study of Sr x NbO 3." *Physical Review B* **49**(5): 3534.

Janjua, R. A., et al. (2018). "Na+-driven nucleation of NaYF4: Yb, Er nanocrystals and effect of temperature on their structural transformations and luminescent properties." *The Journal of Physical Chemistry C* **122**(40): 23242-23250.

Jehng, J. M. and I. E. Wachs (1991). "Structural chemistry and Raman spectra of niobium oxides." *Chemistry of Materials* **3**(1): 100-107.

Jethva, S., et al. (2019). "Effect of strain on the modifications in electronic structure and resistive switching in Ca-doped BiFeO3 films." *Journal of applied physics* **125**(8): 082510.

Ji, Q., et al. (2020). "The role of oxygen vacancies of ABO 3 perovskite oxides in the oxygen reduction reaction." *Energy & Environmental Science* **13**(5): 1408-1428.

Jia, Y. (1991). "Crystal radii and effective ionic radii of the rare earth ions." *Journal of Solid State Chemistry* **95**(1): 184-187.

Jiang, C., et al. (2009). "Effects of Eu substituting positions and concentrations on luminescent, dielectric, and magnetic properties of SrTiO 3 ceramics." *Applied Physics Letters* **94**(7): 071110.

Jin, L., et al. (2019). "Exsolution of SrO during the Topochemical Conversion of LaSr3CoRuO8 to the Oxyhydride LaSr3CoRuO4H4." *Inorganic chemistry* **58**(21): 14863-14870.

Jin, T., et al. (2018). "1D nanomaterials: design, synthesis, and applications in sodium–ion batteries." *Small* **14**(2): 1703086.

Julien, C. M., et al. (2014). "Comparative issues of cathode materials for Li-ion batteries." *Inorganics* **2**(1): 132-154.

Jyothi, G., et al. (2017). "Site selective substitution and its influence on photoluminescence properties of Sr 0.8 Li 0.2 Ti 0.8 Nb 0.2 O 3: Eu 3+ phosphors." *RSC Advances* **7**(45): 28438-28451.

Kaneko, M., et al. (2019). "First-principles study on visible light absorption of defected SrNbO3." *Journal of Photochemistry and Photobiology A: Chemistry* **375**: 175-180.

Karppinen, M., et al. (2002). "Oxygen content analysis of functional perovskite-derived cobalt oxides." *Journal of Materials Chemistry* **12**(6): 1761-1764.

Kasap, S., et al. (2017). Electrical conduction in metals and semiconductors. *Springer Handbook of Electronic and Photonic Materials*, Springer**:** 1-1.

Kawanaka, H., et al. (2018). "Magnetic properties of perovskite Ca1− x Sr x FeO3." *AIP Advances* **8**(10): 101418.

Kim, T. H., et al. (2019). "Some Insights into Atomic Layer Deposition of MoN x Using Mo (CO) 6 and NH3 and Its Diffusion Barrier Application." *Chemistry of Materials* **31**(20): 8338-8350.

Kiselev, Y. M. (2007). "Stabilization of oxidation states in transition metals." *Russian Journal of Inorganic Chemistry* **52**(11): 1717-1725.

Kizilkaya, O., et al. (2014). *High-throughput Toroidal Grating Beamline for Photoelectron Spectroscopy at CAMD*. Journal of Physics: Conference Series, IOP Publishing.

Kobayashi, J., et al. (1983). "X-ray and optical studies on phase transition of PbTi O 3 at low temperatures." *Physical Review B* **28**(7): 3866.

Kresse, G. and J. Furthmüller (1996). "Efficiency of ab-initio total energy calculations for metals and semiconductors using a plane-wave basis set." *Computational materials science* **6**(1): 15-50.

Kresse, G. and J. Furthmüller (1996). "Efficient iterative schemes for ab initio total-energy calculations using a plane-wave basis set." *Physical Review B* **54**(16): 11169.

Kriston, A., et al. (2019). "Quantification and simulation of thermal decomposition reactions of Li-ion battery materials by simultaneous thermal analysis coupled with gas analysis." *Journal of Power Sources* **435**: 226774.

Kuepper, K., et al. (2005). "Electronic structure of A-and B-site doped lanthanum manganites: A combined X-ray spectroscopic study." *The Journal of Physical Chemistry B* **109**(19): 9354-9361.

Larsson, A. and R. Von Dreele (1994). "General Structure Analysis System (GSAS)." *Los Alamos, NM: Los Alamos Laboratory*.

Laubach, S., et al. (2009). "Changes in the crystal and electronic structure of LiCoO 2 and LiNiO 2 upon Li intercalation and de-intercalation." *Physical Chemistry Chemical Physics* **11**(17): 3278-3289.

Leach, M. and L. Dry (2018). Global Energy Demand to Soar; Lead Batteries Poised to Meet Renewable Energy Storage Needs. Markets Insider, Essential Energy Everyday. **2018**.

Lee, H. W., et al. (2012). "Synthesis and size control of tetragonal barium titanate nanopowders by facile solvothermal method." *Journal of the American Ceramic Society* **95**(8): 2429-2434.

Lee, J.-H. and J. Woo (2020). "Green New Deal Policy of South Korea: Policy Innovation for a Sustainability Transition." *Sustainability* **12**(23): 10191.

Lee, J. H., et al. (2017). "Strongly coupled magnetic and electronic transitions in multivalent strontium cobaltites." *Scientific Reports* **7**(1): 1-8.

Lee, W., et al. (2018). "Synthesis of Ag/Mn Co-Doped CdS/ZnS (Core/Shell) Nanocrystals with Controlled Dopant Concentration and Spatial Distribution and the Dynamics of Excitons and Energy Transfer between Co-Dopants." *Nano letters* **19**(1): 308-317.

Lehmann, S., et al. (2015). "Crystal phase control in GaAs nanowires: opposing trends in the Ga- and As-limited growth regimes." *Nanotechnology* **26**(30): 301001.

Lemaire, P., et al. (2019). "Elucidating the Origin of the Electrochemical Capacity in a Proton-Based Battery H x IrO4 via Advanced Electrogravimetry." *ACS applied materials & interfaces* **12**(4): 4510-4519.

Li, J., et al. (2019). "Hybrid additive manufacturing method for selective plating of freeform circuitry on 3D printed plastic structure." *Advanced Materials Technologies* **4**(2): 1800529.

Li, J., et al. (2016). "Synthesis of Nanoparticles via Solvothermal and Hydrothermal Methods 12."

Li, K. and D. Xue (2006). "Estimation of electronegativity values of elements in different valence states." *The Journal of Physical Chemistry A* **110**(39): 11332-11337.

Li, L., et al. (2017). "recent research progress in surface modification of LiFePO4 cathode materials." *Journal of The Electrochemical Society* **164**(9): A2138.

Li, Q., et al. (2019). "Dynamic imaging of crystalline defects in lithium-manganese oxide electrodes during electrochemical activation to high voltage." *Nature Communications* **10**(1): 1-7.

Li, W., et al. (2020). "Defects in complex oxide thin films for electronics and energy applications: challenges and opportunities." *Materials Horizons* **7**(11): 2832-2859.

Li, Y. and J. Lu (2017). "Metal–air batteries: will they be the future electrochemical energy storage device of choice?" *ACS Energy Letters* **2**(6): 1370-1377.

Lima, A., et al. (2016). "Structural characterization and photoluminescence behavior of pure and doped potassium strontium niobates ceramics with tetragonal tungsten–bronze structure." *Ceramics International* **42**(4): 4709-4714.

Liu, F., et al. (2017). "Unusual Fe–H bonding associated with oxygen vacancies at the (001) surface of Fe3O4." *Surface science* **655**: 25-30.

Liu, H., et al. (2020). "Screening stable and metastable ABO3 perovskites using machine learning and the materials project." *Computational materials science* **177**: 109614.

Liu, L., et al. (2013). "Preparation of single crystalline NaSr2Nb5O15 particles with acicular morphology." *Powder technology* **246**: 395-397.

Lück, J. and A. Latz (2019). "The electrochemical double layer and its impedance behavior in lithium-ion batteries." *Physical Chemistry Chemical Physics* **21**(27): 14753-14765.

Lutterotti, L. (2006). "Introduction to diffraction and the Rietveld method." *Laboratorio Scienza e Tecnologia dei Materiali*: 6-20.

Ma, X.-H., et al. (2019). "Highly Sensitive and Selective PbTiO3 Gas Sensors with Negligible Humidity Interference in Ambient Atmosphere." *ACS applied materials & interfaces* **11**(5): 5240-5246.

Ma, Z., et al. (2015). "In situ catalytic synthesis of high-graphitized carbon-coated LiFePO4 nanoplates for superior Li-ion battery cathodes." *ACS applied materials & interfaces* **7**(4): 2937-2943.

Macquart, R. B., et al. (2010). "Neutron diffraction study of phase transitions in perovskite-type strontium molybdate SrMoO3." *Journal of Solid State Chemistry* **183**(1): 250-255.

Madsen, G. K., et al. (2018). "BoltzTraP2, a program for interpolating band structures and calculating semi-classical transport coefficients." *Computer Physics Communications* **231**: 140-145.

Madsen, G. K. and D. J. Singh (2006). "BoltzTraP. A code for calculating band-structure dependent quantities." *Computer Physics Communications* **175**(1): 67-71.

Maeno, Y., et al. (1994). "Superconductivity in a layered perovskite without copper." *Nature* **372**(6506): 532-534.

Mai, T. T., et al. (2018). Electrification futures study: Scenarios of electric technology adoption and power consumption for the United States, National Renewable Energy Lab.(NREL), Golden, CO (United States).

Mallikarjunaiah, K., et al. (2008). "Study of molecular dynamics and cross relaxation in tetramethylammonium hexafluorophosphate (CH3) 4NPF6 by 1H and 19F NMR." *Solid state nuclear magnetic resonance* **34**(3): 180-185.

Mao, Y., et al. (2003). "Hydrothermal synthesis of perovskite nanotubes." *Chemical Communications* (3): 408-409.

Mao, Y. and S. S. Wong (2005). "Composition and shape control of crystalline Ca1–xSrxTiO3 perovskite nanoparticles." *Advanced Materials* **17**(18): 2194-2199.

Martha, S. K., et al. (2011). "On the thermal stability of olivine cathode materials for lithium-ion batteries." *Journal of The Electrochemical Society* **158**(10): A1115.

McKeen, L. W. (2017). *Film properties of plastics and elastomers*, William Andrew.

Mehmood, S., et al. (2019). "First-Principles Study of Perovskite Molybdates AMoO 3 (A= Ca, Sr, Ba)." *Journal of Electronic Materials* **48**(3): 1730-1739.

Meng, C., et al. (2013). "A flexible super-capacitive solid-state power supply for miniature implantable medical devices." *Biomedical microdevices* **15**(6): 973-983.

Mitsui, T. and W. B. Westphal (1961). "Dielectric and X-Ray Studies of Ca x Ba 1− x Ti O 3 and Ca x Sr 1− x Ti O 3." *Physical Review* **124**(5): 1354.

Mundaca, L. and J. L. Richter (2015). "Assessing 'green energy economy'stimulus packages: Evidence from the US programs targeting renewable energy." *Renewable and sustainable energy reviews* **42**: 1174-1186.

Music, D., et al. (2017). "Adsorption of film-forming species on NbO and NbO2 surfaces." *Journal of Vacuum Science & Technology A: Vacuum, Surfaces, and Films* **35**(6): 061512.

Neagu, D. and J. T. Irvine (2011). "Enhancing electronic conductivity in strontium titanates through correlated A and B-site doping." *Chemistry of Materials* **23**(6): 1607-1617.

Neiner, D., et al. (2009). "Synthesis and characterization of K8− x (H2) y Si46." *Inorganic chemistry* **49**(3): 815-822.

Ni, H., et al. (2013). "Carbon-coated LiFePO 4–porous carbon composites as cathode materials for lithium ion batteries." *Nanoscale* **5**(5): 2164-2168.

Nie, Z., et al. (2020). "Probing transport limitations in thick sintered battery electrodes with neutron imaging." *Molecular Systems Design & Engineering* **5**(1): 245-256.

Nikam, R. D., et al. (2019). "Controlled Ionic Tunneling in Lithium Nanoionic Synaptic Transistor through Atomically Thin Graphene Layer for Neuromorphic Computing." *Advanced Electronic Materials*: 1901100.

Nothwang, W. (2012). Multi-Functional Materials for Defense DoD Perspective on Sensing, ARMY RESEARCH LAB ADELPHI MD SENSORS AND ELECTRON DEVICES DIRECTORATE.

O'Regan, B. and M. Grätzel (1991). "A low-cost, high-efficiency solar cell based on dye-sensitized colloidal TiO 2 films." *Nature* **353**(6346): 737-740.

Oberhofer, H., et al. (2017). "Charge transport in molecular materials: An assessment of computational methods." *Chemical reviews* **117**(15): 10319-10357.

Ofoegbuna, T., et al. (2020). "Photoluminescence detection of symmetry transformations in low-dimensional ferroelectric ABO3 perovskites." *Journal of Materials Chemistry C* **8**(31): 10767-10773.

Ofoegbuna, T., et al. (2019). "Stabilizing the B-site oxidation state in ABO 3 perovskite nanoparticles." *Nanoscale* **11**(30): 14303-14311.

Oka, D., et al. (2014). "Possible ferroelectricity in perovskite oxynitride SrTaO 2 N epitaxial thin films." *Scientific Reports* **4**: 4987.

Oka, D., et al. (2018). "Anion-Substitution-Induced Non-Rigid Variation of Band Structure in SrNbO3− x N x (0≤ x≤ 1) Epitaxial Thin Films." *ACS applied materials & interfaces*.

Oka, D., et al. (2018). "Anion-Substitution-Induced Nonrigid Variation of Band Structure in SrNbO3–x N x (0≤ x≤ 1) Epitaxial Thin Films." *ACS applied materials & interfaces* **10**(41): 35008-35015.

Ouillon, R., et al. (2002). "A Raman scattering study of the phase transitions in SrTiO3 and in the mixed system (Sr1-xCax) TiO3 at ambient pressure from T= 300 K down to 8 K." *Journal of Physics: Condensed Matter* **14**(8): 2079.

Ouyang, R. (2019). "Exploiting ionic radii for rational design of halide perovskites." *Chemistry of Materials* **32**(1): 595-604.

Palneedi, H., et al. (2018). "High-performance dielectric ceramic films for energy storage capacitors: progress and outlook." *Advanced Functional Materials* **28**(42): 1803665.

Pang, Y., et al. (2018). "Core-shell Fe3O4@ Fe ultrafine nanoparticles as advanced anodes for Li-ion batteries." *Journal of Alloys and Compounds* **735**: 833-839.

Pantea, D., et al. (2003). "Electrical conductivity of conductive carbon blacks: influence of surface chemistry and topology." *Applied Surface Science* **217**(1-4): 181-193.

Paolella, A., et al. (2016). "Accelerated removal of Fe-antisite defects while nanosizing hydrothermal LiFePO4 with Ca2+." *Nano letters* **16**(4): 2692-2697.

Park, K.-S., et al. (2012). "Enhanced charge-transfer kinetics by anion surface modification of LiFePO4." *Chemistry of Materials* **24**(16): 3212-3218.

Park, M., et al. (2010). "A review of conduction phenomena in Li-ion batteries." *Journal of Power Sources* **195**(24): 7904-7929.

Park, Y., et al. (2020). "SrNbO 3 as a transparent conductor in the visible and ultraviolet spectra." *Communications Physics* **3**(1): 1-7.

Pask, J. A. (1989). "Structural ceramics." *Journal of Materials Engineering* **11**(4): 267-274.

Patterson, A. (1939). "The Scherrer formula for X-ray particle size determination." *Physical Review* **56**(10): 978.

Perdew, J. P., et al. (1996). "Generalized gradient approximation made simple." *Physical review letters* **77**(18): 3865.

Pihlatie, M., et al. (2011). "Electrical conductivity of Ni–YSZ composites: Degradation due to Ni particle growth." *Solid State Ionics* **189**(1): 82-90.

Posadas, A. B., et al. (2014). "Band gap of epitaxial in-plane-dimerized single-phase NbO2 films." *Applied Physics Letters* **104**(9): 092901.

Qian, D., et al. (2012). "Lithium lanthanum titanium oxides: a fast ionic conductive coating for lithium-ion battery cathodes." *Chemistry of Materials* **24**(14): 2744-2751.

Qin, S., et al. (2000). "Phase transitions in Ca1− xSrxTiO3 perovskites: effects of composition and temperature." *Journal of Materials Chemistry* **10**(7): 1609-1615.

Qin, S., et al. (2002). "Micro-Raman study of perovskites in the CaTiO 3–SrTiO 3 system." *Journal of the Chemical Society, Dalton Transactions* (19): 3751-3755.

Qiu, J., et al. (2014). "Blue hydrogenated lithium titanate as a high-rate anode material for lithium-ion batteries." *Journal of Materials Chemistry A* **2**(18): 6353-6358.

Qiu, J., et al. (2014). "Hydrogenation synthesis of blue TiO2 for high-performance lithium-ion batteries." *The Journal of Physical Chemistry C* **118**(17): 8824-8830.

R Bajgiran, K., et al. (2019). "Effects of Weak Electric Field on the Photoluminescence Behavior of Bi3+-Doped YVO4: Eu3+ Core–Shell Nanoparticles." *The Journal of Physical Chemistry C* **123**(20): 13027-13035.

Rabuffetti, F. A., et al. (2008). "Synthesis-dependent first-order Raman scattering in SrTiO3 nanocubes at room temperature." *Chemistry of Materials* **20**(17): 5628-5635.

Raccichini, R., et al. (2019). "Critical Review of the Use of Reference Electrodes in Li-Ion Batteries: A Diagnostic Perspective." *Batteries* **5**(1): 12.

Raengthon, N., et al. (2016). "Relationship between tolerance factor and temperature coefficient of permittivity of temperature-stable high permittivity BaTiO3–Bi (Me) O3 compounds." *Journal of Advanced Dielectrics* **6**(01): 1650002.

Ragone, D. V. (1968). Review of battery systems for electrically powered vehicles, SAE Technical Paper.

Ramirez, M. O., et al. (2019). "Emergent room temperature polar phase in CaTiO3 nanoparticles and single crystals." *Apl Materials* **7**(1): 011103.

Rane, A. V., et al. (2018). Methods for synthesis of nanoparticles and fabrication of nanocomposites. *Synthesis of inorganic nanomaterials*, Elsevier**:** 121-139.

Ravel, B. and M. Newville (2005). "ATHENA, ARTEMIS, HEPHAESTUS: data analysis for X-ray absorption spectroscopy using IFEFFIT." *Journal of synchrotron radiation* **12**(4): 537-541.

Reddy, M., et al. (2013). "Metal oxides and oxysalts as anode materials for Li ion batteries." *Chemical reviews* **113**(7): 5364-5457.

Reddy, Y. V. and D. Mergel (2006). "Structural and electrical properties of RuO 2 thin films prepared by rf-magnetron sputtering and annealing at different temperatures." *Journal of Materials Science: Materials in Electronics* **17**(12): 1029-1034.

Rez, P. and A. Blackwell (2011). "Ca L23 spectrum in amorphous and crystalline phases of calcium carbonate." *The Journal of Physical Chemistry B* **115**(38): 11193-11198.

Ridgley, D. and R. Ward (1955). "The Preparation of a Strontium-Niobium Bronze with the Perovskite Structure1." *Journal of the American Chemical Society* **77**(23): 6132-6136.

Rietveld, H. (1969). "A profile refinement method for nuclear and magnetic structures." *Journal of applied crystallography* **2**(2): 65-71.

Rini, M., et al. (2009). "Transient electronic structure of the photoinduced phase of Pr 0.7 Ca 0.3 MnO 3 probed with soft x-ray pulses." *Physical Review B* **80**(15): 155113.

Rischau, C. W., et al. (2017). "A ferroelectric quantum phase transition inside the superconducting dome of Sr 1− x Ca x TiO 3− δ." *Nature Physics* **13**(7): 643.

Rödel, J., et al. (2009). "Development of a roadmap for advanced ceramics: 2010–2025." *Journal of the European Ceramic Society* **29**(9): 1549-1560.

Roh, S., et al. (2018). "Oxygen vacancy induced structural evolution of SrFeO 3− x epitaxial thin film from brownmillerite to perovskite." *Physical Review B* **97**(7): 075104.

Rojas, O. G., et al. (2020). "Synthesis of new sodium strontium niobates via (emim) OAc ionic liquid and an imidazole: choline chloride deep eutectic solvent." *Open Ceramics* **4**: 100032.

Rojas, O. G., et al. (2017). "Fast and scalable synthesis of strontium niobates with controlled stoichiometry." *Crystengcomm* **19**(36): 5351-5355.

Rösler, J., et al. (2007). *Mechanical behaviour of engineering materials: metals, ceramics, polymers, and composites*, Springer Science & Business Media.

Ryabtsev, A., et al. (2000). "Extended analysis of the Nb II spectrum and term system." *Physica Scripta* **62**(5): 368.

Ryll, T., et al. (2010). "Electrical conductivity and crystallization of amorphous bismuth ruthenate thin films deposited by spray pyrolysis." *Physical Chemistry Chemical Physics* **12**(42): 13933-13942.

Safavinia, B., et al. (2020). "Enhancing Ce x Zr1–x O2 Activity for Methane Dry Reforming Using Subsurface Ni Dopants." *ACS Catalysis* **10**(7): 4070-4079.

Saint-Girons, G., et al. (2016). "Epitaxy of SrTiO3 on silicon: the knitting machine strategy." *Chemistry of Materials* **28**(15): 5347-5355.

Salg, P., et al. (2020). "Oxygen diffusion barriers for epitaxial thin-film heterostructures with highly conducting SrMoO3 electrodes." *Journal of applied physics* **127**(6): 065302.

Sansonetti, J. and G. Nave (2010). "Wavelengths, transition probabilities, and energy levels for the spectrum of neutral strontium (Sr I)." *Journal of Physical and Chemical Reference Data* **39**(3): 033103.

Sawaguchi, E. and M. L. Charters (1960). "Symmetry of the low-temperature phase of barium titanate." *Physical Review* **117**(2): 465.

Schinzer, C. (2012). Distortion of perovskites, Retrieved.

Sengodan, S., et al. (2015). "Layered oxygen-deficient double perovskite as an efficient and stable anode for direct hydrocarbon solid oxide fuel cells." *Nature Materials* **14**(2): 205-209.

Seo, J., et al. (2018). "Efficient Solar-Driven Water Oxidation over Perovskite-Type BaNbO2N Photoanodes Absorbing Visible Light up to 740 nm." *Advanced Energy Materials* **8**(24): 1800094.

Shang, C., et al. (2019). "Electron correlations engineer catalytic activity of pyrochlore iridates for acidic water oxidation." *Advanced Materials* **31**(6): 1805104.

Sharifi-Asl, S., et al. (2019). "Oxygen Release Degradation in Li-Ion Battery Cathode Materials: Mechanisms and Mitigating Approaches." *Advanced Energy Materials* **9**(22): 1900551.

Shibagaki, S. and K. Fukushima (1999). "XPS analysis on Nb–SrTiO3 thin films deposited with pulsed laser ablation technique." *Journal of the European Ceramic Society* **19**(6-7): 1423-1426.

Shin, J.-Y., et al. (2012). "Oxygen-deficient TiO2− δ nanoparticles via hydrogen reduction for high rate capability lithium batteries." *Chemistry of Materials* **24**(3): 543-551.

Simon, P. and Y. Gogotsi (2010). "Charge storage mechanism in nanoporous carbons and its consequence for electrical double layer capacitors." *Philosophical Transactions of the Royal Society A: Mathematical, Physical and Engineering Sciences* **368**(1923): 3457-3467.

Souza, A., et al. (2012). "Photoluminescence of SrTiO3: influence of particle size and morphology." *Crystal Growth & Design* **12**(11): 5671-5679.

Stanulis, A., et al. (2019). "Temperature-Induced Structural Transformations in Undoped and Eu3+-Doped Ruddlesden–Popper Phases Sr2SnO4 and Sr3Sn2O7: Relation to the Impedance and Luminescence Behaviors." *Inorganic chemistry* **58**(17): 11410-11419.

Stokes, K., et al. (2019). "Tunable Core–Shell Nanowire Active Material for High Capacity Li-Ion Battery Anodes Comprised of PECVD Deposited aSi on Directly Grown Ge Nanowires." *ACS applied materials & interfaces* **11**(21): 19372-19380.

Stoner, J. L., et al. (2019). "Chemical control of correlated metals as transparent conductors." *Advanced Functional Materials* **29**(11): 1808609.

Strout, N. (2020). "The Department of Defense wants better batteries."

Sun, C., et al. (2020). "Recent advances in perovskite-type oxides for energy conversion and storage applications." *Advanced Energy Materials:* 2000459.

Sun, Y.-F., et al. (2016). "New opportunity for in situ exsolution of metallic nanoparticles on perovskite parent." *Nano letters* **16**(8): 5303-5309.

Sun, Y., et al. (2018). "Strongly correlated perovskite lithium ion shuttles." *Proceedings of the National Academy of Sciences* **115**(39): 9672-9677.

Surmin, A., et al. (2006). "Modulated structure of potassium sodium strontium barium niobates (KNSBN): harmonic solution." *Acta Crystallographica Section B: Structural Science* **62**(2): 228-235.

Swarnkar, A., et al. (2019). "Are chalcogenide perovskites an emerging class of semiconductors for optoelectronic properties and solar cell?" *Chemistry of Materials* **31**(3): 565-575.

Szot, K., et al. (2002). "Localized metallic conductivity and self-healing during thermal reduction of SrTiO 3." *Physical review letters* **88**(7): 075508.

Tan, H., et al. (2014). "Oxygen vacancy enhanced photocatalytic activity of pervoskite SrTiO3." *ACS applied materials & interfaces* **6**(21): 19184-19190.

Tanner, P. A. (2013). "Some misconceptions concerning the electronic spectra of tri-positive europium and cerium." *Chemical Society Reviews* **42**(12): 5090-5101.

Tenne, D. A., et al. (2010). "Ferroelectricity in nonstoichiometric SrTiO 3 films studied by ultraviolet Raman spectroscopy." *Applied Physics Letters* **97**(14): 142901.

Thompson, A., et al. (2001). "X-ray data booklet. Lawrence Berkeley National Laboratory." *University of California, Berkeley, CA* **94720**.

Tiwana, P., et al. (2010). "Ultrafast terahertz conductivity dynamics in mesoporous TiO2: influence of dye sensitization and surface treatment in solid-state dye-sensitized solar cells." The *Journal of Physical Chemistry C* **114**(2): 1365-1371.

Togo, A., et al. (2008). "First-principles calculations of the ferroelastic transition between rutile-type and CaCl 2-type SiO 2 at high pressures." *Physical Review B* **78**(13): 134106.

Tomio, T., et al. (1994). "Control of electrical conductivity in laser deposited SrTiO3 thin films with Nb doping." *Journal of applied physics* **76**(10): 5886-5890.

Triggiani, L., et al. (2016). "Promoting oxygen vacancy formation and p-type conductivity in SrTiO 3 via alkali metal doping: A first principles study." *Physical Chemistry Chemical Physics* **18**(41): 28951-28959.

Tsuda, N., et al. (2013). *Electronic conduction in oxides*, Springer Science & Business Media.

Vaithiyanathan, M., et al. (2019). "Luminescent nanomaterials for droplet tracking in a microfluidic trapping array." *Analytical and bioanalytical chemistry* **411**(1): 157-170.

Valdes, L. B. (1954). "Resistivity measurements on germanium for transistors." *Proceedings of the IRE* **42**(2): 420-427.

Varignon, J., et al. (2019). "Origin of band gaps in 3 d perovskite oxides." *Nature Communications* **10**(1): 1-11.

Venezia, A. M. (2003). "X-ray photoelectron spectroscopy (XPS) for catalysts characterization." *Catalysis Today* **77**(4): 359-370.

Vieten, J., et al. (2019). "Materials design of perovskite solid solutions for thermochemical applications." *Energy & Environmental Science* **12**(4): 1369-1384.

Vijaya Kumar, M. S., et al. (2009). "Effect of oxygen partial pressure on the formation of metastable phases from an undercooled YbFeO3 melt using an aerodynamic levitator." *Journal of the American Ceramic Society* **92**(4): 903-910.

Wan, D., et al. (2019). "New family of plasmonic photocatalysts without noble metals." *Chemistry of Materials* **31**(7): 2320-2327.

Wan, D., et al. (2017). "Electron transport and visible light absorption in a plasmonic photocatalyst based on strontium niobate." *Nature Communications* **8**: 15070.

Wan, D., et al. (2017). "Electron transport and visible light absorption in a plasmonic photocatalyst based on strontium niobate." *Nature Communications* **8**.

Wang, C. and J. Hong (2007). "Ionic/electronic conducting characteristics of LiFePO4 cathode materials: The determining factors for high rate performance." *Electrochemical and Solid State Letters* **10**(3): A65.

Wang, J., et al. (2013). "Surface aging at olivine LiFePO 4: a direct visual observation of iron dissolution and the protection role of nano-carbon coating." *Journal of Materials Chemistry A* **1**(5): 1579-1586.

Wang, L., et al. (2016). "Oxygen Vacancy Induced Room-Temperature Metal–Insulator Transition in Nickelate Films and Its Potential Application in Photovoltaics." *ACS applied materials & interfaces* **8**(15): 9769-9776.

Wang, S. and S. Wang (2015). "Impacts of wind energy on environment: A review." *Renewable and sustainable energy reviews* **49**: 437-443.

Wang, V., et al. (2019). "VASPKIT: A pre-and post-processing program for VASP code." *arXiv preprint arXiv:1908.08269*.

Wang, X., et al. (2020). "Toward High-Energy-Density Lithium Metal Batteries: Opportunities and Challenges for Solid Organic Electrolytes." *Advanced Materials* **32**(18): 1905219.

Wang, Y., et al. (2019). "Role of oxygen vacancies and Mn sites in hierarchical Mn2O3/LaMnO3-δ perovskite composites for aqueous organic pollutants decontamination." *Applied Catalysis B: Environmental* **245**: 546-554.

Wang, Y., et al. (2020). "Role of Ce in Manipulating the Photoluminescence of Tb Doped Y2Zr2O7." *Inorganic chemistry*.

Wang, Y., et al. (2006). "High-Rate LiFePO4 Electrode Material Synthesized by a Novel Route from FePO4· 4H2O." *Advanced Functional Materials* **16**(16): 2135-2140.

Wells, M. P., et al. (2018). "Multiphase strontium molybdate thin films for plasmonic local heating applications." *Optical Materials Express* **8**(7): 1806-1817.

Wenner, F. (1916). *A method of measuring earth resistivity*, US Government Printing Office.

Wong, C. H. A., et al. (2012). "Thermally reduced graphenes exhibiting a close relationship to amorphous carbon." *Nanoscale* **4**(16): 4972-4977.

Wu, H.-C. and Y. Lin (2017). "Effects of oxygen vacancy order–disorder phase transition on air separation by perovskite sorbents." *Industrial & engineering chemistry research* **56**(20): 6057-6064.

Wu, Y. F., et al. (2012). "Enhancement of photoluminescence and color purity of CaTiO3: Eu phosphor by Li doping." *Journal of the American Ceramic Society* **95**(4): 1360-1366.

Wu, Z., et al. (2016). "Aligned Li+ Tunnels in Core–Shell Li (Ni x Mn y Co z) O2@ LiFePO4 Enhances Its High Voltage Cycling Stability as Li-ion Battery Cathode." *Nano letters* **16**(10): 6357-6363.

Xie, X., et al. (2012). "Room temperature magnetic properties of Fe/Co-doped barium niobate crystals." *The Journal of Physical Chemistry C* **116**(43): 23041-23046.

Xu, C.-Y., et al. (2007). "Synthesis of single-crystalline niobate nanorods via ion-exchange based on molten-salt reaction." *Journal of the American Chemical Society* **129**(50): 15444-15445.

Xu, X., et al. (2012). "A red metallic oxide photocatalyst." *Nature Materials* **11**(7): 595.

Yang, C. S., et al. (2018). "All-Solid-State Synaptic Transistor with Ultralow Conductance for Neuromorphic Computing." *Advanced Functional Materials* **28**(42): 1804170.

Yang, D., et al. (2016). "Controllable phase transformation and mid-infrared emission from Er 3+-Doped hexagonal-/cubic-NaYF 4 nanocrystals." *Scientific Reports* **6**: 29871.

Yang, Z., et al. (2010). "Metal-insulator transition characteristics of VO 2 thin films grown on Ge (100) single crystals." *Journal of applied physics* **108**(7): 073708.

Yao, F., et al. (2015). "Carbon-based materials for lithium-ion batteries, electrochemical capacitors, and their hybrid devices." *ChemSusChem* **8**(14): 2284-2311.

Yao, Y., et al. (2011). "Highly conductive, mechanically robust, and electrochemically inactive TiC/C nanofiber scaffold for high-performance silicon anode batteries." *ACS nano* **5**(10): 8346-8351.

Yao, Z., et al. (2018). "Enhancing ultrafast lithium ion storage of Li4Ti5O12 by tailored TiC/C core/shell skeleton plus nitrogen doping." *Advanced Functional Materials* **28**(31): 1802756.

Young, R. and D. Wiles (1982). "Profile shape functions in Rietveld refinements." *Journal of applied crystallography* **15**(4): 430-438.

Yu, Y., et al. (2019). "Enhancing the durable performance of LiMn 2 O 4 at high-rate and elevated temperature by nickel-magnesium dual doping." *Scientific Reports* **9**(1): 1-9.

Zanchet, D., et al. (2000). "X-ray Characterization of Nanoparticles." *Characterization of nanophase materials* **1**: 13-36.

Zeng, Z., et al. (2020). "Rare-earth-containing perovskite nanomaterials: design, synthesis, properties and applications." *Chemical Society Reviews* **49**(4): 1109-1143.

Zhang, J., et al. (2018). "Mineralizer effect on facet-controllable hydrothermal crystallization of perovskite structure YbFeO 3 crystals." *Crystengcomm* **20**(4): 470-476.

Zhang, M., et al. (2018). "Modified Co-precipitation Synthesis of Meso-structure Controlled Li-rich Layered Oxides for Minimizing Voltage Degradation." *ACS Applied Energy Materials*.

Zhang, T., et al. (2018). "High Energy Storage Performance of Opposite Double-Heterojunction Ferroelectricity–Insulators." *Advanced Functional Materials* **28**(10): 1706211.

Zhang, W., et al. (2017). "Platinum nanoparticles supported on defective tungsten bronze-type KSr 2 Nb 5 O 15 as a novel photocatalyst for efficient ethylene oxidation." *Journal of Materials Chemistry A* **5**(36): 18998-19006.

Zhang, Y., et al. (2017). "Thermoelectric phase diagram of the SrTiO3–SrNbO3 solid solution system." *Journal of applied physics* **121**(18): 185102.

Zhou, H., et al. (2007). "Probing structure− parameter correlations in the molten salt synthesis of BaZrO3 perovskite submicrometer-sized particles." *Chemistry of Materials* **19**(22): 5238-5249.

Zhu, T., et al. (2019). "Exsolution and electrochemistry in perovskite solid oxide fuel cell anodes: Role of stoichiometry in Sr (Ti, Fe, Ni) O3." *Journal of Power Sources* **439**: 227077.

Vita

Tochukwu Ofoegbuna was born in Enugu, Nigeria in 1992. He moved to Houston, Texas, USA where earned a Bachelor of Science (B.S.) degree in Chemical Engineering from the University of Houston in May 2015. He subsequently attended the Louisiana State University in Baton Rouge, Louisiana, USA where he is working on his Doctor of Philosophy (PhD) degree in Chemical Engineering. During his PhD work, he received several awards and distinctions such as Flagship Graduate Fellowship (2016), Graduate Student Association Travel Award (2018), Graduate Student in Material Science Certification (2019), Journal of Materials Chemistry C Cover Artwork (2020), and the American Institute of Chemical Engineers Graduate Student Award (2020).

Publications and Presentations

Ofoegbuna, T., Peterson, B., Moura, N.S., Nepal, R., Smith, C., Kizilkaya, O., Jin, R., Plaisance, C., Flake, J.C., Dorman, J.A., Modifying the Electronic Properties of Metastable Sr1-xBO3-δ (B=Nb, Ta, and Mo) Perovskite Nanoparticles, In Preparation

Wang, Y., Darapaneni, P., **Ofoegbuna, T.**, Gupta, S.K., Kizilkaya, O., Mao, Y., Dorman, J.A., Effect of Oxide Ion Distribution on a Uranium Structure in Highly U-Doped RE2Hf2O7 (RE= La and Gd) Nanoparticles, Inorganic Chemistry, 2020, 59 (19), 14070-14077.

Willis, D.E., Taheri, M.M., Kizilkaya, O., Leite, T.R., Zhang, L., **Ofoegbuna, T.**, Ding, K., Dorman, J.A., Baxter, J.B., McPeak, K.M.. Critical Coupling of Visible Light Extends Hot-Electron Lifetimes for H2O2 Synthesis, Applied Materials and Interfaces, 2020, 12 (20), 22778-22788.

Ofoegbuna, T., R. Bajgiran, K., Kizilkaya, O., Thomson, S.A.J., Melvin, A.T., Dorman, J.A., Photoluminescence Detection of Symmetry Transformations in Low-Dimensional Ferroelectric ABO3 Perovskites, Journal of Materials Chemistry C, 2020, 8, 10767-10773

Ofoegbuna, T., Darapaneni, P., Sahu, S., Plaisance, C., Dorman, J.A., Stabilizing the B-site Oxidation State in ABO3 Perovskite Nanoparticles, Nanoscale, 2019, 11 (30), 14303

Ofoegbuna, T., Peterson, B., Moura, N.S., Dorman, J.A. (November 2020), Defect Engineering in Strained Low-Dimensional ABO3 Perovskite Nanoparticles for Next-Generation Energy

Storage Devices. Oral presentation at the annual meeting for the American Institute of Chemical Engineers.

Ofoegbuna, T., Darapaneni, P., Bajgiran, K. R., Kizilkaya, O., Dorman, J.A. (November 2019), Controlling Structural Transformations in Sr(Ti,Nb)O3 Nanocrystals using Defect Chemistry for Next Generation Ferroelectric Devices. Oral presentation at the annual meeting for the American Institute of Chemical Engineers.

Ofoegbuna, T., Darapaneni, P., Dorman, J.A. (November 2018), Low Dimensional Sr1-xNbO3-δ Nanoparticles for Defect-induced Infrared Light Harvesting. Oral presentation at the annual meeting for the Material Research Society.

Ofoegbuna, T., Darapaneni, P., Dorman, J.A. (November 2018), Strained Low Dimensional Sr1-xNbO3-δ Nanoparticles for Infrared Light Harvesting. Oral presentation at the annual meeting for the American Institute of Chemical Engineers.

Ofoegbuna, T., Darapaneni, P., Shelton, W., Dorman, J.A. (August 2018), Plasmon Resonance in Low Dimensional Sr1-xNbO3+δ Nanoparticles. Oral presentation at the Fall meeting for the American Chemical Society.

Ofoegbuna, T., Shelton, W., Dorman, J.A. (March 2018), Plasmonic Excitations in Strained Sr1-xNb1-yO3+δ Nanoparticles. Oral presentation at the Spring meeting for the American Chemical Society.